International Journal of Molecular Imaging

Single Photon Emission Computed Tomography

Single Photon Emission Computed Tomography

International Journal of Molecular Imaging

Single Photon Emission Computed Tomography

Editorial Board

Contents

Hindawi Publishing Corporation
International Journal of Molecular Imaging
Volume 2011, Article ID 106068, 6 pages
doi:10.1155/2011/106068

Review Article

SPECT/CT for Lymphatic Mapping of Sentinel Nodes in Early Squamous Cell Carcinoma of the Oral Cavity and Oropharynx

Haerle Stephan K.[1] and Stoeckli Sandro J.[2]

[1] *Department of Otolaryngology-Head and Neck Surgery, University Hospital Zurich, Frauenklinikstrasse 24, 8091 Zurich, Switzerland*
[2] *Department of Otolaryngology-Head and Neck Surgery, Kantonsspital St. Gallen, Rorschacherstraße 95, 9000 St. Gallen, Switzerland*

Correspondence should be addressed to Stoeckli Sandro J., sandro.stoeckli@kssg.ch

Received 15 July 2010; Accepted 24 August 2010

Academic Editor: Domenico Rubello

Adequate staging and treatment of the neck in squamous cell carcinoma of the oral cavity and oropharynx (OSCC) is of paramount importance. Elective neck dissection (END) of the clinical N0-neck is widely advocated as neck treatment. With regard to the prevalence of 20–40% of occult neck metastases found in the ND specimens, the majority of patients undergo surgery of the lymphatic drainage basin without therapeutic benefit. Sentinel node biopsy (SNB) has been shown to be a safe, reliable and accurate alternative treatment modality for selected patients. Using this technique, lymphatic mapping is crucial. Previous reports suggested a benefit of single photon emission computed tomography with CT (SPECT/CT) over dynamic planar lymphoscintigraphy (LS) alone. SPECT/CT allows the surgeon for better topographical orientation and delineation of sentinel lymph nodes (SLN's) against surrounding structures. Additionally, SPECT/CT has the potential to detect more SLN's which might harbour occult disease, than LS. SPECT/CT is recommended to be used routinely, although SPECT/CT is not indispensable for successful SNB.

1. Background

Squamous cell carcinoma of the oral cavity and oropharynx (OSCC) accounts for one of the most common cancers worldwide, with more than a quarter million new cases annually [1]. The presence or absence of lymph node involvement is of paramount importance for prognosis and therapy decision [2, 3]. Therefore, an adequate staging and management of the neck is needed. The most challenging issue remains the treatment of the clinically and radiologically negative neck. Most centers throughout the world advocate elective neck dissection (END) for histopathologic staging and removal of microscopic disease in this situation. With regard to the prevalence of 20%–40% of occult neck metastases found in the neck dissection specimens, the majority of patients undergo surgery of the lymphatic drainage basin without therapeutic benefit. Sentinel node biopsy (SNB) has been shown to be very accurate in selecting patients who benefit from elective neck treatment and sparing the costs and morbidity to the others. Detection of the sentinel nodes by lymphatic mapping is crucial with this technique. Single-photon emission computed tomography with CT (SPECT/CT) has been recently introduced to enhance the diagnostic accuracy of preoperative lymphoscintigraphy.

2. Sentinel Node Biopsy

By definition, the sentinel lymph node (SLN) is the first draining lymph node to receive lymphatic drainage from a primary tumor of a specific site [4]. In case of lymphatic spread, the lymphatic drain will first pass the SLN. All following nodes may be reached only subsequently by the disease. Therefore, selective excision of the SLN with subsequent thorough histopathologic work-up reflects adequately the nodal status of the remaining neck [5]. Since Alex and Krag [6] have described their first experience with SNB for OSCC, the technique has gained large popularity and many centers followed with validation and observational studies [7–9]. Lymphatic mapping of the SLN in the complex head and neck area has been shown to be essential [10]. The problems

in the head and neck area are threefold: first, there is a high density of lymph nodes, second, the structure of these nodes shows an unique complexity of lymphatic pathways, and third, the SLNs are located in close proximity to the primary tumor. Therefore, sophisticated lymphatic mapping techniques are required. During the preoperative setting, a dynamic lymphoscintigraphy (LS) assesses the individual draining pattern after injection of radiolabeled particles around the primary tumor. The intraoperative use of a hand-held gamma probe helps the surgeon to localise and excise the first echelon lymph nodes. The success of this technique has been abundantly reported in the literature and well-documented guidelines do exist [11]. As with breast cancer, preliminary reports showed a new imaging technology with promising results: SPECT/CT.

3. Patient's Selection

For SNB of the OSCC, patients with stages I and II (T1 and T2) disease and no clinical and radiological evidence of cervical lymph node involvement are eligible. Absence of suspicious or metastatic lymph nodes is based on palpation, ultrasound with fine needle aspiration cytology (FNAC), or contrast-enhanced computed tomography (CT), or magnetic resonance imaging (MRI), or ^{18}F-fluoro-2-deoxy-D-glucose positron emission tomography (^{18}F-FDG-PET)/CT. With regard to conventional imaging, lymph nodes greater than 1.5 cm in level II and greater than 1 cm in all other levels, or lymph nodes with round shape, central necrosis, and peripheral contrast enhancement are considered pathologic. In metabolic imaging, a lymph node with a clearly higher FDG-uptake compared to the background and anatomically corresponding to a lymph node in the low-dose CT scan is considered pathologic.

4. Tracer

To assess the individual lymphatic drainage pattern, a peritumoral injection of radiolabeled particles is performed. The particles will enter the lymphatic capillaries and accumulate in the first draining node. There is a variety of colloidal and soluble tracers available although most trials report using Tc-99m-labeled human serum albumin colloid (Nanocoll, GE Healthcare). With its particle size of 8–30 nm, Nanocoll migrates to the sentinel node within minutes and remains there until the next day [11, 12]. This allows a flexible way for planning surgery to take place.

5. Imaging

A standard technique for preoperative imaging is the use of a gamma camera for lymphoscintigraphy to assess the individual drainage pattern of the injected radiolabeled tracer via the capillaries to the larger collector lymphatics [13]. Imaging will be performed either the day before or the day of surgery. According to *the joint practice guidelines for radionuclide lymphoscintigraphy*, the setting of the camera is proposed to be as follows. A large-field-of-view gamma camera provided with a high- or ultrahigh-resolution low-energy collimator should be used, with a 10%–20% window centered on the 140-keV energy peak of Tc-99m [11]. The gamma camera should be routinely checked for quality control as proposed in published protocols [14].

Immediately after the injection of the radiotracer, the lymphatic drainage is monitored dynamically with the gamma camera in the anteroposterior projection (1 image/3 minutes). The lymphatic drainage is then observed by the nuclear medicine specialist and the HN-surgeon at the monitor. When accumulation of the radiotracer in the first echelon node(s) occurs, the dynamic imaging can be interrupted and static imaging in the anterior-posterior, lateral and, if necessary, anterior oblique view can be performed. For the different projections, a three-headed camera is recommended. To be able to localize the nodes in a three-dimensional view, static images in at least two projections are needed. The patient is imaged in the supine position with head up [11].

Most reports in the literature use the term sentinel node interchangeably for lymphoscintigraphy and SNB. As most tracer accumulations or *hot spots* detected by lymphoscintigraphy or SPECT/CT correspond to more than one ultimately excised sentinel lymph node, the term *hot spot* should be used in the context of planar imaging or fused imaging whereas *sentinel lymph node* should be used in the context of surgical SNB.

Intraoperatively, the surgeon will be guided to the sentinel nodes by a hand-held gamma probe containing a radiation detector with surrounding metal shielding and a collimated tip. The response related to the detected count rate is provided by a connected analyzer [11].

Using this technique, SNB has become a safe and reliable method to detect SLNs with a previously published SLN detection rate of 96% [5].

6. SPECT/CT for Sentinel Node Mapping in HNSCC: A Comparison in the Literature

Besides the previously described imaging technique using a preoperative lymphoscintigraphy, novel systems composed of a gamma camera and a CT scan combined in the same device have been recently introduced into clinical practice. Single photon emission CT (SPECT) and CT data are acquired at the same clinical setting without changing the patient's positioning, thus allowing for generation of accurate fused images combining the functional data of SPECT with the anatomical data of the CT scan (Figure 1). Different centers have already reported on their experience with SPECT/CT for SLN mapping in early OSCC, however, with contradictory results [11, 15–24]. In 2000, Even-Sapir et al. described the fusion of the SPECT lymphoscintigraphy data with CT using a hybrid gamma-camera and a low-dose CT system that allows SPECT and CT to be performed at the same time without changing the patient's position [25]. Three years later, the same author introduced the hybrid SPECT/CT system into sentinel node mapping of HNSCC [15]. In 2004, two feasibility studies using planar

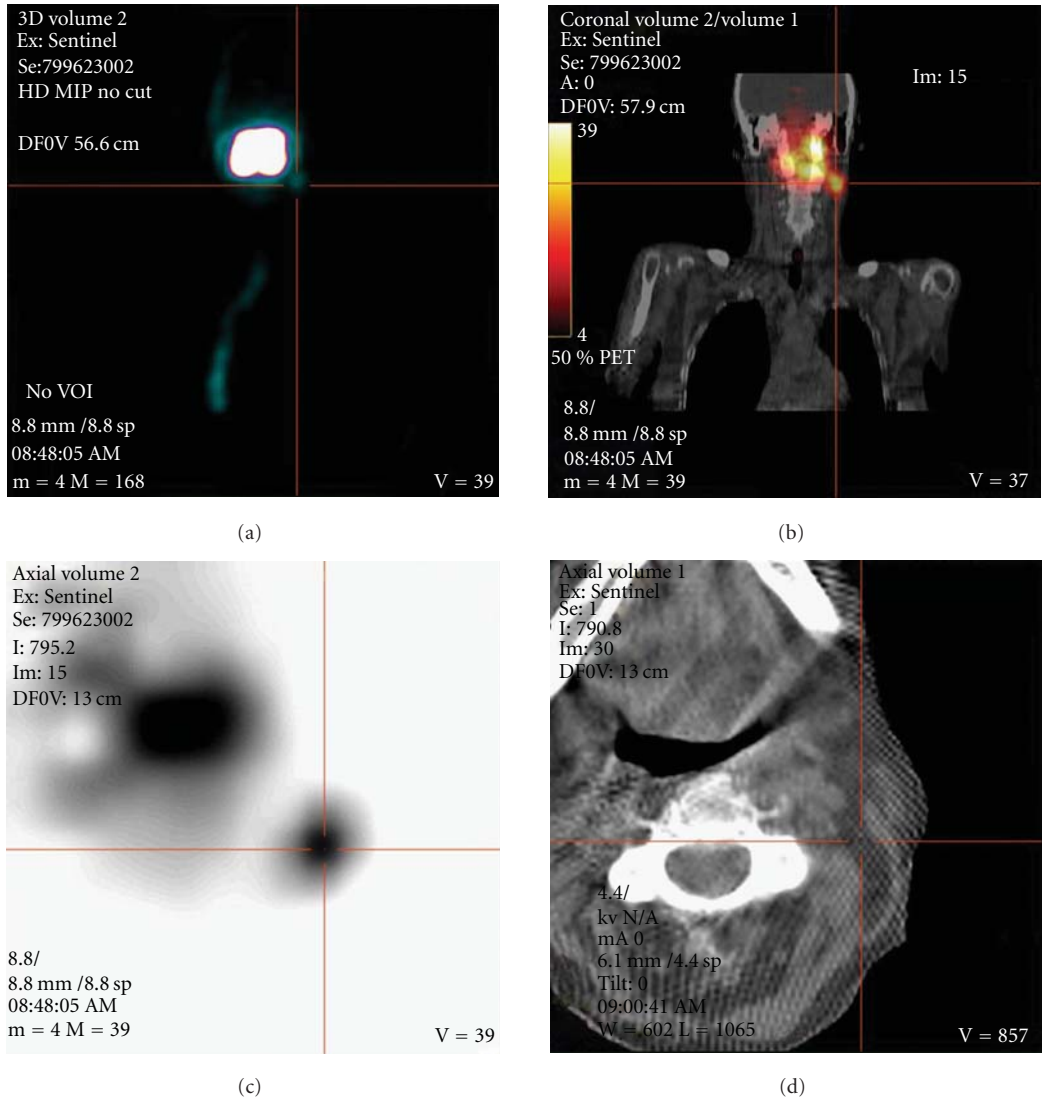

Figure 1: 64-year-old female suffering from a left-sided tongue cancer. (a) shows the MIP (maximum intensity projection)—image of SPECT acquisition in anteroposterior view. A large uptake is seen at the injection site with a small, focal uptake of the left lower boarder (cross hair). (b) shows a fused coronal SPECT/CT image that localises the small focal uptake in the neck region level IIA/B. (c) shows the axial SPECT image with the corresponding cross hair in the sentinel node with a clear delineation from the injection site. (d) shows the corresponding low-dose CT scan localising the uptake by linked cross hair into the neck level IIA/B.

lymphoscintigraphy and SPECT/CT were published [16, 17]. Lopez et al. included ten patients stating that they believe that SPECT/CT will become a useful tool for sentinel node mapping [16]. Wagner et al. found an additional value by using SPECT/CT for sentinel node mapping than lymphoscintigraphy alone [17]: they have found an additional lymph node nearby the submandibular gland which has only been detected by SPECT/CT. This lymph node has been overlooked by planar lymphoscintigraphy and the intraoperative gamma probe as the radioactive scattering from the primary obscured the location of the radiolabeled SLNs. The same problem has been shown by other authors in the earlier period of radioguided imaging [26, 27] and was thought be resolved by introducing SPECT/CT. Thomsen et al. found SLNs close to the primary difficult to detect. Therefore, added oblique planar images and/or tomographic scans would help to overcome this problem [18]. Terada et al. also performed a feasible study on SPECT/CT and HN mucosal carcinoma and concluded that they were able to extract all the SLNs based on the fusioned images and to confirm its radioactivity with the gamma probe without the adverse effect of overlapping radioactivity from the primary site [19]. Khafif et al. included 22 patients with biopsy proven OSCC and found an improved identification of the SLNs of 30% compared to planar imaging [20]. Bilde et al. included 34 consecutive patients with stages I and II OSCC undergoing planar lymphoscintigraphy and SPECT/CT. After all, SPECT/CT demonstrated an extra SLN in 47% compared to lymphoscintigraphy alone [21]. In the same year, Keski-Säntti et al. were the first and only authors who found

Table 1: An overview of various studies using SPECT/CT in the context of lymphatic mapping for SNB in OSCC.

Study group	Number of patients (n)	SPECT/CT and the reported detection of SLN's	The value of SPECT/CT according to the authors
Even-Sapir et al. [15]	6	3 additional nodes detected in 6 patients compared to lymphoscintigraphy alone	SPECT/CT adds data that is of clinical relevance to SNB in patients with mucosal HNSCC
Lopez et al. [16]	10	100% visualization of the SLN's by SPECT/CT	SPECT/CT is shown to be an effective method for anatomic localization of the SLN's in N0 OSCC
Wagner et al. [17]	30	11 additional nodes out of 49 SLNs detected compared to lymphoscintigraphy alone	SPECT/CT adds additional information regarding nodes that are adjacent to the primary lesion
Thomsen et al. [18]	40	SPECT/CT and/or added oblique images revealed extra nodes in 15/40 patients.	SPECT/CT has added information which could not have been obtained from planar lymphoscintigraphy
Terada et al. [19]	15	100% visualization of the SLN's by SPECT/CT	SPECT/CT proved to be an easy, accurate, and reliable method
Khafif et al. [20]	20	SPECT/CT improved SLN identification and/or localization compared with planar images in 6 patients (30%)	SPECT/CT provides additional preoperative data of clinical relevance to SNB in patients with OSCC
Bilde et al. [21]	34	SPECT/CT demonstrated extra SLN's compared to planar imaging in 15 out of 32 patients (47%)	SPECT/CT detects more SLN's than lymphoscintigraphy and provides additional anatomical and spatial information about their localization.
Keski-Säntti et al. [22]	15	1 additional SLN located in the jugular chain detected compared to lymphoscintigraphy alone	SPECT/CT enables more accurate localization of the SLN's, but it rarely reveals SLN's, that are not detected on planar images.
Haerle et al. [23]	58	11 additional hot spots could be revealed by SPECT/CT compared to lymphoscintigraphy alone. In one case even with additional occult disease.	SPECT/CT has the potential to detect more SLN's, which might harbour occult disease, than lymphoscintigraphy alone.

SNB: sentinel node biopsy; OSCC: oral/oropharyngeal squamous cell carcinoma; HNSCC: head and neck squamous cell carcinoma; SLN: sentinel lymph node.

no additionally revealed SLNs by SPECT/CT compared to planar imaging [22]. They concluded that despite the better topographical orientation achieved by SPECT/CT, it is not necessarily needed for preoperative lymphatic mapping. The largest single institutional cohort study was done by Haerle et al. A total of 58 patients undergoing SNB with preoperative lymphoscintigraphy and SPECT/CT have been described. Lymphoscintigraphy showed full concordance with SPECT/CT in 81% of the cases. SPECT/CT was able to detect additional HS in eleven patients, in one case even with additional metastatic disease. Therefore, in conclusion, SPECT/CT has the potential to detect more SLNs, which might harbour occult disease, than Lymphoscintigraphy alone. However, with regard to the excellent results achieved with LS and the intraoperative use of the gamma probe, SPECT/CT is not indispensable for successful SNB. The additional hot spots have all been detected in the same levels or in levels close to those in which lymphoscintigraphy has already shown hot spots. Therefore, both imaging modalities have difficulties in detecting level I sentinel nodes close to the injection site [23]. In summary, the reported series looking at preoperative sentinel node mapping for OSCC were all smaller series apart from the latter series [23]. An overview of the different series is shown in Table 1.

7. In the Future

Wherever applicable and affordable, SPECT/CT might become a routine preoperative imaging solution in the context of SNB for OSCC. As technical developments in SPECT/CT are ongoing [28] and high-resolution multislice CT scanners and the use of intravenous contrast will be integrated in SPECT/CT systems, even further improved spatial resolution of CT images and a better delineation of tumor adjacent structures are available. Together with the use of novel portable gamma-camera systems tested recently [29], possibly the future will provide an integrated system that combines fused imaging with an intraoperative hand-held gamma-camera enabling three-dimensional visualization [30]. Apart from imaging development, new tracers may be integrated in the process of more accurate detection of the sentinel lymph nodes.

8. Conclusions

The technique of SNB offers a reliable, safe, and individual treatment plan for each patient's unique lymphatic drainage pattern causing low morbidity. The use of this successful technique allows the surgeon to select patients for elective

neck dissection of the N0-neck. The use of preoperative planar lymphoscintigraphy and an intraoperative hand-held gamma probe results in excellent sentinel node-detection rates. SPECT/CT allows the surgeon for better topographical orientation and delineation of SLNs against surrounding structures, for example, muscles, vessels, and bones. Additionally, the surgical time may be reduced with regard to better spatial resolution. SPECT/CT has the potential to detect more SLNs, which might harbour occult disease, than lymphoscintigraphy alone. Therefore, we recommend using SPECT/CT routinely, although SPECT/CT is not indispensable for successful SNB.

References

[1] D. M. Parkin, F. Bray, J. Ferlay, and P. Pisani, "Global cancer statistics, 2002," *CA: Cancer Journal for Clinicians*, vol. 55, no. 2, pp. 74–108, 2005.

[2] D. M. Don, Y. Anzai, R. B. Lufkin, Y.-S. Fu, and T. C. Calcaterra, "Evaluation of cervical lymph node metastases in squamous cell carcinoma of the head and neck," *Laryngoscope*, vol. 105, no. 7, pp. 669–674, 1995.

[3] C. G. Gourin, B. T. Conger, E. S. Porubsky, W. C. Sheils, P. A. Bilodeau, and T. A. Coleman, "The effect of occult nodal metastases on survival and regional control in patients with head and neck squamous cell carcinoma," *Laryngoscope*, vol. 118, no. 7, pp. 1191–1194, 2008.

[4] L. H. Sobin and C. H. Wittekind, Eds., *TNM Classification of Malignant Tumors*, John Wiley & Sons, New York, NY, USA, 6th edition, 2002.

[5] S. J. Stoeckli, "Sentinel node biopsy for oral and oropharyngeal squamous cell carcinoma of the head and neck," *Laryngoscope*, vol. 117, no. 9, pp. 1539–1551, 2007.

[6] J. C. Alex and D. N. Krag, "The gamma-probe-guided resection of radiolabeled primary lymph nodes," *Surgical Oncology Clinics of North America*, vol. 5, no. 1, pp. 33–41, 1996.

[7] J. C. Alex, C. T. Sasaki, D. N. Krag, B. Wenig, and P. B. Pyle, "Sentinel lymph node radiolocalization in head and neck squamous cell carcinoma," *Laryngoscope*, vol. 110, no. 2, pp. 198–203, 2000.

[8] T. Shoaib, D. S. Soutar, J. E. Prosser et al., "A suggested method for sentinel node biopsy in squamous cell carcinoma of the head and neck," *Head and Neck*, vol. 21, no. 8, pp. 728–733, 1999.

[9] S. J. Stoeckli, H. Steinert, M. Pfaltz, and S. Schmid, "Sentinel lymph node evaluation in squamous cell carcinoma of the head and neck," *Otolaryngology—Head and Neck Surgery*, vol. 125, no. 3, pp. 221–226, 2001.

[10] G. L. Ross, D. S. Soutar, T. Shoaib et al., "The ability of lymphoscintigraphy to direct sentinel node biopsy in the clinically N0 neck for patients with head and neck squamous cell carcinoma," *British Journal of Radiology*, vol. 75, no. 900, pp. 950–958, 2002.

[11] L. W. T. Alkureishi, Z. Burak, J. A. Alvarez, et al., "Joint practice guidelines for radionuclide lymphoscintigraphy for sentinel node localization in oral/oropharyngeal squamous cell carcinoma," *Annals of Surgical Oncology*, vol. 16, no. 11, pp. 3190–3210, 2009.

[12] A. J. Wilhelm, G. S. Mijnhout, and E. J. F. Franssen, "Radiopharmaceuticals in sentinel lymph-node detection—an overview," *European Journal of Nuclear Medicine*, vol. 26, pp. S36–S42, 1999.

[13] S. Modi, A. W. B. Stanton, P. S. Mortimer, and J. R. Levick, "Clinical assessment of human lymph flow using removal rate constants of interstitial macromolecules: a critical review of lymphoscintigraphy," *Lymphatic Research and Biology*, vol. 5, no. 3, pp. 183–202, 2007.

[14] IEC/TR 61948-2 Ed. 1.0, "Nuclear medicine instrumentation-Routine tests-Part 2: scintillation cameras and single photon emission computed tomography imaging," Tech. Rep., International Electrotechnical Commission, Geneva, Switzerland, 2001.

[15] E. Even-Sapir, H. Lerman, G. Lievshitz et al., "Lymphoscintigraphy for sentinel node mapping using a hybrid SPECT/CT system," *Journal of Nuclear Medicine*, vol. 44, no. 9, pp. 1413–1420, 2003.

[16] R. Lopez, P. Payoux, P. Gantet, J. P. Esquerré, F. Boutault, and J. R. Paoli, "Multimodal image registration for localization of sentinel nodes in head and neck squamous cell carcinoma," *Journal of Oral and Maxillofacial Surgery*, vol. 62, no. 12, pp. 1497–1504, 2004.

[17] A. Wagner, K. Schicho, C. Glaser et al., "SPECT-CT for topographic mapping of sentinel lymph nodes prior to gamma probe-guided biopsy in head and neck squamous cell carcinoma," *Journal of Cranio-Maxillofacial Surgery*, vol. 32, no. 6, pp. 343–349, 2004.

[18] J. B. Thomsen, J. A. Sørensen, P. Grupe, and A. Krogdahl, "Sentinel lymph node biopsy in oral cancer: validation of technique and clinical implications of added oblique planar lymphoscintigraphy and/or tomography," *Acta Radiologica*, vol. 46, no. 6, pp. 569–575, 2005.

[19] A. Terada, Y. Hasegawa, M. Goto et al., "Sentinel lymph node radiolocalization in clinically negative neck oral cancer," *Head and Neck*, vol. 28, no. 2, pp. 114–120, 2006.

[20] A. Khafif, S. Schneebaum, D. M. Fliss et al., "Lymphoscintigraphy for sentinel node mapping using a hybrid single photon emission CT (SPECT)/CT system in oral cavity squamous cell carcinoma," *Head and Neck*, vol. 28, no. 10, pp. 874–879, 2006.

[21] A. Bilde, C. Von Buchwald, J. Mortensen et al., "The role of SPECT-CT in the lymphoscintigraphic identification of sentinel nodes in patients with oral cancer," *Acta Oto-Laryngologica*, vol. 126, no. 10, pp. 1096–1103, 2006.

[22] H. Keski-Säntti, S. Mätzke, T. Kauppinen, J. Törnwall, and T. Atula, "Sentinel lymph node mapping using SPECT-CT fusion imaging in patients with oral cavity squamous cell carcinoma," *European Archives of Oto-Rhino-Laryngology*, vol. 263, no. 11, pp. 1008–1012, 2006.

[23] S. K. Haerle, T. F. Hany, K. Strobel, D. Sidler, and S. J. Stoeckli, "Is there an additional value of spect/ct over planar lymphoscintigraphy for sentinel node mapping in oral/oropharyngeal squamous cell carcinoma?" *Annals of Surgical Oncology*, vol. 16, no. 11, pp. 3118–3124, 2009.

[24] L. Vermeeren, W. M. C. Klop, M. W. M. van den Brekel, A. J. M. Balm, O. E. Nieweg, and R. A. Valdés Olmos, "Sentinel node detection in head and neck malignancies: innovations in radioguided surgery," *Journal of Oncology*, vol. 2009, Article ID 681746, 10 pages, 2009.

[25] E. Even-Sapir, Z. Keidar, J. Sachs et al., "The new technology of combined transmission and emission tomography in evaluation of endocrine neoplasms," *Journal of Nuclear Medicine*, vol. 42, no. 7, pp. 998–1004, 2001.

[26] W. M. Koch, M. A. Choti, A. C. Civelek, D. W. Eisele, and J. R. Saunders, "Gamma probe-directed biopsy of the sentinel node in oral squamous cell carcinoma," *Archives of Otolaryngology—Head and Neck Surgery*, vol. 124, no. 4, pp. 455–459, 1998.

[27] D. R. Colnot, E. J. C. Nieuwenhuis, M. W. M. van den Brekel et al., "Head and neck squamous cell carcinoma: us-guided fine-needle aspiration of sentinel lymph nodes for improved staging—initial experience," *Radiology*, vol. 218, no. 1, pp. 289–293, 2001.

[28] A. K. Buck, S. Nekolla, S. Ziegler et al., "SPECT/CT," *Journal of Nuclear Medicine*, vol. 49, no. 8, pp. 1305–1319, 2008.

[29] L. Vermeeren, R. A. Valdés Olmos, W. M. Klop, A. J. Balm, and M. W. van den Brekel, "A portable gamma-camera for intraoperative detection of sentinel nodes in the head and neck region," *Journal of Nuclear Medicine*, vol. 51, no. 5, pp. 700–703, 2010.

[30] T. Wendler, A. Hartl, T. Lasser et al., "Towards intra-operative 3D nuclear imaging: reconstruction of 3D radioactive distributions using tracked gamma probes," *Medical Image Computing and Computer-Assisted Intervention*, vol. 10, no. 2, pp. 909–917, 2007.

Hindawi Publishing Corporation
International Journal of Molecular Imaging
Volume 2011, Article ID 630813, 6 pages
doi:10.1155/2011/630813

Research Article

Reduction of Collimator Correction Artefacts with Bayesian Reconstruction in Spect

Tuija Kangasmaa,[1] Antti Sohlberg,[2] and Jyrki T. Kuikka[3,4]

[1] *Department of Radiation Therapy, Vaasa Central Hospital, Hietalahdenkatu 2-4, 65100 Vaasa, Finland*
[2] *HERMES Medical Solutions, Skeppsbron 44, 11130 Stockholm, Sweden*
[3] *Department of Clinical Physiology and Nuclear Medicine, Kuopio University Hospital, P.O. Box 1777, 70211 Kuopio, Finland*
[4] *Niuvanniemi Hospital, 70211 Kuopio, Finland*

Correspondence should be addressed to Jyrki T. Kuikka, jyrki.kuikka@kuh.fi

Received 30 July 2010; Revised 29 September 2010; Accepted 29 October 2010

Academic Editor: Thomas Beyer

Poor resolution of single photon emission computed tomography (SPECT) has degraded its use in clinical practice. Collimator correction has been shown to improve the reconstructed resolution, but the correction can generate ringing artefacts, which lower image quality. This paper investigates whether Bayesian reconstruction methods could reduce these artefacts. We have applied and tested three Bayesian reconstruction methods: smoothing prior, median root prior, and anatomical prior. To demonstrate the efficacy of these methods, we compared their physical and visual performance both in phantom and patient studies. All the three Bayesian reconstruction methods reduced the collimator correction artefacts. Images reconstructed using the smoothing prior and the median root prior had slightly lower contrast than the standard reconstruction with collimator correction, whereas the anatomical prior produced images with good resolution and contrast.

1. Introduction

Collimator response correction during iterative SPECT reconstruction has recently gained a lot of attention. The collimator response correction has been shown to simultaneously increase reconstructed resolution and lower image noise level [1]. This improvement in resolution-noise trade-off has further been shown to lead to better lesion detection performance [2, 3] and higher quantitative accuracy [4].

The improved resolution-noise trade-off has also given rise to the idea of half-time imaging; that is with the new correction methods it could be possible to acquire data with at least the currently accepted image quality, only at half the acquisition time [5, 6]. The advantages of the half-time imaging are remarkable: with the imaging time reduced to half, artefacts caused by patient movement are to decrease and the imaging would become more conceivable for patients that find it hard to stay still during long acquisitions. Decreased imaging time would also allow more patients to be imaged per day or the current imaging time could be kept the same but the injected activity would be reduced to half, which would reduce the radiation dose and the amount of the radiopharmaceutical used.

Despite its many benefits, collimator response correction has its disadvantages. Iterative reconstruction with collimator correction complicates the reconstruction algorithm markedly and leads to longer reconstruction times. This, however, is not a major problem nowadays due to the increased computing power of modern computers. Collimator response correction has also been noticed to generate severe Gibbs-like ringing artefacts (see Figure 1) [7, 8]. The nature of these artefacts has not been well documented in the literature, and methods how to reduce these artefacts have not been widely published.

The ringing artefacts are generated, when the collimator correction algorithm tries to recover fine details that have been lost due to the low spatial resolution of the gamma camera. The correction is not perfect and might lead to edge over- and undershoots.

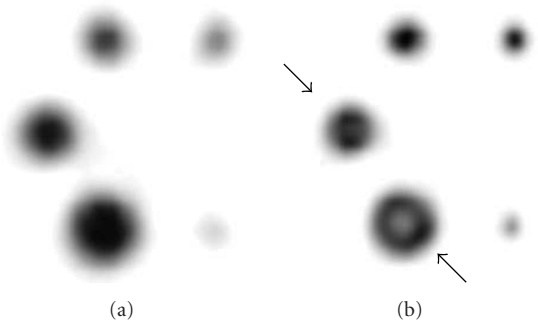

(a) (b)

Figure 1: An example of the Gibbs-like ringing artefacts. Image (a) represents a reconstructed transverse slice of a phantom with active spheres with different diameters without collimator response correction, and image (b) shows a transverse slice with collimator response correction. While the collimator response correction improves the image resolution, it generates an artefact that can be seen as a hole in the middle of the two biggest circles, indicated by black arrows.

Noise can also be considered as pixel value over- and undershoots. Bayesian reconstruction methods can reduce these over- and undershoots by favouring images whose adjacent pixel values are close to each other and thus they can offer effective noise suppression [9]. The aim of this work was to investigate whether Bayesian reconstruction methods could reduce the ringing artefacts by stabilising the reconstruction.

2. Materials and Methods

2.1. Implementation of the Reconstruction Methods. The reconstruction methods used in this work were based on the reconstruction engine of HERMES HybridRecon (HERMES Medical Solutions, Stockholm, Sweden). The ordered subset expectation maximisation (OSEM) algorithm in the engine was implemented as

$$f_j^{\text{new}} = \frac{f_j^{\text{old}}}{\sum_{i\in S_n} a_{ij}} \sum_{i\in S_n} a_{ij} \frac{p_i}{\sum_k a_{ik} f_k^{\text{old}}}, \quad (1)$$

where f is the reconstructed image, p the measured projections, j (or k) reconstruction voxel index, i projection pixel index, a_{ij} the probability that emission from voxel j is detected in pixel i, and S_n the nth subset. The image-update in OSEM consists of sequential forward- and back-projection operations. The estimated projections are obtained by forward-projecting the current image estimate ($\sum_k a_{ik} f_k^{\text{old}}$), and correction factors that are used to update the old image are formed by back-projecting the ratio of the measured and estimated projections ($\sum_{i\in S_n} a_{ij}(p_i/\sum_k a_{ik} f_k^{\text{old}})$). The forward- and back-projectors were implemented as rotation-based [10] and included attenuation and detector response compensation. Attenuation correction factors for each voxel were calculated simply by summing the rotated attenuation map along columns. The attenuation map was generated from a CT using bilinear conversion. Collimator correction was implemented using Gaussian diffusion [11].

The Bayesian reconstruction methods were implemented as the one step late (OSL) algorithm [12]:

$$f_j^{\text{new}} = \frac{f_j^{\text{old}}}{\sum_{i\in S_n} a_{ij} + \beta(\partial U(f^{\text{old}})/\partial f^{\text{old}})} \sum_{i\in S_n} a_{ij} \frac{p_i}{\sum_k a_{ik} f_k^{\text{old}}}, \quad (2)$$

where β is the Bayesian weight and U is the energy function that defines the penalty. In the OSL algorithm, the current image estimate is updated by multiplying it with two factors: the OSEM correction factor ($c_j^I = \sum_{i\in S_n} a_{ij}(p_i/\sum_k a_{ik} f_k^{\text{old}})$) and the penalty factor ($c_j^P = 1/(\sum_{i\in S_n} a_{ij} + \beta(\partial U(f^{\text{old}})/\partial f^{\text{old}}))$). Three different penalties were implemented.

The first one was the quadratic smoothing prior and its penalty factor was implemented in a relative form defined in [13]:

$$c_j^P = \frac{1}{\sum_{i\in S_n} a_{ij} + \beta\left(\left(f_j^{\text{old}} - A_j\right)/A_j\right)}, \quad (3)$$

where $A_j = \sum_{k\in N_j} w_{jk} f_k^{\text{old}}$, N_j is the neighbourhood of voxel j and w_{jk} is the prior weight. The prior weights were defined as the inverse of the distance from the centre voxel.

The second penalty was the median root prior with the following penalty factor:

$$c_j^P = \frac{1}{\sum_{i\in S_n} a_{ij} + \beta\left(\left(f_j^{\text{old}} - M_j\right)/M_j\right)}, \quad (4)$$

where M_j is the median voxel value in the neighbourhood of voxel j [13].

The third penalty was the Bowsher prior [14, 15]. The penalty factor of the Bowsher prior is similar to the quadratic smoothing prior with the exception that the factor A_j is calculated using only B-number of voxels in the neighbourhood N_j that are the most similar with the centre voxel j according to a similarity criterion. The most similar voxels were found by comparing the absolute difference in CT values. A block diagram of the implementation of the reconstruction methods is illustrated in Figure 2.

2.2. Phantoms. Two different phantoms were used: PTW-Freiburg's PET/SPECT-Phantom, set T43004.1.008-0106 (PTW, Freiburg, Germany), which included a hot-sphere insert and Veenstra Instruments' SPECT-phantom model PS-101 (Veenstra Instruments, Joure, Netherlands) with three different inserts for image quality control. All the images were acquired with Philips Precedence SPECT/CT scanner at the Clinical Physiology and Nuclear Medicine Department of Kuopio University Hospital. The scanner has a 6-slice CT combined with a dual-head gamma camera.

PTW-Freiburg's hot sphere insert has six hollow glass spheres with inner, active diameters of 10, 13, 17, 22, 28, and 37 mm, though the phantom used in this study was missing the 13 mm sphere. The spheres were mounted via thin rods into a plastic plate that could be used as the cover for the phantom body. The phantom body was a cylinder with outer

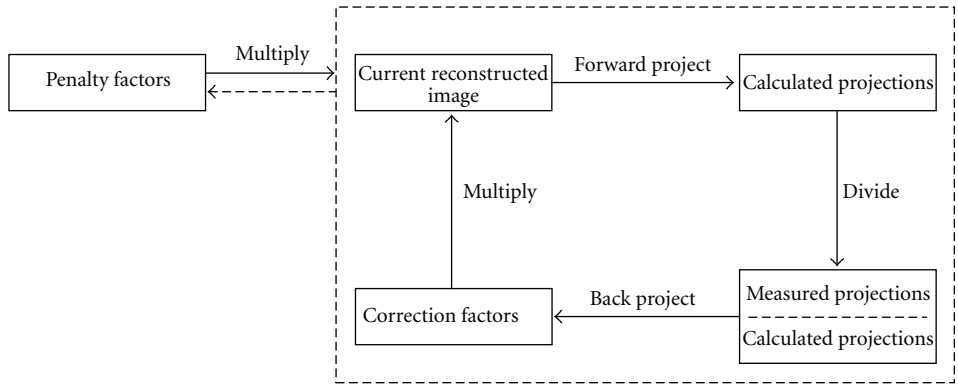

Figure 2: Block diagram of OSEM and OSL reconstruction algorithms. OSEM iteration (inside the dashed rectangle) consists of the following steps: forward-projection of the current reconstructed image, division of measured and calculated projections, back-projection of the quotient, and multiplication of the current reconstructed image and the back-projected correction factors. OSL iteration differs only by the multiplication with the penalty factors that have been calculated by using the current reconstructed image.

(a) (b)

Figure 3: PTW-Freiburg's phantom with the hot-sphere insert attached (a) and the hot-sphere insert (b) on its own. The insert includes hollow spheres with different diameters, which can be filled via thin capillaries.

diameter of 236 mm. Figure 3 shows images of this phantom and the hot-sphere insert.

The spheres were filled with Tc-99m-water compound with activity concentration of 4 MBq/ml, while the phantom body was filled with water. The CT images were acquired as low-dose images with 140 kV and 20 mAs, matrix size of 512 × 512, pixel size of 1.17 mm and slice to slice separation 4.27 pixels. The SPECT images were acquired with circular orbit, 360 degree acquisition with 128 angles. We used 128 × 128 matrix size and 25 s acquisition time per angle. The detectors were set for the smallest possible radius of rotation, in this case 24 cm.

Veenstra Instruments' SPECT-phantom has hot and cold lesion resolution insert with different diameters, a linearity insert with crossed grid pattern, and free segment which is used for homogeneity tests. These are shown in Figure 4. The inserts were in a cylinder shaped tank with inner diameter of 215 mm. The cold lesion insert consisted of 7 plastic rods with active diameters of 5.9, 7.3, 9.2, 11.4, 14.3, 17.9, and 22.3 mm, while the hot lesion insert had 8 pairs of holes with active diameters of 4.7, 5.9, 7.3, 9.2, 11.4, 14.3, 17.9, and 22.3 mm. 250 MBq of Tc-99m elute was added to the tank filled with water. The CT and SPECT data were acquired with the same imaging parameters as the data for the hot-sphere phantom.

2.3. Clinical Data. In addition to the phantom studies, a bone SPECT data was reconstructed with the five algorithms to show the effect of the different reconstruction methods on clinical data. The patient had a Tc-99m-MDP injection of 925 MBq. The images were acquired with Siemens Symbia SPECT/CT scanner. The SPECT data was obtained as a 360 degree acquisition, with matrix size of 128 × 128 and pixel size of 4.8 mm. 64 projections were imaged while time per angle was 20 s. The CT data was obtained as low-dose images with 130 kV and 28 mAs, matrix size of 512 × 512, pixel size of 0.98 mm, and slice to slice separation of 5.12 pixels.

2.4. Reconstruction and Data Analysis. Both phantoms were reconstructed using OSEM (16 subsets and 5 iterations) with/without collimator response correction and using the three Bayesian reconstruction methods (16 subsets and 5 iterations) defined above. The neighbourhood size was set to 3 × 3 × 3 and the Bayesian weight to 0.3 for the smoothing prior and median root prior. Eighteen closest neighbours were scanned in the Bowsher prior and 9 most

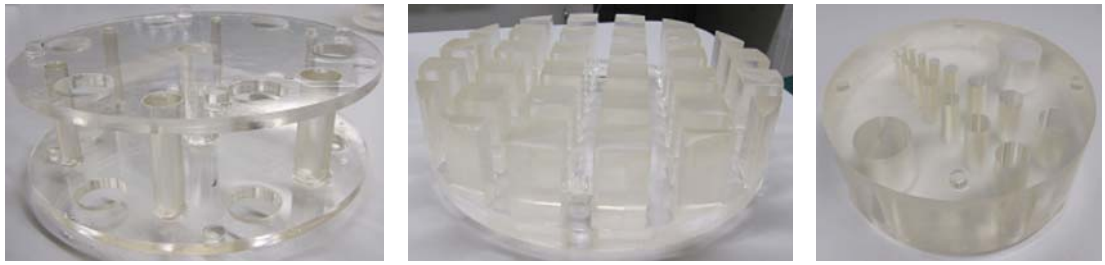

(a) (b) (c)

Figure 4: Veenstra Instruments' SPECT-phantom's inserts. Images (a)–(c) show the cold lesion insert, the grid insert, and the hot lesion insert, respectively.

similar voxels were selected. These parameters were selected according to initial phantom tests, where we tried to find the best compromise between resolution, noise level, and collimator correction artefact reduction.

CT-based attenuation correction was applied in all reconstructions. OSEM reconstructions of the Veenstra Instruments' SPECT-phantom were postfiltered with a 3D Gaussian postfilter with 0.75 cm full-width at half maximum. The clinical study was reconstructed using the same parameters as the phantom studies with the exception that 8 subsets and 10 iterations were used and in the Bowsher prior 6 most similar voxels were selected for the penalty calculation. OSEM reconstructions were postfiltered with 1.0 cm Gaussian postfilter.

The collimator correction artefacts were studied by taking profiles through the active spheres of the PTW-Freiburg's PET/SPECT-Phantom. We also measured contrasts of the four biggest spheres by drawing concentric circular ROIs around the spheres. The smaller ROIs were drawn on the hot sphere, and the nonoverlapping area between the smaller and larger ROIs served as the background in the contrast calculations. The contrasts were calculated as

$$C = \frac{A_{\text{sph}} - A_{\text{bg}}}{A_{\text{sph}} + A_{\text{bg}}} \times 100\%, \tag{5}$$

where A_{sph} is the activity of the hot sphere and A_{bg} the background activity. The ROI areas were drawn on the CT data that was resampled to fit the SPECT data and copied to every reconstructed data, so their position and area were equal in every image. The overall image quality was investigated using the Veenstra Instruments' SPECT-phantom.

3. Results

The hot-sphere phantom was used to study the reconstruction artefacts caused by the collimator correction. The images of the hot-sphere insert with the measured profiles of the largest sphere are shown in Figure 5. The theoretical profile of the active sphere, scaled to the maximum value of the reconstructed image, was also plotted to show the actual profile of the insert. OSEM with collimator correction image and profile in Figure 5 shows the common artefact for collimator correction, showing a hole in the middle of the sphere and therefore making the profile two-peaked. The reconstruction artefact is best seen with the largest sphere. We assume that in smaller spheres the two "edge-peaks" partly merge into one peak and overestimate the activity-concentration. The artefact is nearly fully corrected in the three following images calculated with the other reconstruction methods. The median root prior and smoothing prior, however, have slightly lower resolution than OSEM with collimator correction. The profile shape of the Bowsher prior is close to the true shape, but a more distinct "halo" can be seen around the hot spheres than with the rest of the reconstruction algorithms.

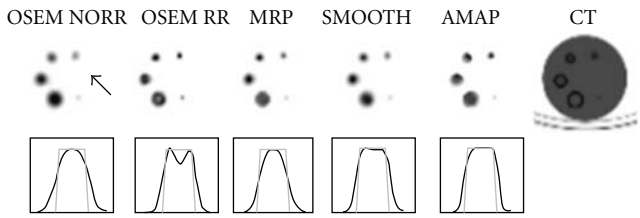

Figure 5: A representative slice taken from the PTW-Freiburg's PET/SPECT phantom with the hot-sphere insert with the five different reconstruction methods used and also the equivalent CT slice. Below, the images profiles for the largest sphere (black line) and the corresponding theoretical profile (grey line) scaled to the reconstructed image's maximum value are shown. From left to right: OSEM without collimator correction (OSEM NORR), OSEM reconstruction with collimator correction (OSEM RR), Median root prior (MRP), Quadratic smoothing prior (SMOOTH), Bowsher prior (AMAP), and low-dose CT slice, which has been resampled to SPECT image size. The black arrow marks the location of the missing sphere.

The contrast values for each reconstruction method are shown in Table 1. OSEM without collimator correction produced lowest contrast values for every sphere. Collimator correction increases the contrasts. Median root prior and smoothing prior are inferior to OSEM with collimator correction, but clearly superior to OSEM without collimator correction. The Bowsher prior produces the highest contrast values overall.

Figure 6 shows one representative slice from every insert of the Veenstra Instruments' SPECT-phantom with every reconstruction method and the equivalent CT slice.

Table 1: Contrast values of the 4 biggest spheres for the five different reconstruction methods: OSEM without collimator correction (OSEM NORR), OSEM reconstruction with collimator correction (OSEM RR), Median root prior (MRP), Quadratic smoothing prior (SMOOTH), and Bowsher prior (AMAP).

Method	OSEM NORR	OSEM RR	MRP	SMOOTH	AMAP
Sphere 1	0.741	0.888	0.871	0.810	0.910
Sphere 2	0.691	0.849	0.817	0.776	0.898
Sphere 3	0.595	0.802	0.768	0.701	0.802
Sphere 4	0.519	0.782	0.702	0.620	0.742

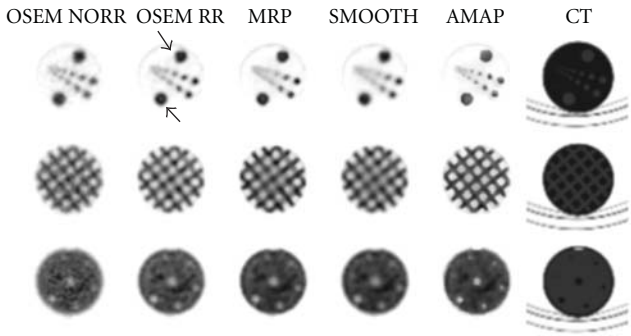

Figure 6: A representative slice taken from the three inserts of the Veenstra Instruments' SPECT-phantom with the different reconstruction methods used and also the equivalent CT slice. From left to right: OSEM without collimator correction (OSEM NORR), OSEM with collimator correction (OSEM RR), Median root prior (MRP), Quadratic smoothing prior (SMOOTH), Bowsher prior (AMAP), and low-dose CT slice, which has been resampled to SPECT image size. Arrows show faint ringing artefacts on the largest rods.

The Bowsher prior produces highest resolution and effective partial volume effect correction, but the hot rods look blocky due to the large voxel size. The images reconstructed via smoothing prior and median root prior methods are a bit too smoothed. OSEM without collimator correction has a relatively good resolution, but the images are quite grainy due to noise. OSEM with collimator correction provides better resolution, but ringing artefacts can be seen on the largest hot rods.

Reconstruction times for the five reconstruction methods have been listed in Table 2. OSEM reconstruction without collimator correction is the fastest, and collimator correction increases the reconstruction time by a factor of 1.3. The Bayesian reconstruction methods are slower than OSEM, because they require scanning of the neighbourhood of every image voxel when the penalty is calculated. Median root prior and Bowsher prior also have to organise the scanned values into ascending order, which takes additional time. For the Bowsher prior, the sorting order can, however, be precalculated before the actual reconstruction, because only the anatomical image is used for sorting.

Figure 7 shows the results for the bone SPECT reconstructions. The same effects can be seen in these images as in the Figures 5 and 6. Bowsher prior produced images with highest resolution while median root prior and smoothing prior make the slices look slightly too smooth. OSEM without collimator correction image has the lowest resolution, and OSEM with collimator correction image is noisier than images reconstructed using the Bayesian methods.

Table 2: Reconstruction times with Dell Optiplex 755. 2 × 2.33 GHz processors and 8 GB RAM of the Veenstra Instruments' SPECT-phantom for the five different reconstruction methods: OSEM without collimator correction (OSEM NORR), OSEM reconstruction with collimator correction (OSEM RR), Median root prior (MRP), Quadratic smoothing prior (SMOOTH), and Bowsher prior (AMAP).

Method	OSEM NORR	OSEM RR	MRP	SMOOTH	AMAP
Time (min)	3.0	3.8	7.0	4.4	4.3

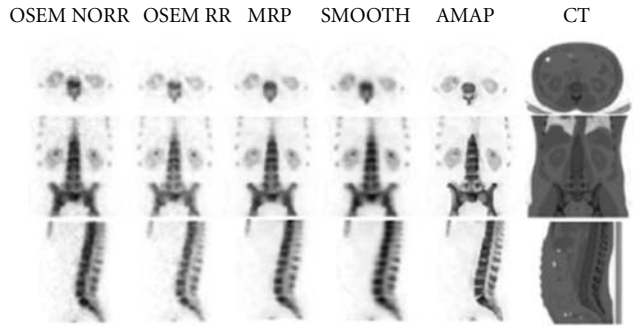

Figure 7: Clinical bone SPECT reconstructed with the five different algorithms. From left to right: OSEM without collimator correction (OSEM NORR), OSEM with collimator correction (OSEM RR), Median root prior (MRP), Quadratic smoothing prior (SMOOTH), Bowsher prior (AMAP), and low-dose CT slice, which has been resampled to SPECT image size.

4. Discussion

This paper studied the effect of three Bayesian reconstruction methods on SPECT collimator correction artefacts. The penalties of these reconstruction methods can be considered to belong into three different categories: simple smoothing penalty, edge-preserving penalty, and anatomically set penalty. These three methods were chosen due to their ease of implementation and usage. They require only slight modification to the common OSEM algorithm, and they are easy to use because they do not have many free parameters.

The quadratic smoothing prior is probably the most commonly used penalty. It penalises images, whose voxel values differ a lot in a near neighbourhood and thus it provides smooth images. This same feature also reduces the collimator correction ringing artefacts. The high edges and deep valleys are penalised during reconstruction and images with less ringing artefacts and with very low noise level will be produced as can be seen from Figures 5–7. Unfortunately the smoothing prior also penalises real edges and easily generates overly smooth images.

The median root prior is an edge-preserving penalty. In contrast to penalising images whose local neighbourhood is not uniform, median root prior penalises images which

are not locally monotonic. This behaviour allows median root prior to pass edges without a penalty, but still reduce noise effectively. Median root prior can produce images, whose resolution is better than the resolution of images reconstructed with the smoothing prior (Figures 5–7). Median root prior cannot always fully separate the false edges generated by the collimator correction from real edges and thus faint collimator correction artefacts might be seen if the Bayesian weight is set to a too low value.

The Bowsher prior is an anatomically set penalty. It tries to restrict smoothing into anatomical regions whose voxel values in the anatomical image are similar. This behaviour provides good collimator correction artefact reduction (Figures 5–7), because, for example, in the PTW-Freiburg's PET/SPECT phantom study, the smoothing was partly restricted inside and outside of the spheres. The voxel size used in this study was relatively big when compared to the size of the spheres or the targets in the Veenstra Instruments' SPECT-phantom as can be seen from the blocky features shown in the CT images in Figures 5 and 6. This lowers the performance of the Bowsher prior.

The success of anatomically set penalties is limited by the registration accuracy of the anatomical and the SPECT image and also by the fact how well the anatomical and molecular images match. Many anatomically set penalties also require image segmentation into different tissue classes [16, 17], which greatly adds complexity to the reconstruction algorithm. Fortunately, the Bowsher prior operates with original voxel values and does not need segmentation. Full clinical utilisation of the Bowsher prior, however, still require much more work.

The clinical effects of the collimator correction artefacts are unknown. It is possible that lesion detection performance or quantitative accuracy is not adversely affected by the ringing artefacts. It is also possible that for example, the slightly lower resolution of the smoothing prior or the median root prior decompensates the gain that the lack of collimator correction artefacts provides. Despite all this, it is still important to acknowledge that collimator correction is not artefact-free and the possible existence the artefacts should be kept in mind when evaluating SPECT images reconstructed using standard OSEM algorithms.

5. Conclusions

All the three Bayesian reconstruction methods presented in this work reduced the collimator correction artefacts. The Bowsher prior provided the reduction without adverse effects on reconstructed resolution or contrast.

References

[1] Y. H. Lau, B. F. Hutton, and F. J. Beekman, "Choice of collimator for cardiac SPET when resolution compensation is included in iterative reconstruction," *European Journal of Nuclear Medicine*, vol. 28, no. 1, pp. 39–47, 2001.

[2] H. C. Gifford, M. A. King, R. Glenn Wells, W. G. Hawkins, M. V. Narayanan, and P. H. Pretorius, "LROC analysis of detector-response compensation in SPECT," *IEEE Transactions on Medical Imaging*, vol. 19, no. 5, pp. 463–473, 2000.

[3] E. C. Frey, K. L. Gilland, and B. M. W. Tsui, "Application of task-based measures of image quality to optimization and evaluation of three-dimensional reconstruction-based compensation methods in myocardial perfusion SPECT," *IEEE Transactions on Medical Imaging*, vol. 21, no. 9, pp. 1040–1050, 2002.

[4] B. He, Y. Du, X. Song, W. P. Segars, and E. C. Frey, "A Monte Carlo and physical phantom evaluation of quantitative In-111 SPECT," *Physics in Medicine and Biology*, vol. 50, no. 17, pp. 4169–4185, 2005.

[5] E. G. DePuey, R. Gadiraju, J. Clark, L. Thompson, F. Anstett, and S. C. Shwartz, "Ordered subset expectation maximization and wide beam reconstruction "half-time" gated myocardial perfusion SPECT functional imaging: a comparison to "full-time" filtered backprojection," *Journal of Nuclear Cardiology*, vol. 15, no. 4, pp. 547–563, 2008.

[6] T. M. Bateman, G. V. Heller, A. I. McGhie et al., "Multicenter investigation comparing a highly efficient half-time stress-only attenuation correction approach against standard rest-stress Tc-99m SPECT imaging," *Journal of Nuclear Cardiology*, vol. 16, no. 5, pp. 726–735, 2009.

[7] S. Liu and T. H. Farncombe, "Collimator-detector response compensation in quantitative SPECT reconstruction," in *Proceedings of the IEEE Nuclear Science Symposium and Medical Imaging Conference*, pp. 3955–3960, November 2007.

[8] D. L. Snyder, M. I. Miller, L. J. Thomas, and D. G. Politte, "Noise and edge artefacts in maximum likelihood reconstruction for emission tomography," *IEEE Transactions on Medical Imaging*, vol. 6, no. 3, pp. 228–238, 1987.

[9] D. S. Lalush and B. M. W. Tsui, "Simulation evaluation of Gibbs prior distributions for use in maximum a posteriori SPECT reconstructions," *IEEE Transactions on Medical Imaging*, vol. 11, no. 2, pp. 267–275, 1992.

[10] E. V. R. Di Bella, A. B. Barclay, R. L. Eisner, and R. W. Schafer, "A comparison of rotation-based methods for iterative reconstruction algorithms," *IEEE Transactions on Nuclear Science*, vol. 43, no. 6, pp. 3370–3376, 1996.

[11] A. W. McCarthy and M. I. Miller, "Maximum likelihood SPECT in clinical computation times using mesh-connected parallel computers," *IEEE Transactions on Medical Imaging*, vol. 10, no. 3, pp. 426–436, 1991.

[12] P. J. Green, "Bayesian reconstructions from emission tomography data using a modified EM algorithm," *IEEE Transactions on Medical Imaging*, vol. 9, no. 1, pp. 84–93, 1990.

[13] S. Alenius and U. Ruotsalainen, "Generalization of median root prior reconstruction," *IEEE Transactions on Medical Imaging*, vol. 21, no. 11, pp. 1413–1420, 2002.

[14] J. E. Bowsher, H. Yuan, L. W. Hedlund et al., "Utilizing MRI information to estimate F18-FDG distributions in rat flank tumors," in *Proceedings of the IEEE Nuclear Science Symposium Conference Record*, pp. 2488–2492, October 2004.

[15] A. Atre, K. Vunckx, K. Baete, A. Reilhac, and J. Nuyts, "Evaluation of different MRI-based anatomical priors for PET brain imaging," in *Proceedings of the IEEE Nuclear Science Symposium Conference Record*, pp. 2774–2780, October 2009.

[16] C. Comtat, P. E. Kinahan, J. A. Fessler et al., "Clinically feasible reconstruction of 3D whole-body PET/CT data using blurred anatomical labels," *Physics in Medicine and Biology*, vol. 47, no. 1, pp. 1–20, 2002.

[17] K. Baete, J. Nuyts, K. V. Laere et al., "Evaluation of anatomy based reconstruction for partial volume correction in brain FDG-PET," *NeuroImage*, vol. 23, no. 1, pp. 305–317, 2004.

Hindawi Publishing Corporation
International Journal of Molecular Imaging
Volume 2011, Article ID 893129, 12 pages
doi:10.1155/2011/893129

Research Article

Longitudinal Evaluation of Fatty Acid Metabolism in Normal and Spontaneously Hypertensive Rat Hearts with Dynamic MicroSPECT Imaging

Bryan W. Reutter, Ronald H. Huesman, Kathleen M. Brennan, Rostyslav Boutchko, Stephen M. Hanrahan, and Grant T. Gullberg

Department of Radiotracer Development & Imaging Technology, Lawrence Berkeley National Laboratory, One Cyclotron Road, Berkeley, CA 94720, USA

Correspondence should be addressed to Bryan W. Reutter, bwreutter@lbl.gov

Received 2 August 2010; Revised 15 September 2010; Accepted 16 September 2010

Academic Editor: Seigo Kinuya

The goal of this project is to develop radionuclide molecular imaging technologies using a clinical pinhole SPECT/CT scanner to quantify changes in cardiac metabolism using the spontaneously hypertensive rat (SHR) as a model of hypertensive-related pathophysiology. This paper quantitatively compares fatty acid metabolism in hearts of SHR and Wistar-Kyoto normal rats as a function of age and thereby tracks physiological changes associated with the onset and progression of heart failure in the SHR model. The fatty acid analog, ^{123}I-labeled BMIPP, was used in longitudinal metabolic pinhole SPECT imaging studies performed every seven months for 21 months. The uniqueness of this project is the development of techniques for estimating the blood input function from projection data acquired by a slowly rotating camera that is imaging fast circulation and the quantification of the kinetics of ^{123}I-BMIPP by fitting compartmental models to the blood and tissue time-activity curves.

1. Introduction

Hypertrophic cardiomyopathy is a condition in which the heart muscle becomes thick, forcing the heart to work harder to pump blood. Under normal conditions the heart uses glucose (~30%), fatty acids (~60%), and lactate (~10%) as primary energy sources, in addition to amino acids and ketone bodies [1–3]. In the case of cardiac hypertrophy, however, there is an increase in cardiac mass and a switch to a reliance on glucose metabolism. To be able to detect and interpret the early onset of this change, there is the need to develop methodology for sensitive predictors for early detection, prognosis and to follow the response to therapy for hypertrophic cardiomyopathy. In clinical settings, the abnormalities of fatty acid metabolism in hypertrophic cardiomyopathy can be recognized by the decreased uptake in single-photon emission computed tomography (SPECT) images [4]. It has also been demonstrated that compartmental analysis and dynamic SPECT imaging make it possible to detect abnormalities of fatty acid utilization earlier than SPECT imaging, with the potential to provide an even earlier prediction of the onset of cardiac hypertrophy [5]. There is a need to develop technology for imaging small animal models on clinical SPECT systems that could easily be translated to the clinic for diagnosis and management of patients with cardiac hypertrophy. However, the challenge is to perform compartmental analysis of dynamic studies in small animals with pinhole SPECT using slowly rotating gantries (slow camera rotation with 1 s per view) when the recirculation time in the animals is 6–8 s. This study was designed to follow the changes in fatty acid metabolism in the left ventricular myocardium associated with the progression of hypertrophy in the spontaneously hypertensive rat (SHR) and, in so doing, develop methodology for data acquisition and data processing techniques of pinhole SPECT acquired data [6–11]. The goal of this project is to develop radionuclide molecular imaging technologies using a clinical dual-modality pinhole SPECT/X-ray computed tomography (CT) scanner

(a) (b)

Figure 1: Clinical dual-detector SPECT/CT scanner with custom pinhole collimators used for quantitative dynamic imaging of fatty acid metabolism in the rat heart.

to quantify the changes in metabolism in the heart using the SHR as a model of hypertensive-related pathophysiology (Figure 1).

The SHR (Okamoto and Aoki strain) has hypertension associated with generalized dyslipidemia and insulin resistance. It has been noted that the SHR model has a defective gene (CD36) on chromosome 4 [12]. The gene in the SHR results in a defective fatty acid enzyme (translocase), which functions in long-chain fatty acid transport into the cell. This compromises tissue utilization of fatty acid and increases the basal glucose metabolism and hyperinsulinemia.

Mechanisms involved in the progression of heart failure are believed to be, in part, related to alteration in myocardial energy metabolism [13–15]. Plasma levels of glucose, fatty acids, and lactate determine which of these substrates are oxidized [16]. In the failing heart, energy substrate utilization changes from fatty acid oxidation to one of glycolysis utilization [17, 18]. In the case of pressure overload, there is an increased reliance on carbohydrate oxidation in an attempt to maintain contractile function. The myocardial extraction and retention of fatty acids are impaired in the advanced stage of heart failure [19]. The fatty acid analog, β-methyl-p-[^{123}I]-iodophenyl-pentadecanoic acid (^{123}I-BMIPP), currently being evaluated in human studies to study the progression of heart failure, has been used to image the metabolism of fatty acids [1, 20]. Imaging with ^{123}I-BMIPP in a canine has shown that myocardial fatty acid oxidation begins to be inhibited and that washout of ^{123}I-BMIPP increases in the compensated stage of left ventricular dysfunction. Human, canine, and rodent studies show that in late-stage heart failure there is downregulation of myocardial fatty acid oxidation and accelerated glucose oxidation [21–23]. The reduction in fatty acid oxidation is not caused by changes in fatty acid availability in the blood [24]. The time course and the molecular mechanisms for this switch in substrate oxidation are not well understood [25, 26].

This paper quantitatively compares fatty acid metabolism in the hearts of SHR and Wistar-Kyoto (WKY) normal rats as a function of age, and thereby tracks physiological changes associated with the onset and progression of heart failure in the SHR model. ^{123}I-BMIPP was used in longitudinal metabolic pinhole SPECT imaging studies performed every seven months for 21 months. The uniqueness of this project is the development of techniques for estimating the blood input function from projection data acquired by a slowly-rotating camera imaging fast circulation in a rat, and the quantification of the kinetics of ^{123}I-BMIPP by fitting compartmental models to the blood input function and tissue uptake/washout time-activity curves (TACs).

In previous work, we addressed issues associated with reconstructing dynamic data acquired with use of a slowly-rotating camera [27–29]. The work presented here also addresses quantitative effects of limited spatial resolution in dynamic pinhole SPECT that result in underestimation of the metabolic rate of ^{123}I-BMIPP in the rat myocardium. In particular, the partial volume effect blurs activity between the left ventricular blood pool and surrounding myocardial tissue and decreases contrast between the blood input and tissue uptake TACs [11, 30, 31]. Standard compartmental modeling straightforwardly accounts for the spillover of blood activity into tissue volumes [32]. However, accounting for the spillover of tissue activity into blood volumes is more problematic, and is a focus of the work presented here. Results are presented for imaging studies performed on two SHRs and two WKY normal rats at three ages.

This paper is organized as follows. Section 2 begins by describing the data acquisition protocol for acquiring dynamic ^{123}I-BMIPP data in a rat with use of a slowly-rotating dual-detector pinhole SPECT system. This section then provides overviews of our multiresolution methods for fully 3D reconstruction of a late static SPECT image (to determine the spatial locations for the left ventricular blood pool and myocardial tissue) and for fully 4-D reconstruction of an early dynamic SPECT image represented by 4-D splines that are piecewise constant in space and piecewise quadratic in time. Section 2 concludes with details of our fully 4-D penalized least-squares reconstruction algorithm that uses a smooth 4-D image prior, as well as our methods for jointly estimating the blood input function and fatty acid metabolism from the reconstructed dynamic SPECT

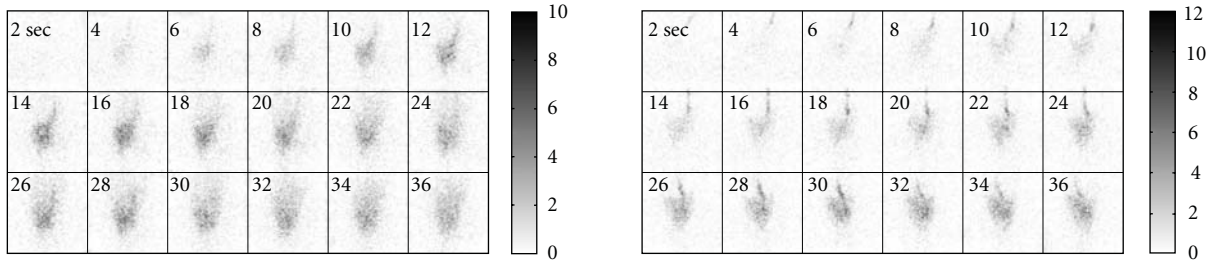

(a) WKY normal A, 14 months

(b) SHR A, 14 months

Figure 2: Dynamic cardiac ^{123}I-BMIPP pinhole SPECT projection data acquired by one detector head during the interval 2–36 s for (a) a WKY normal rat and (b) an SHR. These early time frames show the arrival of the injected bolus at the heart, followed by initial uptake in the myocardium. The maximum numbers of counts in a detector bin are 10 and 12 for the WKY normal rat and SHR, respectively.

image. Section 3 presents results obtained with use of these algorithms applied to dynamic SPECT imaging studies performed on two SHR and two WKY normal rats when the rats were age 7, 14, and 21 months (one SHR died before 21 months). The paper concludes with a discussion of the results and future work in Section 4.

2. Materials and Methods

2.1. Pinhole SPECT System Modeling and Data Acquisition. With use of methods described in [8, 9], dynamic cardiac pinhole SPECT projection data and pinhole geometric calibration data were acquired with slow gantry rotation on a dual-detector GE Millennium VG Hawkeye SPECT/CT scanner equipped with custom tungsten pinhole collimators having a 1.5 mm by 2 mm retangular aperture (Figure 1). The NaI(Tl) crystal in each detector has an area of 540 mm by 400 mm and is 9.5 mm thick. At an energy of 140 keV, the intrinsic spatial resolution is 3.9 mm and the energy resolution is 9.8%.

In the geometric configuration used for imaging rats (Figure 1), the pinhole collimators magnify the center of the field of view by a factor of about 4.8 on the faces of the large detectors. In a phantom study that we performed in this configuration [8, 9], the system could easily resolve the smallest features of the micro-Jaszczak phantom, which are 1.2 mm "cold" rod sources separated by 1.2 mm in a radioactive background [33]. Collimator response was modeled via ray tracing and excluded the effects of collimator penetration. The system model also excluded the effects of attenuation and scatter; however, we are currently studying these effects via Monte Carlo simulation in a separate investigation [34, 35].

^{123}I-BMIPP was obtained from Molecular Insight Pharmaceuticals. All imaging studies were performed in accordance with an Institutional Animal Care and Use Committee (IACUC) approved protocol. Rats were anesthetized throughout the entire procedure with use of 2–2.5% isoflurane inhalation anesthesia. A slow (10–30 s) injection of about 4 mCi (150 MBq) of ^{123}I-BMIPP, via an IV catheter placed in the tail vein, was performed shortly after the dynamic data acquisition began. Data were acquired for 60 min in 1-s time frames with an angular step of 4 degrees per frame (Figure 2). For the biodistributions associated with these studies, overall system sensitivity was about 2000 cps/mCi (55 cps/MBq). The energy of the primary photopeak for ^{123}I is 159 keV.

2.2. Multiresolution Fully 3D Late Static SPECT Image Reconstruction. To determine spatial locations for the left ventricular blood pool and myocardial tissue, late data acquired 1.5–60 min after injection were summed and a static image was reconstructed with use of a 3D version of the penalized least-squares image reconstruction that we describe in Section 2.4. The late static spatial distribution of ^{123}I-BMIPP was modeled with use of 3D multiresolution spatial B-splines that were piecewise constant. The 3D spatial splines were organized on a $20 \times 20 \times 20$ 3D grid that provided uniform sampling of 3.2 mm in each dimension. Inside the volume containing the heart, a $6 \times 6 \times 6$ neighborhood of these lower-resolution splines was replaced by a $12 \times 12 \times 12$ neighborhood of higher-resolution splines that provided uniform sampling of 1.6 mm.

2.3. Multiresolution Fully 4-D Early Dynamic SPECT Image Reconstruction. The time-varying spatial distribution of ^{123}I-BMIPP was modeled with use of 4-D multiresolution B-splines that were piecewise constant in space and piecewise quadratic in time. The 4-D splines were spatially organized on a $10 \times 10 \times 10$ 3D grid that provided uniform sampling of 6.4 mm in each dimension. Inside the volume containing the heart, a $3 \times 3 \times 3$ neighborhood of these lower-resolution splines was replaced by a $12 \times 12 \times 12$ neighborhood of higher-resolution splines that provided uniform sampling of 1.6 mm. The 4-D splines were temporally organized on a 1D grid that provided nonuniform sampling intervals of 0–2.4, 2.4–9.4, 9.4–30, and 30–90 s during the first gantry rotation (Figure 3).

With use of the fully 4-D algorithm for penalized least-squares image reconstruction that we describe in Section 2.4, B-spline TACs for the multiresolution voxels were estimated directly from the dynamic pinhole SPECT projection data. This yielded estimates of temporal B-spline coefficients

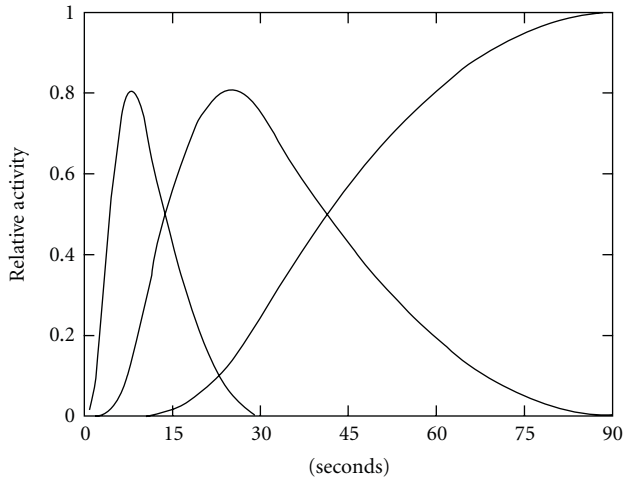

Figure 3: Piecewise quadratic temporal B-spline basis functions used to reconstruct dynamic data acquired during the first gantry rotation.

$\{\hat{a}_{mn};\ m = 1,\ldots,M;\ n = 1,\ldots,N\}$, where M is the number of spatial voxels and N is the number of temporal B-spline basis functions. The estimated TAC for the mth voxel is

$$\hat{A}^m(t) = \sum_{n=1}^{N} \hat{a}_{mn} V^n(t), \tag{1}$$

where $V^n(t)$ are temporal B-spline basis functions (Figure 3).

2.4. Fully 4-D Penalized Least-Squares Reconstruction Algorithm with a Smooth 4-D Image Prior. A dynamic SPECT projection data model that relates detected events to a 4-D spatiotemporal B-spline representation of a time-varying radiotracer distribution can be written as

$$\mathbf{p} = \mathbf{F}\mathbf{a}, \tag{2}$$

where $\mathbf{p}$ is an I-element column vector of modeled dynamic projection data values, $\mathbf{F}$ is an $I \times (MN)$ system matrix, $\mathbf{a}$ is an (MN)-element column vector of B-spline coefficients, and I is the total number of projection measurements acquired by the SPECT detectors. The system matrix $\mathbf{F}$ incorporates the spline model for time variation of the radiotracer distribution, as well as physical effects such as collimator response that affect detection of gamma rays emitted by the radiotracer distribution.

At the outset, the least-squares criterion to be minimized, χ^2, is simply the sum of squared differences between the measured projections, $\mathbf{p}^*$, and the modeled projections

$$\chi^2 = (\mathbf{p}^* - \mathbf{F}\mathbf{a})^{\mathrm{T}} (\mathbf{p}^* - \mathbf{F}\mathbf{a}), \tag{3}$$

where the superscript "T" denotes the matrix transpose. Minimizing the criterion χ^2 yields an estimate, $\hat{\mathbf{a}}$, of coefficients for the 4-D B-spline basis functions that represent the time-varying radiotracer distribution

$$\hat{\mathbf{a}} = \left(\mathbf{F}^{\mathrm{T}}\mathbf{F}\right)^{-1} \mathbf{F}^{\mathrm{T}}\mathbf{p}^*. \tag{4}$$

The corresponding minimum value for the criterion χ^2 is

$$\chi^2_{\min} = (\mathbf{p}^* - \mathbf{F}\hat{\mathbf{a}})^{\mathrm{T}} (\mathbf{p}^* - \mathbf{F}\hat{\mathbf{a}}). \tag{5}$$

To reduce noise, we now wish to add a penalty term to the criterion χ^2 that encourages the reconstructed image to be smooth in both space and time. Insight into what a reasonable penalty term might be can be obtained by expressing χ^2 in terms of its minimum value

$$\begin{aligned}
\chi^2 &= (\mathbf{p}^* - \mathbf{F}\mathbf{a})^{\mathrm{T}} (\mathbf{p}^* - \mathbf{F}\mathbf{a}) \\
&= \left[(\mathbf{p}^* - \mathbf{F}\hat{\mathbf{a}}) - \mathbf{F}(\mathbf{a} - \hat{\mathbf{a}})\right]^{\mathrm{T}} \left[(\mathbf{p}^* - \mathbf{F}\hat{\mathbf{a}}) - \mathbf{F}(\mathbf{a} - \hat{\mathbf{a}})\right] \\
&= \chi^2_{\min} - 2(\mathbf{p}^* - \mathbf{F}\hat{\mathbf{a}})^{\mathrm{T}} \mathbf{F}(\mathbf{a} - \hat{\mathbf{a}}) + (\mathbf{a} - \hat{\mathbf{a}})^{\mathrm{T}} \mathbf{F}^{\mathrm{T}}\mathbf{F}(\mathbf{a} - \hat{\mathbf{a}}) \\
&= \chi^2_{\min} + (\mathbf{a} - \hat{\mathbf{a}})^{\mathrm{T}} \mathbf{F}^{\mathrm{T}}\mathbf{F}(\mathbf{a} - \hat{\mathbf{a}}).
\end{aligned} \tag{6}$$

Note that the term that is linear with respect to $(\mathbf{a} - \hat{\mathbf{a}})$ vanishes because the model error $\mathbf{p}^* - \mathbf{F}\hat{\mathbf{a}}$ lies in the null space of the backprojection operator $\mathbf{F}^{\mathrm{T}}$. Inspecting (6), one sees that differences from the least-squares solution $\hat{\mathbf{a}}$ are penalized by the term $(\mathbf{a} - \hat{\mathbf{a}})^{\mathrm{T}} \mathbf{F}^{\mathrm{T}}\mathbf{F}(\mathbf{a} - \hat{\mathbf{a}})$.

To mimic this effect for purposes of reducing noise, we propose to add a penalty term that resembles $(\mathbf{a} - \boldsymbol{\alpha})^{\mathrm{T}} \mathbf{F}^{\mathrm{T}}\mathbf{F}(\mathbf{a} - \boldsymbol{\alpha})$, where $\boldsymbol{\alpha}$ is a smooth 4-D image prior obtained by normalizing a simple backprojection of the measured projections

$$\boldsymbol{\alpha} = \left(\mathbf{F}^{\mathrm{T}}\mathbf{p}^*\right) \cdot / \left(\mathbf{F}^{\mathrm{T}}\mathbf{F}[\mathbf{1}]\right), \tag{7}$$

where the operator "$\cdot/$" denotes pointwise division of elements in the left operand by the corresponding elements in the right operand and "$[\mathbf{1}]$" denotes an (MN)-element column vector of ones. Note that normalization by $\mathbf{F}^{\mathrm{T}}\mathbf{F}[\mathbf{1}]$ ensures that backprojecting the noiseless projections of a constant image yields the original constant image. Note also that the image prior $\boldsymbol{\alpha}$ has the desirable physiologic property of being nonnegative—thus, the reconstructed image is encouraged to have nonnegative 4-D B-spline coefficients.

The penalty term that we propose to use is

$$\sum_{i=1}^{I} \sum_{m=1}^{M} \sum_{n=1}^{N} \left[F_i^{mn}(a_{mn} - \alpha_{mn})\right]^2, \tag{8}$$

where F_i^{mn} is the $[i, m + (n-1)M]$th element of the system matrix $\mathbf{F}$, a_{mn} is the $[m + (n-1)M]$th element of the spline coefficient vector $\mathbf{a}$, and α_{mn} is the $[m + (n-1)M]$th element of the smooth image prior $\boldsymbol{\alpha}$. For the resulting negatively correlated, zero-mean elements in the vector $(\mathbf{a} - \boldsymbol{\alpha})$, (8) imposes a penalty that is greater than the penalty imposed by $(\mathbf{a} - \boldsymbol{\alpha})^{\mathrm{T}} \mathbf{F}^{\mathrm{T}}\mathbf{F}(\mathbf{a} - \boldsymbol{\alpha})$, and is more effective at suppressing "checkerboard" noise patterns. Note that the latter penalty can be expressed in summation notation as

$$\sum_{i=1}^{I} \left[\sum_{m=1}^{M} \sum_{n=1}^{N} F_i^{mn}(a_{mn} - \alpha_{mn})\right]^2. \tag{9}$$

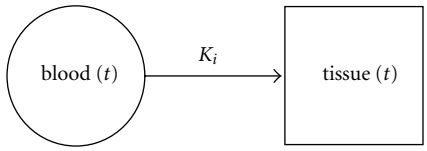

Figure 4: One-tissue-compartment model used for quantifying fatty acid metabolism during the first 90 s after injection of ^{123}I-BMIPP.

In general, the penalties (8) or (9) may be scaled by a smoothing parameter β. The penalized least-squares criterion that we minimized for the work presented here is

$$\Psi^2 = \sum_{i=1}^{I}\left[p_i^* - \sum_{m=1}^{M}\sum_{n=1}^{N} F_i^{mn} a_{mn}\right]^2 + \beta \sum_{i=1}^{I}\sum_{m=1}^{M}\sum_{n=1}^{N}\left[F_i^{mn}(a_{mn} - \alpha_{mn})\right]^2, \quad (10)$$

where the first term on the right-hand side is the least-squares criterion (3) expressed in summation notation and the second term is the scaled penalty (8). The criterion Ψ^2 is minimized by the following estimate, $\hat{\mathbf{a}}$, of coefficients for the 4-D B-spline basis functions that represent the time-varying radiotracer distribution

$$\hat{\mathbf{a}} = \left[(\mathbf{1} + \beta\mathbf{I}) \cdot \mathbf{F}^{\mathrm{T}}\mathbf{F}\right]^{-1}\left[\mathbf{F}^{\mathrm{T}}\mathbf{p}^* + \beta\,\mathrm{diag}\left(\mathbf{F}^{\mathrm{T}}\mathbf{F}\right) \cdot \boldsymbol{\alpha}\right], \quad (11)$$

where "$\mathbf{1}$" is an $(MN) \times (MN)$ matrix of ones, $\mathbf{I}$ is an $(MN) \times (MN)$ identity matrix, "$\cdot$" denotes the Hadamard product (i.e., pointwise multiplication of elements in the left operand by the corresponding elements in the right operand), and $\mathrm{diag}(\mathbf{F}^{\mathrm{T}}\mathbf{F})$ is an (MN)-element column vector whose $[m + (n-1)M]$th element is the $[m + (n-1)M]$th diagonal element of $\mathbf{F}^{\mathrm{T}}\mathbf{F}$.

Note that when the smoothing parameter β is zero, (11) simplifies to (4); whereas, the image estimate $\hat{\mathbf{a}}$ approaches the smooth image prior $\boldsymbol{\alpha}$ as β approaches infinity. By virtue of (6), a reasonable value is $\beta = 1$, which was used for the work presented here.

2.5. Joint Estimation of Blood Input and Fatty Acid Metabolism. To obtain a quantitative estimate of the metabolic rate of ^{123}I-BMIPP in the myocardium, a one-tissue-compartment model (Figure 4) is fitted to TACs for higher-resolution voxels in a $7 \times 7 \times 7$ neighborhood centered on the blood pool. Early myocardial tissue uptake is modeled with a single, irreversible compartment

$$\mathrm{tissue}(t) = K_i \cdot \int_0^t \mathrm{blood}(\tau)d\tau, \quad (12)$$

where K_i is the metabolic rate of ^{123}I-BMIPP. Each voxel is modeled as a mixture of blood input and tissue uptake, taking into account partial volume effects

$$\mathrm{voxel}(t) = [f_v \cdot \mathrm{blood}(t)] + \left[(1 - f_v)K_i \cdot \int_0^t \mathrm{blood}(\tau)d\tau\right], \quad (13)$$

where f_v is the fraction of vasculature in the tissue and also incorporates the effect of spillover from the blood pool to surrounding tissue voxels. For blood voxels, the factor $(1 - f_v)K_i$ incorporates the effect of spillover from surrounding tissue voxels.

Because of tissue spillover, there is no reconstructed voxel that contains a pure blood TAC; thus, the blood input function is assumed to be unknown and is modeled by a B-spline TAC

$$B(t) = \sum_{n=1}^{N} b_n V^n(t). \quad (14)$$

The temporal B-spline coefficients $\{b_n;\ n = 1, \ldots, N\}$ are jointly estimated with compartmental model parameters $\{(f_v^m, k^m);\ m \in \Omega\}$ for each voxel by minimizing the following least-squares criterion:

$$\sum_{m\in\Omega}\int_0^T \left\{\hat{A}^m(t) - \left[f_v^m B(t) + k^m \int_0^t B(\tau)d\tau\right]\right\}^2 dt, \quad (15)$$

where Ω denotes the $7 \times 7 \times 7$ neighborhood of voxels centered on the blood pool, $T = 90$ s, and $k^m = (1 - f_v^m)K_i^m$. Thus, there is a total of $(2 \cdot 7^3) + 3 = 689$ parameters to jointly estimate (i.e., two compartmental model parameters f_v^m and k^m for each of the 343 voxels in the neighborhood Ω, and three blood curve B-spline coefficients b_1, b_2, and b_3).

The minimization proceeds by first initializing $B(t)$ to the TAC for the voxel at the center of the neighborhood Ω. Then, optimal values for the B-spline coefficients $\{b_n;\ n = 1, \ldots, N\}$ for $B(t)$ are found with use of an iterative search algorithm. Note that one does not need to search explicitly for optimal values for the conditionally linear compartmental model parameters $\{(f_v^m, k^m);\ m \in \Omega\}$, as there are unique optimal values for these parameters given $B(t)$ [36, 37].

Values for K_i reported in the results are based on the final estimate for $B(t)$ and the average of TACs for 12 myocardial tissue voxels identified in static 3D images reconstructed from summed late data acquired 1.5–60 min after injection (Figure 5).

3. Results

In the late 3D static images (Figure 5), more trapping of ^{123}I-BMIPP is evident in the WKY normal hearts (top two rows), compared to the SHR hearts (bottom two rows). These static images have been normalized to one another by normalizing by the injected dose per unit body weight. Table 1 lists the body weight of each rat for each study.

For the early 4-D dynamic images, the use of nonuniform time sampling with splines that varied quadratically in time,

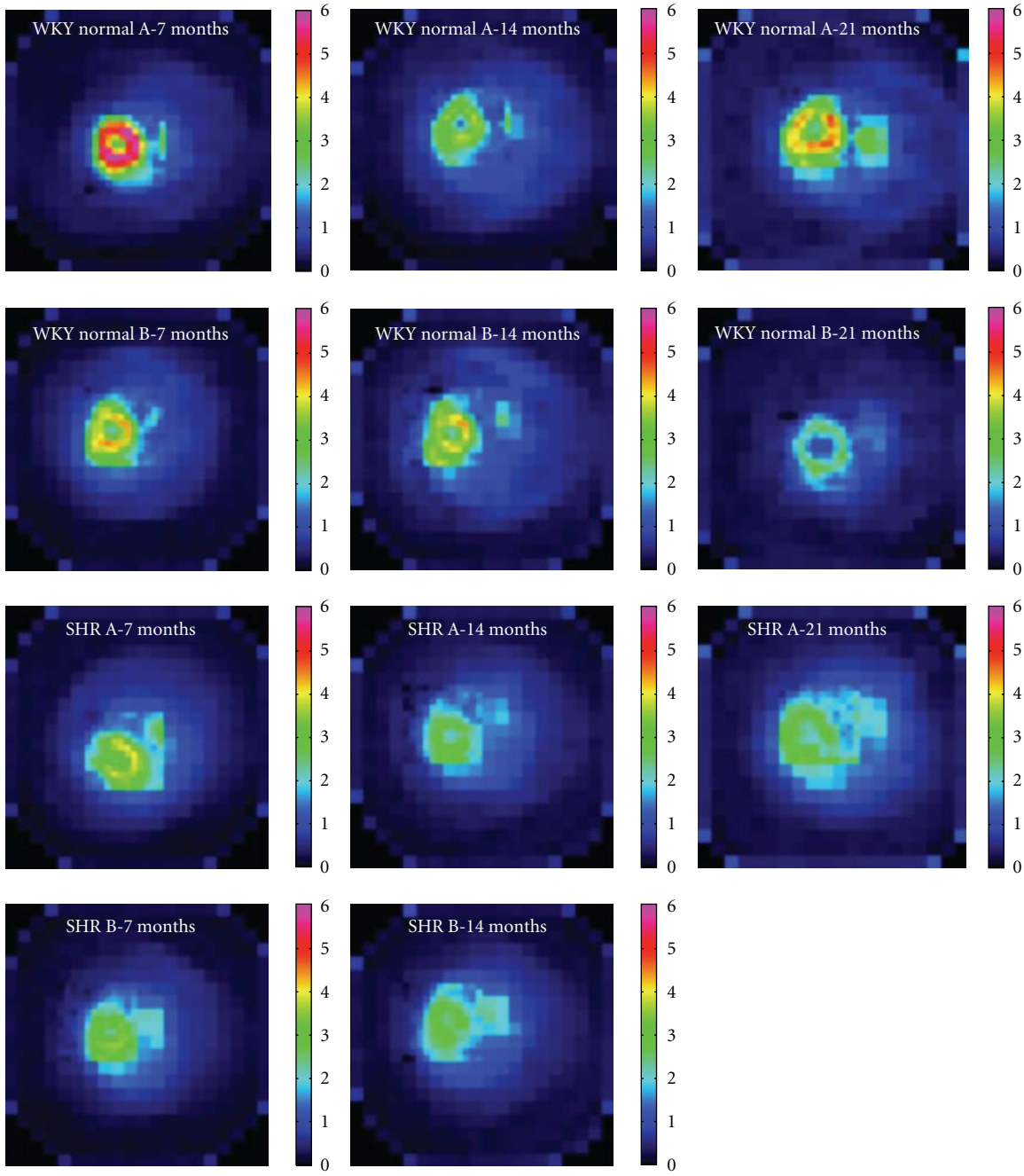

Figure 5: Typically, more trapping of ^{123}I-BMIPP is evident in late 3D static images of the WKY normal hearts (top two rows), compared to the SHR hearts (bottom two rows). Trapping also tends to decrease with age (left column, 7 months; middle column, 14 months; right column, 21 months). SHR B died of congestive heart failure before 21 months. These static images have been normalized to one another by normalizing by the injected dose per unit body weight.

along with the use of a smooth 4-D image prior, yielded smooth time-activity curves that captured the relatively fast rise and fall of ^{123}I-BMIPP in the left ventricular blood pool, as well as the uptake and initial trapping of the radiotracer in the left ventricular myocardium. Figure 6 shows time-activity curves for the spillover-corrected blood input function and myocardial uptake (triangles and circles, resp.), as well as the compartmental model fit (solid line) to the myocardial uptake curve, for each study.

The spillover of tissue activity into the left ventricular blood pool averaged 19 ± 10% across all 11 studies. Tissue spillover correction compensated for partial volume effects and improved the contrast between the blood input and myocardial uptake curves for all studies and visually

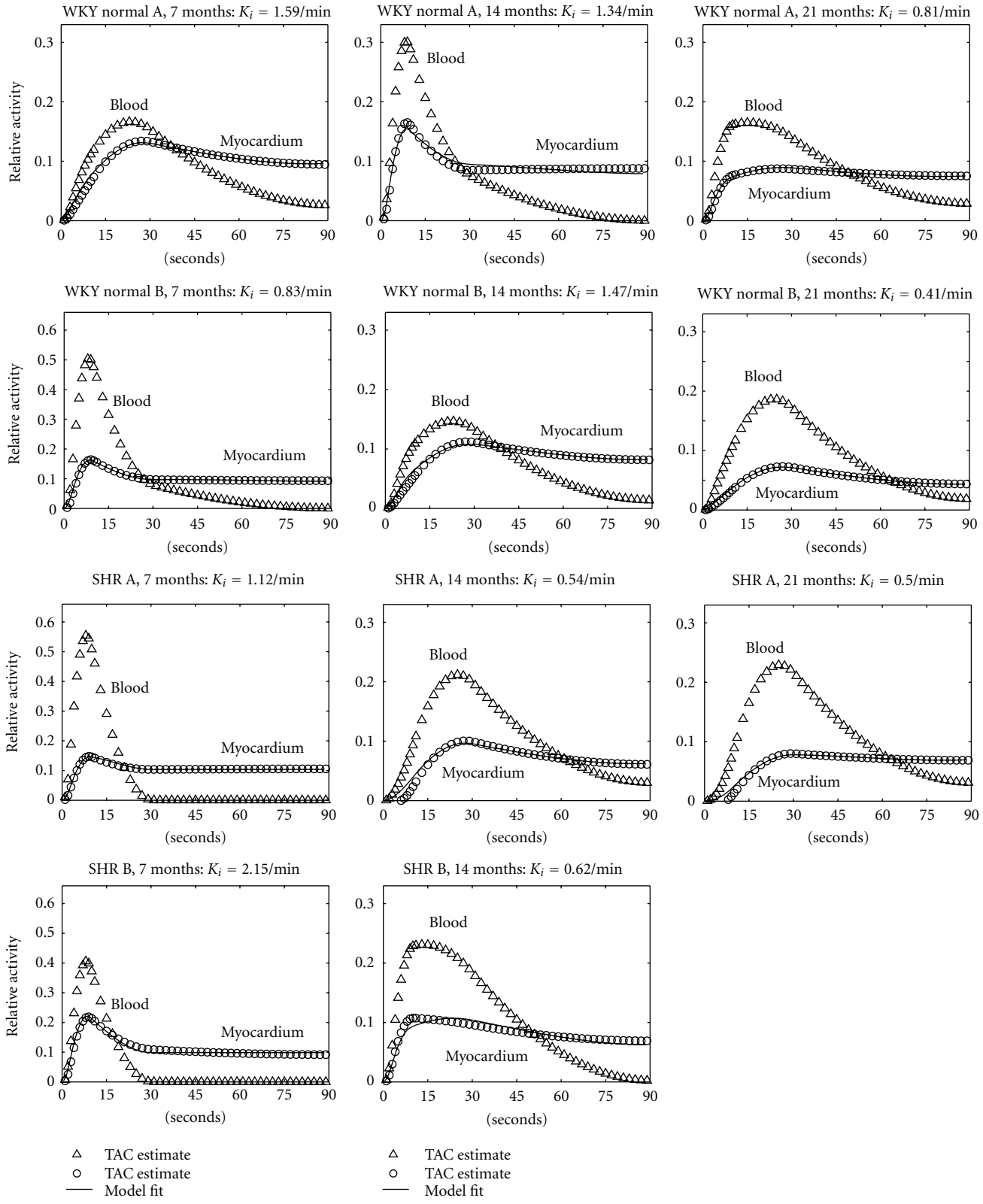

Figure 6: Time-activity curves for the WKY normal rats (top two rows) and the SHRs (bottom two rows) capture quantitative differences between their spillover-corrected blood inputs and myocardial uptakes (triangles and circles, resp.). Compartmental models (solid lines) provide good fits to the myocardial uptake curves. Left column, 7 months; middle column, 14 months; right column, 21 months. SHR B died of congestive heart failure before 21 months.

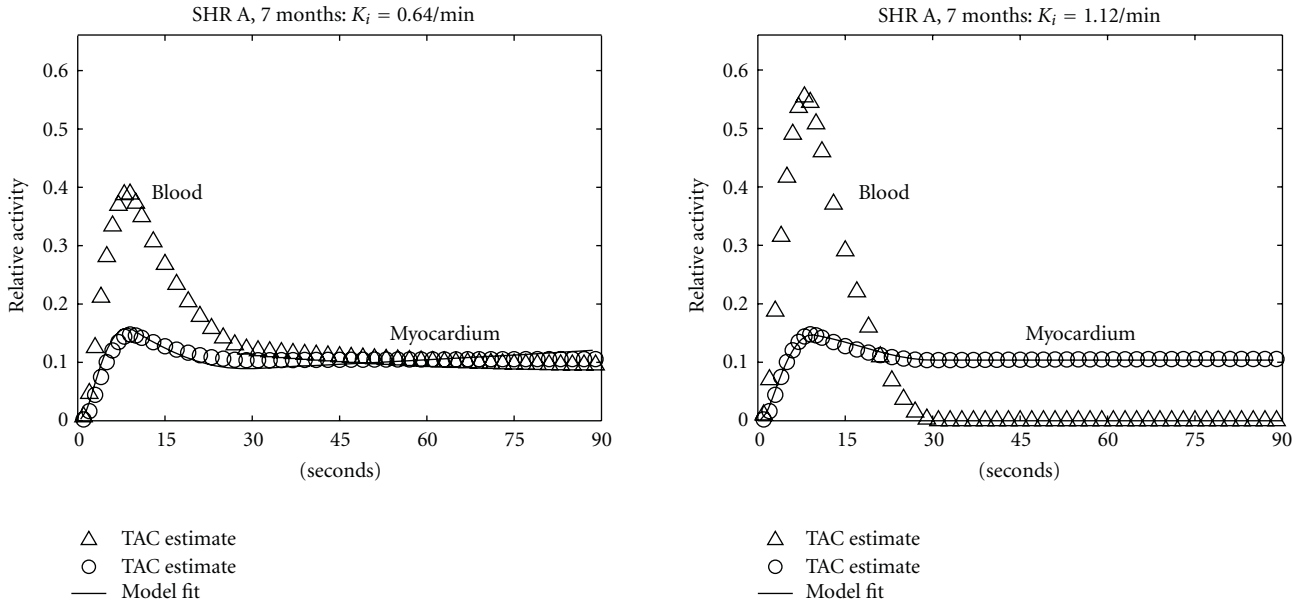

(a) Blood curve not corrected for spillover from myocardium

(b) Result of tissue spillover correction

Figure 7: Time-activity curves for SHR A at 7 months estimated (a) without and (b) with tissue spillover correction for the blood curve. Spillover correction improves contrast between the blood input and myocardial uptake (triangles and circles, resp.), improves the fit of the compartmental model (solid line), and yields a metabolic rate estimate (K_i) that nearly doubles, from 0.64 min^{-1} to 1.12 min^{-1}.

Table 1: Body weight of each rat for each study. SHR B died of congestive heart failure before 21 months.

	Body weight		
	7 Months	14 Months	21 Months
WKY normal A	420 g	482 g	545 g
WKY normal B	432 g	494 g	564 g
SHR A	430 g	465 g	416 g
SHR B	403 g	446 g	—

improved the fit of the compartmental model for some studies (Figure 7). Metabolic rate estimates (K_i) increased by an average of 72 ± 45% across all 11 studies, compared to estimates obtained without spillover correction.

Estimates of K_i obtained from corrected blood curves are plotted as a function of age for all 11 studies in Figure 8. The general decline with age is what one expects. Slower rates of fatty acid metabolism in the SHRs at 14 months, compared to the WKY normal rats, is also expected as the SHR hearts switch to a reliance on glycolysis as the primary pathway for energy production during the development of heart failure. SHR B died of congestive heart failure before 21 months.

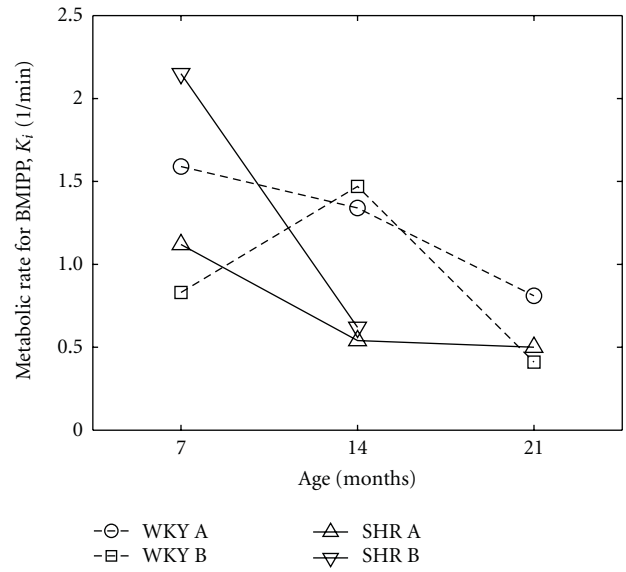

Figure 8: Metabolic rate of ^{123}I-BMIPP in the myocardium as a function of age. SHR B died of congestive heart failure before 21 months.

4. Discussion

We showed that it is potentially feasible to estimate the blood and myocardial tissue time-activity curves in rat models from projection measurements for dynamic data acquired with slow camera rotation of 1 s per projection, even when recirculation times are on the order of 6–8 s. The tissue spillover correction method compensated for partial volume effects and resulted in an increase of 72 ± 45% in estimates of metabolic rates K_i, compared to estimates obtained without spillover correction. The results appear to indicate higher fatty metabolism in the control WKY rats as compared with SHRs. The fatty acid metabolic rate also decreases with age in both animal models.

The review of Nohara [1] describes how BMIPP behaves in normal and diseased hearts at the cellular and molecular level. BMIPP is a 15-carbon chain with a methyl group in the β-position which inhibits oxidative metabolism and reduces myocardial washout kinetics. In the cell, 60% of BMIPP will be retained mostly in the triglyceride (TG) pool and has a longer retention than triglyceride, and 10% will be more or less metabolized to be washed out of the cell. Other than metabolizing to TG, the metabolites of ^{123}I-BMIPP are mostly intermediate or final metabolites in the mitochondria, where ^{123}I-BMIPP is metabolized to p-^{123}I-iodophenyl acetic acid (PIPA) by alpha-oxidation as the first step, followed by a beta-oxidation process to lactate. ^{123}I-BMIPP reflects fatty acid uptake and the size of the lipid pool, and back diffusion of ^{123}I-BMIPP and lactate production are good markers of ischemia. A 10-fold increase in the concentration of free fatty acid (FFA) in the blood will decrease ^{123}I-BMIPP extraction by 25% and increase washout by 25%, whereas a 2-fold increase in the glucose concentration in the blood does not inhibit ^{123}I-BMIPP uptake into the cell.

Lipid transport in the blood and in the cell is dependent upon it being bound to proteins or lipid proteins such as VLDL in the blood. Lipid is extracted into the cell by membrane proteins and is affected by albumin/FFA ratio in the blood. Higher lipid or FFA/albumin level results in greater uptake of lipid into the cell. Fatty acid binding protein (FABP) in the cytosole is one factor that regulates lipid flux. Lipid will be used either for oxidation, triglyceride or phospholipid formation. Carnitine palmityl transferese is the key enzyme for the entrance of lipid into mitochondria, and oxidative enzymes such as long chain acyl CoA dehydrogenase (LCAD) will determine lipid use into the TCA cycle. The eventual production of ATP in the mitochondria will limit the size of TG storage. The several lipid enzymes in the cell are regulated by nuclear genes that are individually activated by peroxisome proliferator activated receptors (PPARs). There are many endothelial proteins that are also involved in the storage and metabolism of lipid. The amount of medium chain acyl CoA dehydrogenase (MCAD) is closely related to the progression of heart failure. In the compensated phase of hypertrophy, m-RNA level of MCAD is reduced.

Even with species differences, our results (here for fatty acid metabolism, and [6, 7] for glucose metabolism) and other results obtained with the SHR model [38–40] corroborate studies in humans, which show that there are abnormalities in myocardial metabolic function manifested by reduced rates of fatty acid utilization and oxidation and an increase in glucose metabolism associated with hypertension-induced left ventricular hypertrophy (LVH) and idiopathic cardiomyopathy [21, 41]. In a separate positron emission tomography (PET) study imaging ^{18}F-fluorodeoxyglucose (FDG) with use of a microPET scanner, we observed that glucose metabolism in the SHR model was greater than that in the WKY control [6, 7], and that the glucose metabolism in both decreased with age. Present results differ from results imaging fatty acid utilization in patients with heart failure [13], where it was shown that myocardial fatty acid uptake in patients with heart failure was higher than that expected for the normal heart, whereas myocardial glucose uptake rates were lower. It may be that in the hypertrophied heart before heart failure there is greater dependency on glucose and with eventual heart failure there is a shift to fatty acid metabolism, and that this shift is an indication of impaired energy efficiency in the failing heart.

Our work also corresponds to work by Okizaki et al. [5]. Using dynamic SPECT imaging of ^{123}I-BMIPP, they showed that fatty acid metabolism was higher in patients with hypertrophic cardiomyopathy. Using mathematical modeling, they showed that compartmental model rate parameters might be a sensitive predictor for early detection of hypertrophic cardiomyopathy and could be a useful index to evaluate its progression. A two-compartment model was used where the first compartment was a reversible compartment (cytoplasma) and the second compartment (triglyceride pool) was an irreversible compartment corresponding to the long retention of BMIPP if incorporated into the triglyceride pool. The compartmental analysis suggested that a fatty acid shift (rate of transport into the TG pool higher than normal and a decreased volume of distribution for the first compartment) from cytoplasm to the triglyceride pool occurs in hypertrophic cardiomyopathy, even in the early phase of the disease when no apparent change was observed upon visual interpretation by nuclear medicine physicians. Because of the computational demands, we were able to model only the first 90 s of the kinetics in the myocardium. We used a single, irreversible tissue compartment, and therefore were able to measure only the uptake of ^{123}I-BMIPP, which we consider to be a measure of the metabolic rate of ^{123}I-BMIPP. It is anticipated that an additional, reversible tissue compartment will be needed to account for washout of ^{123}I-BMIPP from the myocardium over longer time scales.

^{123}I-BMIPP imaging changes in the ischemic condition [1]. Disparity between ^{123}I-BMIPP uptake in the hypertrophied myocardium and delayed ^{201}Tl redistribution images in rest/stress studies indicate that myocardial ischemia plays an important role in impaired fatty acid utilization and metabolism in hypertrophied myocardium [4]. Myocardial ischemia is present with hypertrophic cardiomyopathy for several reasons: small coronary artery disease, coronary artery spasms, left coronary artery compression, inadequate capillary density in relation to the increased myocardial mass, and impaired coronary flow reserve. Lipid metabolic regulation completely differs from normal in the very early phase of cardiac hypertrophy and with deteriorating heart failure, and metabolic switching from lipid to glucose will occur [1]. A slight reduction in flow will be reflected in an increase in glucose metabolism to a level 4-5 times the resting value, but the lipid metabolism will remain constant [1]. At less than 40% of resting flow, both lipid and glucose metabolisms decrease remarkably [1]. Extraction of lipids will decrease in cases of prolonged ischemia [1]. The myocardial accumulation of ^{123}I-BMIPP is also related to ATP content, and thus may reflect pO2 levels [4]. Decreased myocardial ^{123}I-BMIPP uptake in areas of stress-induced ischemia on ^{201}Tl imaging indicated that exercised-induced metabolic changes persisted even in the resting condition

[4]. The possibility of an unknown hereditary fatty acid metabolic abnormality that could account for reduced ^{123}I-BMIPP accumulation in hypertrophic cardiomyopathy has also been reported [4].

Our studies show a decrease in fatty acid metabolism in both the SHR and WKY rat with age. In one study in humans it was observed that myocardial fatty acid utilization (MFAU) and myocardial fatty acid oxidation (MFAO) declined with age while myocardial glucose utilization (MGU) did not change; thus, the proportional contribution of glucose used to overall substrate utilization relative to fatty acids was increased [42]. The decline in MFAO and MFAU with age may reflect a decline in mitochondrial long-chain fatty acid uptake [43], and alterations in mitochondrial lipid content, composition, and protein interactions, leading to significant membrane dysfunction [44] and effects of impaired myocardial vasodilator capacity [45]. The study in humans [42] appears to correlate with some studies in mouse and rat experimental models that show that the contribution of MFAO to overall myocardial substrate metabolism declines with age, and that the proportion of glucose metabolism to overall substrate metabolism increases [46]. However, one study in rats [47] appears to contradict these results showing that during the transition from adulthood to senescence, there is an increase in palmitate (fatty acid) oxidation and a decrease in lactate oxidation, and that this is associated with significant deterioration in cardiac function and efficiency. This paper suggests that the metabolic changes occur in parallel with hypertrophy. Thus, if hypertrophy is involved there could be an accompanied disproportionate enlargement in cell length causing an increase in the cell length-to-width ratio [48]. Cell loss, which increases with age [49], may also play an increasing role in the transition to heart failure by placing a greater workload on the remaining viable cells. The detrimental effect of increased fatty acid utilization observed in the senescent heart may be attributed to the fact that fatty acids are a less efficient fuel in terms of myocardial oxygen consumption (MVO2) [50].

Limitations of our present study are (1) small sample size (two WKY, two SHR), (2) animals were not fasted, (3) no blood pressure data, (4) no independent validation of the input function either from blood samples or from simulation, (5) data were not corrected for attenuation or scatter, and (6) only the first 90 s of the dynamic data were processed. Regarding fasting, it was felt that the animals had fairly similar free fatty acid, insulin, and glucose levels, which we verified in another study in which we sampled blood. Blood pressure is very difficult to obtain in these animals. Presently, simulations with known blood input functions are underway to determine the bias and variance that one would obtain with the experimental data. In future studies we plan to implement attenuation and scatter correction using the transmission source on the GE Hawkeye SPECT/CT system. We have performed simulations that showed improvement in quantitation using scatter and attenuation correction [35]. In a rat it improves quantitation by 10–15%. Future work will also include addressing computational issues associated with reconstructing a 4-D dynamic image from the entire 60 min of projection data.

Our injected dose of 4 mCi (150 MBq) is high when compared with dose/weight ratios of what one would give a human. The injected dose was based on our past experience [8, 9] as to what we anticipated the photon counting statistics needed to be to perform the data analysis. Our statistical uncertainties appear to be reasonable. Nonetheless, this still needs to be evaluated in an extensive study of statistical precision based on injected dose in rats. We have not found any harmful effects to the animals using this dose; however, an extensive radiobiology study has not been performed.

The work presented here relates primarily to the development of technology for dynamic pinhole SPECT imaging of small animals. The results are the first to report on being able to measure fatty acid metabolic rate in rats with use of a clinical pinhole SPECT system with slowly-rotating detectors. From a technical standpoint, this measurement was made possible in part because of the slow (10–30 s) injection of ^{123}I-BMIPP, which allowed good angular sampling of the projections of the blood input function. The slow injection was also necessary, so as not to overwhelm the rat's circulatory system with the additional volume ($\sim$1 mL) of the injectate. For faster injections of smaller volumes of injectate, an imaging system with stationary detectors, such as the U-SPECT II preclinical scanner [51], is better-suited for tomographic imaging of the resulting faster kinetics. The U-SPECT II also has the advantage of having a collimator with 75 1-mm pinholes for use with imaging rats, which provides about 13 times the sensitivity of our two-pinhole system and the ability to resolve 0.8-mm "cold" rods in a radioactive background [51]. Sensitivity and spatial resolution of our system could also be improved by judiciously increasing the number of and decreasing the size of the pinholes.

Our methods can also be applied to other imaging modalities, such as dynamic PET. We are presently studying fatty acid metabolism as a function of age in SHR and WKY rats using microPET imaging of the fatty acid analog, 14(*R*, *S*)-[^{18}F]fluoro-6-thia-heptadecanoic acid (^{18}F-FTHA) [52]. Combining new dynamic and conventional clinical imaging protocols with improved descriptions of the heart (physiological, mechanical, and biochemical) will allow better specification of the heart's properties. This, in turn, will facilitate the study of how these properties are affected by molecular changes in the heart caused by disease.

Disclaimer

the United States Government or any agency thereof, or The Regents of the University of California. The views and opinions of authors expressed herein do not necessarily state or reflect those of the United States Government or any agency thereof or The Regents of the University of California.

Acknowledgment

This paper was supported by the National Institutes of Health of the U. S. Department of Health and Human Services under Grants R01-EB00121, R01-EB007219, R01-HL50663, and R01-HL71253; and by the Director, Office of Science, Office of Biological and Environmental Research of the U. S. Department of Energy under contract DE-AC02-05CH11231.

References

[1] R. Nohara, "Lipid metabolism in the heart: contribution of BMIPP to the diseased heart," *Annals of Nuclear Medicine*, vol. 15, no. 5, pp. 403–409, 2001.

[2] L. H. Opie, *The Heart: Physiology and Metabolism*, Raven Press, New York, NY, USA, 2nd edition, 1991.

[3] J. R. Neely and H. E. Morgan, "Relationship between carbohydrate and lipid metabolism and the energy balance of heart muscle," *Annual Review of Physiology*, vol. 36, pp. 413–459, 1974.

[4] S. Matsuo, Y. Nakamura, M. Takahashi, K. Mitsunami, and M. Kinoshita, "Myocardial metabolic abnormalities in hypertrophic cardiomyopathy assessed by iodine-123-labeled beta-methyl-branched fatty acid myocardial scintigraphy and its relation to exercise-induced ischemia," *Japanese Circulation Journal*, vol. 62, no. 3, pp. 167–172, 1998.

[5] A. Okizaki, N. Shuke, J. Sato et al., "A compartment model analysis for investigation of myocardial fatty acid metabolism in patients with hypertrophic cardiomyopathy," *Nuclear Medicine Communications*, vol. 28, no. 9, pp. 726–735, 2007.

[6] G. T. Gullberg, R. H. Huesman, J. Qi, B. W. Reutter, A. Sitek, and Y. Yang, "Evaluation of cardiac hypertrophy in spontaneously hypertensive rats using metabolic rate of glucose estimated from dynamic microPET image data," *Molecular Imaging*, vol. 3, no. 3, p. 225, 2004.

[7] G. T. Gullberg, R. H. Huesman, B. W. Reutter et al., "A study of changes in deformation and metabolism in the left ventricle as a function of hypertrophy in spontaneous hypertensive rats using microPET technology," *Journal of Nuclear Cardiology*, vol. 12, no. 2, p. S74, 2005.

[8] J. Hu, A. Sitek, B. W. Reutter, R. H. Huesman, and G. T. Gullberg, "A new approach of dynamic pinhole SPECT imaging for evaluation of sympathetic nervous system function in animal models of cardiac hypertrophy," in *Proceedings of the IEEE Nuclear Science Symposium and Medical Imaging Conference Record*, B. Yu, Ed., pp. 2542–2546, 2005.

[9] J. Hu, A. Sitek, B. W. Reutter, R. H. Huesman, and G. T. Gullberg, "Dynamic molecular imaging of cardiac innervation using a dual head pinhole SPECT system," Tech. Rep. LBNL-60008, Lawrence Berkeley National Laboratory, 2006.

[10] A. B. Hwang, B. W. Reutter, R. H. Huesman et al., "High resolution simultaneous I-125 and Tc-99 m cardiac imaging of a rat using a conventional SPECT system with pin-hole collimators," *Journal of Nuclear Medicine*, vol. 45, no. 5, pp. 422P–423P, 2004.

[11] A. B. Hwang, B. L. Franc, G. T. Gullberg, and B. H. Hasegawa, "Assessment of the sources of error affecting the quantitative accuracy of SPECT imaging in small animals," *Physics in Medicine and Biology*, vol. 53, no. 9, pp. 2233–2252, 2008.

[12] T. Hajri, A. Ibrahimi, C. T. Coburn et al., "Defective fatty acid uptake in the spontaneously hypertensive rat is a primary determinant of altered glucose metabolism, hyperinsulinemia, and myocardial hypertrophy," *Journal of Biological Chemistry*, vol. 276, no. 26, pp. 23661–23666, 2001.

[13] M. Taylor, T. R. Wallhaus, T. R. Degrado et al., "An evaluation of myocardial fatty acid and glucose uptake using PET with [18F]fluoro-6-thia-heptadecanoic acid and [18F]FDG in patients with congestive heart failure," *Journal of Nuclear Medicine*, vol. 42, no. 1, pp. 55–62, 2001.

[14] O. D. Mjos, "Effect of free fatty acids on myocardial function and oxygen consumption in intact dogs," *Journal of Clinical Investigation*, vol. 50, no. 7, pp. 1386–1389, 1971.

[15] H. Taegtmeyer, "Energy metabolism of the heart: from basic concepts to clinical applications," *Current Problems in Cardiology*, vol. 19, no. 2, pp. 59–113, 1994.

[16] F. C. Visser, "Imaging of cardiac metabolism using radiolabelled glucose, fatty acids and acetate," *Coronary Artery Disease*, vol. 12, supplement 1, pp. S12–S18, 2001.

[17] S. P. Bishop and R. A. Altschuld, "Increased glycolytic metabolism in cardiac hypertrophy and congestive failure," *The American Journal of Physiology*, vol. 218, no. 1, pp. 153–159, 1970.

[18] M. E. Chiste and R. L. Rodgers, "Altered glucose and fatty acid oxidation in hearts of the spontaneously hypertensive rat," *Journal of Molecular and Cellular Cardiology*, vol. 26, no. 10, pp. 1371–1375, 1994.

[19] K. Kataoka, R. Nohara, R. Hosokawa et al., "Myocardial lipid metabolism in compensated and advanced stages of heart failure: evaluation by canine pacing model with BMIPP," *Journal of Nuclear Medicine*, vol. 42, no. 1, pp. 124–129, 2001.

[20] F. F. Knapp Jr. and J. Kropp, "BMIPP-design and development," *International Journal of Cardiac Imaging*, vol. 15, no. 1, pp. 1–9, 1999.

[21] V. G. Dávila-Román, G. Vedala, P. Herrero et al., "Altered myocardial fatty acid and glucose metabolism in idiopathic dilated cardiomyopathy," *Journal of the American College of Cardiology*, vol. 40, no. 2, pp. 271–277, 2002.

[22] F. A. Recchia, P. I. McConnell, R. D. Bernstein, T. R. Vogel, X. Xu, and T. H. Hintze, "Reduced nitric oxide production and altered myocardial metabolism during the decompensation of pacing-induced heart failure in the conscious dog," *Circulation Research*, vol. 83, no. 10, pp. 969–979, 1998.

[23] M. N. Sack, T. A. Rader, S. Park, J. Bastin, S. A. McCune, and D. P. Kelly, "Fatty acid oxidation enzyme gene expression is downregulated in the failing heart," *Circulation*, vol. 94, no. 11, pp. 2837–2842, 1996.

[24] C. Brunold, Z. El Alaoui-Talibi, M. Moravec, and J. Moravec, "Palmitate oxidation by the mitochondria from volume-overloaded rat hearts," *Molecular and Cellular Biochemistry*, vol. 180, no. 1-2, pp. 117–128, 1998.

[25] J. J. Lehman and D. P. Kelly, "Gene regulatory mechanisms governing energy metabolism during cardiac hypertrophic growth," *Heart Failure Reviews*, vol. 7, no. 2, pp. 175–185, 2002.

[26] M. N. Sack and D. P. Kelly, "The energy substrate switch during development of heart failure: gene regulatory mechanisms (Review)," *International Journal of Molecular Medicine*, vol. 1, no. 1, pp. 17–24, 1998.

[27] B. W. Reutter, G. T. Gullberg, R. Boutchko et al., "Fully 4-D dynamic cardiac SPECT image reconstruction using spatiotemporal B-spline voxelization," in *Proceedings of the IEEE Nuclear Science Symposium and Medical Imaging Conference Record*, B. Yu, Ed., pp. 4217–4221, 2007.

[28] B. W. Reutter, R. Boutchko, R. H. Boutchko et al., "Dynamic pinhole SPECT imaging and compartmental modeling of fatty acid metabolism in the rat heart," in *Proceedings of the IEEE Nuclear Science Symposium and Medical Imaging Conference Record*, P. Sellin, Ed., pp. 4478–4481, 2008.

[29] B. W. Reutter, R. Boutchko, R. H. Huesman, A. C. Sauve, and G. T. Gullberg, "Penalized least-squares dynamic pinhole SPECT image reconstruction using a smooth 4-D image prior and multiresolution spatiotemporal B-splines," in *Proceedings of the 10th International Conference on Fully Three-Dimensional Image Reconstruction in Radiology and Nuclear Medicine*, B. M. W. Tsui and Z. Chen, Eds., pp. 110–113, 2009.

[30] B. F. Hutton and A. Osiecki, "Correction of partial volume effects in myocardial SPECT," *Journal of Nuclear Cardiology*, vol. 5, no. 4, pp. 402–413, 1998.

[31] P. H. Pretorius and M. A. King, "Diminishing the impact of the partial volume effect in cardiac SPECT perfusion imaging," *Medical Physics*, vol. 36, no. 1, pp. 105–115, 2009.

[32] R. H. Huesman, B. L. Knittel, B. M. Mazoyer et al., "Notes on RFIT: a program for fitting compartmental models to region-of-interest dynamic emission tomography data," Tech. Rep. LBL-37621, Lawrence Berkeley National Laboratory, 1995.

[33] R. J. Jaszczak, J. Li, H. Wang, M. R. Zalutsky, and R. E. Coleman, "Pinhole collimation for ultra-high-resolution, small-field-of-view SPECT," *Physics in Medicine and Biology*, vol. 39, no. 3, pp. 425–437, 1994.

[34] A. Sauve, W. Choong, R. Boutchko et al., "Quantitative imaging of cardiovascular function with pinhole SPECT in mice and rats—effects of attenuation and scatter," *Journal of Nuclear Medicine*, vol. 48, no. 5, pp. 424P–425P, 2007.

[35] A. C. Sauve, B. W. Reutter, R. Boutchko et al., "Multi-slice SPECT attenuation and scatter correction using Monte Carlo simulated system matrices," in *Proceedings of the IEEE Nuclear Science Symposium and Medical Imaging Conference Record*, P. Sellin, Ed., pp. 4273–4276, 2008.

[36] B. W. Reutter, G. T. Gullberg, and R. H. Huesman, "Kinetic parameter estimation from attenuated SPECT projection measurements," *IEEE Transactions on Nuclear Science*, vol. 45, no. 6, pp. 3007–3013, 1998.

[37] B. W. Reutter, S. Oh, G. T. Gullberg, and R. H. Huesman, "Improved quantitation of dynamic SPECT via fully 4-D joint estimation of compartmental models and blood input function directly from projections," in *Proceedings of the IEEE Nuclear Science Symposium and Medical Imaging Conference Record*, B. Yu, Ed., pp. 2337–2341, 2005.

[38] O. H. L. Bing, C. H. Conrad, M. O. Boluyt, K. G. Robinson, and W. W. Brooks, "Studies of prevention, treatment and mechanisms of heart failure in the aging spontaneously hypertensive rat," *Heart Failure Reviews*, vol. 7, no. 1, pp. 71–88, 2002.

[39] O. H. Cingolani, X.-P. Yang, M. A. Cavasin, and O. A. Carretero, "Increased systolic performance with diastolic dysfunction in adult spontaneously hypertensive rats," *Hypertension*, vol. 41, no. 2, pp. 249–254, 2003.

[40] J. E. Jalil, C. W. Doering, J. S. Janicki, R. Pick, S. G. Shroff, and K. T. Weber, "Fibrillar collagen and myocardial stiffness in the intact hypertrophied rat left ventricle," *Circulation Research*, vol. 64, no. 6, pp. 1041–1050, 1989.

[41] L. de las Fuentes, P. F. Soto, B. P. Cupps et al., "Hypertensive left ventricular hypertrophy is associated with abnormal myocardial fatty acid metabolism and myocardial efficiency," *Journal of Nuclear Cardiology*, vol. 13, no. 3, pp. 369–377, 2006.

[42] A. M. Kates, P. Herrero, C. Dence et al., "Impact of aging on substrate metabolism by the human heart," *Journal of the American College of Cardiology*, vol. 41, no. 2, pp. 293–299, 2003.

[43] J. A. Odiet, M. E. T. I. Boerrigter, and J. Y. Wei, "Carnitine palmitoyl transferase-I activity in the aging mouse heart," *Mechanisms of Ageing and Development*, vol. 79, no. 2-3, pp. 127–136, 1995.

[44] G. Paradies, F. M. Ruggiero, G. Petrosillo, M. N. Gadaleta, and E. Quagliariello, "The effect of aging and acetyl-L-carnitine on the function and on the lipid composition of rat heart mitochondria," *Annals of the New York Academy of Sciences*, vol. 717, pp. 233–243, 1994.

[45] A. Chauhan, R. S. More, P. A. Mullins, G. Taylor, M. C. Petch, and P. M. Schofield, "Aging-associated endothelial dysfunction in humans is reversed by L-arginine," *Journal of the American College of Cardiology*, vol. 28, no. 7, pp. 1796–1804, 1996.

[46] J. B. McMillin, G. E. Taffet, H. Taegtmeyer, E. K. Hudson, and C. A. Tate, "Mitochondrial metabolism and substrate competition in the aging Fischer rat heart," *Cardiovascular Research*, vol. 27, no. 12, pp. 2222–2228, 1993.

[47] J. Sample, J. G. F. Cleland, and A.-M. L. Seymour, "Metabolic remodeling in the aging heart," *Journal of Molecular and Cellular Cardiology*, vol. 40, no. 1, pp. 56–63, 2006.

[48] A. M. Gerdes, T. Onodera, X. Wang, and S. A. McCune, "Myocyte remodeling during the progression to failure in rats with hypertension," *Hypertension*, vol. 28, no. 4, pp. 609–614, 1996.

[49] G. Olivetti, M. Melissari, J. M. Capasso, and P. Anversa, "Cardiomyopathy of the aging human heart. Myocyte loss and reactive cellular hypertrophy," *Circulation Research*, vol. 68, no. 6, pp. 1560–1568, 1991.

[50] C. S. Apstein, "Increased glycolytic substrate protection improves ischemic cardiac dysfunction and reduces injury," *American Heart Journal*, vol. 139, no. 2, part 3, pp. S107–S114, 2000.

[51] F. D. Van Have, B. Vastenhouw, R. M. Ramakers et al., "U-SPECT-II: an ultra-high-resolution device for molecular small-animal imaging," *Journal of Nuclear Medicine*, vol. 50, no. 4, pp. 599–605, 2009.

[52] H. Wahnishe, J. O'Neil, M. Janabi et al., "Cardiac metabolism as a function of cardiac hypertrophy using microPET/CT imaging of [F-18]FTHA and [F-18]FDG," *Journal of Nuclear Medicine*, vol. 51, supplement 2, p. 324, 2010.

Hindawi Publishing Corporation
International Journal of Molecular Imaging
Volume 2011, Article ID 803920, 7 pages
doi:10.1155/2011/803920

Review Article

Role of Single Photon Emission Computed Tomography in Epilepsy

Sita Jayalakshmi,[1] Pushpalatha Sudhakar,[2] and Manas Panigrahi[3]

[1] *Department of Neurology, Krishna Institute of Medical Sciences, 1-8-31/1, Minister Road, Secunderabad, Andhra Pradesh 500 003, India*
[2] *Department of Nuclear Medicine, Krishna Institute of Medical Sciences, Hyderabad, 1-8-31/1, Minister Road, Secunderabad, Andhra Pradesh 500 003, India*
[3] *Department of Neurosurgery, Krishna Institute of Medical Sciences, Hyderabad, 1-8-31/1, Minister Road, Secunderabad, Andhra Pradesh 500 003, India*

Correspondence should be addressed to Sita Jayalakshmi, sita_js@hotmail.com

Received 1 August 2010; Accepted 25 October 2010

Academic Editor: Abass Alavi

Molecular imaging with ictal single photon emission computed tomography (SPECT) is an established functional imaging modality for the presurgical evaluation of patients with refractory partial onset seizures. SPECT coregistered on to the MRI has greater sensitivity to identify the ictal onset zone. Ictal SPECT should always be interpreted in the context of other presurgical investigations. Ictal SPECT is sensitive method for the lateralization of TLE, but ictal SPECT is more sensitive when MRI is normal. Ictal SPECT and interictal PET are complementary to each other in lateralizing the side in patients with TLE and normal MRI. In extratemporal epilepsy, ictal SPECT will guide the placement of surface grid and depth electrodes.

1. Introduction

Molecular imaging with ictal and interictal single photon emission computed tomography (SPECT) is an established functional imaging modality for the presurgical evaluation of patients with refractory partial onset seizures. Ictal SPECT has the potential to localize the ictal onset zone noninvasively and accurately and provides complementary data during multimodality evaluation of the epileptogenic zone. Ictal SPECT is more sensitive than structural imaging [1] but gives little indication about the underlying pathology. SPECT co-registered on to the MRI has greater sensitivity to identify the ictal onset zone. It is usually assumed that the largest and most intense ictal hyperperfusion region is the ictal onset zone. Ictal SPECT injection should be performed in the video EEG unit by trained technicians. The dye should be injected fast [2, 3]. High resolution SPECT and MRI scanner are important with a need for good cooperation between neurology and nuclear medicine departments for a successful programme to be implemented.

2. Brain Perfusion Tracers

The brain perfusion tracers that cross the blood brain barrier with a long retention time in the brain are ^{99m}technetium (^{99m}TC-labeled agents). The two commonly used tracers are ^{99m}hexamethylene propylene amino (^{99m}TC-HMPAO) and ^{99m}TC-ethyl cysteinate dimer (^{99m}TC-ECD). ^{99m}TC-ECD is stable 6 to 8 hours and ^{99m}TC-HMPAO for 4 hours. ^{99m}TC-ECD is cleared from the body more rapidly than ^{99m}TC HMPAO and gives a higher brain to soft tissue activity ratio, and this improves the image quality [4] D.S.Lee et al. found that ^{99m}TC-HMPAO ictal SPECT was superior to ^{99m}TC-ECD ictal SPECT for localization of epileptogenic zone [5]. Early ictal injection is an important criterion for best results and is associated with high concordance with other studies [6]. S. K. Lee et al. reported that an injection delay of less than 20 seconds after seizure onset was significantly correlated with correct localization [7]. The SPECT images can be acquired up to 4 hours after this termination of the seizure.

2.1. Limiting Factors. Ictal SPECT has a poor time resolution. After injection of the tracer, it takes about 30s to reach the brain, and around 70% of the radioligand is taken up during first pass. An ictal perfusion SPECT image displays both ictal onset zone and seizure propagation pathways. The region with largest and most intense hyperperfusion is considered as the ictal onset zone. It has been shown that these regions may also represent ictal propagation [8]. Earlier ictal injection given during a seizure more likely suggests that the largest and most intense ictal perfusion area represents the ictal onset zone than the seizure propagation. Contralateral spread of ictal activity restricted to a region homotopic to the ictal onset zone results in a mirror image [9].

2.2. Interictal SPECT. The rationale for interictal SPECT imaging is to serve as a baseline reference study for the interpretation of ictal SPECT images. Interictal SPECT should be done after a seizure-free period of at least 24 hours, and the dye should be injected during EEG monitoring when there is no epileptiform activity.

2.3. Role of Ictal SPECT during Presurgical Evaluation of Refractory Partial Epilepsy. Ictal EEG is the gold standard investigation for the ictal onset zone. However scalp ictal EEG will not permit accurate localization in up to 40% patients with temporal lobe epilepsy if used alone. Concordance of ictal scalp EEG with MRI brain, ictal SPECT, and interictal PET improves the surgical outcome. As invasive EEG evaluation is associated with serious complications like intracerebral hemorrhage and infections, though rare, noninvasive modalities of presurgical evaluation strategies should always be performed to improve the accuracy of localization of epileptogenic zone.

The interpretation of ictal SPECT should always be done in the context of a full presurgical evaluation. The neurologist/epileptologist plays an important role in the interpretation of the SPECT images. The injection time should be known, as early injections give the best results.

2.4. SPECT in Temporal Lobe Epilepsy. The temporal lobes are best viewed by reconstructing transaxial slices parallel to the temporal lobe with coronal slices perpendicular to this plane [10–12]. The anterior-posterior commisure (AC-PC) line can be approximated by joining the bottom of the frontal lobe and occipital lobe on a midline sagittal slice, and temporal lobe plane is then derived from this line (Figure 1). Any asymmetry of more than 10% over the anterior temporal lobes during quantification is significant. Visual impression is a good indicator for interpretation, and quantification is usually only performed for research purposes [12, 13].

2.5. Interictal SPECT. Interictal SPECT has low sensitivity and accuracy in temporal lobe epilepsy when compared to FDGPET, as interictal blood flow changes are less marked than metabolic changes. In patients with temporal lobe epilepsy, interictal SPECT showed hypoperfusion in the side of epileptogenic focus in 55% and contralateral hypoperfusion leading to false lateralization in 10% [14]. The hypoperfusional most commonly involves the anterior pole of the temporal lobe and medial temporal region. The lateral temporal cortex and ipsilateral frontal and parietal cortex hypoperfusion may also be seen. The presence of left temporal lobar hypoperfusion has been shown to reduce the risk of a postoperative decline in verbal short-term memory function following left temporal lobectomy [15]. The present clinical role of interictal SPECT is to provide as a baseline for comparison and interpretation of ictal SPECT studies

2.6. Ictal SPECT. Ictal studies are obtained during the seizure. Posticta studies are obtained by injection after the completion of a seizure. The term peri-ictal SPECT refers to ictal and early postictal injections. Ictal SPECT is sensitive with correct identification of the seizure focus being achieved in more than 90%, and seizure-free outcome has been achieved in 60–80% of patients [11, 12, 16–25]. False lateralization has been reported in less than 5% of cases. The sensitivity of postictal SPECT injection was 70%, and false localization was reported in less than 5% of the cases [26].

2.7. Ictal SPECT Patterns. The ictal SPECT hyperperfusion patterns were classified by Ho et al. into typical, typical with posterior extension, bilateral, and atypical patterns [27] (Figure 2). The outcome for seizure freedom at two years was 60%, 69%, 67% in the typical, typical with posterior extension, and bilateral pattern groups, suggesting that extended patterns of ictal perfusion represent seizure propagation pathways rather than intrinsically epileptogenic tissue. Atypical pattern group had a worse outcome with only 33% being seizure free and indicates diffuse or extra-temporal epileptogenicity.

Temporal lobe hyperperfusion typically involves the anterior pole and medial temporal lobe with variable degree of involvement of the lateral temporal cortex. Hyperperfusion of the ipsilateral basal ganglia is common and correlates well with dystonic posturing of the contralateral arm during the seizure [28]. Hyperperfusion of ipsilateral thalamus may also be seen, but infrequent. Propagation of the seizure may lead to hyperperfusion of the contralateral medial temporal lobe, but it is less extensive and less in intensity than in the temporal lobe, where the ictal onset occurs [29]. Ipsilateral insula cortex and basal frontal lobe may also be involved. Ictal hyperperfusion is seen in TLE due to mesial temporal sclerosis and also with structural lesions [27].

The injected seizure type and ictal semiology should be known for a correct interpretation of ictal SPECT. The results are best during the injection of complex partial seizures while secondarily generalized seizures show hyperperfusion of multiple areas [30].

2.8. Ictal SPECT in TLE with Normal MRI. Patients with refractory partial seizures and normal MRI brain are a difficult subgroup in terms of presurgical evaluation. The diagnosis of mesial temporal lobe epilepsy in this group may be suggested by ictal semiology, interictal epileptiform discharges, or ictal EEG pattern [31]. Both ictal SPECT and interictal PET are sensitive methods for the lateralization of TLE, but ictal SPECT is more sensitive when MRI is normal

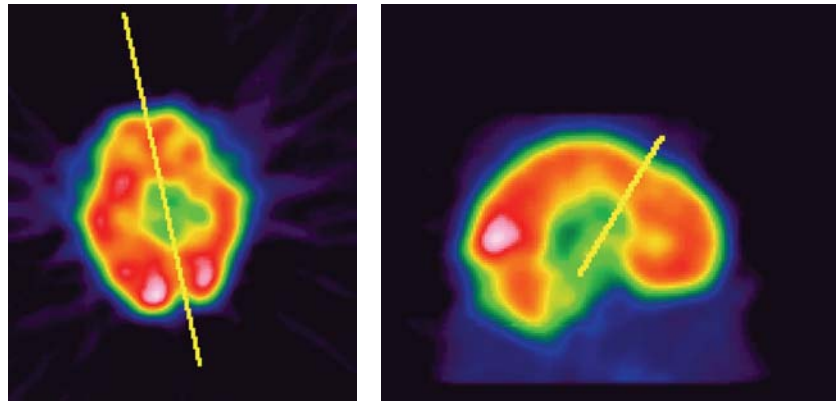

(a) (b)

Figure 1: Reconstruction of temporal lobes (a) transaxial slices parallel to the temporal lobe with (b) coronal slices perpendicular to this plane.

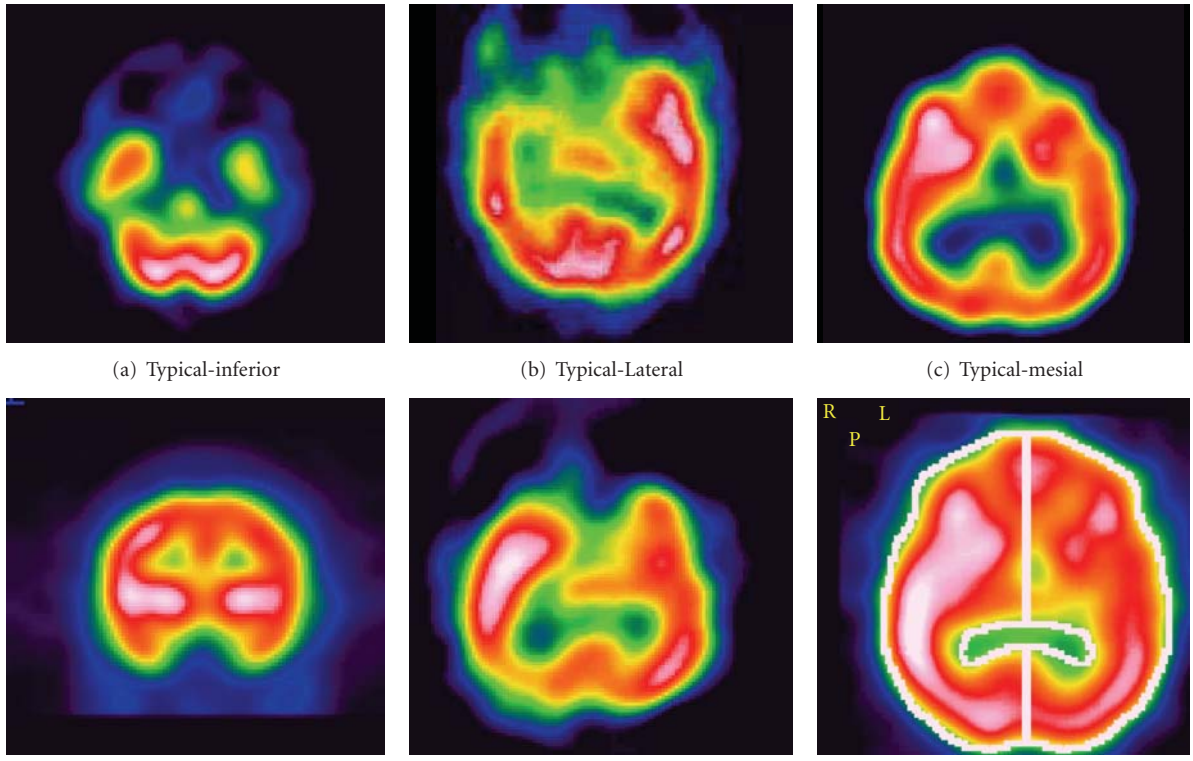

(a) Typical-inferior (b) Typical-Lateral (c) Typical-mesial

(d) Typical-bilateral (e) Typical with posterior extension (f) atypical pattern

Figure 2: Ictal SPECT patterns in temporal epilepsy as described by Ho et al. [27].

[32]. Ictal SPECT and interictal PET are complementary to each other in lateralizing the side in patients with TLE and normal MRI (Figure 3).

2.9. SPECT in Extratemporal Lobe Epilepsy. In extra-temporal lobe epilepsies with normal MRI, the localization of ictal onset zone is difficult, and an extensive invasive monitoring using intracerebral grid and depth electrodes is required. In spite of invasive monitoring the outcomes in extra-temporal lobe epilepsy surgery are not as good as those achieved in temporal lobe surgery. Ictal SPECT and FDGPET will guide the placement of these electrodes. Lee et al. have shown that seizure-free outcome could be achieved in 47% and upto 90% seizure reduction could be achieved in 80% of the patients with refractory epilepsy and normal MRI, evaluated with ictal SPECT and FDGPET [33]. Ictal SPECT studies may show focal hyperperfusion and help in differentiating temporal from extratemporal epilepsy, confirm the epileptogenecity of a structural lesion, and guide the placement of intracranial electrodes in patients with normal

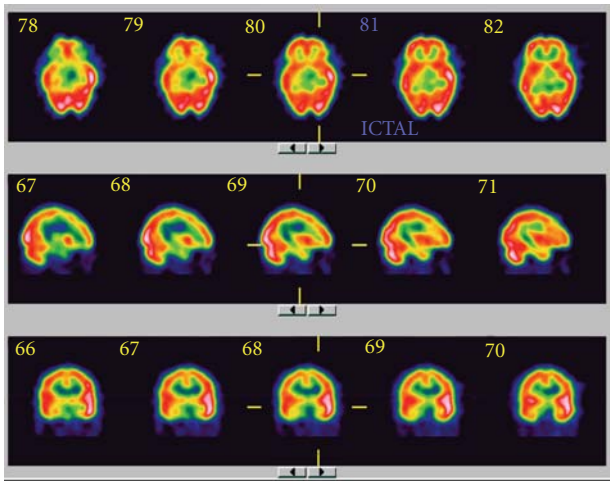

(a) Ictal SPECT-left temporal hyperperfusion

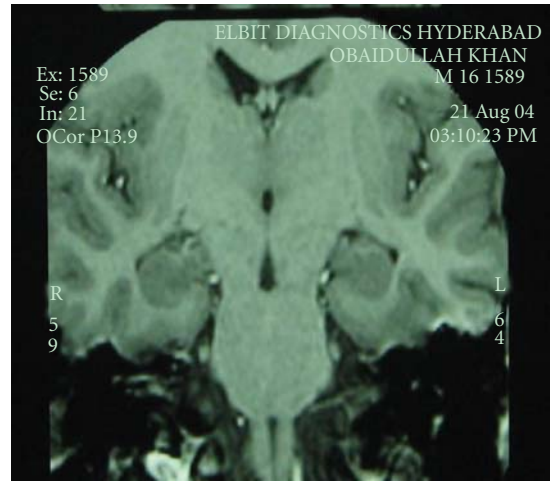

(b) MRI Brain-normal

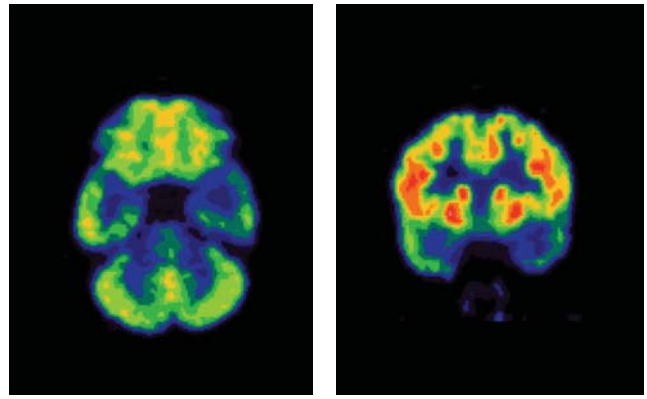

(c) Interictal FDGPET-left temporal hypometabolism

Figure 3: Ictal SPECT and FDGPET in a patient with refractory temporal lobe epilepsy and normal MRI showing lateralization to left. The patient underwent left temporal lobectomy with amygdalohippocampectomy and is seizure free for more than 3 years.

MRI [12, 23, 34, 35]. Ictal SPECT has been demonstrated in the frontal lobes, frequently accompanied by ipsilateral basal ganglia and contralateral cerebellar hyperperfusion [34]. In parietal lobe epilepsy, anterior parietal hyperperfusion was noted with sensorimotor features and posterior parietal hyperperfusion when seizures are psychoparetic in type [36]. Very early ictal injection is required to find a focus in occipital lobe epilepsy (Figure 4). In a study of 17 patients with occipital lobe epilepsy ictal SPECT showed focal occipital hyperperfusion in only 29% [37]. It has been estimated that extratemporal seizures should last 10–15 s after ictal SPECT injection to give good localizing information [38]. Pitfalls of ictal SPECT are that ictal SPECT may show propagated ictal activity and ictal SPECT hyperperfusion does not exclude multifocal seizure onset.

3. SISCOM

Subtraction ictal SPECT with co-registration on MRI (SISCOM) gives good anatomic correlation and highlights an area of relative hyperperfusion or hypoperfusion not readily apparent on visual inspection. Statistical parametric mapping (SPM) improves subtraction image quality. O'Brien et al. [39] reported an excellent outcome when SISCOM localization was concordant with surgical-resection site, but not when SISCOM and resection site were discordant in patients with refractory partial epilepsy and normal MRI. In patients with normal MRI and refractory epilepsy, SISCOM may help to detect subtle focal cortical dysplasia [40]. The indications for SISCOM in patients undergoing a presurgical evaluation include nonsubstrate-directed partial epilepsy multilobar pathology and when there are conflicting results in the noninvasive evaluation [41]. The presence of a SISCOM alteration may obviate the need for intracranial EEG recordings in selected patients. Patients with refractory temporal lobe epilepsy and normal MRI may not require chronic intracranial EEG monitoring if the extracranial ictal EEG pattern and ictal SPECT studies are concordant.

3.1. Ictal SPECT in Other Seizure Disorders. Ictal SPECT has been used to investigate infants with infantile spasms (West syndrome). Focal cortical hyperperfusion has been

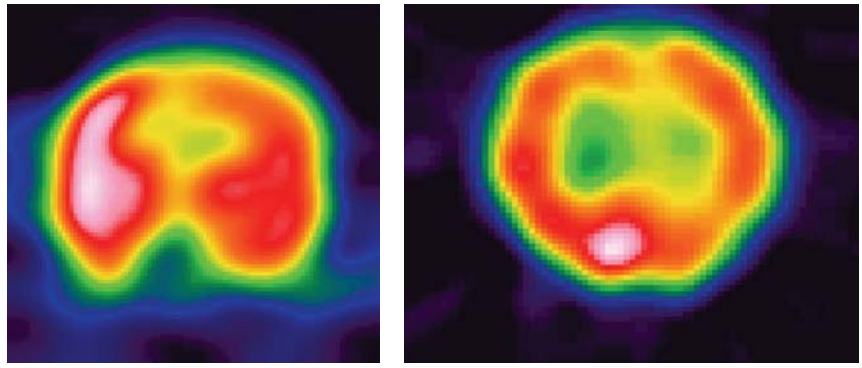

(a) (b)

Figure 4: Ictal SPECT in extra temporal epilepsy showing (a) right frontal hyperperfusion in a patient with frontal lobe epilepsy (b) right occipital hyperperfusion in a patient with occipital lobe epilepsy.

shown in one-third of the cases [42]. The yield for localization in Lennox-Gastaut syndrome is very low and hence ictal SPECT has limited role in this group of patients. Ictal SPECT shows focal or regional hyperperfusion while interictal SPECT will show hypoperfusion in patients with Rassmussen's encephalitis. This may be useful in defining the site for biopsy to confirm the diagnosis [43]. Ictal SPECT shows hyperperfusion of the hamartoma in patients with hypothalamic hamartoma or may show propagation to cortical areas [44]. Ictal SPECT also helps to differentiate true from pseudoseizures when the ictal EEG does not give enough information [45].

3.2. Comparision of Ictal SPECT and FDGPET. In patients with temporal lobe epilepsy, ictal SPECT was found to be marginally more sensitive than FDGPET for the lateralization of the epileptogenic focus, 89% versus 83% [32]. In patients with neocortical epilepsy FDGPET was found to be more sensitive than ictal SPECT and MRI, with a sensitivity of 78%, 70%, and 60%, respectively [46]. In another study FDGPET and ictal SPECT were found to have the same sensitivity of 56% but were complementary to each other [35]. In summary interictal FDGPET and ictal SPECT have similar sensitivity to localize the seizure focus, but complementary when the other modality is not localizing in a given patient [47]. Ictal SPECT should always be read in the context of other presurgical investigations and is useful to localize the epileptogenic zone noninvasively [48].

4. Conclusion

Ictal SPECT is a valuable noninvasive modality during the presurgical evaluation of patients with refractory partial epilepsy. It may obviate the need for intracranial monitoring in patients with refractory temporal lobe epilepsy and normal MRI. Ictal SPECT (SISCOM) guides the placement of depth and grid electrodes in patients with refractory partial epilepsy and normal MRI. Ictal SPECT and FDGPET are complementary for localization of the seizure focus.

References

[1] R. Casse, C. C. Rowe, M. Newton, S. U. Berlangieri, and A. M. Scott, "Positron emission tomography and epilepsy," *Molecular Imaging and Biology*, vol. 4, no. 5, pp. 338–351, 2002.

[2] G. Herrendorf, B. J. Steinhoff, H. J. Bittermann, K. Mursch, J. Meller, and W. Becker, "An easy method to accelerate ictal SPECT," *Journal of Neuroimaging*, vol. 9, no. 2, pp. 129–130, 1999.

[3] H. Vanbilloen, P. Dupont, L. Mesotten et al., "Simple design for rapid self-injection ictal SPET during aura," *European Journal of Nuclear Medicine*, vol. 26, no. 10, pp. 1380–1381, 1999.

[4] J. Leveille, G. Demonceau, and R. C. Walovitch, "Intrasubject comparison between technetium-99m-ECD and technetium-99m- HMPAO in healthy human subjects," *Journal of Nuclear Medicine*, vol. 33, no. 4, pp. 480–484, 1992.

[5] D. S. Lee, S. K. Lee, Y. K. Kim et al., "Superiority of HMPAO ictal SPECT to ECD ictal SPECT in localizing the epileptogenic zone," *Epilepsia*, vol. 43, no. 3, pp. 263–269, 2002.

[6] M. Fukuda, H. Masuda, J. Honma, S. Kameyama, and R. Tanaka, "Ictal SPECT analyzed by three-dimensional stereotactic surface projection in frontal lobe epilepsy patients," *Epilepsy Research*, vol. 68, no. 2, pp. 95–102, 2006.

[7] S. K. Lee, S. Y. Lee, C. H. Yun, H. Y. Lee, J. S. Lee, and D. S. Lee, "Ictal SPECT in neocortical epilepsies: clinical usefulness and factors affecting the pattern of hyperperfusion," *Neuroradiology*, vol. 48, no. 9, pp. 678–684, 2006.

[8] P. Dupont, W. van Paesschen, A. Palmini et al., "Ictal perfusion patterns associated with single MRI-visible focal dysplastic lesions: implications for the noninvasive delineation of the epileptogenic zone," *Epilepsia*, vol. 47, no. 9, pp. 1550–1557, 2006.

[9] G. Huberfeld, M. O. Habert, S. Clemenceau, P. Maksud, M. Baulac, and C. Adam, "Ictal brain hyperperfusion contralateral to seizure onset: the SPECT mirror image," *Epilepsia*, vol. 47, no. 1, pp. 123–133, 2006.

[10] C. C. Rowe, S. F. Berkovic, S. T. B. Sia et al., "Localization of epileptic foci with postictal single photon emission computed tomography," *Annals of Neurology*, vol. 26, no. 5, pp. 660–668, 1989.

[11] M. R. Newton, M. C. Austin, J. G. Chan, W. J. McKay, C. C. Rowe, and S. F. Berkovic, "Ictal SPECT using technetium-99m-HMPAO: methods for rapid preparation and optimal deployment of tracer during spontaneous seizures," *Journal of Nuclear Medicine*, vol. 34, no. 4, pp. 666–670, 1993.

[12] R. Duncan, J. Patterson, R. Roberts, D. M. Hadley, and I. Bone, "Ictal/postictal SPECT in the pre-surgical localisation of complex partial seizures," *Journal of Neurology Neurosurgery and Psychiatry*, vol. 56, no. 2, pp. 141–148, 1993.

[13] C. C. Rowe, S. F. Berkovic, M. C. Austin et al., "Visual and quantitative analysis of interictal SPECT with technetium-99m-HMPAO in temporal lobe epilepsy," *Journal of Nuclear Medicine*, vol. 32, no. 9, pp. 1688–1694, 1991.

[14] M. D. Devous Sr., R. A. Thisted, G. F. Morgan, R. F. Leroy, and C. C. Rowe, "SPECT brain imaging in epilepsy: a meta-analysis," *Journal of Nuclear Medicine*, vol. 39, no. 2, pp. 285–293, 1998.

[15] F. Grunwald, H. F. Durwen, A. Bockisch et al., "Technetium-99m-HMPAO brain SPECT in medically intractable temporal lobe epilepsy: a postoperative evaluation," *Journal of Nuclear Medicine*, vol. 32, no. 3, pp. 388–394, 1991.

[16] W. Shen, B. I. Lee, H. M. Park et al., "HIPDM-SPECT brain imaging in the presurgical evaluation of patients with intractable seizures," *Journal of Nuclear Medicine*, vol. 31, no. 8, pp. 1280–1284, 1990.

[17] J. Bauer, H. Stefan, H. Feistel et al., "Ictal and interictal SPECT measurements using Tc-HMPAO in patients suffering from temproal lobe epilepsies," *Nervenarzt*, vol. 62, no. 12, pp. 745–749, 1991.

[18] O. N. Markand, V. Salanova, R. M. Worth, H. M. Park, and H. H. Wellman, "Ictal brain imaging in presurgical evaluation of patients with medically intractable complex partial seizures," *Acta Neurologica Scandinavica, Supplement*, vol. 89, no. 152, pp. 137–144, 1994.

[19] M. R. Newton, S. F. Berkovic, M. C. Austin, C. C. Rowe, W. J. McKay, and P. F. Bladin, "Ictal postictal and interictal single-photon emission tomography in the lateralization of temporal lobe epilepsy," *European Journal of Nuclear Medicine*, vol. 21, no. 10, pp. 1067–1071, 1994.

[20] O. N. Markand, V. Salanova, R. Worth, H. M. Park, and H. N. Wellman, "Comparative study of interictal PET and ictal SPECT in complex partial seizures," *Acta Neurologica Scandinavica*, vol. 95, no. 3, pp. 129–136, 1997.

[21] S. K. Lee, S. H. Lee, S. K. Kim, D. S. Lee, and H. Kim, "The clinical usefulness of ictal SPECT in temporal lobe epilepsy: the lateralization of seizure focus and correlation with EEG," *Epilepsia*, vol. 41, no. 8, pp. 955–962, 2000.

[22] J. D. Lee, H. J. Kim, B. I. Lee, O. J. Kim, T. J. Jeon, and M. J. Kim, "Evaluation of ictal brain SPET using statistical parametric mapping in temporal lobe epilepsy," *European Journal of Nuclear Medicine*, vol. 27, no. 11, pp. 1658–1665, 2000.

[23] S. Weil, S. Noachtar, S. Arnold, T. A. Yousry, P. A. Winkler, and K. Tatsch, "Ictal ECD-SPECT differentiates between temporal and extratemporal epilepsy: confirmation by excellent post-operative seizure control," *Nuclear Medicine Communications*, vol. 22, no. 2, pp. 233–237, 2001.

[24] T. R. Velasco, L. Wichert-Ana, J. P. Leite et al., "Accuracy of ictal SPECT in mesial temporal lobe epilepsy with bilateral interictal spikes," *Neurology*, vol. 59, no. 2, pp. 266–271, 2002.

[25] M. R. Newton, S. F. Berkovic, M. C. Austin, C. C. Rowe, W. J. McKay, and P. F. Bladin, "Postictal switch in blood flow distribution and temporal lobe seizures," *Journal of Neurology Neurosurgery and Psychiatry*, vol. 55, no. 10, pp. 891–894, 1992.

[26] C. C. Rowe, S. F. Berkovic, M. C. Austin, W. J. McKay, and P. F. Bladin, "Patterns of postictal cerebral blood flow in temporal lobe epilepsy: qualitative and quantitative analysis," *Neurology*, vol. 41, no. 7, pp. 1096–1103, 1991.

[27] S. S. Ho, M. R. Newton, A. M. McIntosh et al., "Perfusion patterns during temporal lobe seizures: relationship to surgical outcome," *Brain*, vol. 120, no. 11, pp. 1921–1928, 1997.

[28] M. R. Newton, S. F. Berkovic, M. C. Austin, D. C. Reutens, W. J. McKay, and P. F. Bladin, "Dystonia, clinical lateralization, and regional blood flow changes in temporal lobe seizures," *Neurology*, vol. 42, no. 2, pp. 371–377, 1992.

[29] W. C. Shin, S. B. Hong, W. S. Tae, and S. E. Kim, "Ictal hyperperfusion patterns according to the progression of temporal lobe seizures," *Neurology*, vol. 58, no. 3, pp. 373–380, 2002.

[30] W. C. Shin, S. B. Hong, W. S. Tae, and S. E. Kim, "Ictal hyperperfusion patterns according to the progression of temporal lobe seizures," *Neurology*, vol. 58, no. 3, pp. 373–380, 2002.

[31] K. Radhakrishnan, E. L. So, P. L. Silbert et al., "Predictors of outcome of anterior temporal lobectomy for intractable epilepsy: a multivariate study," *Neurology*, vol. 51, no. 2, pp. 465–471, 1998.

[32] S. S. Ho, S. F. Berkovic, S. U. Berlangieri et al., "Comparison of ictal SPECT and interictal PET in the presurgical evaluation of temporal lobe epilepsy," *Annals of Neurology*, vol. 37, no. 6, pp. 738–745, 1995.

[33] S. K. Lee, S. Y. Lee, K. K. Kim, K. S. Hong, D. S. Lee, and C. K. Chung, "Surgical outcome and prognostic factors of cryptogenic neocortical epilepsy," *Annals of Neurology*, vol. 58, no. 4, pp. 525–532, 2005.

[34] D. A. Marks, A. Katz, P. Hoffer, and S. S. Spencer, "Localization of extratemporal epileptic foci during ictal single photon emission computed tomography," *Annals of Neurology*, vol. 31, no. 3, pp. 250–255, 1992.

[35] K. S. Hong, S. K. Lee, J. Y. Kim, D. S. Lee, and C. K. Chung, "Pre-surgical evaluation and surgical outcome of 41 patients with non-lesional neocortical epilepsy," *Seizure*, vol. 11, no. 3, pp. 184–192, 2002.

[36] S. S. Ho, S. F. Berkovic, M. R. Newton, M. C. Austin, W. J. McKay, and P. F. Bladin, "Parietal lobe epilepsy: clinical features and seizure localization by ictal SPECT," *Neurology*, vol. 44, no. 12, pp. 2277–2284, 1994.

[37] S. K. Kim, D. S. Lee, S. K. Lee et al., "Diagnostic performance of [F]FDG-PET and ictal [Tc]-HMPAO SPECT in occipital lobe epilepsy," *Epilepsia*, vol. 42, no. 12, pp. 1531–1540, 2001.

[38] A. Kaminska, C. Chiron, D. Ville et al., "Ictal SPECT in children with epilepsy: comparison with intracranial EEG and relation to postsurgical outcome," *Brain*, vol. 126, no. 1, pp. 248–260, 2003.

[39] T. J. O'Brien, E. L. So, B. P. Mullan et al., "Subtraction peri-ictal SPECT is predictive of extratemporal epilepsy surgery outcome," *Neurology*, vol. 55, no. 11, pp. 1668–1677, 2000.

[40] W. Zhang, P. G. Simos, H. Ishibashi et al., "Multimodality neuroimaging evaluation improves the detection of subtle cortical dysplasia in seizure patients," *Neurological Research*, vol. 25, no. 1, pp. 53–57, 2003.

[41] G. D. Cascino, J. R. Buchhalter, B. P. Mullan, and E. L. So, "Ictal SPECT in the definition of the seizure onset zone," in *Presurgical Assessment of Epilepsies with Clinical Neurophysiology and Functional Imaging*, F. Rosenow and H. O. Luders,

Eds., vol. 3 of *Handbook of Clinical Neurophysiology*, pp. 147–154, Elsevier, Amsterdam, The Netherlands, 2004.

[42] K. Haginoya, M. Munakata, H. Yokoyama et al., "Mechanism of tonic spasms in West syndrome viewed from ictal SPECT findings," *Brain and Development*, vol. 23, no. 7, pp. 496–501, 2001.

[43] R. English, N. Soper, B. J. Shepstone, J. M. Hockaday, and G. Stores, "Five patients with Rasmussen's syndrome investigated by single-photon-emission computed tomography," *Nuclear Medicine Communications*, vol. 10, no. 1, pp. 5–14, 1989.

[44] M. P. DiFazio and R. G. Davis, "Utility of early single photon emission computed tomography (SPECT) in neonatal gelastic epilepsy associated with hypothalamic hamartoma," *Journal of Child Neurology*, vol. 15, no. 6, pp. 414–417, 2000.

[45] M. V. Spanaki, S. S. Spencer, M. Corsi, J. MacMullan, J. Seibyl, and I. G. Zubal, "The role of quantitative ictal SPECT analysis in the evaluation of nonepileptic seizures," *Journal of Neuroimaging*, vol. 9, no. 4, pp. 210–216, 1999.

[46] S. I. Hwang, J. H. Kim, S. W. Park et al., "Comparative analysis of MR imaging, positron emission tomography, and ictal single-photon emission CT in patients with neocortical epilepsy," *American Journal of Neuroradiology*, vol. 22, no. 5, pp. 937–946, 2001.

[47] C. Rowe, "Single-photon emission computed tomography in epilepsy," in *Magnetic Resonance in Epilepsy*, R. I. Kuzniecky and G. D. Jackson, Eds., pp. 385–394, Elsevier, Amsterdam, The Netherlands, 2005.

[48] W. van Paesschen, "Ictal SPECT," *Epilepsia*, vol. 45, no. 4, pp. 35–40, 2004.

Hindawi Publishing Corporation
International Journal of Molecular Imaging
Volume 2011, Article ID 682949, 7 pages
doi:10.1155/2011/682949

Review Article

Ventilation/Perfusion SPECT for Diagnosis of Pulmonary Embolism and Other Diseases

Marika Bajc and Björn Jonson

Department of Clinical Physiology, Lund University, 22185 Lund, Sweden

Correspondence should be addressed to Marika Bajc, marika.bajc@med.lu.se

Received 5 October 2010; Accepted 10 November 2010

Academic Editor: Leonard M. Freeman

V/P_{SPECT} has the potential to become a first hand tool for diagnosis of pulmonary embolism based on standardized technology and new holistic interpretation criteria. Pretest probability helps clinicians choose the most appropriate objective test for diagnosis or exclusion of PE. Interpretation should also take into account all ventilation and perfusion patterns allowing diagnosis of other cardiopulmonary diseases than PE. In such contexts, V/P_{SPECT} has excellent sensitivity and specificity. Nondiagnostic reports are $\leq$3%. V/P_{SPECT} has no contraindication; it is noninvasive and has very low radiation exposure. Moreover, acquisition time for V/P_{SPECT} is only 20 minutes. It allows quantification of PE extension which has an impact on individual treatment. It is uniquely useful for followup and research.

1. Introduction

Prior to the development of CT angiography, planar ventilation/perfusion scans were the primary noninvasive method for diagnosis of pulmonary embolism (PE). However, the technique suffered disrepute since the PIOPED I study showed that 65% of scans were nondiagnostic [1]. As will be reviewed below, results from later studies based upon modern imaging techniques and new holistic principles (combining clinical information, pretest probability, results of chest radiograph, and patterns typical of PE or other diseases) reduce the number of nondiagnostic findings to 3% or less, while sensitivity and specificity are excellent [2, 3].

Since the early 1980s, the advantage of tomography over planar imaging for PE detection was indicated [4]. Since then, numerous studies have shown such advantages of ventilation/perfusion single photon emission computed tomography (V/P_{SPECT}) over alternative techniques, which indicated that lung scintigraphy is again appreciated as a first line method for diagnosis of PE.

An important issue is to estimate the clinical probability for PE before performing imaging tests as is elaborated upon in the European Guidelines for Lung Scintigraphy [2] and by Mamlouk et al. [5]. The object of this paper is to show the advantages of V/P_{SPECT} in accordance with the European Guidelines for V/P_{SPECT} [2, 3]. It will be emphasized that V/P_{SPECT} gives diagnostic information in other conditions such as pneumonia, COPD, and left heart failure. The presentation will focus on basic requirements on diagnostic methods for PE:

(1) fast procedure,

(2) low radiation dose,

(3) no contraindications,

(4) high diagnostic accuracy and few nondiagnostic reports,

(5) utility for selection of treatment strategy,

(6) suitability for followup and research.

2. Agents Used for Imaging of Ventilation

Gases are distributed strictly according to regional ventilation. The only gas that is useful for V/P_{SPECT} is krypton, ^{81m}Kr. Its short half life (13 s) implies that it disappears

from the alveoli by decay rather than by exhalation. After some minutes of test gas breathing, when the alveolar concentration has approached a steady state reflecting alveolar ventilation, V/P_{SPECT} is performed. The rubidium generator that delivers ^{81m}Kr has a half life of 4.6 h. Limited availability and high costs prevent a general use of ^{81m}Kr.

Inhalation of a radio-aerosol is used in nearly all centers for ventilation scintigraphy. Aerosol particles are liquid or solid. Particles larger than 2 μm are deposited in large airways (hot spots). Smaller particles are deposited by sedimentation and diffusion in small airways and alveoli. Particles smaller than 1 μm are mainly deposited in alveoli by diffusion. Aerosol deposition is modified by flow pattern. High flow rates at forced breathing patterns and turbulent flow enhance particle deposition in airways and augment tendencies to hot spots in ventilation images, particularly in Chronic Obstructive Pulmonary Disease (COPD).

The mass median aerodynamic diameter, MMAD, reflects radioactivity carried by each liquid particle. Half of the radioactivity resides in particles smaller than MMAD and 50% in larger ones. It is often recommended that the maximum droplet size inhaled by the patient should not exceed 2 μm. Because of the complex physics behind aerosol deposition pattern, the performance of a nebuliser must be clinically tested.

Diethylenetriaminepentaacetic acid labelled with technetium, ^{99m}Tc-DTPA, is in general use for ventilation scintigraphy with liquid aerosols. The size of the water solvable molecule is 492 Dalton [6]. Therefore, ^{99m}Tc-DTPA diffuses through the alveolocapillary membrane to the blood. In a healthy patient, clearance of ^{99m}Tc-DTPA occurs with a half life of about 70 minutes. Increased clearance, leading to a shorter half life is observed with alveolar inflammation of any kind, such as alveolitis of allergic or toxic nature and even in smokers [7–9].

Technegas is an aerosol of extremely small carbon particles, 0.005–0.2 μm, generated in a high temperature furnace [10–12]. The small particle size implies that they are distributed in the lungs almost like a gas and are deposited in alveoli by diffusion [13, 14]. Technegas provides images which are equivalent to those with ^{81m}Kr [14–18].

Recently, a head to head study of deposition patterns using Technegas and ^{99m}Tc-DTPA performed in a group of patients routinely admitted for V/P_{SPECT} and in a group of patients with known COPD was published [19]. Technegas reduced problems of central airway deposition and peripheral hotspots. Unevenness of radiotracer deposition and degree of central deposition were less with Technegas, particularly in the obstructive patients, Figure 1. In some patients, mismatched perfusion defects were only identified using Technegas because the marked peripheral unevenness of ^{99m}Tc-DTPA obscured mismatch and thereafter PE might have been overlooked in COPD patients using ^{99m}Tc-DTPA. In a few patients, ^{99m}Tc-DTPA yielded images of poor quality. It was concluded that Technegas is the superior radio-aerosol, particularly in patients with obstructive lung disease. Another advantage of using Technegas is that a few breaths are sufficient to achieve an adequate amount of activity in the lungs.

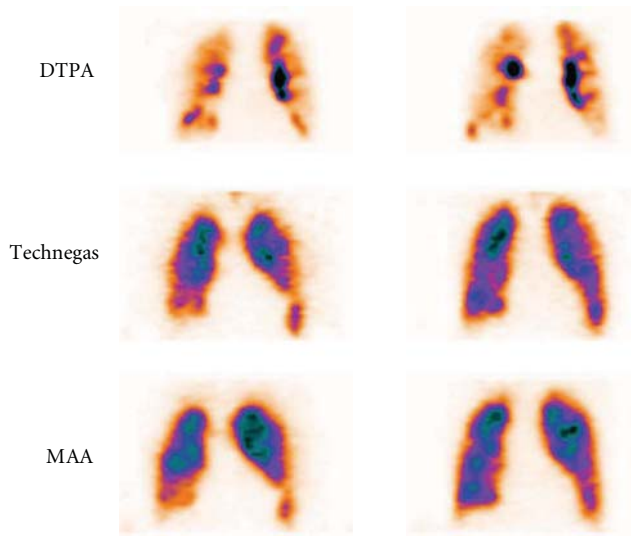

Figure 1: Frontal slices in patient with COPD. Ventilation study with DTPA and technegas with corresponding perfusion images.

3. Agent Used for Imaging of Perfusion

For perfusion scintigraphy, radio-labelled MAA, sized 15–100 μm, is injected intravenously. This causes microembolization of pulmonary capillaries and precapillary arterioles, reflecting regional perfusion if at least 60 000 particles are injected [20]. Routinely, about 400 000 particles are injected. As there are over 280 billion pulmonary capillaries and 300 million precapillary arterioles, only a small fraction of the pulmonary bed will be obstructed. Fewer particles might be used in patients with known pulmonary hypertension or after single lung transplantation.

4. How to Perform V/P_{SPECT}

4.1. Image Acquisition. Using a dual head camera, Palmer et al. developed a fast and efficient clinical method for V/P_{SPECT} [21]. The total acquisition time is only 20 minutes. A new algorithm allows calculation of the quotient between ventilation and perfusion and presentation of $V/P_{quotient}$ images for easier diagnosis and quantification of PE extension.

The ventilation study starts with inhalation of 25–30 MBq ^{99m}Tc-DTPA or Technegas. Immediately after ventilation SPECT, a dose of 100–120 MBq ^{99m}Tc MAA is given intravenously for perfusion imaging. During the examination, the supine patient carefully maintains the position between ventilation and perfusion acquisitions. Immobilization for only 20 minutes is usually well tolerated by patients. Examination in the supine position is comfortable even for most of critically ill patients. It is also more convenient for the staff.

When clearance measurements are required, ^{99m}Tc-DTPA may be used. Clearance is then calculated from initial and final anteroposterior SPECT projections [21].

4.2. Radiation Exposure. The doses of 30 MBq and 120 MBq for ventilation and perfusion, respectively, allow excellent V/P_{SPECT} quality at an effective radiation dose of 1.8 mSv [22].

4.3. Reconstruction and Calculation of $V/P_{quotient}$ Images. Iterative reconstruction is performed using ordered subset expectation maximization (OSEM), for example, with 8 subsets and 2 iterations. In processing the images, the ventilation background was subtracted from the perfusion tomograms and a normalized V/P image set calculated, $V/P_{quotient}$. The algorithms for $V/P_{quotient}$ were developed by Palmer et al. and further amended by Bajc et al. [21, 23]. The main consideration in the creation of $V/P_{quotient}$ images was to scale smoothened ventilation and perfusion data sets to display $V/P_{quotient}$ in a fixed linear scale allowing separation of normal regions from those with mismatch (Figure 2).

4.4. Presentation of V/P_{SPECT}. The basic format for V/P_{SPECT} presentation is displayed slices in frontal, sagittal, and transversal projections, available on any modern system. The slices must be accurately aligned so that ventilation and perfusion slices match each other and can be correctly compared. It is of value to achieve this acquisition in one session with maintained body position. This is also a prerequisite for the calculation of $V/P_{quotient}$ images, which greatly facilitates identification and quantification of PE.

Volume rendered images, such as "Maximum Intensity Projection", are available with almost all SPECT systems, allowing rotating 3D views. Such displays might be useful, particularly for quantification and followup of PE patients [24].

4.5. Primary Validation of the V/P_{SPECT} Method. Using a porcine model based upon ^{201}Tl-marked emboli as a "gold standard", Bajc et al. validated the new V/P_{SPECT} method for diagnosis of PE and confirmed the superior value of tomography over planar imaging and improved interobserver agreement of defects on the subsegmental level [25]. In a following clinical head to head comparison between planar imaging and V/P_{SPECT}, it was shown that 53% more mismatch points were identified with V/P_{SPECT} compared to the planar technique [26]. Similar results have been found by others [27, 28]. SPECT eliminates superimposed structures, clarifying the segmental and subsegmental nature of perfusion defect caused by PE.

5. Interpretation with Emphasis on PE

Lung scintigraphy for diagnosis of PE and other diseases should routinely include ventilation and perfusion studies [21, 23, 25, 27, 29]. In PE, a perfusion defect is due to an embolus blocking blood flow. Because there is no corresponding blockage in the airway, ventilation remains normal causing a mismatch pattern. The distinction of whether a given perfusion defects is matched or mismatched is fundamental. The next step is to characterize the perfusion defects. Perfusion defects due to blockage of a pulmonary artery should reflect the branching of pulmonary circulation and its classical segmental anatomy. A segmental defect is wedge shaped and with its base on the pleura as will be illustrated (Figure 3).

The European guidelines [2, 3] advocate the new holistic interpretation and reporting of lung SPECT. Freeman et al. argued that "the expert's successful interpretation of lung scans exceeds the best accuracy achievable by algorithms, which, by definition, are distillations of decision making into finite linear steps. The subjective of the whole is superior to any possible attempt to define its discrete parts" [30].

A holistic interpretation of V/P_{SPECT} images includes (1) clinical information and pretest probability for PE, (2) chest X-ray when available, (3) recognition of patterns typical for PE based upon segmental charts, and (4) recognition of patterns of other diseases than PE whenever possible [21, 23].

This is as important as the imaging technique. The clinician can only benefit from reports, which clearly express the presence or absence of PE. This goal was not reached with previous probabilistic reporting methods according to PIOPED or modified PIOPED, which defied how planar scans are reported [1, 31]. Large V/P_{SPECT} studies show that this is achievable if all patterns representing ventilation together with perfusion are considered [23, 32–34]. Conclusive reports were given in 97 to 99% of studies.

Recommended criteria for reading V/P_{SPECT} with respect to acute PE described in the European Guidelines are as follows.

No PE is reported if there are any of the following features:

(i) normal perfusion pattern conforming to the anatomic boundaries of the lungs,

(ii) matched or reversed mismatch V/P defects of any size, shape, or number in the absence of mismatch,

(iii) mismatch that does not have a lobar, segmental or subsegmental pattern.

PE is reported if there is

(i) V/P mismatch of at least one segment or two subsegments that conforms to the pulmonary vascular anatomy.

Nondiagnostic for PE is reported if there are

(i) multiple V/P abnormalities not typical of specific diseases.

In PE, it is fundamental that mismatched areas are conical with the base of the cone along the pleura and conform to known sub-segmental and segmental vascular anatomy. With such interpretation criteria, recent V/P_{SPECT} studies in over 3000 cases showed according to a recent review a negative predictive value of 97–99%, a sensitivity of 96–99%, and a specificity of 91–98% for PE [3]. The rate of nondiagnostic findings was 1–3% [23, 32–34]. Using our technique, V/P_{SPECT} yields ventilation and perfusion images in exactly the same projections. This makes calculation of $V/P_{quotient}$ images possible and facilitates recognition of mismatch, particularly important in the middle lobe and

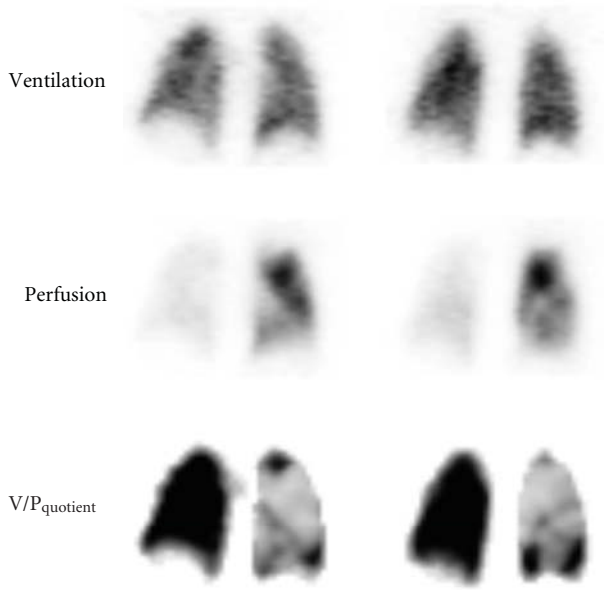

Figure 2: Frontal slices in patient with massive PE. Absent perfusion in the right lung and sub-segmental defects in the left are clearly delineated in $V/P_{quotient}$ images.

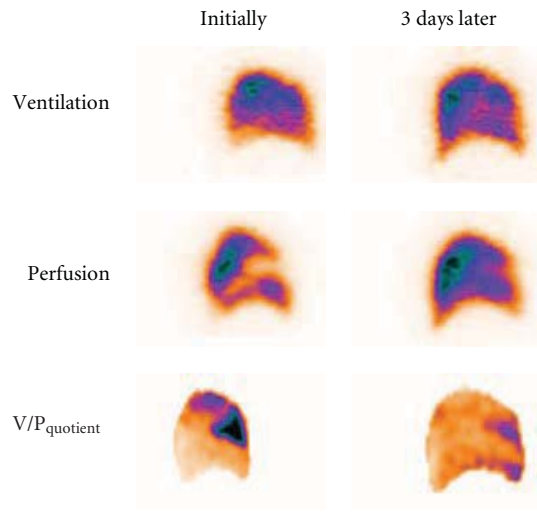

Figure 3: Sagittal slice in patient with segmental PE. Perfusion defect in anterior segment initially, nicely delineated in $V/P_{quotient}$ image. After 3 days, resolution is observed.

lingula where mismatch may be overlooked if the lung is not accurately delineated by its ventilation images [35].

V/P_{SPECT} is the method of choice for quantification of the extent of embolism, because all emboli in the whole lung are recognised and it has greater sensitivity compared to MDCT [27, 32, 33]. The number of segments and sub-segments indicating for PE typical mismatch are counted and expressed in % of the total lung parenchyma [24]. A segmental reduction or a sub-segmental total deficiency of function is attributed 1 point, and a segmental total deficiency is attributed 2 points. Therefore, the 9 segments of each lung can be represented by the total of 18 points. Mismatch defects are expressed as mismatch points, which after division by 36 give the fraction of the lung that is embolized. The reduction in total overall lung function can be estimated by adding the number of regions with reduced ventilation and/or perfusion.

Patients with up 40% PE could be safely treated at home if ventilation abnormalities engaged not more that 20% of the lung. Since 2004, the University Hospital of Lund has safely treated about 60% of patients with PE at home (approximately 1500).

6. Diagnosis of Pulmonary Embolism

V/P_{SPECT} images allow clear identification of segmental and sub-segmental perfusion defects, as in Figure 2 from a woman with extensive PE.

Figure 3 shows a well-delineated segmental perfusion defect. Followup after three days showed an almost normal pattern, confirming the diagnosis of PE.

Importantly, mismatch findings without a segmental character do not indicate PE. Such findings are often observed in patients with heart failure, mediastinal adenopathy, postradiation therapy, and so forth.

6.1. Indications for V/P_{SPECT}

6.1.1. Diagnostic Accuracy and Methodological Considerations. The clinical value of V/P_{SPECT} has been confirmed in several studies [27, 29, 32–34]. This has been highlighted by Stein et al. in a recent review [36]. V/P_{SPECT} is today the method recommended by the European Association of Nuclear Medicine for clinical diagnosis, followup, and research [2].

6.1.2. Selection of Therapeutic Strategy. Management of PE was previously confined to in-hospital therapy, using thrombolysis or heparin injections followed by oral anticoagulants for extended periods of time.

V/P_{SPECT} allows objective quantification of PE. It has been shown that out-patient treatment is safe when based upon V/P_{SPECT} that quantifies PE extension and identifies V/P defects of other etiologies [24]. V/P_{SPECT} is accordingly a tool to guide the individual treatment.

6.1.3. Followup. For followup, V/P_{SPECT} is the method recommended by the European Association of Nuclear medicine due to its high sensitivity, noninvasiveness, low radiation exposure, and absence of contraindications [2].

Clinical reasons for followup are

(i) persistent V/P mismatches often occur after PE;

(ii) PE may recur in identical locations;

(iii) a prior study will help determine the age of a new defect;

(iv) There is an impact on therapy decision.

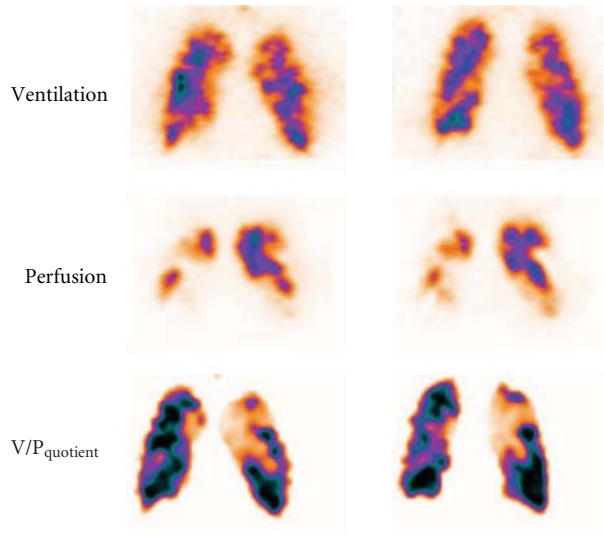

Figure 4: Patient with COPD and extensive PE. On frontal slices, uneven ventilation with peripheral hot spots is observed, and perfusion images showed multiple perfusion defects, clearly delineated on $VP_{quotient}$ images.

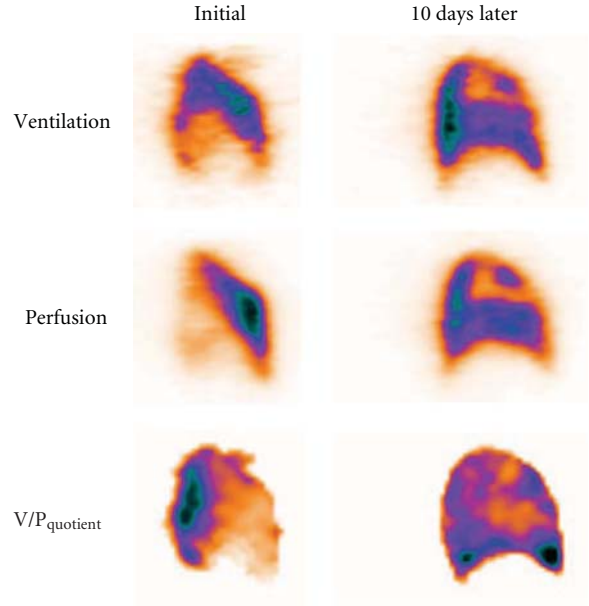

Figure 5: Patient with heart failure. Sagittal slice on the left panel shows redistribution of perfusion towards anterior region; ventilation is less affected causing mismatch of non-segmental character. Right panel shows control after 10 days of treatment with normalization of ventilation and perfusion distribution but with new ventilation and perfusion defect in upper lobe due to pneumonia.

Obviously, evaluation of different drugs and treatment strategies merits the use of V/P_{SPECT} because of its high sensitivity and quality with regards to quantification.

7. Additional Findings

V/P_{SPECT} allows diagnosis of several other diseases which have different scintigraphic appearances to PE, as detailed below [2, 3, 37].

7.1. Chronic Obstructive Pulmonary Disease (COPD). In COPD matched areas with defects in ventilation and perfusion are observed. Ventilation defects are commonly more prominent than those of perfusion which leads to a pattern called reverse mismatch [19]. V/P_{SPECT} frequently provides the first indication of COPD. Notably, V/P_{SPECT} allows the diagnosis of PE even in the presence of COPD [32, 37], Figure 4.

7.2. Heart Failure. In left heart failure, redistribution of perfusion towards upper lung regions is well recognised since long [38]. Ventilation is usually not affected to the same degree as perfusion, which leads to a mismatch pattern. Importantly, this pattern does not conform to segmental anatomy of pulmonary arteries and it is not of a segmental character. Among patients referred for suspected PE, redistribution of perfusion to upper ventral regions indicated heart failure in 15% of cases [39]. The positive predictive value of the referred V/P_{SPECT} pattern was 88%. Figure 5 shows V/P_{SPECT} before and after treatment for heart failure.

7.3. Pneumonia. Pneumonic regions lack ventilation while perfusion may partly be upheld. The most frequent finding is a matched defect [40]. In case of partly preserved perfusion, reversed mismatch is observed [40, 41]. Preserved perfusion along the pleural border leads to a "stripe sign" [42, 43]. V/P_{SPECT} frequently shows this sign because no overlaying structures obscure the images, Figure 6.

The combination of PE and pneumonia is common [32]. Suspicion or knowledge that a patient has pneumonia does not contraindicate V/P_{SPECT}. On the contrary, V/P_{SPECT} may be life-saving in the most complex cases [44].

8. Concluding Remarks

The qualities of V/P_{SPECT} rely upon adequate and standardized technology of combined ventilation and perfusion studies as well as new holistic interpretation criteria as discussed.

V/P_{SPECT} has excellent sensitivity and specificity. The rate of nondiagnostic reports is $\leq 3\%$. V/P_{SPECT} is noninvasive and can be performed in all patients. The radiation exposure is low. With efficient technique and effective organization, V/P_{SPECT} acquisition time is only 20 minutes. Furthermore, it allows quantification of PE that in some centres has impact on choice of treatment. V/P_{SPECT} is uniquely useful for followup and research. Its outstanding qualities merit consideration of its use as the primary diagnostic method for PE in all hospitals in which nuclear medicine is practiced. V/P_{SPECT} frequently gives diagnosis of both PE as well as comorbid conditions as COPD, left heart failure, and pneumonia.

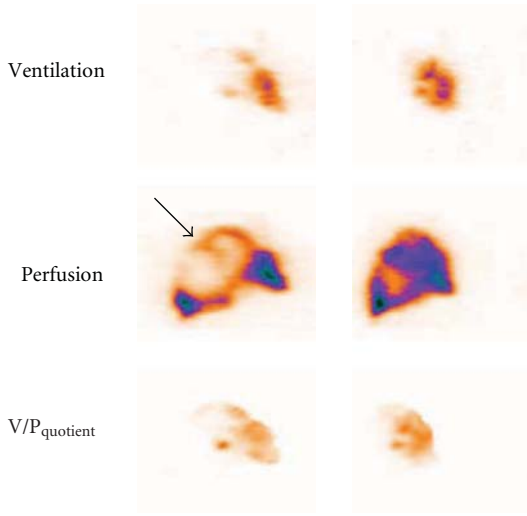

Figure 6: Patient with extensive pneumonia. Sagittal slices in a 79-year-old man who felt general illness, shivering, and low blood pressure. Chest X-ray was interpreted as pleural effusion. The ventilation study of the left lung showed almost absent ventilation, while perfusion was mainly preserved, and a stripe sign is observed. Diagnosis with V/P_{SPECT} was bilateral pneumonia, and this was confirmed later at autopsy.

References

[1] C. E. Vreim, H. A. Saltzmann, A. Alavai et al., "Value of the ventilation/perfusion scan in acute pulmonary embolism. Results of the prospective investigation of pulmonary embolism diagnosis (PIOPED)," *Journal of the American Medical Association*, vol. 263, no. 20, pp. 2753–2759, 1990.

[2] M. Bajc, J. B. Neilly, M. Miniati, C. Schuemichen, M. Meignan, and B. Jonson, "EANM guidelines for ventilation/perfusion scintigraphy: part 2. Algorithms and clinical considerations for diagnosis of pulmonary emboli with V/P_{SPECT} and MDCT," *European Journal of Nuclear Medicine and Molecular Imaging*, vol. 36, no. 9, pp. 1528–1538, 2009.

[3] M. Bajc, J. B. Neilly, M. Miniati, C. Schuemichen, M. Meignan, and B. Jonson, "EANM guidelines for ventilation/perfusion scintigraphy: part 1. Pulmonary imaging with ventilation/perfusion single photon emission tomography," *European Journal of Nuclear Medicine and Molecular Imaging*, vol. 36, no. 8, pp. 1356–1370, 2009.

[4] J. S. Magnussen, P. Chicco, A. W. Palmer et al., "Single-photon emission tomography of a computerised model of pulmonary embolism," *European Journal of Nuclear Medicine*, vol. 26, no. 11, pp. 1430–1438, 1999.

[5] M. D. Mamlouk, E. vanSonnenberg, R. Gosalia et al., "Pulmonary embolism at CT angiography: implications for appropriateness, cost, and radiation exposure in 2003 patients," *Radiology*, vol. 256, no. 2, pp. 625–632, 2010.

[6] G. R. Mason, A. M. Peters, E. Bagdades, M. J. Myers, D. Snook, and J. M. B. Hughes, "Evaluation of pulmonary alveolar epithelial integrity by the detection of restriction to diffusion of hydrophilic solutes of different molecular sizes," *Clinical Science*, vol. 100, no. 3, pp. 231–236, 2001.

[7] C. Beadsmoore, H. K. Cheow, K. Szczepura, P. Ruparelia, and A. M. Peters, "Healthy passive cigarette smokers have increased pulmonary alveolar permeability," *Nuclear Medicine Communications*, vol. 28, no. 2, pp. 75–77, 2007.

[8] J. Rinderknecht, L. Shapiro, and M. Krauthammer, "Accelerated clearance of small solutes from the lungs in interstitial lung disease," *American Review of Respiratory Disease*, vol. 121, no. 1, pp. 105–117, 1980.

[9] D. B. Yeates and J. Mortensen, Eds., *Textbook of Respiratory Medicine*, vol. 1, WB Saunders, Philadelphia, Pa, USA, 3rd edition, 2000.

[10] W. M. Burch, P. J. Sullivan, F. E. Lomas et al., "Lung ventilation studies with technetium-99m pseudogas," *Journal of Nuclear Medicine*, vol. 27, no. 6, pp. 842–846, 1986.

[11] M. Lemb, T. H. Oei, H. Eifert, and B. Gunther, "Technegas: a study of particle structure, size and distribution," *European Journal of Nuclear Medicine*, vol. 20, no. 7, pp. 576–579, 1993.

[12] T. J. Senden, K. H. Moock, J. F. Gerald et al., "The physical and chemical nature of technegas," *Journal of Nuclear Medicine*, vol. 38, no. 8, pp. 1327–1333, 1997.

[13] T. Inoue, N. Watanabe, N. Oriuchi et al., "Clinical evaluation of lung scintigraphy with 99mTc-technegas," *Nippon Igaku Hoshasen Gakkai Zasshi*, vol. 50, no. 12, pp. 1590–1600, 1990.

[14] J. M. James, J. J. Lloyd, B. C. Leahy et al., "99Tcm-Technegas and krypton-81m ventilation scintigraphy: a comparison in known respiratory disease," *British Journal of Radiology*, vol. 65, no. 780, pp. 1075–1082, 1992.

[15] G. Cook and S. E. M. Clarke, "An evaluation of Technegas as a ventilation agent compared with krypton-81m in the scintigraphic diagnosis of pulmonary embolism," *European Journal of Nuclear Medicine*, vol. 19, no. 9, pp. 770–774, 1992.

[16] I. J. C. Hartmann, P. J. Hagen, M. P. M. Stokkel, O. S. Hoekstra, and M. H. Prins, "Technegas Versus ^{81m}Kr Ventilation–Perfusion Scintigraphy: A Comparative Study in Patients with Suspected Acute Pulmonary Embolism," *Journal of Nuclear Medicine*, vol. 42, no. 3, pp. 393–400, 2001.

[17] J. Magnant, L. Vecellio, M. de Monte et al., "Comparative analysis of different scintigraphic approaches to assess pulmonary ventilation," *Journal of Aerosol Medicine*, vol. 19, no. 2, pp. 148–159, 2006.

[18] P. Peltier, P. De Faucal, A. Chetanneau, and J. F. Chatal, "Comparison of technetium-99m aerosol and krypton-81m in ventilation studies for the diagnosis of pulmonary embolism," *Nuclear Medicine Communications*, vol. 11, no. 9, pp. 631–638, 1990.

[19] J. Jögi, B. Jonson, M. Ekberg, and M. Bajc, "Ventilation-perfusion SPECT with 99mTc-DTPA versus Technegas: a head-to-head study in obstructive and nonobstructive disease," *Journal of Nuclear Medicine*, vol. 51, no. 5, pp. 735–741, 2010.

[20] L. L. Heck and J. W. Duley, "Statistical considerations in lung imaging with 99mTc albumin particles," *Radiology*, vol. 113, no. 3, pp. 675–679, 1974.

[21] J. Palmer, U. Bitzén, B. Jonson, and M. Bajc, "Comprehensive ventilation/perfusion SPECT," *Journal of Nuclear Medicine*, vol. 42, no. 8, pp. 1288–1294, 2001.

[22] J. Valentin, "Radiation dose to patients from radiopharmaceuticals (Addendum 2 to ICRP publication 53)," *Annals of the ICRP*, vol. 28, no. 3, pp. 1–126, 1998.

[23] M. Bajc, C.-G. Olsson, J. Palmer, and B. Jonson, "Quantitative ventilation/perfusion SPECT (QV/P_{SPECT}): a primary method for diagnosis of pulmonary embolism," in *Nuclear Medicine Annual*, L. M. Freeman, Ed., pp. 173–186, Lippincott Williams & Wilkins, Philadelphia, Pa, USA, 2004.

[24] C. G. Olsson, U. Bitzén, B. Olsson et al., "Outpatient tinzaparin therapy in pulmonary embolism quantified with ventilation/perfusion scintigraphy," *Medical Science Monitor*, vol. 12, no. 2, pp. PI9–PI13, 2006.

[25] M. Bajc, U. Bitzén, B. Olsson, V. Perez de Sá, J. Palmer, and B. Jonson, "Lung ventilation/perfusion SPECT in the artificially embolized pig," *Journal of Nuclear Medicine*, vol. 43, no. 5, pp. 640–647, 2002.

[26] M. Bajc, C. G. Olsson, B. Olsson, J. Palmer, and B. Jonson, "Diagnostic evaluation of planar and tomographic ventilation/perfusion lung images in patients with suspected pulmonary emboli," *Clinical Physiology and Functional Imaging*, vol. 24, no. 5, pp. 249–256, 2004.

[27] P. Reinartz, J. E. Wildberger, W. Schaefer, B. Nowak, A. H. Mahnken, and U. Buell, "Tomographic imaging in the diagnosis of pulmonary embolism: a comparison between V/Q lung scintigraphy in SPECT technique and multislice spiral CT," *Journal of Nuclear Medicine*, vol. 45, no. 9, pp. 1501–1508, 2004.

[28] H. Gutte, J. Mortensen, C. V. Jensen et al., "Comparison of V/Q SPECT and planar V/Q lung scintigraphy in diagnosing acute pulmonary embolism," *Nuclear Medicine Communications*, vol. 31, no. 1, pp. 82–86, 2010.

[29] M. Lemb and H. Pohlabeln, "Pulmonary thromboembolism: a retrospective study on the examination of 991 patients by ventilation/perfusion SPECT using Technegas," *Nuklearmedizin*, vol. 40, no. 6, pp. 179–186, 2001.

[30] L. M. Freeman, B. Krynyckyi, and L. S. Zuckier, "Enhanced lung scan diagnosis of pulmonary embolism with the use of ancillary scintigraphic findings and clinical correlation," *Seminars in Nuclear Medicine*, vol. 31, no. 2, pp. 143–157, 2001.

[31] P. D. Stein, R. D. Hull, W. A. Ghali et al., "Tracking the uptake of evidence: two decades of hospital practice trends for diagnosing deep vein thrombosis and pulmonary embolism," *Archives of Internal Medicine*, vol. 163, no. 10, pp. 1213–1219, 2003.

[32] M. Bajc, B. Olsson, J. Palmer, and B. Jonson, "Ventilation/Perfusion SPECT for diagnostics of pulmonary embolism in clinical practice," *Journal of Internal Medicine*, vol. 264, no. 4, pp. 379–387, 2008.

[33] H. Gutte, J. Mortensen, C. V. Jensen et al., "Detection of pulmonary embolism with combined ventilation-perfusion SPECT and low-dose CT: head-to-head comparison with multidetector CT angiography," *Journal of Nuclear Medicine*, vol. 50, no. 12, pp. 1987–1992, 2009.

[34] M. Leblanc, F. Leveillée, and E. Turcotte, "Prospective evaluation of the negative predictive value of V/Q SPECT using 99mTc-Technegas," *Nuclear Medicine Communications*, vol. 28, no. 8, pp. 667–672, 2007.

[35] M. A. Meignan, "Lung ventilation/perfusion SPECT: the right technique for hard times," *Journal of Nuclear Medicine*, vol. 43, no. 5, pp. 648–651, 2002.

[36] P. D. Stein, L. M. Freeman, H. D. Sostman et al., "SPECT in acute pulmonary embolism," *Journal of Nuclear Medicine*, vol. 50, no. 12, pp. 1999–2007, 2009.

[37] M. Bajc and B. Jonson, "Lung," in *Clinical Nuclear Medicine*, H. J. Biersack and L. Freeman, Eds., pp. 118–137, Springer, Berlin, Germany, 2007.

[38] W. F. Friedman and E. Braunwald, "Alterations in regional pulmonary blood flow in mitral valve disease studied by radioisotope scanning. A simple nontraumatic technique for estimation of left atrial pressure," *Circulation*, vol. 34, no. 3, pp. 363–376, 1966.

[39] J. Jögi, J. Palmer, B. Jonson, and M. Bajc, "Heart failure diagnostics based on ventilation/perfusion single photon emission computed tomography pattern and quantitative perfusion gradients," *Nuclear Medicine Communications*, vol. 29, no. 8, pp. 666–673, 2008.

[40] D. J. Li, I. Stewart, K. A. Miles, and E. P. Wraight, "Scintigraphic appearances in patients with pulmonary infection and lung scintigrams of intermediate or low probability for pulmonary embolism," *Clinical Nuclear Medicine*, vol. 19, no. 12, pp. 1091–1093, 1994.

[41] P. Carvalho and J. P. Lavender, "The incidence and etiology of the ventilation/perfusion reverse mismatch defect," *Clinical Nuclear Medicine*, vol. 14, no. 8, pp. 571–576, 1989.

[42] H. D. Sostman and A. Gottschalk, "The stripe sign: a new sign for diagnosis of nonembolic defects on pulmonary perfusion scintigraphy," *Radiology*, vol. 142, no. 3, pp. 737–741, 1982.

[43] H. D. Sostman and A. Gottschalk, "Prospective validation of the stripe sign in ventilation-perfusion scintigraphy," *Radiology*, vol. 184, no. 2, pp. 455–459, 1992.

[44] C. G. Olsson, M. Bajc, B. Jonson, and U. Albrechtsson, "Value of ventilation/perfusion SPECT detecting extensive pulmonary embolism in a patient with pneumonia," *Thrombosis and Haemostasis*, vol. 93, no. 5, pp. 993–994, 2005.

Hindawi Publishing Corporation
International Journal of Molecular Imaging
Volume 2011, Article ID 782758, 4 pages
doi:10.1155/2011/782758

Case Report

Alleviation of Brain Hypoperfusion after Preventative Treatment with Lomerizine in an Elderly Migraineur with Aura

Joe Aoyagi,[1] Ken Ikeda,[2] Tetsuhito Kiyozuka,[1] Takehisa Hirayama,[2] Yuichi Ishikawa,[2] Ryuta Sato,[1] Yasuhiro Yoshii,[2] Kiyokazu Kawabe,[2] and Yasuo Iwasaki[2]

[1] *Department of Neurology, Mishuku Hospital, 5-33-12 Kamimeguro, Meguroku, Tokyo 153-0051, Japan*
[2] *Department of Neurology, Toho University Omori Medical Center, 6-11-1 Omorinishi, Otaku, Tokyo 143-8541, Japan*

Correspondence should be addressed to Ken Ikeda, keni@med.toho-u.ac.jp

Received 19 July 2010; Accepted 6 December 2010

Academic Editor: Ronald L. Van Heertum

Previous studies of brain single-photon emission tomography (SPECT) showed changes of regional cerebral blood flow (rCBF) in migraineurs during prodromes or headache attacks. Little is known about how successful medication of migraine prevention can reflect rCBF in migraineurs. We highlighted alternation of brain SPECT findings in a migraineur with aura before and after prophylactic treatment with lomerizine, a calcium channel blocker. A 70-year-old man with migraine developed visual disturbance frequently at walking exercise for the recent 3 months. After this visual attack, a mild-degree of throbbing headache occured occasionally. Brain SPECT using ^{99m}Tc-ethyl cysteinate dimer was performed at interictal time of migraine. Brain SPECT before lomerizine treatment revealed hypoperfusion in the frontal, parietal, and occipital regions. He was diagnosed with recurrence of migraine with aura (MA). Lomerizine (10 mg/day, po) was administered for 3 months. MA and visual aura without headache were dramatically improved. Migraine attacks and visual disturbance were not induced at exercise. At 3 months after lomerizine medication, brain SPECT showed remarkable increase of rCBF. These SPECT changes of our patient indicated that antimigraine mechanism of lomerizine could contribute to restoration of cerebral hypoperfusion.

1. Introduction

Regional cerebral blood flow (rCBF) studies have been employed to investigate the pathophysiology of migraine headache [1–3]. The introduction of brain single-photon emission computed tomography (SPECT) using technetium Tc 99m- (^{99m}Tc-) labelled hexamethylpropyleneamine oxime (HMPAO) or ethyl cysteinate dimer (ECD) has facilitated assessment of rCBF. A number of rCBF studies using Tc 99m HMPAO or ECD SPECT have been reported in patients with migraine during prodromes or headache phases [3–8]. However, little is known about the relationship between migraine preventative medication and rCBF. Lomerizine, 1-(bis(4-fluorophenyl)methyl)-4-(2,3,4-trimethoxybenzyl) piperazine dihydrochloride, is a calcium channel blocker with antimigraine properties [9]. This preventative drug is often used in Japan [10–13]. We first report a unique case in which prophylactic treatment with lomerizine recovered brain hypoperfusion on ^{99m}Tc ECD SPECT during interictal period, in addition to dramatic amelioration of migraine attacks.

2. Case Report

A 70-year-old man developed visual disturbance frequently at walking exercise for the recent 3 months. Visual disturbance consisted of scintillating scotoma in both eyes, which continued 5–20 minutes. After this visual attack, a mild-degree of throbbing headache occured occasionally. He had prior history of migraine with aura (MA) and without aura (MO) from 30 years of age. After 60 years of age, migraine attacks were decreased to a few times per one year. Physical and neurological examination was normal during interictal periods. Neuro-ophthalmic examination was normal. Routine laboratory tests suggested mild degree of diabetes mellitus. Fasting blood sugar level was 144 mg/dL, and hemoglobin A1c was 6.6% (normal 4.3–5.8). Cerebrospinal fluid study was normal. Brain magnetic

Table 1: Changes of regional cerebral blood flows before and after lomerizine administration.

	Before lomerizine		After lomerizine	
	Right	Left	Right	Left
Callosomarginal region	47.3	47.4	59.0	59.4
Precentral region	44.8	50.7	59.4	60.0
Central region	45.2	47.6	67.7	63.4
Parietal region	41.7	43.8	61.0	57.6
Angular region	44.3	46.7	59.4	60.0
Temporal region	48.1	50.6	52.4	51.9
Posterior region	48.8	44.2	58.7	58.6
Pericallosal region	53.0	54.1	59.8	59.9
Lenticular nucleus	53.6	52.8	51.1	49.0
Thalamus	48.2	53.1	49.2	51.7
Hippocampus	46.0	42.2	45.1	43.7
Cerebellar hemisphere	58.5	59.2	57.9	57.4

Data were shown in mL/100 g/min.

resonance imaging and angiography were not remarkable. Electroencephalogram was normal.

2.1. Measurement and Analyses of rCBF. Brain SPECT scanning with ^{99m}Tc-ECD was performed at the interictal time of migraine. SPECT was scanned at 10 minutes after intravenous bolus injection of 1.5 mL (600 MBq), ^{99m}Tc-ECD SPECT examination was performed using a rotating γ-camera (Prism 3000; Picker Corp. USA). Brain SPECT data were analyzed by the following two methods. One of SPECT analyses used the revised version of 3-dimensional stereotaxic region of interest template (3DSRT) by Takeuchi et al. [14]. A total of 636 ROIs were set in bilateral cerebral cortexes and cerebellar hemispheres. Global CBF was calculated from all data of 636 ROIs in whole brain, including both cerebral hemispheres and cerebellum. SPECT images were divided as regional CBF into 24 symmetrical (right and left) regions per patient: the callosomarginal, the precentral, the central region, the parietal region, the angular region, the temporal region, the posterior region, the pericallosal region, the lenticular nucleus, the thalamus, the hippocampus region and the cerebellar hemisphere. Quantification of rCBF was assessed using the noninvasive Patlak plot method without blood sampling [15]. Data of global and regional CBFs were shown in mL/100 g/min.

Another method was analyzed by easy Z-score imaging system (eZIS).

2.2. rCBF Alternation before and after Lomerizine Administration. Brain ^{99m}Tc-ECD SPECT before lomerizine treatment revealed hypoperfusion in the frontal, temporal, parietal, and occipital lobes (Table 1). Reduction of rCBF was detected predominantly in the right hemisphere (Figure 1). He was diagnosed with recurrence of MA. Lomerizine (10 mg/day, po) was administered for 3 months. MA or visual aura without headache was dramatically improved. There were no migraine attacks and visual disturbance whenever he walked and exercised for long time. The second ^{99m}Tc-ECD SPECT was performed. As compared to pretreatment with lomerizine, rCBF was increased in most of the cerebral cortex (Table 1). Restoration of frontoparietal hypoperfusion was found on eZIS imaging (Figure 2).

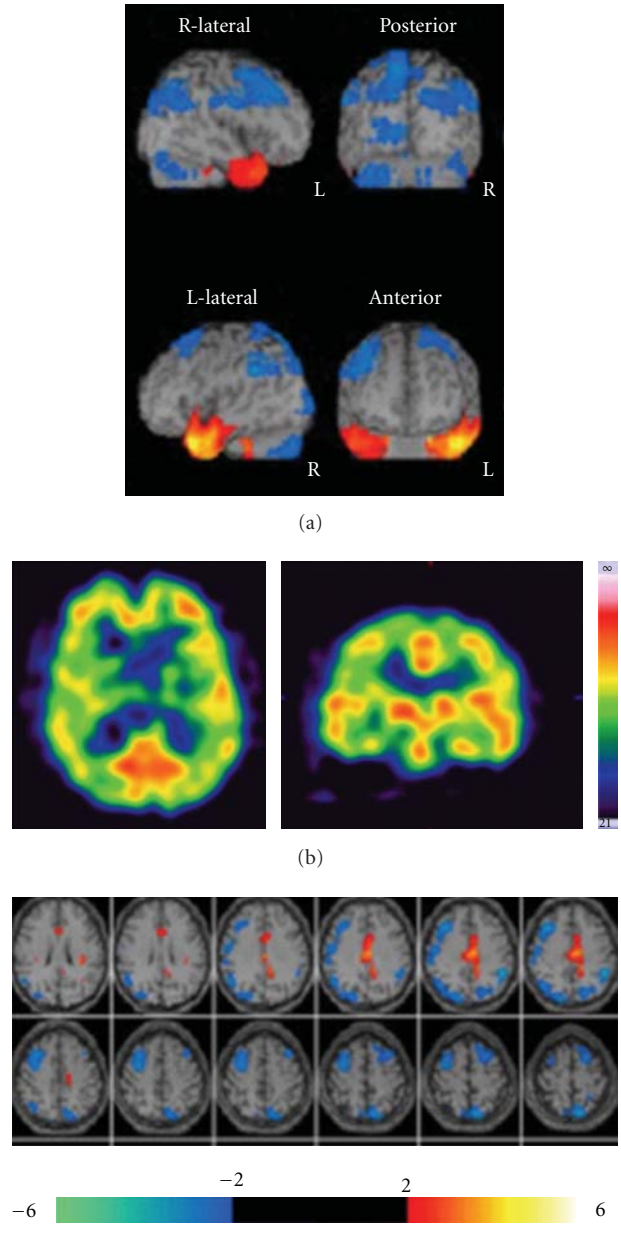

Figure 1: Brain ^{99m}Tc-ECD SPECT imaging before lomerizine treatment, CBF is decreased in bilateral frontoparietal and the left occipital regions on eZIS imaging.

3. Discussion

We showed that prophylactic treatment with lomerizine ameliorated brain hypoperfusion during the interictal period in a patient with MA, together with complete prevention of migraine attacks and visual auras.

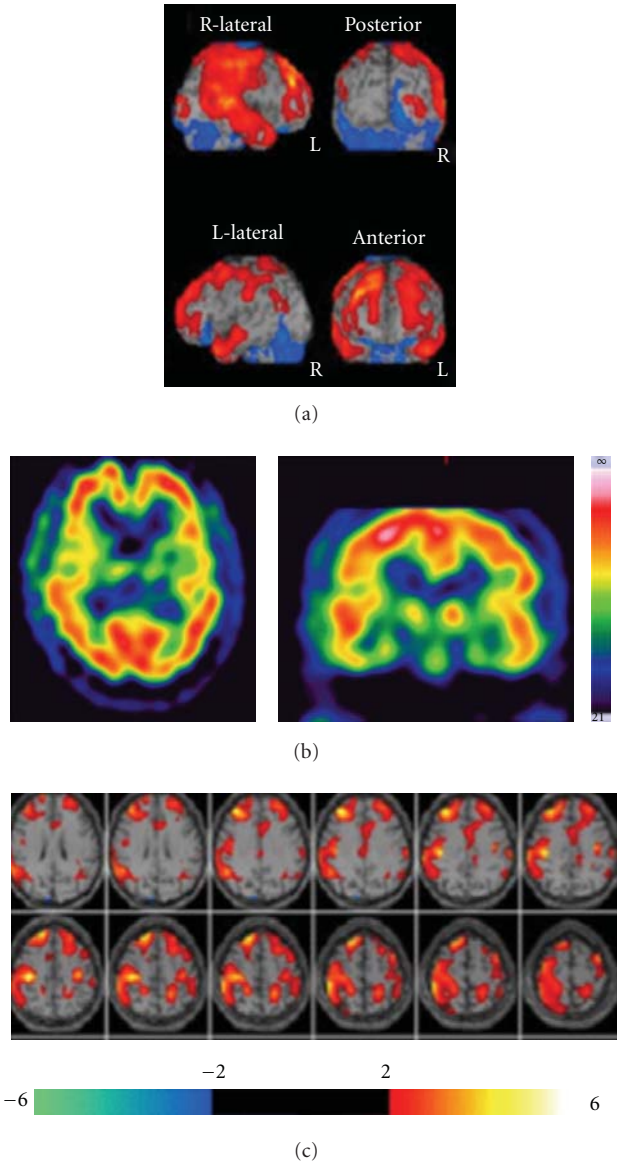

Figure 2: Brain ^{99m}Tc-ECD SPECT imaging after lomerizine treatment. As compared to pretreatment with lomerizine, CBF is increased in the bilateral frontoparietal regions on eZIS imaging. Cerebral hypoperfusion is improved markedly.

Lomerizine, an antimigraine calcium channel blocker, is prescribed widely in Japanese migraineurs [10–13]. Effectiveness of this prophylactic medication is approximately 50%. Lomerizine belongs to the same class of diphenylpiperazine-type calcium antagonists as flunarizine [9], and this drug is prescribed for migraine prophylaxis in Japan. Previous clinical trials of lomerizine suggested that this drug reduced the frequency of migraine attacks over 12 weeks [10–12]. Propranolol, amitriptyline, and valproate sodium are used internationally as preventative medication. Little is known about how these drugs influence rCBF on brain SPECT during the headache attack or the interictal phase in migraineurs. Prophylactic effects of magnesium citrate supplementation (600 mg/day, po) were assessed by means of clinical evaluation, visual evoked potential, and statistical parametric mapping of brain SPECT before and after 3 months treatment. Magnesium treatment significantly increased CBF in the inferolateral frontal, inferolateral temporal, and insular regions [16]. Previous studies disclosed antimigraine effects of lomerizine in animal models [17–20]. Inhibitory effects of lomerizine on the cortical hypoperfusion and expression of c-Fos-like immunoreactivity induced by spreading depression in anaesthetized rats were mediated via the effects of Ca^{2+}-entry blockade, which may include an increase in CBF and the prevention of excessive Ca^{2+} influx into brain cells [17]. These results provide the possibility that lomerizine may potentiate CBF and inhibit cortical spreading depression in migraine [17]. Other animal experiments suggested therapeutic effects of lomerizine on CBF. Lomerizine had a greater effect on CBF than on blood pressure and heart rates in anaesthetized rats and beagle dogs [18]. This drug is reported to inhibit voltage-dependent Ca^{2+} channels and 5-hydroxytryptamine $(5\text{-HT})_{2A}$ receptors, leading to suppression of 5-HT-induced contraction in rat basilar artery [19]. Recent study has disclosed that lomerizine recovered visual function in an experimental animal model of optic nerve injury [20]. Therefore, these experimental profiles supported that lomerizine could be clinically effective in cerebral circulatory disturbances, such as migraine status. We first highlighted therapeutic effects of lomerizine on rCBF in a migraineur with aura. This antimigraine drug can regulate rCBF during the interictal phase in migraineurs. Further SPECT studies with numerous migraineurs are needed to elucidate the precise prophylactic mechanism of lomerizine.

4. Conclusions

After lomerizine administration had improved MA or visual aura in our patient, brain SPECT revealed restoration of decreased CBFs during the interictal period. Clinicoradiological features of our patients indicated that antimigraine mechanism of lomerizine could contribute to alleviation of interictal cerebral hypoperfusion.

References

[1] J. Olesen, B. Larsen, and M. Lauritzen, "Focal hyperemia followed by spreading oligemia and impaired activation of rCBF in classic migraine," *Annals of Neurology*, vol. 9, no. 4, pp. 344–352, 1981.

[2] M. Lauritzen and J. Olesen, "Regional cerebral blood flow during migraine attacks by Xenon-133 inhalation and emission tomography," *Brain*, vol. 107, no. 2, pp. 447–461, 1984.

[3] J. Olesen, L. Friberg, T. S. Olsen et al., "Timing and topography of cerebral blood flow, aura, and headache during migraine attacks," *Annals of Neurology*, vol. 28, no. 6, pp. 791–798, 1990.

[4] E. Merckx, C. Schiepers, A. Verbruggen, J. Janssens, and M. De Roo, "Brain perfusion scintigraphy with ^{99m}Tc ethylcysteinate dimer for migraine accompagnee," *Clinical Nuclear Medicine*, vol. 19, no. 10, pp. 922–923, 1994.

[5] H. Seto, M. Shimizu, R. Futatsuya et al., "Basilar artery migraine reversible ischemia demonstrated by Tc-99m

HMPAO brain SPECT," *Clinical Nuclear Medicine*, vol. 19, no. 3, pp. 215–218, 1994.

[6] M. D. Ferrari, J. Haan, J. A. K. Blokland et al., "Cerebral blood flow during migraine attacks without aura and effect of sumatriptan," *Archives of Neurology*, vol. 52, no. 2, pp. 135–139, 1995.

[7] S. Soriani, L. Feggi, P. A. Battistella, C. Arnaldi, L. De Carlo, and S. Stipa, "Interictal and ictal phase study with Tc 99m HMPAO brain SPECT in juvenile migraine with aura," *Headache*, vol. 37, no. 1, pp. 31–36, 1997.

[8] I. La Spina, A. Vignati, and D. Porazzi, "Basilar artery migraine: transcranial doppler EEG and SPECT from the aura phase to the end," *Headache*, vol. 37, no. 1, pp. 43–47, 1997.

[9] T. Iwamoto, T. Morita, T. Kanazawa, H. Ohtaka, and K. Ito, "Effects of KB-2697, a new calcium antagonist, and other diphenylpiperazines on [3H]nitrendipine binding," *Japanese Journal of Pharmacology*, vol. 48, no. 2, pp. 241–247, 1988.

[10] F. Gotoh, K. Tashiro, N. Kutsuzawa et al., "Clinical evaluation of KB-2796 (lomerizine hydrochloride) on migraine: late phase II study," *Clinical Evaluation*, vol. 23, pp. 13–37, 1995 (Japanese).

[11] F. Gotoh, Y. Fukuuchi, K. Tashiro et al., "Clinical evaluation of lomerizine on migraine: double-blind study in comparison with demetotiazine," *Clinical Evaluation*, vol. 23, pp. 183–214, 1995 (Japanese).

[12] F. Gotoh, Y. Fukuuchi, K. Tashiro et al., "Long-term trial of lomerizine hydrochloride for migraine," *Japanese Pharmacology and Therapeutics*, vol. 23, pp. 1445–1460, 1995 (Japanese).

[13] N. Imai, T. Konishi, M. Serizawa, and T. Okabe, "Do the effects of long-term lomerizine administration differ with age?" *Internal Medicine*, vol. 46, no. 10, pp. 683–684, 2007.

[14] R. Takeuchi, Y. Yonekura, H. Matsuda, and J. Konishi, "Usefulness of a three-dimensional stereotaxic ROI template on anatomically standardised ^{99m}Tc-ECD SPET," *European Journal of Nuclear Medicine*, vol. 29, no. 3, pp. 331–341, 2002.

[15] H. Matsuda, A. Yagishita, S. Tsuji, and K. Hisada, "A quantitative approach to technetium-99m ethyl cysteinate dimer: a comparison with technetium-99m hexamethylpropylene amine oxime," *European Journal of Nuclear Medicine*, vol. 22, no. 7, pp. 633–637, 1995.

[16] E. Köseoglu, A. Talaslioglu, A. S. Gönül, and M. Kula, "The effects of magnesium prophylaxis in migraine without aura," *Magnesium Research*, vol. 21, no. 2, pp. 101–108, 2008.

[17] M. Shimazawa, H. Hara, T. Watano, and T. Sukamoto, "Effects of Ca channel blockers on cortical hypoperfusion and expression of c-Fos-like immunoreactivity after cortical spreading depression in rats," *British Journal of Pharmacology*, vol. 115, no. 8, pp. 1359–1368, 1995.

[18] H. Hara, M. Shimazawa, M. Sasaoka et al., "Selective effects of lomerizine, a novel diphenylmethylpiperazine Ca^{2+} channel blocker, on cerebral blood flow in rats and dogs," *Clinical and Experimental Pharmacology and Physiology*, vol. 26, no. 11, pp. 870–876, 1999.

[19] M. Ishii, S. Kobayashi, M. Ohkura, R. Yamamoto, S. Shimizu, and Y. Kiuchi, "Inhibitory effect of lomerizine, a prophylactic drug for migraines, on serotonin-induced contraction of the basilar artery," *Journal of Pharmacological Sciences*, vol. 111, no. 2, pp. 221–225, 2009.

[20] M. Selt, C. A. Bartlett, A. R. Harvey, S. A. Dunlop, and M. Fitzgerald, "Limited restoration of visual function after partial optic nerve injury; a time course study using the calcium channel blocker lomerizine," *Brain Research Bulletin*, vol. 81, no. 4-5, pp. 467–471, 2010.

Hindawi Publishing Corporation
International Journal of Molecular Imaging
Volume 2011, Article ID 197381, 8 pages
doi:10.1155/2011/197381

Research Article

Quantitative Accuracy of Low-Count SPECT Imaging in Phantom and *In Vivo* Mouse Studies

Ciara M. Finucane, Iain Murray, Jane K. Sosabowski, Julie M. Foster, and Stephen J. Mather

Centre for Molecular Oncology and Imaging, Barts Cancer Institute, Queen Mary University of London, London EC1M 6BQ, UK

Correspondence should be addressed to Ciara M. Finucane, c.finucane@qmul.ac.uk

Received 1 September 2010; Revised 12 December 2010; Accepted 19 January 2011

Academic Editor: Habib Zaidi

We investigated the accuracy of a single photon emission computed tomography (SPECT) system in quantifying a wide range of radioactivity concentrations using different scan times in both phantom and animal models. A phantom containing various amounts of In-111 or Tc-99m was imaged until the activity had decayed close to background levels. Scans were acquired for different durations, employing different collimator pinhole sizes. VOI analysis was performed to quantify uptake in the images and the values compared to the true activity. The phantom results were then validated in tumour-bearing mice. The use of an appropriate calibration phantom and disabling of a background subtraction feature meant that absolute errors were within 12% of the true activity. Furthermore, a comparison of *in vivo* imaging and biodistribution studies in mice showed a correlation of 0.99 for activities over the 200 kBq to 5 MBq range. We conclude that the quantitative information provided by the NanoSPECT camera is accurate and allows replacement of dissection studies for assessment of radiotracer biodistribution in mouse models.

1. Introduction

In vivo imaging of radiopharmaceutical uptake by single photon emission tomography (SPECT) in small animal models is an important tool with great potential for the development of new and improved radiopharmaceutical agents for targeted diagnosis and therapy of cancer [1–3]. In addition to providing high-quality images for qualitative interpretation, accurate quantification is required to determine the amount of uptake in tissues of interest and the pharmacokinetics of a compound *in vivo* [4]. SPECT studies are advantageous as they reduce the number of animals required compared to necropsy studies and allow longitudinal studies in the same animal [5].

Radionuclide imaging techniques such as SPECT and positron emission tomography (PET) are widely used for preclinical radiopharmaceutical development [6, 7] because of the possibility of direct translation of results from preclinical laboratories to the human clinical setting [8]. PET imaging has been seen as the more accurately quantifiable technique due to its higher sensitivity; however, development of SPECT imaging systems in recent years has led to higher resolution and sensitivity capabilities, making it an attractive option for quantitative *in vivo* imaging using longer-lived gamma-emitting radionuclides [8].

Three types of radionuclide quantification study are described in the literature. The first is a semiquantitative comparison of different regions of the image such as measurement of target-to-background uptake. The second is quantification of physiologic parameters such as perfusion rate in dynamic studies. The third type, and the focus of this paper, is absolute physical quantification, the measurement of the absolute activity concentration found in a volume-of-interest (VOI) [6, 9]. A number of physical quantities influence the absolute quantification of SPECT images. These include photon attenuation, scatter, and partial volume errors [9].

Forrer et al. [10] previously found quantification *in vivo* using the SPECT imaging system to be highly accurate. However, they injected approximately 50 MBq of their compound into each animal with a minimum uptake in the organ of interest of 0.74% injected dose per gram (%ID/g) giving an amount of activity in the target organ of around 1.4 MBq. We were interested in exploring the quantification

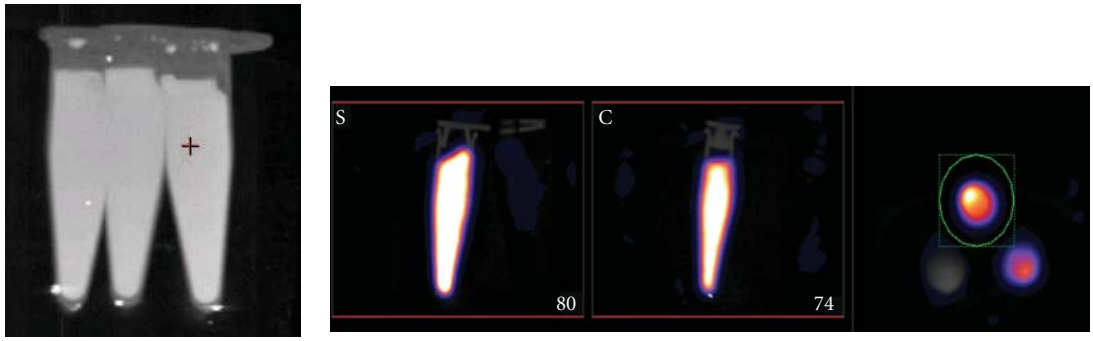

(a) (b)

Figure 1: (a) Phantom used in imaging studies. The 3 microcentrifuge tubes were mounted in the centre of a polystyrene holder. The three activity concentrations were approximately 20, 10 (In111)/5 (Tc99m), and 1 MBq/250 μL. (b) Reconstructed image slices with volume-of-interest drawn in the transaxial plane highlighted in green.

accuracy further by trying to quantify even lower levels of activity. The administered activity of a radionuclide that must be used for an animal imaging study largely depends on its specific activity, the radiolabelling efficiency, and purity of the compound and can range from approximately 1 to 50 MBq. Uptake in organs of interest typically varies from <1 to 30% [1, 11]. Consequently, there is a need to determine the validity of the measurements from SPECT imaging when working with low injected activities and low uptake in organs of interest.

Our aim was to determine the accuracy of the NanoSPECT/CT preclinical imaging system for achieving absolute quantification data with both high and low activity concentrations and to use the results in protocol design for future experiments. We investigated the minimum activity concentration and acquisition duration required to collect enough count statistics for accurate quantitative data by performing phantom and *in vivo* studies. This information can in turn determine required animal imaging times and subsequently will influence experimental design.

2. Materials and Methods

2.1. Imaging Studies. The NanoSPECT/CT preclinical imaging camera (Bioscan, Inc., Washington DC) is a 4-head gamma camera which also incorporates a cone beam CT imaging system. In order to provide high levels of sensitivity and spatial resolution, multi-pinhole collimators are used. For this study, two sets of collimators were tested with pinhole sizes of 1.4 mm and 2 mm. Both collimator sets had a field of view of 30 × 16 mm and consisted of 9 pinholes per head. The sensitivities of the pinhole collimators are approximately >2200 cps/MBq and >3500 cps/MBq with a resolution of ≤1 mm or ≤1.45 mm for the 1.4 mm and 2 mm apertures, respectively.

The use of multiple pinholes results in multiple overlapping projections, thus making full use of the detector surface available and maximising sensitivity. However, the nature of these projections means that it is not possible to use Filtered Back Projection as a means of tomographic image reconstruction. Hence, an Ordered-Subsets Expectation Maximisation (OSEM) algorithm [12] is used for all tomographic reconstructions. This algorithm does not include any correction for either attenuation or scatter.

Images are not reconstructed with units of radioactivity concentration per se. A conversion from dimensionless image count values to units of radioactivity concentration in megabecquerel is made by the InVivoScope analysis software (supplied with the camera) incorporating a user defined calibration factor stored within the software. Calibrations must be made for each radionuclide-aperture combination as required.

The camera was calibrated for In-111 and Tc-99m for both 1.4 mm and 2 mm apertures using a syringe filled with a known concentration of activity previously measured in a dose calibrator (VD 404, Veenstra, the Netherlands). The time of the measurement was also noted. Since dose calibrators are known to be less accurate at low activity levels we measured the calibration syringe with high activity, approximately 50 MBq and a known volume (measured by weight) of In-111 or Tc-99m.

The syringe was imaged acquiring a minimum of 100,000 counts per frame and the scan was reconstructed using the OSEM reconstruction algorithm with a 35% Gaussian filter (this is the manufacturer's description of the FWHM of the Gaussian filter) applied to the 2D projection data to reduce noise, 9 iterations, and a 0.4 mm voxel size. To mimic the attenuation caused by the body of the mouse, the syringe was placed inside a 2.5 cm diameter plexiglass phantom filled with water.

2.2. Phantom Measurements. A phantom containing a range of activity concentrations was prepared using three 250 μL microcentrifuge tubes. The tubes were completely filled with a total activity of 20 MBq, 10 MBq (In-111) or 5 MBq (Tc-99m), and 1 MBq of either In-111 or Tc-99m in a volume of 250 μL and inserted into a homemade polystyrene support (Figure 1). The radionuclides used for the phantom studies were taken from the same batch of solution used for the calibration. Each tube was weighed before and after addition

of the radionuclide to determine the exact volume present. The radioactivity present in each microcentrifuge tube was calculated by weight based on the measured concentration in the calibration syringe.

For the In-111 studies, the phantom was imaged every day for 11 days until the activity present in the low activity microcentrifuge tubes had decayed through approximately 4 half-lives. For the Tc-99m studies, the phantom was imaged at intervals for 2 days (8 half-lives).

Circular CT scans were acquired in 180 projections, at 45 kVp with 1000 ms exposure time and 3 minute scan duration. The scan range was 26 mm. Helical SPECT scans were acquired with either 30 seconds or 120 seconds per projection frame resulting in acquisition times of either 5 or 20 minutes. Each scan was repeated 4 times to test the reproducibility of the system.

2.3. Attenuation Measurements. The attenuation of the phantom versus the syringe used to calibrate the camera was investigated to see how it affected the accuracy of quantifying the image data. This was achieved by measuring weighed amounts (20 MBq) of isotope into either a syringe (1.5 mL) or a microcentrifuge tube (250 μL). The activity present in each was measured using the dose calibrator. The syringe (inside the plexiglass attenuation phantom) and microcentrifuge tube were individually imaged using the same acquisition settings for ten minutes. The resultant files were then reconstructed using the same parameters as the phantom studies and the quantification results were compared. The percentage difference between the two methods was recorded.

2.4. Animal Studies (Imaging and Biodistribution). All animal studies were performed in accordance with British Home Office regulations governing animal experimentation and Advisory Committee for Dangerous Pathogens guidelines in a level 2 containment facility. 5×10^6 A431 cells, transfected with CC-K2 receptors, were injected into the shoulders of 26 female immunodeficient beige SCID mice (Charles River, UK) and allowed to develop into tumours of approximately 5–10 mm in diameter for use in imaging and biodistribution studies.

10 days after injection, the mice were injected intravenously in the tail with 1 of 12 different In-111-labelled compounds ($n = 2/3$ per condition). Approximately 11–18 MBq in 200 μL was injected into each mouse. Each injected compound was a peptide with different affinities for the CCK-2 receptor expressed by the tumours [13]. The different biodistribution pattern for each compound resulted in a range of uptake values per gram of organ, therefore testing the limits of the quantification accuracy of the camera.

At 4 hours after injection, the mice were anaesthetised with 2% isoflurane gas and 0.5 L/min oxygen and imaged using the NanoSPECT/CT camera. The animals were kept warm throughout the acquisition using a heated bed system (Minerve, France). Whole body SPECT images were acquired in 20 projections over 45 minutes using the 2 mm pinhole collimators, as indicated by the phantom studies. CT images were acquired with a 45 kVp tube voltage in 190 projections over 6 minutes. Images were reconstructed using the same reconstruction parameters as the phantom studies.

Postimaging the mice were culled by cervical dislocation, and the tumour and kidneys were harvested for quantification analysis. Standards were prepared from a sample of the original injected material and each tissue sample was weighed and counted in a gamma-counter (LKB Compugamma) along with the standards. The percentage injected dose per organ and gram of tissue was determined for each tissue type.

2.5. Image Reconstruction and Statistical Analysis. All SPECT scans were reconstructed in a 256×256 matrix using HiSPECT (Scivis GmbH, Germany) software. The same reconstruction parameters were applied for all datasets: 35% Gaussian filtering, 9 iterations with a voxel size of 0.4 mm. Image reconstructions were carried out both with and without a "preclean" background correction option provided by the manufacturer. This consists of an algorithm designed to remove isolated single counts from pixels for which the neighbouring pixels contain no counts.

All images were analysed and fused with the CT image using InVivoScope, proprietary Bioscan software. For the phantom studies, a three-dimensional VOI was defined around each tube using the CT image as a reference and the activity present in megabecquerels was calculated. The same VOI was used for all subsequent phantom image analyses. For the animal studies, the uptake in the tumour and kidneys was also quantified using three-dimensional VOIs and the CT as a guide. For tumours with irregular shapes, multiple VOIs were created and the activities were summed together. The percentage injected dose per organ and gram was calculated using the weight of the tissue obtained after dissection. These results were then correlated with the results of the biodistribution study to determine the accuracy of the SPECT camera. All measured activities were corrected for decay and were compared to the true activity. Statistical analysis was calculated using linear regression analysis using the GraphPad PRISM analysis program.

3. Results

3.1. Phantom Studies. Reconstructed image slices (sagittal, coronal and transversal) of the phantom are shown in Figure 1 with the defined volume-of-interest highlighted in green. The sum of the activity (total activity) in all slices of the tubes was selected for the quantification measurements. The average uptake of four scans for each condition was calculated and used for analysis. We found the system to be reproducible with a coefficient of variation below 1% for activities higher than 0.5 MBq and below 4% for activities lower than 0.5 MBq.

Initially after reconstructing and quantifying the Tc-99m data with the "preclean background subtraction" included, a significant negative bias was observed at low levels of radioactivity. This was more pronounced for the scans with the shorter frame time. For example, the deviation from true values was within 10% for activities above 0.2 MBq. Below this, the deviation grew significantly to approximately

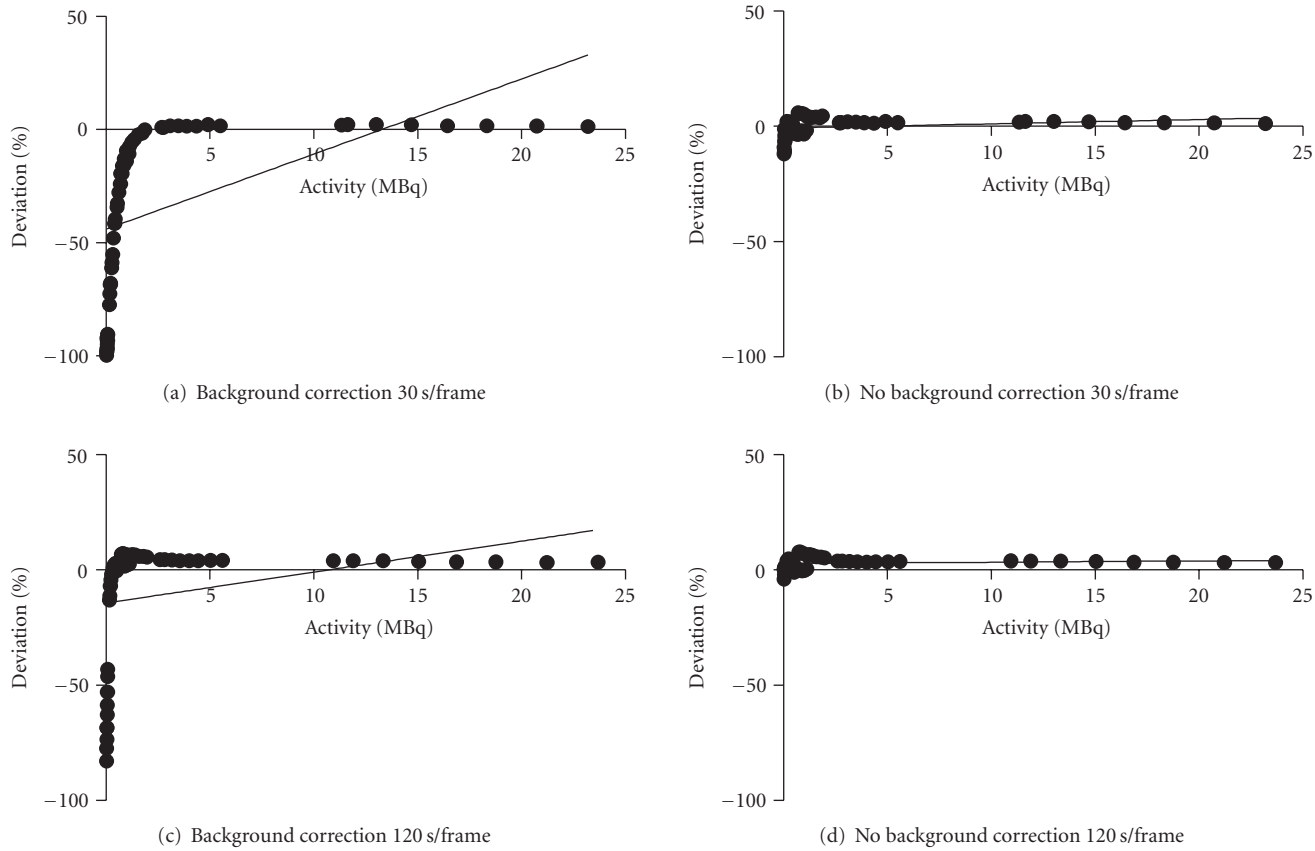

(a) Background correction 30 s/frame

(b) No background correction 30 s/frame

(c) Background correction 120 s/frame

(d) No background correction 120 s/frame

Figure 2: Plot of % deviation of measured activity values from true activity values with Tc-99m using the 1.4 mm pinhole apertures. Each graph represents the full range of activity values measured for all 3 microcentrifuge tubes. The negative bias at low activities introduced by background subtraction is clear in (a) and (c). This bias is eliminated for short and long frame times without any background removal, (b) and (d), respectively.

82% for 0.03 MBq using the longer frame time. However, with the shorter frame time the deviation with 0.2 MBq in the phantom was almost 70% and with activities as low as 0.035 MBq the deviation was 100%. Figures 2(a)–2(d) illustrate the percentage deviation of the measured SPECT data from the true activity in the phantom over a large range of activity using Tc-99m and the 1.4 mm pinhole apertures. It is clear from Figures 2(a) and 2(c) that there is a significant negative bias at low activities with a large deviation from true values ($P < .001$ for 30 s frames and $P < .01$ for 120 s frames).

The reconstructions were repeated without the default "preclean" subtraction switched on. A marked difference in results was observed. These are shown in Figures 2(b) and 2(d) which represent acquisitions with 30-second or 120-second frame, respectively. With the background correction removed during the reconstruction this negative bias is eliminated and there is no significant deviation from true activity over the whole activity range. The results are also comparable for both the short and long frame times. For both frame times, the observed deviation from the theoretical value for the total activity was consistent over the range of activities imaged. The 120 s frame time activities were within 4% of reference whilst the 30 s frame activities were within 10%.

The In-111 phantom results for this aperture pinhole size also showed a significant negative bias at low activities with the background subtraction on ($P < .01$). This major negative bias was eliminated after removing the background subtraction; however, the percentage deviation from true activity was still significant even with the background subtraction switched off during reconstruction. As a result, acquisitions and quantification with In-111 using larger pinhole (2 mm) apertures were performed to see if this would improve the results due to the higher sensitivity and ensuing increased count rates of these pinholes.

Figures 3(a)–3(d) show the results obtained using In-111 with the 2 mm pinhole apertures. Once more, a significant deviation from true activity was found when the background was subtracted during the reconstruction for the 30 second frame time but interestingly not for the 120-second frame time where even with the background correction switched on there was no significant deviation from true activity over the range of activities. For the scans without background removal there was no significant deviation from true activity values with either the short or the long frame time. For both frame times with the subtraction off, there was a range in deviation of $\leq$12% across the entire range of activity values, the lowest being approximately 0.087 MBq. It should

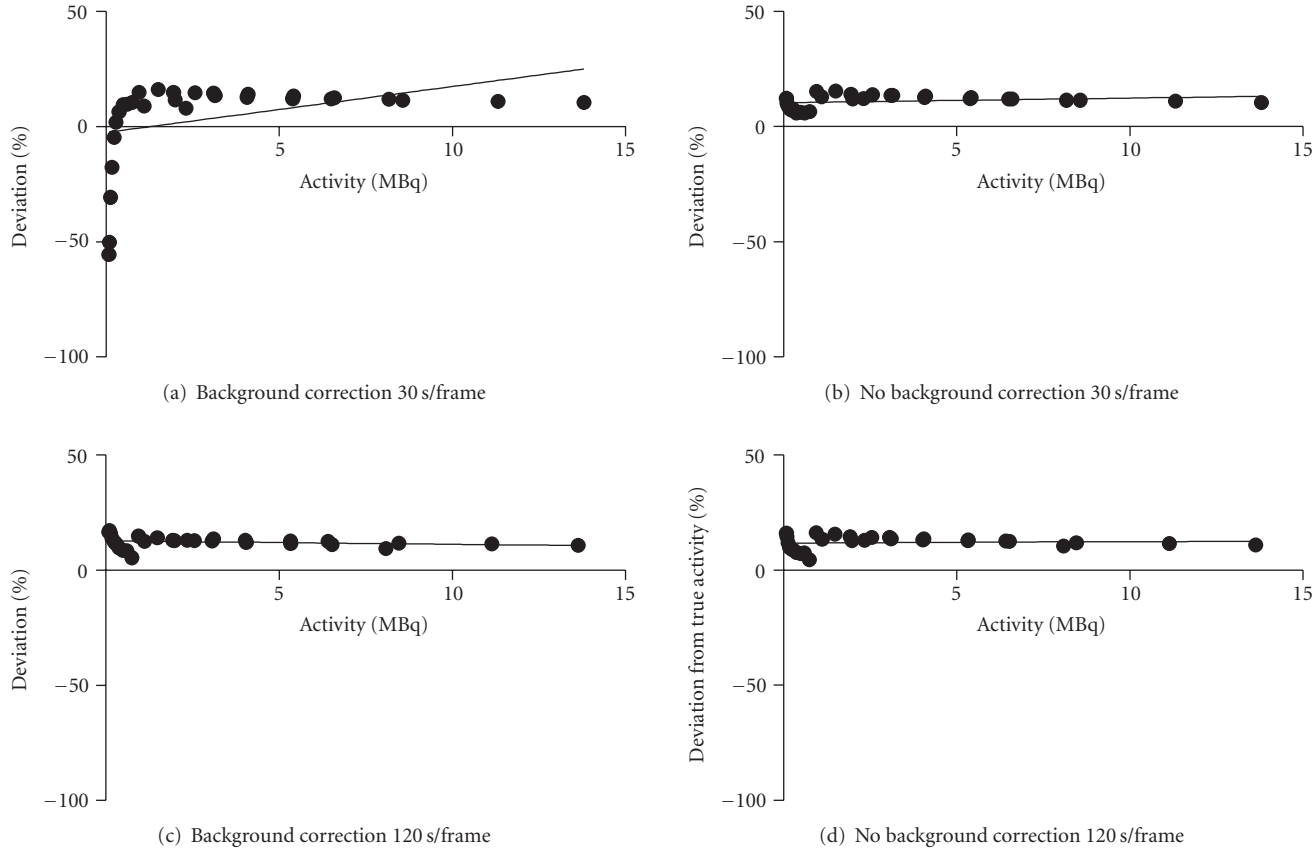

Figure 3: Plot of % deviation of measured activity values from true activity values with In-111 using the 2 mm pinhole apertures. Each graph represents the full range of activity values measured for all 3 microcentrifuge tubes. The negative bias at low activities introduced by background subtraction is also evident for short frame times in (a) whereas in (c) there is no significant deviation due to the longer frame time with a higher number of counts collected. This bias is eliminated for short and long frame times without any background removal, (b) and (d), respectively. An offset of approximately 8–10% exists due to attenuation differences between measurements of the calibration syringe and the samples.

be noted, however, that the percentage deviation while constant over the range of activities did display an offset of approximately 11%, that is, the deviation was consistently overestimated regardless of scan duration. This is in contrast with the Tc-99m results where the percentage deviation was close to zero.

3.2. Attenuation Measurements. To investigate this offset seen in the In-111 studies, the attenuation of the calibration syringe and the phantom tubes were compared as detailed in the methods section. The difference in absolute quantification of the radioactivity in the phantom tube compared to the calibration syringe was 7.8%.

3.3. Animal Studies. All compounds showed uptake in the tumour and kidneys of the injected mice; an example image is shown in Figure 4. The absolute activity present in the organs was calculated from the NanoSPECT/CT data by drawing VOIs using the CT as a reference. After necropsy and counting of tissue samples, the percentage of the injected dose in the tumour and kidney tissues was determined at 4 hours after injection for each mouse ($n = 26$). The uptake values ranged from 0.5–8.4%ID for the tumours and 0.1–93%ID for the kidneys, resulting in very low absolute levels of activity in some of the tumour samples, as little as 0.02 MBq. The results from the necropsy and imaging data sets were then compared. As shown in Figure 5, there is a highly significant correlation between the biodistribution data and the NanoSPECT/CT acquired data for both the tumour (a) and kidneys (b). Linear regression analysis confirmed these observations with $r^2 \geq 0.8174$ for the tumour measurements and $r^2 \geq 0.9953$ and for the kidney measurements.

4. Discussion

We have demonstrated that, once the automatic background subtraction feature of the software was disabled, consistent quantification of low activities is feasible with the NanoSPECT/CT preclinical imaging system. It is known that removal of counts from the acquired projection data can lead to non-Poisson statistics [14]. Under these circumstances,

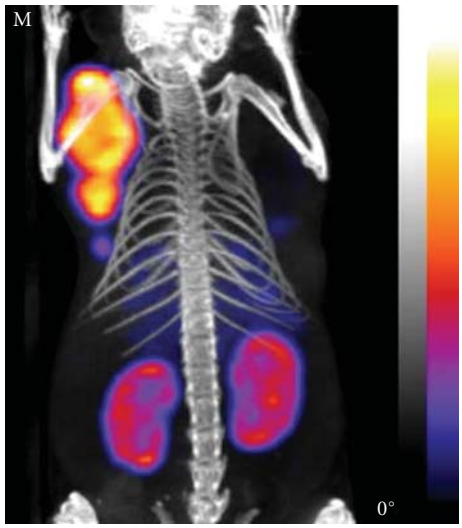

Figure 4: Representative NanoSPECT/CT image of 1 compound showing the tumour and kidney uptake at 4 hours after injection.

the OSEM algorithm which is based upon an assumption of Poisson statistics in the acquired data will become increasingly biased with respect to the quantitation of radioactivity. Furthermore, as the counts acquired are reduced, the background algorithm would seem to be increasingly likely to remove counts originating from the distribution of radiopharmaceutical within the animal/phantom itself.

Although our results demonstrate errors of <12% in absolute quantitation, in particular with regards to In-111, it is important to note that this deviation is consistent over the range of activities imaged.

In addition, we expanded on our phantom results by performing animal imaging experiments which yielded an excellent correlation with *ex vivo* measurements. The frame times used were as short as 30 seconds resulting in a total scan time of 5 minutes with activities as low as 136 kBq/mL, thereby simulating typical tumour tissue uptake concentrations. This enables us to validate the quantification of animal studies even in situations where the uptake in a target organ is relatively low.

For the In-111 studies, a decrease in pinhole size resulted in increased deviation which was significantly different from the true values. A reason for this discrepancy with In-111 could be because the count rate for In-111 was not as high as with Tc-99m since, due to the higher energy of this isotope the sensitivity of this detector is greater for Tc-99m than for In-111. This inferior count rate will lead to poorer statistics during the reconstruction process and lead to more errors in quantification calculation. A similar pattern of results was observed as with the Tc-99m data but the quantification deviation was higher with the In-111 phantoms. To address this, the phantom study was repeated using 2 mm pinhole apertures. The results of the In-111 experiment with the 2 mm pinholes showed improved correlation. No significant deviation from true activity over the entire range of activities measured was observed, and no difference in deviation for the different frame times was found, even at very low activities. This is likely to be because the larger pinhole size results in an increased sensitivity and higher count rates meaning that scan times can be shorter that those required for smaller pinholes. The reason why there was no significant deviation between the measured and true values for the longer frame time even with the background subtraction switched on is likely to be because of the acquisition of larger number of counts in the image.

As can be seen in Figure 3, there was a consistent offset for the In-111 phantom studies for both sets of apertures. The offset was approximately 8–11% from true values and was apparent even at high activities. This offset was therefore constant over all activity ranges and frame durations. The offset was also present with the background subtraction either switched on or disabled during the reconstruction. There could be two reasons for this offset. Firstly, this could be a systematic error introduced during the initial dispensing of activity. This is especially relevant for the 1 MBq tube which had a higher offset, as there can be greater uncertainty when measuring out smaller volumes. In fact, this explanation is unlikely as the volumes dispensed were accurately weighed into the phantom tubes to ensure that the exact volume was present. Alternatively, the offset for the In-111 measurement may be due to attenuation differences between the calibration syringe measurements and those of the microcentrifuge tubes. When the camera was calibrated, the syringe was inserted into a 2.5 cm diameter plexiglass phantom to mimic the attenuation of a mouse. However, the microcentrifuge tubes used for the phantom imaging experiments were imaged without such a device and consequently present only a very thin layer of plastic (~0.5 mm) to attenuate the electrons and photons emitted by the radionuclide. It was thought likely that this difference in attenuation of the two types of plastic containers could account for the consistent overestimation of activity values for the phantom studies. After imaging both types of plastic containers containing exactly the same amount activity, a difference of 7.8% was found between the two indicating that attenuation is likely to be the cause of the offset for the In-111 studies. Of note is the fact that this overestimation was not observed during the animal studies, strengthening the hypothesis that this offset was due to differences in the attenuation by the syringe and plexiglass phantoms and that this calibration phantom is a good device for mimicking the attenuation of a mouse.

For all the In-111 acquisitions for each pinhole size, the number of counts emitted from each tube in the phantom each day was recorded. This data was normalised for frame time and plotted against the equivalent percentage deviation to determine the optimal total count rate per frame for accurately quantifiable data (see Figure 6).

It can be seen that a minimum of 10,000 counts per frame is required to obtain data that is within 10% of the true activity values when background subtraction is applied. Lower count rates per frame than this will be prone to higher levels of deviation from true activity. With no background subtraction, the percentage deviation was approximately 9.4% with acquisitions of 9,000 total counts per frame and

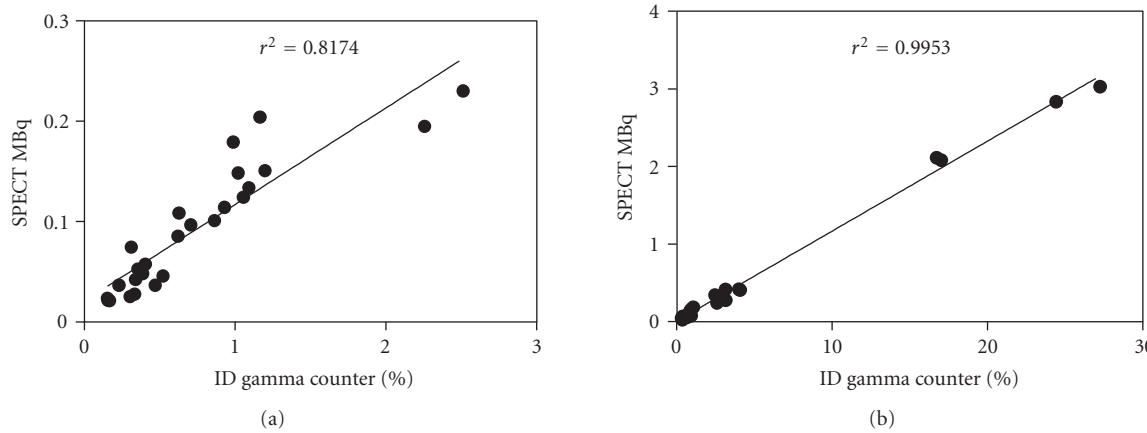

Figure 5: Correlation between SPECT measured results in MBq and *ex vivo* % ID measured in the gamma counter for tumours (a) and kidneys (b). There is a statistically significant correlation between the SPECT data and the biodistribution data which confirms the phantom results that the quantification is reliable at low activities.

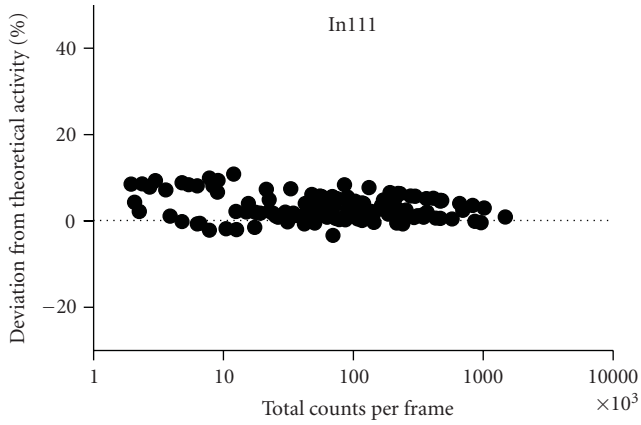

Figure 6: The count rate per second for each activity concentration as a product of frame time (30 s or 120 s) was plotted against the % deviation to determine the optimal total count rate per frame for accurately quantifiable data.

0.5% with 100,000 total counts per frame when using In-111. Since the count rate, or number of counts per second, is dependent on the activity of the source and the sensitivity of the camera, the frame time can be varied accordingly by the user to achieve a certain total number of counts and, therefore, quantifiable data. This can be used as a guideline for planning future imaging studies in terms of the activity and the scan times required per animal.

Although the results of the phantom studies indicate that the quantification performed with the NanoSPECT/CT scanner is accurate, results obtained from animal studies represent a situation closer to that pertaining to real life. The results from the animal data indicate that there is a highly significant correlation between the measured SPECT data and the *ex vivo* biodistribution data and suggest that results obtained by imaging can potentially replace those obtained from dissection and counting studies. This allows the kinetics and biodistribution of radiotracers to be determined over time in the same animal in longitudinal studies which enables fewer animals to be sacrificed to obtain the same information. The results of the different frame time analyses are also promising because they show that accurate quantification of dynamic imaging of mice using short scan times is achievable.

One of the limitations of our paper is that it only addresses quantitation of activity in mice using either Tc-99m or In-111. We did not explore the accuracy of measurements in larger animals such as rats or lower energy isotopes such as I-125. In both of these situations, the effect of attenuation will become more significant. For example, in simulations of preclinical imaging without attenuation correction, Chen et al. [15] calculated that imaging of I-125 would result in a deviation of up to 40% from the true activity and Hwang and Hasegawa [16] simulated a 50% reduction in measured activity using I-125 in a rat-sized water phantom which was later confirmed in animal experiments. The emitted low-energy photons (27–35 keV) are more strongly attenuated than with Tc-99m [17]. Wu et al. [18] calculated an underestimation of 10–30% in Tc-99m activity concentration of phantom and rats in studies without attenuation and scatter correction applied. These errors were reduced to −6 to +4% after these corrections were applied. Although we have shown that calibration using an appropriate phantom can correct for the lower levels of attenuation caused by the mouse body when radionuclides of medium-higher energies are used, this may not be the case when either larger animals or lower energy radionuclides are employed.

5. Conclusion

We found that once the automatic background feature of this iterative OSEM algorithm used to implement image reconstruction in this multi-pinhole preclinical SPECT camera was disabled, it resulted in consistent quantitation of

Tc-99 m and In-111 over a range of activities and imaging times. The use of an appropriate calibration phantom meant that absolute errors were within 12% of the true activity. Furthermore a comparison of *in vivo* imaging and biodistribution showed a correlation of 0.99 for activities over the 200 kBq to 5 MBq range.

We conclude that the quantitative information provided by the NanoSPECT imager is sufficiently accurate and reproducible to allow replacement of some dissection studies for assessment of radiotracer biodistribution.

Acknowledgments

The authors gratefully acknowledge Dr. Torkjel Matzow and Mr David Ellison for their valuable assistance with cellular preparations. C. M. Finucane is financially supported by Bioscan Inc., Washington DC.

References

[1] J. K. Sosabowski, T. Matzow, J. M. Foster et al., "Targeting of CCK-2 receptor-expressing tumors using a radiolabeled divalent gastrin peptide," *Journal of Nuclear Medicine*, vol. 50, no. 12, pp. 2082–2089, 2009.

[2] L. R. MacDonald, B. E. Patt, J. S. Iwanczyk et al., "Pinhole SPECT of mice using the LumaGEM gamma camera," *IEEE Transactions on Nuclear Science*, vol. 48, no. 3, pp. 830–836, 2001.

[3] R. Torres Martin De Rosales, C. Finucane, S. J. Mather, and P. J. Blower, "Bifunctional bisphosphonate complexes for the diagnosis and therapy of bone metastases," *Chemical Communications*, no. 32, pp. 4847–4849, 2009.

[4] S. K. Carlson, K. L. Classic, E. M. Hadac et al., "In vivo quantitation of intratumoral radioisotope uptake using micro-single photon emission computed tomography/computed tomography," *Molecular Imaging and Biology*, vol. 8, no. 6, pp. 324–332, 2006.

[5] Y. Seo, "Quantification of SPECT and PET for drug development," *Current Radiopharmaceuticals*, vol. 1, pp. 17–21, 2008.

[6] P. L. Wen, J. S. Lewis, J. Kim et al., "DOTA-$_{D}$-Tyr^{1}-octreotate: a somatostatin analogue for labeling with metal and halogen radionuclides for cancer imaging and therapy," *Bioconjugate Chemistry*, vol. 13, no. 4, pp. 721–728, 2002.

[7] M. Rudin and R. Weissleder, "Molecular imaging in drug discovery and development," *Nature Reviews Drug Discovery*, vol. 2, no. 2, pp. 123–131, 2003.

[8] B. L. Franc, P. D. Acton, C. Mari, and B. H. Hasegaway, "Small-animal SPECT and SPECT/CT: important tools for preclinical investigation," *Journal of Nuclear Medicine*, vol. 49, no. 10, pp. 1651–1663, 2008.

[9] A. B. Hwang, B. L. Franc, G. T. Gullberg, and B. H. Hasegawa, "Assessment of the sources of error affecting the quantitative accuracy of SPECT imaging in small animals," *Physics in Medicine and Biology*, vol. 53, no. 9, pp. 2233–2252, 2008.

[10] F. Forrer, R. Valkema, B. Bernard et al., "In vivo radionuclide uptake quantification using a multi-pinhole SPECT system to predict renal function in small animals," *European Journal of Nuclear Medicine and Molecular Imaging*, vol. 33, no. 10, pp. 1214–1217, 2006.

[11] T. Garrood, M. Blades, D. O. Haskard, S. Mather, and C. Pitzalis, "A novel model for the pre-clinical imaging of inflamed human synovial vasculature," *Rheumatology*, vol. 48, no. 8, pp. 926–931, 2009.

[12] H. M. Hudson and R. S. Larkin, "Accelerated image reconstruction using ordered subsets of projection data," *IEEE Transactions on Medical Imaging*, vol. 13, no. 4, pp. 601–609, 1994.

[13] J. Sosabowski, C. Finucane, J. Foster, D. Ellison, J. Burnet, and S. Mather, "Comparison of 111In-labelled CCK2-receptor targetingpeptides using NanoSPECT/CT imaging," Submitted to *European Journal of Nuclear Medicine and Molecular Imaging*.

[14] E. J. Hoffman, S. C. Huang, M. E. Phelps, and D. E. Kuhl, "Quantitation in positron emission computed tomography—4. Effect of accidental coincidences," *Journal of Computer Assisted Tomography*, vol. 5, no. 3, pp. 391–400, 1981.

[15] C. L. Chen, Y. Wang, J. J. S. Lee, and B. M. W. Tsui, "Toward quantitative small animal pinhole SPECT: Assessment of quantitation accuracy prior to image compensations," *Molecular Imaging and Biology*, vol. 11, no. 3, pp. 195–203, 2009.

[16] A. B. Hwang and B. H. Hasegawa, "Attenuation correction for small animal SPECT imaging using x-ray CT data," *Medical Physics*, vol. 32, no. 9, pp. 2799–2804, 2005.

[17] C. Vanhove, M. Defrise, A. Bossuyt, and T. Lahoutte, "Improved quantification in single-pinhole and multiple-pinhole SPECT using micro-CT information," *European Journal of Nuclear Medicine and Molecular Imaging*, vol. 36, no. 7, pp. 1049–1063, 2009.

[18] C. Wu, F. van der Have, B. Vastenhouw, R. A. J. O. Dierckx, A. M. J. Paans, and F. J. Beekman, "Absolute quantitative total-body small-animal SPECT with focusing pinholes," *European Journal of Nuclear Medicine and Molecular Imaging*, vol. 37, pp. 2127–2135, 2010.

Hindawi Publishing Corporation
International Journal of Molecular Imaging
Volume 2011, Article ID 796025, 15 pages
doi:10.1155/2011/796025

Review Article

Molecular SPECT Imaging: An Overview

Magdy M. Khalil,[1] Jordi L. Tremoleda,[1] Tamer B. Bayomy,[2] and Willy Gsell[1]

[1] *Biological Imaging Centre, MRC Clinical Sciences Centre, Imperial College School of Medicine, Hammersmith Hospital Campus, Du Cane Road, London W12 0NN, UK*
[2] *Nuclear Medicine Section, Medical Imaging Department, King Fahad Specialist Hospital, P.O. Box 11757, Dammam 31463, Saudi Arabia*

Correspondence should be addressed to Magdy M. Khalil, magdy.khalil@imperial.ac.uk

Received 1 August 2010; Accepted 5 February 2011

Academic Editor: Hiroshi Watabe

Molecular imaging has witnessed a tremendous change over the last decade. Growing interest and emphasis are placed on this specialized technology represented by developing new scanners, pharmaceutical drugs, diagnostic agents, new therapeutic regimens, and ultimately, significant improvement of patient health care. Single photon emission computed tomography (SPECT) and positron emission tomography (PET) have their signature on paving the way to molecular diagnostics and personalized medicine. The former will be the topic of the current paper where the authors address the current position of the molecular SPECT imaging among other imaging techniques, describing strengths and weaknesses, differences between SPECT and PET, and focusing on different SPECT designs and detection systems. Radiopharmaceutical compounds of clinical as well-preclinical interest have also been reviewed. Moreover, the last section covers several application, of μSPECT imaging in many areas of disease detection and diagnosis.

1. Introduction

Small animal imaging has become an integral part of molecular medicine. Translation of ideas from bench to the clinic needs a verification and validation step where molecular diagnostic modalities are substantial tools in developing new tracers, drug design and therapeutic regimens. In the last few years, there was a tremendous change and focus on the development of new microscale imaging systems of spatial resolution and detection sensitivity that relatively cope with the requirements of imaging small animals such as mice and rats. The focus was not only on instrumentation but also was accompanied by contrast agents/probes/biomarkers that target specific biological processes. Similarly, as these molecular agents are developed to suit particular biochemical targets, there are corresponding imaging techniques able to detect this particular signal. There is a relatively large array of imaging modalities that have their individual characteristics. The molecular imaging arena has been revolutionized also by hybridization/fusion of these techniques into single imaging devices. The best example that can be drawn from the literature as well as from the clinical practice is the recent implementation of PET/CT and (SPECT/CT) in clinical oncology and other important areas of disease detection. Apparent PET/MRI implementation and direct incorporation in routine practice is still controversial and active research is underway and its spread in the market will be determined in the near future [1].

However, there are emerging promising approaches that are undergoing extensive research work and investigation (with some successful results) for possible translation into the clinic. These include contrast-enhanced molecular ultrasound with molecularly targeted contrast microbubbles, optical imaging with fluorescent molecular probes, Raman spectroscopy/microscopy and more recently, photoacoustic imaging; a hybrid optical and ultrasound technique (see [2–4] for review).

Nuclear medicine has an established role in this context and tomographic tools such as single photon emission computer tomography (SPECT) and Positron Emission Tomography (PET) have their significant contribution to the world of molecular imaging [4, 5]. However, anatomical

techniques such as CT and MRI through their high spatial resolution capabilities serve to identify morphological changes in small structures. When these imaging modalities are combined in one imaging session, the amount of information obtained can synergically and significantly improve the diagnostic process and its outcome when compared to a single diagnostic technique [6].

Another important aspect of preclinical imaging is the ability to study the physiology over several time points referred to as longitudinal studies. A significant reduction of cost, number of animals as well as reduction of intervariability among subjects are among the most important outcomes of this technology. Thus, one can avoid animal dissection, *ex vivo* tissue counting and other autoradiographic studies.

2. Instrumentation

2.1. Strengths and Weaknesses. Diagnostic modalities can generally be distinguished based on whether they are structural or functional imaging techniques. Computerized tomography (CT) and magnetic resonance imaging (MRI) are well-known diagnostic tools that provide very high structural information of the tissue under investigation when compared to functional techniques such as SPECT or PET. MRI provides better soft tissue contrast even in absence of contrast media, a feature that is absent in CT scanning. Ultrasound procedures use high-frequency ultrasound waves to differentiate between different anatomical structures and safe (radiationless) diagnostic imaging technique. However, it has less functional or physiological significance when compared to nuclear modalities. Optical imaging such as bioluminescence and fluorescence are also functional modalities, but their limited spatial resolution, limited penetration capabilities and other factors contribute to their unease of transition to clinical practice [3].

The relative weaknesses and strengths that exist among imaging techniques are important to be understood. One can notice that the spatial resolution of MRI and CT is significantly higher than that of SPECT and PET. However, the detection sensitivity of SPECT and PET is significantly higher than those given by structural modalities and moreover can detect tracer concentration in the picomolar or nanomolar range. Both approaches use the tracer principal to detect physiological abnormality or disturbed biochemical process.

The key elements in radionuclide imaging are a biomarker and an imaging device. The first should have high specific, as well as sensitive characteristics to optimally study a molecular or cellular phenomenon. The imaging device is a radiation detector with specific performance to localize activity distribution within the human body or the animal. The most commonly used instrument in SPECT imaging is the conventional gamma camera that was invented in the middle of the last century by Anger [7]. However, for detection of coincidence events and localization of PET-administered compounds, a PET scanner is normally used. Both imaging devices have witnessed a significant change in the last decade in terms of performance characteristics as well as diagnostic quality.

On the other hand, MRI techniques do not relay on ionizing radiation, and thus, it is one of the features that characterize magnetic resonance procedures over other methods. Because of these inherent differences, there has been a large interest to combine more than one or two modalities into one imaging system able to morphologically and functionally address pathophysiologic questions. The present review will generally discuss many aspects of small animal micro-SPECT (μSPECT) imaging including instrumentation, molecular imaging probes used in preclinical and clinical practice, and the last section will cover some important and valuable preclinical applications. Before this discussion, the author would like to outline some major differences that exist between SPECT and PET imaging.

2.2. SPECT versus PET. In clinical practice, almost all nuclear medicine procedures that use single photon emission tracers rely on the use of the gamma camera. It is a gamma ray position sensitive detector that typically consists of large slab of scintillator crystal with position circuitry and energy determination. To localize the emission site of the released photons, a multihole collimator is mounted on the front face of the system to provide a spatial correlation of the detected events.

Hal Anger introduced the gamma camera as a novel detection technique able to localize an activity distribution of an administered radionuclide. However, his original prototype in 1953 was a camera in which a photographic X-ray film was in contact with NaI(Tl) intensifying screen. He used a *pinhole collimation* and small detector size to project the distribution of gamma rays onto the scintillation screen [7]. Initially, the camera was used to scan patients administered by therapeutic doses of 131-I. Disadvantages of this prototype were (1) small field of view of the imaging system (4 inch in diameter) and (2) poor image quality unless a high injected dose or long exposure time are applied. In 1958, Anger succeeded in developing the first efficient scintillation camera, and marked progress in the detection efficiency was realized by using an NaI(Tl) crystal, photomultiplier (PMT) tubes, and a larger field of view.

Spatial resolution and detection sensitivity are two important performance characteristics that play an important role in molecular imaging research using SPECT and PET tracers. Although the clinical gamma camera can provide a tomographic resolution of about 10 mm, some preclinical SPECT scanners can provide a submillimeter spatial resolution pushing down to subhalf millimeters using a specialized dedicated multipinhole geometry [8]. This situation is different in clinical and preclinical PET imaging where the spatial resolution of preclinical PET scanners is about 1-2 mm while that of clinical PET scanners lies in the range of 4–6 mm. Dedicated brain PET scanners, however, can achieve a slightly better spatial resolution ($\approx$2.5 mm) in the centre field of view. These resolution differences are mainly due to the fact that SPECT systems are not affected by some physical and fundamental limits that hinder the PET camera to reach sub-millimeter ranges although some research groups were able to achieve a resolution of less than

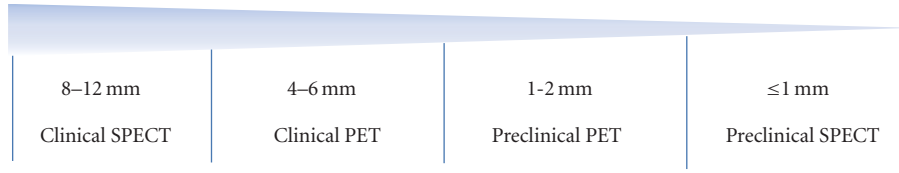

Figure 1: Spatial resolution across the clinical and preclinical SPECT and PET imaging scanners.

1 mm using fine segmented lutetium orthosilicate (LSO) crystal [9]. Figure 1 clearly defines the position of μSPECT in the molecular imaging matrix.

Many factors serve to impact the final reconstructed images of data acquired from a PET scanner. These are crystal size, positron range, photon acollinearity, intercrystal interaction and scatter, depth of interaction and the reconstruction algorithm. In preclinical PET machines, positron range appears to be the most important challenge that needs to be tackled to improve the spatial resolution of the PET images. However, the current generation of clinical PET scanners is slightly affected by the positron range, but correction of the phenomenon was shown to be effective in positron emitters of high maximum kinetic energy [10–12]. These issues are obviously absent in clinical as well as preclinical SPECT systems. The gamma camera relies on hardware collimators to determine the photons trajectory and hence able to localize the emission site by analyzing the electronic signal detected by the imaging detector. This hardware collimation plays a significant role in reducing the overall system sensitivity as well as the spatial resolution.

The intrinsic resolution of gamma camera is about 3-4 mm and tomographic SPECT acquisition reveals a spatial resolution, as mentioned above, not better than 10 mm. However, a new trend of designing semiconductor systems is emerging in the field, providing a significant improvement in spatial resolution, and other performance measures [13, 14].

SPECT degrading factors have been extensively studied in the literature and, namely, include attenuation, scatter and resolution effects, in addition to motion artifacts. Apart from the later, most of these physical issues can be resolved in great part by the use of SPECT/CT systems. These imaging degrading factors have a relatively smaller impact on the overall image quality in small animal imaging due to the smaller size of the rodents (mouse 20–40 g, rat 250–550 g) in comparison to standard human (75 kg). Nevertheless, correction for photon attenuation, scatter and partial volume would collectively improve the detection and estimation task [15]. This is particularly important for small structures and in small energy radionuclides such as I-125 [16].

Unlike PET, single photon emitting radiopharmaceuticals have several features in the context of molecular imaging such as cost and wide availability of the radioligands as well as relative ease of labeling. Small animal imaging using preclinical scanners and PET radiopharmaceuticals showed better capability in tracer kinetic studies when compared to its SPECT counterparts. PET compounds have been extensively used in compartmental modeling and kinetic analysis. Furthermore, small animal PET scanners showed a large axial field of view such that distant tissues/organs can be covered when image derived input function such as left ventricle is sought for calculations.

2.3. Pinhole Geometry: Pros and Cons. Hal Anger used a pinhole collimation which is an important element when we come across μSPECT imaging. The early work done on small animal imaging using SPECT tracer was to use a gamma camera equipped with pinhole collimator(s) of very small aperture size. Although parallel hole is the most commonly used collimator in many nuclear medicine procedures, pinhole imaging has a well-recognized role particularly for small organs such as thyroid and parathyroid imaging. In bone joints as well as in some pediatric studies, pinhole can also improve the spatial resolution by magnifying small structures of different tracer uptakes.

In recent years, pinhole geometry was found an increasing interest in designing SPECT scanners with superb spatial resolution and this has been attained by minimizing the aperture size to sub-millimeter range and specialized collimator geometry. However, the cost paid for this improved spatial resolution is a reduction of the detection efficiency. The later was partially tackled by increasing the number of holes for improvement of count collection and statistical quality. Pinhole geometry is not similar to parallel hole geometry where one-to-one magnification is achieved. The geometric magnification provided by pinhole geometry is a function of the object distance from the aperture as well as distance of the aperture from the detector surface in addition to the effective aperture diameter. Nothing is free, this takes place with a reduction of the imaging field of view. Another problem encountered when pinhole collimator is used in tomographic acquisition is data insufficiency and the resulting images could suffer from reconstruction errors.

Image reconstruction using iterative techniques have solved many problems that were not possible to achieve with analytic approaches. In clinical and preclinical arena involving both SPECT and PET imaging, iterative reconstructions were found superior to analytic approaches in many aspects of diagnostic quality and quantitative accuracy. μSPECT imaging has received large benefit from the use of iterative reconstruction by incorporating as many degrading factors in the system matrix. Besides its treatment to image noise, iterative reconstruction for pinhole geometry can correct for photon attenuation, scatter, and system response function. Edge penetration and parallax errors can also be modeled in the reconstruction scheme reducing the blurring effect allowing for enhanced spatial resolution [17].

2.4. Detectors. A conventional gamma camera can be used by manufacturing pinhole collimators of very small aperture size. It provides large field of view such that better magnification can be achieved. The other alternative is to use pixilated detectors that have better intrinsic properties or semiconductor detectors that fit with the resolution requirements of small animal imaging and, meanwhile, better than that provided by the conventional gamma camera. Regardless of their cost, semiconductor detectors are more compact and allow for system portability and can be manufactured in pixilated structure providing better spatial resolution.

Using a large field of view gamma camera serves to improve the magnification by providing large projection area onto the detector surface for the subject under investigation. However, some recent scanners are implementing pixilated detectors that have an intrinsic resolution equivalent to the segmentation size. This, to some extent, obviates the need to use detector width of size equivalent to the standard clinical gamma camera [5]. Thallium-activated sodium iodide NaI(Tl) crystal is the conventional scintillator used in most clinical designs. However, there are also some scintillators that have been used such as Cesium Iodide-Thallium doped and Cesium Iodide-Sodium doped and Yttrium Aluminum Perovskite (CsI(Tl), CsI(Na), and YAP, resp.). New designs of photodetectors such as position sensitive PMT, avalanche photodiode and position sensitive avalanche photodiode can be of value in μSPECT systems. For example, Funk et al. [18] have designed a multipinhole small animal imaging based on position sensitive avalanche photodiode (PSAPD) detectors coupled to CsI(Tl) scintillator. The system showed submillimeter spatial resolution and high detection efficiency when compared to dual head gamma camera, permitting shortened acquisition time and a reduced injected dose.

2.5. Designs. Several designs were proposed for pinhole geometry, including rotating gamma camera, stationary detector but rotating collimators, or completely stationary camera [19]. In U-SPECT II (MILabs, The Netherlands), the three-headed gamma cameras is equipped with interchangeable multihole collimators that can achieve high spatial resolution [20]. The collimator is cylindrical in shape with relatively large number of pinholes (i.e., 75), providing a good count collection for the high spatial resolution. A resolution of 0.35 mm can be achieved with an aperture size of 0.35 mm while a spatial resolution of 0.45 mm can be obtained with a 0.6 mm gold pinhole aperture size. The values are less in case of rat imaging (0.8 mm) using the standard whole body rat collimator. A recent release of the MILab company is the simultaneous acquisition of SPECT and PET tracers with resolution that can reach below 1 mm for the former [21].

The Inveon is another commercial design provided by Siemens Medical Solutions. The scanner is a trimodality imaging system that has three imaging modules namely PET, SPECT and CT. The SPECT and CT are coplanar and mounted on the same rotating gantry. The SPECT portion can be two or four 150 mm $\times$ 150 mm NaI(Tl) pixilated detectors (2.2 mm pitch) and 10 mm crystal thickness. The heads can be equipped with various parallel-hole, single- or multipinhole collimators, including mouse general body as well as mouse brain imaging with possible submillimeter spatial resolution.

Another two commercial μSPECT designs provided by Gamma-Medica Ideas and Bioscan. The Triumph Trimodality scanner (Gamma Medica, Inc) is an integrated SPECT/PET/CT hardware and software platform designed for small animals in preclinical and biomedical research applications. The system combines PET (LabPET), SPECT (X-SPECT) and CT (X-O) modalities. The SPECT module utilizes solid-state cadmium zinc telluride (CZT) detector technology. It provides opportunities to scan individual organs or whole body images. The SPECT system accommodates single and multiple pinhole collimators as well as parallel hole collimators to address a broad range of study needs. It can be configured to have 1,2,3 or 4 CZT cameras providing a variety of spatial resolution, detection sensitivity, and scanning field of view [20].

The Bioscan system has a four-detector head that consist of NaI(Tl) crystal. The scanner uses the spiral path to scan the object (24 to 270 mm) and also has stationary and circular detector motion. It has a variety of collimator options that can reach <1 mm spatial resolution in addition to high detection sensitivity [22]. It uses a patented multiplexed-multipinhole collimator design that can reach 36 pinholes or eve more. Commercially available μSPECTs are shown in Figure 2.

2.6. Hybrid SPECT Systems. μSPECT scanners can produce functional images with high spatial resolution; however, anatomical correlation using structural imaging modalities is still needed. For this reason, CT or MRI have been incorporated in some μSPECT systems. In addition to SPECT/CT and SPECT/MRI other hybrid systems such as SPECT-optical devices have also been investigated [23, 24]. The common underlying idea is to get and extract more information about the biological question in one imaging session and preferably with the same spatial and/or temporal framework. Figure 3 shows bone imaging in mouse using an SPECT/CT preclinical scanner. CT devices provide several advantages to the SPECT. They produce high resolution anatomical images in addition to generating a subject-specific attenuation map able to correct for photon attenuation. MRI machines can have a better soft tissue contrast, not relying on ionizing radiation, and provide high spatial resolution as mentioned earlier.

microCT (μCT) has been advanced in the last few years providing a spatial resolution in the order of few microns. A resolution of 10 μm or even better can be achieved giving more insights into structural abnormalities for *in vivo* as well as *ex vivo* samples. Nowadays, μCT is not only for attenuation and anatomical localizations but the benefits were extended to blood vessels imaging which is known as CT angiography. A number of reports were recently released discussing the utility of μCT in many preclinical applications [25, 26]. SPECT/MRI systems were also designed, and it is worthy mentioning that image of the year 2008 (in the annual meeting of the Society of Nuclear Medicine) was selected where diabetic feet using SPECT were coregistered

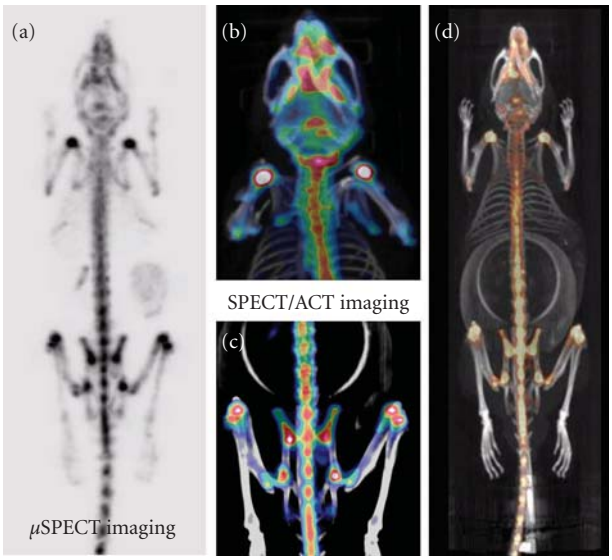

Figure 2: Invivo SPECT and SPECT/CT with ^{99m}Tc-MDP in C57BL/6 mice (3 hrs after injection dose 120 MBq i.v.). Note the high uptake in glenohumeral, the hip, and the femorotibial joints as shown in the whole body mouse (a). In (b) and (c), upper and lower extremities are shown where SPECT and CT images are coregistered. The whole body fused SPECT and CT is shown in (d). Images were acquired with the Inveon system (Siemens Medical Solutions) using dual detectors each mounted with a 5-pinhole collimator. The pinhole aperture size was 1.0 mm.

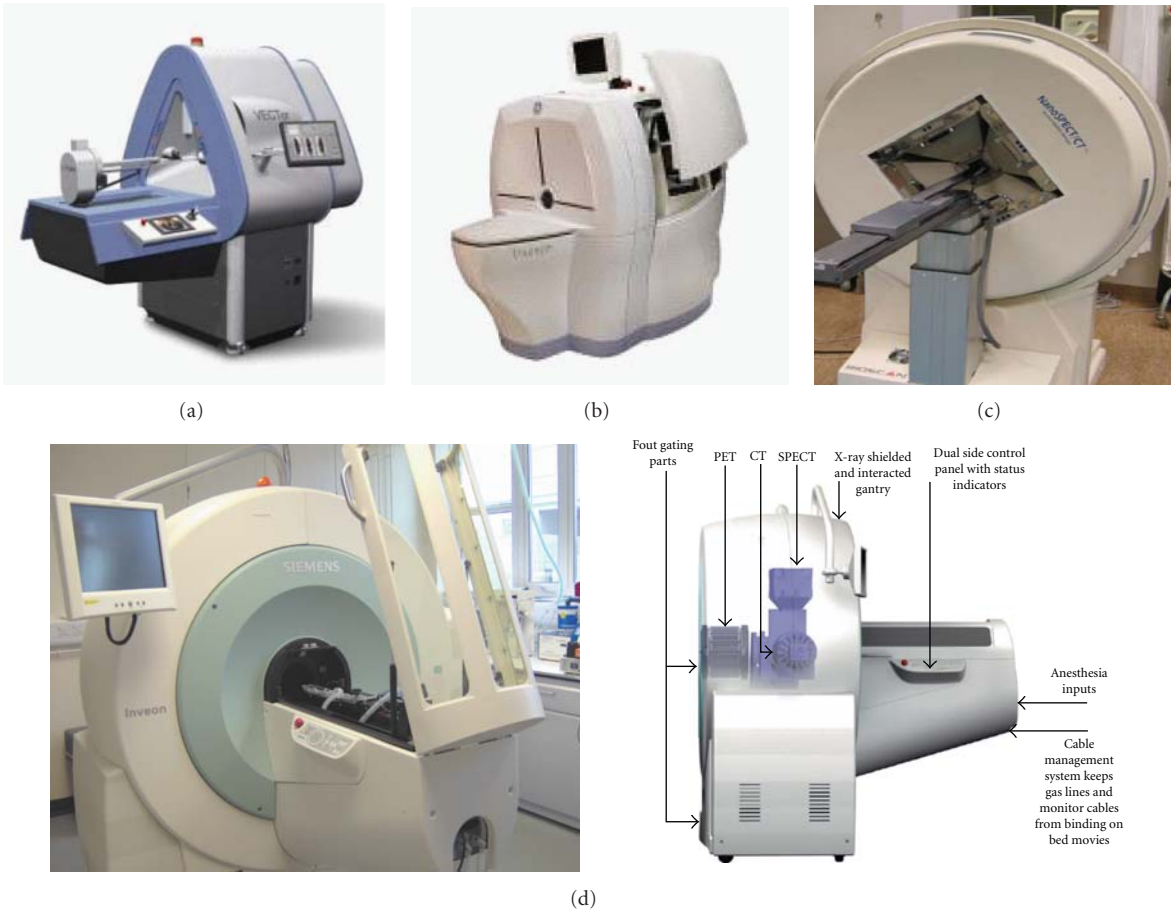

Figure 3: Some commercial preclinical SPECT systems. (a) A preclinical hybrid PET/SPECT device, the VECTor (Image courtesy of MI Labs), (b) Triumph Trimodality scanner (courtesy of Gamma Medica), (c) NanoSPECT (courtesy of BioScan, Inc), and (d) Inveon system (courtesy of Siemens Medical Solution) with internal components demonstrated (courtesy of Siemens Medical Solution).

with the patient MRI providing anatomolecular diagnosis of the extent and location of the disease. In preclinical context, the interest was given to PET/MRI rather than SPECT/MRI. However, new photodiodes that are less prone to magnetic fields can be very helpful in such designs.

3. Radiopharmaceuticals

Molecular imaging is an emerging field of study that deals with imaging of disease on a cellular or genetic level rather than on a gross level [27]. With the emergence of the new field of molecular imaging, there is an increasing demand for developing sensitive and specific novel imaging agents that can rapidly be translated from small animal models into patients. SPECT and PET imaging techniques have the ability to detect and serially monitor a variety of biological and pathophysiological processes, usually with tracer quantities of radiolabeled peptides, drugs, and other molecules at doses free of pharmacologic side effects [28].

3.1. Radiolabeled Molecular Imaging Probes (RMIPs). RIMPs are highly specific radiolabeled imaging agents used to visualize, characterize, and measure biological processes in living systems. Both, endogenous molecules and exogenous probes can be molecular imaging agents. The ultimate goal of molecular medicine is to treat the disease in its early stages with an appropriate patient-specific "targeted molecular therapy." In order to achieve this goal, it is essential to develop highly specific RMIPs. In the design and development of an ideal RMIP, it is important to identify first a molecular imaging probe (MIP), which may be a biochemical or a synthetic molecule, specific for a biological process (such as metabolism, angiogenesis, and apoptosis) or a molecular target (such as hexokinase, thymidine kinase, and neuroreceptor) in an organ, or tissue of interest.

General Rules for the Design of RMIPs. An ideal RMIP should be designed to fulfill the following characteristics [29].

(i) Rapid plasma clearance to reduce blood pool background in the target tissue.

(ii) Rapid washout or clearance from non specific areas.

(iii) Low nonspecific binding and preferably no peripheral metabolism.

(iv) High membrane permeability and intracellular trapping.

(v) Target specificity and high affinity for molecular targets.

(vi) Specific activity must be high to prevent saturation of specific binding sites.

(vii) Tissue distribution, localization, and target binding should be favorable for developing simple kinetic modeling to estimate quantitative data.

(viii) Radiation dosimetry of RMIP must be favorable for multiple diagnostic imaging studies (if necessary).

(ix) Synthesis of RMIP must be rapid and suitable for automation using automated synthesis modules.

Radiolabeling of RMIPs. Generally, the radiolabeling process of molecular imaging agents can be categorized as follows.

Isotope Exchange. Where the preparation is obtained by direct exchange of stable atom(s) of an element in a molecule with one or more nuclide of a radioisotope of the same element.

Introduction of Foreign Element. This is the most common method of radiolabeling of RMIPs, however, the RMIP will have a chemical structure and in vivo behavior different from that of the parent MIP.

Metal Chelation. In this method, a chelating agent (radiometal such as ^{99m}Tc and ^{111}In) is being introduced into an organic compound producing a ligand with different biological and chemical features than both the conjugated two partners. Certain peptides and monoclonal antibodies can successfully be labeled by the metal chelation procedure but only in the presence of a bifunctional chelate (BFC) by conjugation with the peptide or protein first and then bind the radiometal to the BFC conjugated molecule.

Classification of RMIPs. Based on their clinical utility and the nature of application for which they are designed as tools in the drug development program, four classes of RMIPs have been identified [30].

(a) *Radiolabeled drug substance* in which the cold stable atom is replaced by a radioisotope of the same element, which can be used for assessing the pharmacokinetics and biodistribution of the parent drug.

(b) *Radioligand* with good binding affinity for a biological target, which can be used to evaluate the effect of other unlabeled compounds at that target.

(c) *Pathway marker* interacting with one component of a set of related biological molecules, which may be used to probe the overall status of that system.

(d) *Biomarker*, or surrogate marker, which provides a more general readout at the level of cell or organ for a specific biological process.

3.1.1. Peptides and Proteins

(1) *Radiolabeled Monoclonal Antibodies (MAbs).* Antibodies are immunoglobulins (Ig) produced *in vivo* in response to the administration of an antigen to a human or animal tissue and bind specifically to this antigen forming an antigen-antibody complex [31]. Since the advent of hybridoma technology for production of MoAbs in 1975 [32] which was designed originally as an in vivo tumor localizing agents, only few have reached a point of proven clinical utility [33].

Labeling of MAbs can be accomplished with several radionuclides, among which In-111, Tc-99m, I-131, I-123, and I-125, where most of them are commonly used in nuclear medicine [34] and listed in Table 1. A number of monoclonal labeled antibodies using In-111 or Y-90 radionuclides are described in Table 2.

Table 1: Commonly used single photon emitting radionuclides.

Radionuclide	Half-life	Energy	Mode of decay
Tc-99m	6.02 h	142 keV	IT (100%)
I-131	8.03 days	364 keV	β^- (100%)
I-123	13.22 h	159 keV	EC (100)
In-111	2.80 days	171, 245 keV	EC (100%)

IT: isomeric transition, β^-: beta-minus, EC: electron capture.

(2) *^{99m}Tc-labeled Monoclonal Antibodies*

Arcitumomab (CEA Scan). Carcinoembryonic Antigen (CEA) or CEA-Scan kit (introduced by Mallinckrodt Medical) as a single dosage kit contains the active ingredient Fab$^-$ fragment of arcitumomab, a murine monoclonal antibody IMMU-4. CEA is expressed in a variety of carcinomas, particularly of the gastrointestinal tract (GIT) and can be detected in the serum. IMMU-4 is specific for the classical 200 kDa CEA that is found predominantly on the cell membrane. ^{99m}Tc-CEA-Scan complexes the circulating CEA and binds to CES on the cell surface. Fab$^-$ fragment of arcitumomab is cleared rapidly by urinary tract and plasma clearance due to its small particular size [38]. The IMMU-4 antibody is targeted against the carcinoembryonic antigens of the colorectal tumors, and, therefore, ^{99m}Tc-CEA-scan is used for the detection of recurrence and/or metastatic carcinomas of the colon or rectum particularly when high levels of CEA are detected [39]. However, it is an uncommon procedure following PET/CT scan.

Sulesomab (LeukoScan). The kit vial contains the active ingredient Fab$^-$ fragment, called sulesomab, obtained from the murine monoclonal antigranulocyte antibody, IMMU-MN3. It is a single-dose kit introduced by Immunomedics Europe in 1997. The labeling yield should be more than 90% [40]. ^{99m}Tc-sulesomab targets the granulocytes, and therefore is primarily used to detect infection and inflammation, particularly in patients with osteomyelitis, joint infection involving implants, inflammatory bowel disease, and diabetic patients with foot ulcers [41].

Annexin V (Apomate). Annexin V is a human protein with a molecular weight of 36 kDa has a high affinity for cell membranes with bound phosphatidyl serine (PS) [42]. In vitro assays have been developed that use Annexin V to detect apoptosis in hematopoietic cells, neurons, fibroblasts, endothelial cells, smooth muscle cells, carcinomas, and lymphomas. ^{99m}Tc-annexin V has also been suggested as an imaging agent to detect thrombi in vivo, because activated platelets express large amounts of PS on their surfaces [43].

(3) *Radiolabeled Peptides.* High background activity difficulties which usually appear when imaging with radiolabeled MAbs which is attributed to the slow tumor uptake and plasma clearance due to their relatively large molecular sizes. This can be mitigated by peptides whose molecular size is smaller than that of proteins and where the peptidases can act for rapid excretion by degradation of the peptides. Peptides have been labeled with ^{111}In and ^{99m}Tc in the same manner of the monoclonal antibodies. Some useful labeled compounds are listed in Table 3.

3.1.2. RMIPs for Metabolism. Metabolic imaging can be achieved using natural or exogenous radiolabeled substrates which participate in the particular metabolic process. The design of such tracers is based on the physiological concepts such as turnover of oxygen, glucose, amino acids, fatty acids, or DNA precursors. Commonly, ^{123}I and ^{99m}Tc derivatives are used as SPECT tracers for this function, however, the obvious chemical changes occur with this conjugation which can alter the physiological properties of the tracer module limits their application in molecular imaging.

(1) *Glucose Metabolism.* Although there are intensive research trials to find a sugar derivative labeled with ^{123}I and ^{99m}Tc, none of these were able to provide an SPECT substitute for ^{18}F-FDG to act as glucose metabolism imaging agent [51–53].

(2) *Amino Acid Metabolism.* Diagnosis of various neurological diseases as well as tumor evaluation (detection, grading and therapy monitoring) can be obtained by quantitative assessment of protein synthesis rate that is provided when using radiolabeled amino acids as a radiolabeled molecular imaging probe (RMIP). Radiolabeled amino acids pass the blood-brain barrier and are accumulated in tissues via a specific amino acid transport system [54]. $_{\text{L}}$-3-^{123}I-Iodo-α-methyltyrosine (^{123}I-IMT) is a good example of radiolabeled amino acids, it is evidenced that it accumulates in the brain via a specific facilitating L-amino acid transport system. In analogy with PET, IMT is not incorporated into proteins [55] and its uptake reflects amino acid transport [56]. IMT can be prepared by electrophilic substitution via in situ oxidation of ^{123}I-Iodide by chloramines-T, hydrogen peroxide, iodogen, or iodate with radiochemical yields of 70%–80%.

(3) *Nucleosides Metabolism (Gene Reporter Imaging).* Nucleosides or nucleoside analogs can be transported across the cell membrane by selective transporters and can then be phosphorylated intracellularly by specific kinases to the corresponding phosphate derivatives, and, ultimately, they can be incorporated into DNA. As thymidine kinase 1 (tk1) shows an S-phase dependant expression, the intracellular accumulation of labeled nucleosides that are substrates for TK1 reflects DNA synthesis and thus tumor proliferation. I-131-[57] and I-124-[58] labeled 2-arabino-fluro-5-iodo-2-deoxyuridine (FIAU) has been used successfully as nucleoside analog for tumor proliferation detection. Nucleoside derivatives that are selective substrates for herpes simplex virus thymidine kinase (HSVtk) have been developed for the in vivo visualization of transgene expression using the HSVtk gene as a reporter gene. Radioiodine labeled uracil compounds (e.g., FIAU) are widely applicable derivatives.

Table 2: List of In-111- and Y-90-labeled monoclonal antibodies.

Compound	Description	Applications	Remarks
In111-Capromab pendetide (ProstaScint)	A conjugation between the murine antibody 7E11.C5.3 and ^{111}In in the source of $^{111}InCl_3$ by the action of the GYK-DTPA as a chelating agent.	Indicated for use in immunoscintigraphy, proven prostate carcinoma and patients who have undergone a prostatectomy and have rising prostate specific antigen (PSA) values and equivocal nonevidenced metastasis.	It is not indicated with patients with a high clinical suspicion of occult metastatic disease or for screening of prostate carcinoma.
In111-Satumomab pendetide (OncoScint)	It contains the murine MAb B72.3 which is directed to tumor-associated glycoprotein. It is labeled with $^{111}InCl_3$ by conjugation with the chelating agent, GYK-DTPA.HCl.	Used for the detection of colorectal and ovarian cancers [35].	After an incubation time of 30 min, the labeled mixture is suitable for use in the first 8 hours.
In111-Imciromab pentetate (MyoScint)	An antibody produced against myosin in the cell culture, and therefore binds to the heavy chain of myosin after in vivo administration.	Detection of myocardial infarction.	Contains the Fab fragment of a murine monoclonal antibody that is covalently bound to DTPA giving ^{111} In-Imciromab pentetate.
In-111 and Y90-ibritumomab tiuxetan (Zevalin)	*Zevalin* consists of a murine monoclonal anti-CD20 antibody covalently conjugated to the metal chelator DTPA, which forms a stable complex with ^{111} In for imaging and with ^{90}Y for therapy.	^{90}Y-ibritumomab tiuxetan is used for the treatment of some forms of B cell non-Hodgkin's lymphoma, a myeloproliferative disorder of the lymphatic system while its ^{111} In derivative is used to scan the predicted distribution of a therapeutic dosage of ^{90}Y-ibritumomab in the body [36].	The antibody binds to the CD20 antigen found on the surface of normal and malignant B cells (but not B cell precursors) allowing radiation from the attached isotope (Yetrium-90) and the cytotoxicity induced by the antibody serve to eliminate B cells from the body allowing a new population of healthy B cells to develop from lymphoid stem cells [37].
Rituximab	An earlier version of anti-CD20 antibody and has also been approved under the brand name Rituxan for the treatment of non-Hodgkin's lymphoma (NHL).	It was approved for the treatment of patients with relapsed or refractory, lowgrade or follicular Bcell NHL, including patients with rituximab refractory follicular NHL.	In September 2009, ibritumomab received approval from the FDA for an expanded label for the treatment of patients with previously untreated follicular NHL, who achieve a partial or complete response to first-line chemotherapy.

(4) *Hypoxia Imaging.* Hypoxia, a condition of insufficient O_2 to support metabolism, occurs when the vascular supply is interrupted, as in stroke or myocardial infarction, or when a tumor outgrows its vascular supply. When otherwise healthy tissues lose their O_2 supply acutely, the cells usually die, whereas when cells gradually become hypoxic, they adapt by upregulating the production of numerous proteins that promote their survival. These proteins slow the rate of growth, switch the mitochondria to glycolysis, stimulate growth of new vasculature, inhibit apoptosis, and promote metastatic spread [59].

Most hypoxia markers contain a nitroimidazole moiety as a reactive chemical species. Nitroimidazoles can be used as probes to detect hypoxia as they are reduced intracellularly in all cells, but in absence of adequate supply of O_2, they undergo further reduction to more reactive products which bind to cell components and are finally trapped in the hypoxic tissue [60]. ^{99m}Tc-O-propylene-amine-oxime (^{99m}Tc-pano or BMS-181321) was validated as a proper hypoxia imaging agent in hypoxic myocardium, acutely ischemic brain and solid tumors [61]. BMS-194796 and ^{99m}Tc-HL91 have also been designed as RMIP for imaging hypoxia, however, none of these three probes has been commercially available. Iodine-123 labeled iodoazomycin arabinoside (IAZA) has been validated in animal model in the preclinical phase [62], but no clinical studies with this agent have been reported so far.

(5) *Cell Labeling.* The most common applications of In-111 are in labeling blood cells (white blood cells (WBC) and platelets) for imaging inflammatory processes and thrombi [63]. In blood cell labeling, the plasma transferrin competes for the In-111 and reduces the labeling efficiency because In-111 binds with higher efficiency to transferrin than blood cells, and, therefore, isolation of the desired blood component from plasma permits easy labeling of either platelets or WBCs. ^{99m}Tc-HMPAO is primarily used in brain perfusion imaging, although it is used for leukocyte labeling substituting ^{111}In-Oxine. Stabilization of the ^{99m}Tc-HMPAO primary complex is required due to the high degradation rate of its radiochemical purity. This could be achieved by

Table 3: Tc99m- and In-111-labeled peptides.

Compound	Description	Uses	Remarks
		In-111 labeled compounds	
In-111 pentetreotide (OctreoScan)	^{111}In has been conjugated to octreotide as DTPA chelated compound to form the labeled somatostatin tracer (^{111}In-DTPA-octeriotide).	Octreoscan is an agent designed for the scintigraphic localization of primary and metastatic somatostatin receptor positive neuroendocrine tumors, such as carcinoids, gastrinoma, neuroblastomas, pituitary adenomas, and medullary thyroid carcinomas [44].	Pentetreotide only binds with high affinity to the somatostatin receptor subtype SSTR2 with moderate affinity to SSTR3 and SSTR5 and not to SSTR1 and SSTR4 [30].
In-111 lanreotide (Somatuline)	This peptide is modified with DOTA and labeled with ^{111}In in a similar way as octreotide [45, 46].	The high binding affinity of lanreotide to SSTR3 and SSTR4 makes it suitable to be used as a proper agent for visualization of certain tumors, such as intestinal adenocarcinomas which is not visualized by ^{111}In-pentetreotide scintigraphy [47].	
		^{99m}Tc-labeled peptides	
Depreotide (NeoSpect)	Depreotide is a synthetic peptide that binds with high affinity to somatostatin receptors (SSTR) in normal as well as abnormal tissues it has been shown that. It accumulate in pulmonary nodules 1.5–2 hours following the i.v injection [48].	This agent is used to detect SSTR-bearing pulmonary masses in patients proven or suspected to have pulmonary lesions by CT and/or chest X-ray. Negative results with ^{99m}Tc-Depreotide can exclude regional lymph node metastasis with a high degree of probability [49].	Labeling of the depreotide (cyclic decapeptide) with ^{99m}Tc is performed by ligand exchange of intermediary ^{99m}Tc-glucoheptonate [50].
Apcitide (AcuTect)	The kit vial contains a lyophilized mixture of depreotide, sodium glucoheptonate, stannous chloride, and sodium EDTA.	^{99m}Tc-apticide binds to the GP IIb/IIIa receptors on activated platelets that are responsible for aggregation in forming the thrombi and, therefore, is used for the detection of acute deep vein thrombosis (DVT) in lower extremities [28].	

adding stabilizers like methylene blue in phosphate buffer or cobalt (II)-chloride to the reaction vials [64], however, these reagents should not be used when the complex formulation is designed for labeling of leukocytes.

(6) *Iodine-123 as an RMIP.* I-123 is the preferred thyroid imaging agent imparting 1% of thyroid dose per microcurie when compared with I-131. ^{123}I-labeled compounds are commonly used as ^{123}I-MIBG for adrenal scan, ^{123}I-OIH for tubular renal scan, and ^{123}I-iodoamphetamine (^{123}I- IMP) for cerebral perfusion scan [28].

^{123}I-Ioflupane (DaTScan) is a widely used ^{123}I derivative for detection of the loss of nerve cells in an area of the brain called the striatum which release dopamine, a chemical messenger, and therefore, it will be useful in distinguishing between Parkinson's disease and essential tremor (tremors of unknown cause) with a sensitivity of 96.5% [65]. It is also used to help distinguish between "dementia with lewy bodies" and Alzheimer's disease with 75.0% to 80.25% sensitivity [66].

Dopamine transporter (DAT) imaging with tropane derivatives such as FP-CIT (^{123}I-Ioflupane) and β-CIT has been developed to directly measure degeneration of dopamine presynaptic terminal and may be used to quantify changes in DAT density. Ioflupane binds specifically to structures of the nerve cells ending in the striatum area of the brain that are responsible for the transportation of dopamine. This binding can be detected using tomographic imaging [67].

4. SPECT in Preclinical Applications

The application for imaging modalities in preclinical models is highly valuable as it has a great scope for noninvasively studying dynamic biological processes at the molecular and cellular level. The noninvasive nature of imaging provides advantages in investigating the onset and the progression of disease, assessing the biological effects of drug candidates and assisting in the development of disease biomarkers and monitoring the therapeutic effectiveness of new treatment and/or pharmaceuticals. This technology plays a key role in bridging bench studies of disease modelled in vitro to their implementation in clinically relevant animal models of diagnostic or therapeutics for their translation into the clinics. In fact, the implementation of imaging in rodents has a great relevance because of the widespread use of genetically modified mice in biomedical research and the need to characterise the *in vivo* anatomical and functional phenotypes of animal disease models. Another advantage of imaging modalities developed for small animals is that the technology can relatively be translated directly for application to clinical practice.

4.1. Cardiovascular Imaging. Preclinical SPECT systems have a great scope of applications in cardiovascular research,

including the study of myocardial functions (e.g., ejection fraction, regional wall motion abnormalities, perfusion, tissue viability, oxygen consumption, and glucose metabolism [68]) and the investigation of several vascular disorders, including coronary artery disease and related disorders, such as ischemia, infarction and atherosclerosis [69]. Moreover, μSPECT has great applications for developing and testing diagnostic tracers which could assist in understanding the prognosis of disorders and assess new therapeutic approaches for cardiovascular lesions.

^{99m}Tc-labelled radiopharmaceuticals for SPECT imaging have been applied to demonstrate tissue viability and perfusion status in animal models of ischemia and/or impaired myocardial perfusion [70, 71]. Cardiac and respiratory motion is one of the major challenges when imaging rodent (mouse heart rate: 400–800 beats/min). Gated acquisition is therefore required to minimise any movement artefacts. Indeed, ECG-gated micro SPECT can yield accurate measurements of left ventricle volumes and ejection fraction in rats and mice [72, 73].

Another key area is the visualization of necrotic tissues and related tracers during myocardial infarction (MI). Some studies have assessed myocardial ischemia in rat heart models after left coronary artery occlusion by using ^{99m}Tc-glucarate [74]. In vivo visualization of necrosis may help to detect MI at early stages and may provide a good approach for evaluating the antinecrotic effect of developing drugs for ischemic heart disease. On the same vein, the visualization of apoptotic cell death is another important target for non-invasive imaging [75]. Hence, the development of tracers (e.g.,^{99m}Tc-Annexin) that bind to apoptotic cells is a very useful tool for in vivo analysis, especially to investigate apoptotic cell death in cardiomyocytes and the efficacy of cell-based therapies.

Angiogenesis imaging is a key protective/remodelling mechanism in myocardial infarction. Imaging such a mechanism is important for the understanding of infarct healing and post-MI remodelling. Vascular growth factors such as $\alpha_v\beta_3$ integrins have been used as targeted tracers to investigate angiogenesis in postinfarct animal models, with In-111-labelled $\alpha_v\beta_3$ targeted radiotracers in hypoperfused myocardial regions [76].

Another relevant area of cardiovascular imaging is the development of methods to characterise the formation and prognosis of atherosclerotic plaques. Plaque rupture results in severe cardiac events including MI and sudden death, hence, there is an important need for developing tools that can assist in predicting the plaques vulnerability to rupture. Not all the plaques carry the same risk, and the criteria for imaging their vulnerability relies on the detection of inflammatory cell infiltration, platelet aggregation, tissue matrix degradation, large lipid contents and apoptosis. Radiolabeled Annexin and Z2D3 targeted to apoptotic macrophages and smooth muscle cells, respectively, have been used as SPECT tracers to study the pathophysiology of atherosclerosis in animal models [77, 78]. One of the main challenges for imaging plaques is their anatomical localization, as high spatial resolution is needed to image such a small anatomical structure in a motile vessel, hence the importance of co-registering SPECT acquisition with other imaging modalities such as micro-CT.

4.2. Imaging Stem Cells. With advances in research of stem cell-based therapies, the application of imaging technologies may be useful to validate their efficacy and safety in preclinical models, in particular, for studying tracking and engraftment of transplanted cells, assessing their viability, function and differentiation status in addition to monitoring their ability to promote regeneration [79]. Stem cells can be labelled with radionuclides before transplantation. For example, stem cells labelled with the SPECT radiolabels ^{111}In-oxyquinoline have been successfully imaged after transplantation in rat and porcine models of myocardial infarction [80, 81], but, because of the short half-life of the radionuclide (e.g., ^{99m}Tc: 6.02 h; ^{111}In: 2.8 days) and because the activity may still be present after transplantation even if the cell have died, this method may only be applicable for a short-term cell tracking and assessing stem cell homing after transplantation.

To investigate not only long-term engraftment of stem cells but also their viability, a gene imaging approach may be more appropriate. In this case, gene expression is assessed by reporter genes constructs which are translated into a protein and interact with an exogenously given probe (radiolabeled for SPECT detection), resulting in a signal that can be monitored non-invasively. Reporter genes are incorporated into the cells before transplantation, and if the cell remains alive after engraftment, the protein, which is the main target for the nuclides, will be encoded (e.g., enzyme, cell surface receptor). Conversely, the reporter gene will not be expressed if the cell is dead [82].

As mentioned earlier, one of the reporter genes mostly used for SPECT imaging is based on the production of an intracellular enzyme (e.g., herpes simplex virus type 1 thymidine kinase [HSV1tk]) that phosphorylates an exogenously administered substrate that is retained in the cell because of its negative charge. Although normal mammalian cells (without the HSV1-tk) do carry the enzyme, it only minimally phosphorylates the radionuclide probes used in this system. Conversely, in cells carrying the HSV1-tk, the exogenously administered probe undergoes significant phosphorylation and intracellular retention, leading to a robust signal-to-background ratio and enabling accurate monitoring of these cells [83]. This imaging approach has been recently used to monitor the distribution of transplanted human embryonic stem cell derivatives in a live mouse model over a long period of time, up to 3 months [84].

Another approach consists of the encoding of the sodium-iodide symporter (NIS), a thyroid transmembrane protein that, under physiologic conditions, transports iodine into the cells in exchange for sodium. It has the advantage that it can be used for PET (with ^{124}I as the tracer) and SPECT imaging (using ^{123}I or ^{99m}Tc-pertechnetate as tracer). This approach has been used to monitor activity of cardiac-derived stem cells after transplantation to a rat infarct model, confirming the visualization of cells up to 6 days after transplantation [85]. With rapid advances in

stem cell research, and with high demands for testing their regenerative potential in preclinical model, noninvasive stem cell imaging will play a critical role, and we can foresee more studies requiring long-term monitoring of stem cells in preclinical models of disease.

4.3. Oncologic Applications. Imaging techniques play a potential role in preclinical cancer research, enabling sequential analysis of deep-seated tumors and metastases including studies of basic biological processes, tissue pharmacokinetics and pharmacodynamics responses to treatments. Imaging of cancer cells targets have different biological procedures including overexpression of receptor, activated enzymes or relocated molecules, apoptotic levels, sustained angiogenesis, unlimited replicative potential and invasion of tissue, and metastasis [86].

Imaging gene expression *in vivo* is very relevant in cancer preclinical models as it allows the characterization of dynamic changes in several deregulated pathways in cancer cells. As previously mentioned, HSVtk genes are typically used for SPECT, enabling noninvasive imaging of tumor cell growth as demonstrated in an experimental mouse model for lung metastases expressing after injection of HSV1-tk cells [87]. This model may be proven very useful for assessment of anticancer and antimetastases therapies in preclinical efficacy models.

Another used approach is the imaging receptors that are overexpressed in cancer cells and can be used for prognosis and for following therapeutic targeting. This has been successfully applied preclinically as well as clinically by targeting prostate-specific membrane antigen (PSMA). This receptor is overexpressed on the cell surface of prostate cancer cells and provides a useful target for prostate tumor imaging and therapy. As mentioned previously, radiolabeled monoclonal antibodies, such as ^{111}In-Capromab pendetide (ProstaScint), are currently available to detect prostate cancer but suffer from problems associated with poor delivery because of their large size [88]. The feasibility of imaging PSMA receptor expression with low-molecular-weight, high-affinity PSMA ligands labeled with [^{125}I] NaI/Iodogen for SPECT was demonstrated in a study using a prostate tumor mouse model [89].

SPECT technology is extensively used as a diagnostic tool for bone metastases in the clinic. Bone scintigraphy with ^{99m}Tc-labelled diphosphonate is a widely used method for the detection of bone metastases, and other bone disorders. This technique provides a high sensitivity and is able to survey the whole skeleton but unfortunately does not provide enough anatomical resolution to allow precise localization of the radiotracer high uptake lesion. The implementation of a SPECT/CT multimodality system can partly overcome this disadvantage, allowing a coregistration of the functional and the anatomical imaging component, resulting in precise anatomical localisation of the radiotracer. Studies have reported the use of Tc-99m-labeled diphosphonates compounds (e.g., methylene-diphosphonate (MDP)) to detect metastatic bone lesions in immunocompromised mouse models injected with cancer cells. Overall, the application of SPECT imaging in cancer research while remaining challenging have already had a remarkable impact providing new insights into the dynamics of cancer growth, invasion, and metastases, being possible to visualize gene expression, molecular pathways and functional parameters in preclinical models of cancer.

4.4. Neuroimaging Applications. The use of SPECT in preclinical functional neuroimaging provides an excellent application for understanding the pathophysiology of central nervous system (CNS) disorders, including the mechanisms of neurodegeneration, neuropharmacology related to drug abuse, and testing therapeutic strategies. As mentioned earlier, one of the strength of SPECT over other functional modalities such as the PET is the ability to get a spatial resolution below 1 mm, allowing detailed structural and functional information of different region of the brain in animal models. Also, SPECT radioligands have relative longer half-lives, which permits prolonged dynamic function studies and provides a simultaneous dual tracer imaging. The use of pinhole SPECT facilitates accurate and quantitative imaging. Indeed, specific radioligands have been used to study the dopaminergic, serotonergic, and cholinergic neurotransmission system in vivo [90].

SPECT has been applied to study basic mechanisms of degeneration in Parkinson's (PD) and Alzheimer's disease (AD). PD is characterized by a progressive loss of dopaminergic neurons. Animal models of neurodegeneration have been used to evaluate novel radioligands and to study their binding in the dopaminergic synapsis. In vivo quantification of the presynaptic dopamine transporter (DAT) activity which regulates the synaptic dopamine is feasible in the rat striatum using the ^{123}I-*N*-ω-fluoropropyl-2β-carbomethoxy-3β-(4-iodophenyl)-nortropane (^{123}I-FP-CIT) as a DAT radioligand [91], as outlined earlier. This technology is of particular interest for investigating the interrelation of synaptic dopamine and DAT in animal models of PD. Similarly, Acton et al. have characterized the occupancy of dopamine receptors in the mouse brain [92]. SPECT imaging has improved the early diagnosis of AD in patients by detecting the onset of progressive neurodegenerative disorders and vascular brain pathology causing dementia.

The thioflavin derivative, 6-iodo-2-(4′-dimethylamino-) phenyl-imidazo [1,2-a] pyridine, IMPY, which is readily radiolabeled with ^{125}I/^{123}I [^{123}I] IMPY was assessed *ex vivo* in a transgenic mouse model of AD by labeling the deposition of amyloid plaque that is linked to the pathogenesis of AD [93], showing a good binding with brain tissue homogenates of confirmed Alzheimer's disease patients. Overall, these preclinical studies support the use of SPECT for functional imaging in preclinical models of CNS disorders, facilitating the efficacy of translational studies into this field with a direct relevance for developing clinical diagnostic tools and efficacious therapies.

4.5. Drug Discovery. Preclinical imaging has a key role in the drug development, in particular for validating drug targeting, safety, and efficacy. One of the main applications

is the validation in drug binding assays to specific targeted areas, by directly labeling a drug to determine its distribution and pharmacokinetics. This approach is very useful for validating delivery roots and the specificity of novel therapeutic drugs or imaging agents. SPECT imaging has been applied to measure the binding potential of targeted nuclide [^{123}I] Iodobenzamide to the dopamine transporters in the rat brain after specific treatments [94]. Similarly, ^{99m}Tc-labeled liposomes migration has been studied after intratumoral administration to tumor xenograft models in nude rats [95]. Specific skeletal targeted probes (125I labeled) were investigated with particular emphasis on the pharmacokinetics and biodistribution following intravenous administration. This has proved to be of great potential for validating the efficacy of animal models of osteoporosis and other skeletal diseases [96].

Imaging technologies are also very useful for safety validation, as they can measure the functional response of organs to a tested drug candidate, providing information on any toxic or secondary effects related to the treatment. Radiopharmaceuticals that bind to apoptotic cells (e.g., ^{99m}Tc-Annexin) have been used preclinically to validate the possible toxicity effects in developing therapies [97]. Other examples on secondary response to the administration of a candidate drug in preclinical models include measurements in blood flow changes [98] and infiltration of inflammatory cells [99].

Another important application is the development and validation of imaging biomarkers, a surrogate imaging product that simulates a biological compound and/or has some biologic link to the disease process. These biomarkers are becoming very useful to assess therapeutic actions of pharmaceuticals, providing a non-invasive imaging tool for validating the efficacy of treatment. Advances in proteomics and genomics are leading to the discovery of new biomarkers, promoting the use of functional imaging for their validation and translation into the clinics [100].

5. Conclusion

SPECT imaging has a well-defined role in the world of molecular imaging. Recent advances in dedicated preclinical systems are able to provide high spatial and temporal resolution as well as high detection efficiency with more potentiall for further improvement. Hybrid SPECT imaging systems would serve characterizing biological phenomena in one imaging session. Reliable animal models that, mimic human diseases is another innovative field that when combined with SPECT technology will reveal more insights into early disease detection, development of new tracers/therapeutics and treatment strategy. SPECT imaging has a large potential in molecular medicine, and many novel approaches are expected in the near future.

Acknowledgment

Jordi L. Tremoleda and Tamer B. Saleh contributed equally to the work.

References

[1] G. K. Von Schulthess and H. P. W. Schlemmer, "A look ahead: PET/MR versus PET/CT," *European Journal of Nuclear Medicine and Molecular Imaging*, vol. 36, supplement 1, pp. S3–S9, 2009.

[2] M. A. Pysz, S. S. Gambhir, and J. K. Willmann, "Molecular imaging: current status and emerging strategies," *Clinical Radiology*, vol. 65, no. 7, pp. 500–516, 2010.

[3] A. Douraghy and A. F. Chatziioannou, "Preclincal imaging," in *Basic Sciences of Nuclear Medicine*, M. Khalil, Ed., chapter 18, Springer, New York, NY, USA, 2011.

[4] M. E. Phelps, "PET: the merging of biology and imaging into molecular imaging," *Journal of Nuclear Medicine*, vol. 41, no. 4, pp. 661–681, 2000.

[5] S. R. Meikle, P. Kench, M. Kassiou, and R. B. Banati, "Small animal SPECT and its place in the matrix of molecular imaging technologies," *Physics in Medicine and Biology*, vol. 50, no. 22, pp. R45–R61, 2005.

[6] G. K. Von Schulthess and T. F. Hany, "Imaging and PET—PET/CT imaging," *Journal de Radiologie*, vol. 89, no. 3, pp. 438–448, 2008.

[7] H. O. Anger, "Scintillation camera," *Review of Scientific Instruments*, vol. 29, no. 1, pp. 27–33, 1958.

[8] F. D. Van Have, B. Vastenhouw, R. M. Ramakers et al., "U-SPECT-II: an ultra-high-resolution device for molecular small-animal imaging," *Journal of Nuclear Medicine*, vol. 50, no. 4, pp. 599–605, 2009.

[9] J. R. Stickel, J. Qi, and S. R. Cherry, "Fabrication and characterization of a 0.5-mm lutetium oxyorthosilicate detector array for high-resolution PET applications," *Journal of Nuclear Medicine*, vol. 48, no. 1, pp. 115–121, 2007.

[10] A. Sanchez-Crespo, P. Andreo, and S. A. Larsson, "Positron flight in human tissues and its influence on PET image spatial resolution," *European Journal of Nuclear Medicine and Molecular Imaging*, vol. 31, no. 1, pp. 44–51, 2004.

[11] A. Ruangma, B. Bai, J. S. Lewis et al., "Three-dimensional maximum a posteriori (MAP) imaging with radiopharmaceuticals labeled with three Cu radionuclides," *Nuclear Medicine and Biology*, vol. 33, no. 2, pp. 217–226, 2006.

[12] M. R. Palmer, X. Zhu, and J. A. Parker, "Modeling and simulation of positron range effects for high resolution PET imaging," *IEEE Transactions on Nuclear Science*, vol. 52, no. 5, pp. 1391–1395, 2005.

[13] S. S. Gambhir, D. S. Berman, J. Ziffer et al., "A novel high-sensitivity rapid-acquisition single-photon cardiac imaging camera," *Journal of Nuclear Medicine*, vol. 50, no. 4, pp. 635–643, 2009.

[14] K. Erlandsson, K. Kacperski, D. Van Gramberg, and B. F. Hutton, "Performance evaluation of D-SPECT: a novel SPECT system for nuclear cardiology," *Physics in Medicine and Biology*, vol. 54, no. 9, pp. 2635–2649, 2009.

[15] C. L. Chen, Y. Wang, J. J. S. Lee, and B. M. W. Tsui, "Toward quantitative small animal pinhole SPECT: assessment of quantitation accuracy prior to image compensations," *Molecular Imaging and Biology*, vol. 11, no. 3, pp. 195–203, 2009.

[16] A. B. Hwang, B. L. Franc, G. T. Gullberg, and B. H. Hasegawa, "Assessment of the sources of error affecting the quantitative accuracy of SPECT imaging in small animals," *Physics in Medicine and Biology*, vol. 53, no. 9, pp. 2233–2252, 2008.

[17] B. L. Franc, P. D. Acton, C. Mari, and B. H. Hasegaway, "Small-animal SPECT and SPECT/CT: important tools for preclinical investigation," *Journal of Nuclear Medicine*, vol. 49, no. 10, pp. 1651–1663, 2008.

[18] T. Funk, P. Després, W. C. Barber, K. S. Shah, and B. H. Hasegawa, "A multipinhole small animal SPECT system with submillimeter spatial resolution," *Medical Physics*, vol. 33, no. 5, pp. 1259–1268, 2006.

[19] J. Nuyts, K. Vunckx, M. Defrise, and C. Vanhove, "Small animal imaging with multi-pinhole SPECT," *Methods*, vol. 48, no. 2, pp. 83–91, 2009.

[20] http://www.gm-ideas.com/pre_triumph_trimodality_system.html.

[21] http://www.milabs.com/.

[22] A. Del Guerra and N. Belcari, "State-of-the-art of PET, SPECT and CT for small animal imaging," *Nuclear Instruments and Methods in Physics Research A*, vol. 583, no. 1, pp. 119–124, 2007.

[23] J. Peter and W. Semmler, "Performance investigation of a dual-modality SPECT/optical small animal imager," *European Journal of Nuclear Medicine and Molecular Imaging*, vol. 33, p. S117, 2006.

[24] E. Breton, P. Choquet, C. Goetz et al., "Dual SPECT/MR imaging in small animal," *Nuclear Instruments and Methods in Physics Research A*, vol. 571, no. 1-2, pp. 446–448, 2007.

[25] E. L. Ritman, "Molecular imaging in small animals—roles for micro-CT," *Journal of Cellular Biochemistry*, no. 39, pp. 116–124, 2002.

[26] S. J. Schambach, S. Bag, L. Schilling, C. Groden, and M. A. Brockmann, "Application of micro-CT in small animal imaging," *Methods*, vol. 50, no. 1, pp. 2–13, 2010.

[27] C. Nichol and E. E. Kim, "Molecular imaging and gene therapy," *Journal of Nuclear Medicine*, vol. 42, no. 9, pp. 1368–1374, 2001.

[28] F. G. Blankenberg and H. W. Strauss, "Nuclear medicine applications in molecular imaging," *Journal of Magnetic Resonance Imaging*, vol. 16, no. 4, pp. 352–361, 2002.

[29] S. Vallabhajosula, *Molecular Imaging, Radiopharmaceuticals for PET and SPECT*, Springer, New York, NY, USA, 2009.

[30] D. Maclean, J. P. Northrop, H. C. Padgett, and J. C. Walsh, "Drugs and probes: the symbiotic relationship between pharmaceutical discovery and imaging science," *Molecular Imaging and Biology*, vol. 5, no. 5, pp. 304–311, 2003.

[31] G. B. Saha, *Fundamentals of Radiopharmacy*, Springer, Berlin, Germany, 5th edition, 2004.

[32] G. Kohler and C. Milstein, "Continuous cultures of fused cells secreting antibody of predefined specificity," *Nature*, vol. 256, no. 5517, pp. 495–497, 1975.

[33] C. Schiepers, *Diagnostic Nuclear Medicine*, Springer, Berlin, Germany, 2nd edition, 2006.

[34] D. J. Hnatowich, "Recent developments in the radiolabeling of antibodies with iodine, indium, and technetium," *Seminars in Nuclear Medicine*, vol. 20, no. 1, pp. 80–91, 1990.

[35] R. T. Maguire, V. L. Pascucci, A. N. Maroli, and J. V. Gulfo, "Immunoscintigraphy in patients with colorectal, ovarian, and prostate cancer: results with site-specific immunoconjugates," *Cancer*, vol. 72, no. 11, pp. 3453–3462, 1993.

[36] A. Otte, "^{90}Y-Ibritumomab tiuxetan: new drug, interesting concept, and encouraging in practice," *Nuclear Medicine Communications*, vol. 27, no. 7, pp. 595–596, 2006.

[37] S. Han, A. H. Iagaru, H. J. Zhu, and M. L. Goris, "Experience with ^{90}Y-ibritumomab (zevalin) in the management of refractory non-Hodgkin's lymphoma," *Nuclear Medicine Communications*, vol. 27, no. 12, pp. 1022–1023, 2006.

[38] *Immunomedics Europe Product monograph for the CEA-Scan (Arcitumomab) kit for the preparation of Tc-99m CEA-Scan*, Immunomedics Europe, Darmstadt, Germany, 2000.

[39] F. L. Moffat Jr., C. M. Pinsky, L. Hammershaimb et al., "Immunomedics study group clinical utility of external immunoscintigraphy with the IMMU-4 technetium-99m Fab' antibody fragment in patients undergoing surgery for carcinoma of the colon and rectumml: results of a pivotal, phase III trial," *Journal of Clinical Oncology*, vol. 14, pp. 2295–2305, 1996.

[40] *Immunomedics Europe Product monograph for LeukoScan (sulesomab)*, Immunomedics Europe, Darmstadt, Germany, 1997.

[41] S. Gratz, M. L. Schipper, J. Dörner et al., "LeukoScan for imaging infection in different clinical settings: a retrospective evaluation and extended review of the literature," *Clinical Nuclear Medicine*, vol. 28, no. 4, pp. 267–276, 2003.

[42] F. G. Blankenberg, P. D. Katsikis, J. F. Tait et al., "Imaging of apoptosis (programmed cell death) with ^{99m}Tc annexin V," *Journal of Nuclear Medicine*, vol. 40, no. 1, pp. 184–191, 1999.

[43] J. F. Tait, M. D. Cerqueira, T. A. Dewhurst, K. Fujikawa, J. L. Ritchie, and J. R. Stratton, "Evaluation of annexin V as a platelet-directed thrombus targeting agent," *Thrombosis Research*, vol. 75, no. 5, pp. 491–501, 1994.

[44] L. Ha, R. Mansberg, D. Nguyen, and C. Bui, "Increased activity on In-111 octreotide imaging due to radiation fibrosis," *Clinical Nuclear Medicine*, vol. 33, no. 1, pp. 46–48, 2008.

[45] L. K. Kvols and E. A. Woltering, "Role of somatostatin analogs in the clinical management of non-neuroendocrine solid tumors," *Anti-Cancer Drugs*, vol. 17, no. 6, pp. 601–608, 2006.

[46] C. Susini and L. Buscail, "Rationale for the use of somatostatin analogs as antitumor agents," *Annals of Oncology*, vol. 17, no. 12, pp. 1733–1742, 2006.

[47] I. Virgolini, I. Szilvasi, A. Kurtaran et al., "Indium-111-DOTA-lanreotide: biodistribution, safety and radiation absorbed dose in tumor patients," *Journal of Nuclear Medicine*, vol. 39, no. 11, pp. 1928–1936, 1998.

[48] D. Kahn, Y. Menda, K. Kernstine et al., "The utility of ^{99m}Tc-depreotide compared with F-18-fluorodeoxyglucose positron emission tomography and surgical staging in patients with suspected non-small cell lung cancer," *Chest*, vol. 125, no. 2, pp. 494–501, 2004.

[49] R. Danielsson, M. Bååth, L. Svensson, U. Forslöv, and K.-G. Kölbeck, "Imaging of regional lymph node metastases with ^{99m}Tc-depreotide in patients with lung cancer," *European Journal of Nuclear Medicine and Molecular Imaging*, vol. 32, no. 8, pp. 925–931, 2005.

[50] *Berlex Laboratories Product Monograph for the NeoTect Kit for the Preparation of Tc-99m Depreotide*, Berlex Laboratories, Wayne, NJ, USA, 2001.

[51] C. Henry, F. Koumanov, C. Ghezzi et al., "Experimental models, protocols, and reference values for evaluation of iodinated analogues of glucose," *Nuclear Medicine and Biology*, vol. 22, no. 7, pp. 875–885, 1995.

[52] C. Dumas, R. Schibli, and P. A. Schubigert, "Versatile routes to C-2- and C-6-functionalized glucose derivatives of iminodiacetic acid," *Journal of Organic Chemistry*, vol. 68, no. 2, pp. 512–518, 2003.

[53] C. Dumas, J. Petrig, R. Schibli et al., "Functionalisation of glucose for the labeling with ^{99m}Tc-tricarbonyl," *Journal of Labelled Compounds and Radiopharmaceuticals*, vol. 44, pp. S57–S59, 2001.

[54] K. Kawai, Y. Fujibayashi, H. Saji et al., "A strategy for the study of cerebral amino acid transport using iodine-123-labeled amino acid radiopharmaceutical: 3-Iodo-alpha-methyl-L-tyrosine," *Journal of Nuclear Medicine*, vol. 32, no. 5, pp. 819–824, 1991.

[55] K. J. Langen, H. H. Coenen, N. Roosen et al., "SPECT studies of brain tumors wirh L-3-[^{123}I]iodo-α-methyl tyrosine: comparison with PET, 124IMT and first clinical results," *Journal of Nuclear Medicine*, vol. 31, no. 3, pp. 281–286, 1990.

[56] K. J. Langen, N. Roosen, H. H. Coenen et al., "Brain and brain tumor uptake of L-3-[^{123}I]iodo-α-methyl tyrosine: competition with natural L-amino acids," *Journal of Nuclear Medicine*, vol. 32, no. 6, pp. 1225–1229, 1991.

[57] J. G. Tjuvajev, M. Doubrovin, T. Akhurst et al., "Comparison of radiolabeled nucleoside probes (FIAU, FHBG, and FHPG) for PET imaging of HSV1-tk gene expression," *Journal of Nuclear Medicine*, vol. 43, no. 8, pp. 1072–1083, 2002.

[58] F. M. Bengel, M. Anton, T. Richter et al., "Noninvasive imaging of transgene expression by use of positron emission tomography in a pig model of myocardial gene transfer," *Circulation*, vol. 108, no. 17, pp. 2127–2133, 2003.

[59] K. A. Krohn, J. M. Link, and R. P. Mason, "Molecular imaging of hypoxia," *Journal of Nuclear Medicine*, vol. 49, no. 6, pp. 129S–148S, 2008.

[60] J. R. Ballinger, "Imaging hypoxia in tumors," *Seminars in Nuclear Medicine*, vol. 31, no. 4, pp. 321–329, 2001.

[61] S. K. Technetium, *Chemistry and Radiopharmaceutical Applications*, Wiley-VCH, Weinheim, Germany, 2000.

[62] D. Stypinski, S. A. McQuarrie, L. I. Wiebe, Y. K. Tam, J. R. Mercer, and A. J. B. McEwan, "Dosimetry estimations for ^{123}I-IAZA in healthy volunteers," *Journal of Nuclear Medicine*, vol. 42, no. 9, pp. 1418–1423, 2001.

[63] P. A. Thomas and B. Mullan, "Avid In-111 labeled WBC accumulation in a patient with active osteoarthritis of both knees," *Clinical Nuclear Medicine*, vol. 20, no. 11, pp. 973–975, 1995.

[64] C. Solanki, D. J. Li, A. Wong, R. W. Barber, E. P. Wraight, and C. B. Sampson, "Stabilization and multidose use of exametazime for cerebral perfusion studies," *Nuclear Medicine Communications*, vol. 15, no. 9, pp. 718–722, 1994.

[65] J. Booij, J. D. Speelman, M. W. I. M. Horstink, and E. C. Wolters, "The clinical benefit of imaging striatal dopamine transporters with [^{123}I] FP-CIT SPET in differentiating patients with presynaptic parkinsonism from other forms of parkinsonism," *European Journal of Nuclear Medicine*, vol. 28, no. 3, pp. 266–272, 2001.

[66] M. Lorberboym, R. Djaldetti, E. Melamed, M. Sadeh, and Y. Lampl, "^{123}I-FP-CIT SPECT imaging of dopamine transporters in patients with cerebrovascular disease and clinical diagnosis of vascular parkinsonism," *Journal of Nuclear Medicine*, vol. 45, no. 10, pp. 1688–1693, 2004.

[67] J. Lavalaye, J. Booij, L. Reneman, J. B. A. Habraken, and E. A. Van Royen, "Effect of age and gender on dopamine transporter imaging with [^{123}I]FP-CIT SPET in healthy volunteers," *European Journal of Nuclear Medicine*, vol. 27, no. 7, pp. 867–869, 2000.

[68] A. Constantinesco, P. Choquet, L. Monassier, V. Israel-Jost, and L. Mertz, "Assessment of left ventricular perfusion, volumes, and motion in mice using pinhole gated SPECT," *Journal of Nuclear Medicine*, vol. 46, no. 6, pp. 1005–1011, 2005.

[69] B. M. W. Tsui and D. L. Kraitchman, "Recent advances in small-animal cardiovascular imaging," *Journal of Nuclear Medicine*, vol. 50, no. 5, pp. 667–670, 2009.

[70] P. D. Acton and H. F. Kung, "Small animal imaging with high resolution single photon emission tomography," *Nuclear Medicine and Biology*, vol. 30, no. 8, pp. 889–895, 2003.

[71] Z. Liu, G. A. Kastis, G. D. Stevenson et al., "Quantitative analysis of acute myocardial infarct in rat hearts with ischemia-reperfusion using a high-resolution stationary SPECT system," *Journal of Nuclear Medicine*, vol. 43, no. 7, pp. 933–939, 2002.

[72] C. Vanhove, T. Lahoutte, M. Defrise, A. Bossuyt, and P. R. Franken, "Reproducibility of left ventricular volume and ejection fraction measurements in rat using pinhole gated SPECT," *European Journal of Nuclear Medicine and Molecular Imaging*, vol. 32, no. 2, pp. 211–220, 2005.

[73] A. Constantinesco, P. Choquet, L. Monassier, V. Israel-Jost, and L. Mertz, "Assessment of left ventricular perfusion, volumes, and motion in mice using pinhole gated SPECT," *Journal of Nuclear Medicine*, vol. 46, no. 6, pp. 1005–1011, 2005.

[74] Z. Liu, H. H. Barrett, G. D. Stevenson et al., "High-resolution imaging with ^{99m}Tc-glucarate for assessing myocardial injury in rat heart models exposed to different durations of ischemia with reperfusion," *Journal of Nuclear Medicine*, vol. 45, no. 7, pp. 1251–1259, 2004.

[75] P. M. Kang and S. Izumo, "Apoptosis and heart failure: a critical review of the literature," *Circulation Research*, vol. 86, no. 11, pp. 1107–1113, 2000.

[76] D. F. Meoli, M. M. Sadeghi, S. Krassilnikova et al., "Noninvasive imaging of myocardial angiogenesis following experimental myocardial infarction," *Journal of Clinical Investigation*, vol. 113, no. 12, pp. 1684–1691, 2004.

[77] F. D. Kolodgie, A. Petrov, R. Virmani et al., "Targeting of apoptotic macrophages and experimental atheroma with radiolabeled annexin V: a technique with potential for noninvasive imaging of vulnerable plaque," *Circulation*, vol. 108, no. 25, pp. 3134–3139, 2003.

[78] B. A. Khaw, Y. Tekabe, and L. L. Johnson, "Imaging experimental atherosclerotic lesions in ApoE knockout mice: enhanced targeting with ZD-anti-DTPA bispecific antibody and ^{99m}Tc-labeled negatively charged polymers," *Journal of Nuclear Medicine*, vol. 47, no. 5, pp. 868–876, 2006.

[79] J. V. Frangioni and R. J. Hajjar, "In vivo tracking of stem cells for clinical trials in cardiovascular disease," *Circulation*, vol. 110, no. 21, pp. 3378–3383, 2004.

[80] R. Zhou, D. H. Thomas, H. Qiao et al., "In vivo detection of stem cells grafted in infarcted rat myocardium," *Journal of Nuclear Medicine*, vol. 46, no. 5, pp. 816–822, 2005.

[81] B. B. Chin, Y. Nakamoto, J. W. Bulte, M. F. Pittenger, R. Wahl, and D. L. Kraitchman, "111In oxide labeled mesenchymal stem cell SPECT after intravenous administration in myocardial infarction," *Nuclear Medicine Communications*, vol. 24, no. 11, pp. 1149–1154, 2003.

[82] M. Inubushi and N. Tamaki, "Radionuclide reporter gene imaging for cardiac gene therapy," *European Journal of Nuclear Medicine and Molecular Imaging*, vol. 34, supplement 1, pp. S27–S33, 2007.

[83] M. Rodriguez-Porcel, "In vivo imaging and monitoring of transplanted stem cells: clinical applications," *Current Cardiology Reports*, vol. 12, no. 1, pp. 51–58, 2010.

[84] M. G. Pomper, H. Hammond, X. Yu et al., "Serial imaging of human embryonic stem-cell engraftment and teratoma formation in live mouse models," *Cell Research*, vol. 19, no. 3, pp. 370–379, 2009.

[85] J. Terrovitis, K. F. Kwok, R. Lautamäki et al., "Ectopic expression of the sodium-iodide symporter enables imaging of transplanted cardiac stem cells in vivo by single-photon emission computed tomography or positron emission tomography," *Journal of the American College of Cardiology*, vol. 52, no. 20, pp. 1652–1660, 2008.

[86] D. Hanahan and R. A. Weinberg, "The hallmarks of cancer," *Cell*, vol. 100, no. 1, pp. 57–70, 2000.

[87] W. P. Deng, C. C. Wu, C. C. Lee et al., "Serial in vivo imaging of the lung metastases model and gene therapy using HSV1-tk and ganciclovir," *Journal of Nuclear Medicine*, vol. 47, no. 5, pp. 877–884, 2006.

[88] L. E. Ponsky, E. E. Cherullo, R. Starkey, D. Nelson, D. Neumann, and C. D. Zippe, "Evaluation of preoperative ProstaScint™ scans in the prediction of nodal disease," *Prostate Cancer and Prostatic Diseases*, vol. 5, no. 2, pp. 132–135, 2002.

[89] C. A. Foss, R. C. Mease, H. Fan et al., "Radiolabeled small-molecule ligands for prostate-specific membrane antigen: in vivo imaging in experimental models of prostate cancer," *Clinical Cancer Research*, vol. 11, no. 11, pp. 4022–4028, 2005.

[90] S. Sharma and M. Ebadi, "SPECT neuroimaging in translational research of CNS disorders," *Neurochemistry International*, vol. 52, no. 3, pp. 352–362, 2008.

[91] S. Nikolaus, C. Antke, K. Kley, M. Beu, A. Wirrwar, and H. W. Müller, "Pretreatment with haloperidol reduces I-FP-CIT binding to the dopamine transporter in the rat striatumml: an in vivo imaging study with a dedicated small-animal SPECT camera," *Journal of Nuclear Medicine*, vol. 50, no. 7, pp. 1147–1152, 2009.

[92] P. D. Acton, C. Hou, M.-P. Kung, K. Plössl, C. L. Keeney, and H. F. Kung, "Occupancy of dopamine D2 receptors in the mouse brain measured using ultra-high-resolution single-photon emission tomography and [^{123}I]IBF," *European Journal of Nuclear Medicine*, vol. 29, no. 11, pp. 1507–1515, 2002.

[93] M. P. Kung, C. Hou, Z. P. Zhuang, A. J. Cross, D. L. Maier, and H. F. Kung, "Characterization of IMPY as a potential imaging agent for β-amyloid plaques in double transgenic PSAPP mice," *European Journal of Nuclear Medicine and Molecular Imaging*, vol. 31, no. 8, pp. 1136–1145, 2004.

[94] S. Nikolaus, R. Larisch, A. Wirrwar et al., "[^{123}I]Iodobenzamide binding to the rat dopamine D receptor in competition with haloperidol and endogenous dopamine—an in vivo imaging study with a dedicated small animal SPECT," *European Journal of Nuclear Medicine and Molecular Imaging*, vol. 32, no. 11, pp. 1305–1310, 2005.

[95] A. Bao, W. T. Phillips, B. Goins et al., "Potential use of drug carried-liposomes for cancer therapy via direct intratumoral injection," *International Journal of Pharmaceutics*, vol. 316, no. 1-2, pp. 162–169, 2006.

[96] D. Wang, M. Sima, R. L. Mosley et al., "Pharmacokinetic and biodistribution studies of a bone-targeting drug delivery system based on N-(2-hydroxypropyl)methacrylamide copolymers," *Molecular Pharmaceutics*, vol. 3, no. 6, pp. 717–725, 2006.

[97] K. Schimmel, R. Bennink, K. De Bruin et al., "Absence of cardiotoxicity of the experimental cytotoxic drug cyclopentenyl cytosine (CPEC) in rats," *Archives of Toxicology*, vol. 79, no. 5, pp. 268–276, 2005.

[98] M. D. Devous Sr., "Single-photon emission computed tomography in neurotherapeutics," *NeuroRx*, vol. 2, no. 2, pp. 237–249, 2005.

[99] C. Van Montfrans, R. J. Bennink, K. De Bruin et al., "In vivo evaluation of 111In-labeled T-lymphocyte homing in experimental colitis," *Journal of Nuclear Medicine*, vol. 45, no. 10, pp. 1759–1765, 2004.

[100] J.-L. Vanderheyden, "The use of imaging in preclinical drug development," *Quarterly Journal of Nuclear Medicine and Molecular Imaging*, vol. 53, no. 4, pp. 374–381, 2009.

Hindawi Publishing Corporation
International Journal of Molecular Imaging
Volume 2011, Article ID 543267, 12 pages
doi:10.1155/2011/543267

Review Article

SPECT Imaging Agents for Detecting Cerebral β-Amyloid Plaques

Masahiro Ono and Hideo Saji

Graduate School of Pharmaceutical Sciences, Kyoto University, 46-29 Yoshida Shimoadachi-cho, Sakyo-ku, Kyoto 606-8501, Japan

Correspondence should be addressed to Masahiro Ono, ono@pharm.kyoto-u.ac.jp and Hideo Saji, hsaji@pharm.kyoto-u.ac.jp

Received 29 July 2010; Revised 6 November 2010; Accepted 24 January 2011

Academic Editor: Alexander Drzezga

The development of radiotracers for use *in vivo* to image β-amyloid (Aβ) plaques in cases of Alzheimer's disease (AD) is an important, active area of research. The presence of Aβ aggregates in the brain is generally accepted as a hallmark of AD. Since the only definitive diagnosis of AD is by postmortem staining of affected brain tissue, the development of techniques which enable one to image Aβ plaques *in vivo* has been strongly desired. Furthermore, the quantitative evaluation of Aβ plaques in the brain could facilitate evaluation of the efficacy of antiamyloid therapies currently under development. This paper reviews the current situation in the development of agents for SPECT-based imaging of Aβ plaques in Alzheimer's brains.

1. Introduction

Alzheimer's disease (AD) is an age-related, irreversible form of dementia characterized by memory loss, a progressive decline in intellectual ability, language impairment, and personality and behavioral changes that eventually interfere with daily life. The accumulation of β-amyloid (Aβ) aggregates (major protein aggregates of senile plaques) in the brain is considered one of the hallmarks of AD [1, 2]. Today, the clinical diagnosis of AD is primarily based on history and memory testing, which is often difficult and not accurate, as the early cognitive and behavioral symptoms of AD are difficult to distinguish from normal signs of aging. To facilitate the early diagnosis of this disease, there is an urgent need for the sensitive noninvasive detection of biomarkers for the pathophysiology. Toward achieving this goal, nuclear imaging techniques such as positron emission computed tomography (PET) and single photon emission computed tomography (SPECT) have been employed. Radionuclide-labeled agents targeting the Aβ plaques in the brain may greatly facilitate the diagnosis of AD and new antiamyloid therapies [3–7]. The differential diagnosis for AD includes a large number of other diseases such as vascular dementia, frontal temporal lobe dementia (FTLD) complex, and dementia with Lewy bodies (DLB) as well as rarer neurodegenerative diseases such as Creutzfeld-Jacob disease (CJD). Importantly, AD subjects will always have Aβ plaques, whereas Aβ is seen not at all or only sporadically in most of these other diseases. In each case, appropriate prognosis and treatment require accurate diagnostic assessment.

Developing Aβ imaging agents is currently an emerging field of research. The basic requirements for suitable Aβ imaging agents include (i) good penetration of the blood-brain barrier, (ii) selective binding to Aβ plaques, and (iii) clear and contrasting signals between plaques and nonplaques (Figure 1). Based on these requirements, several promising agents with the backbone structure of DDNP, thioflavin-T and Congo Red have been synthesized and evaluated for use *in vivo* as probes to image Aβ plaques in AD brain. Clinical trials in AD patients have been conducted with several PET imaging agents including [^{11}C]PIB [8–10], [^{11}C]SB-13 [6, 11], [^{11}C]BF-227 [12], [^{11}C]AZD2184 [13], [^{18}F]FDDNP [14–16], [^{18}F]BAY94-9172 [7, 17, 18], [^{18}F] AV-45 [19–21], and [^{18}F]GE-067 [22] (Figure 2), indicating the imaging of Aβ plaques in living brain tissue to be useful for the diagnosis of AD. The ^{11}C-labeled agents limit their use to on-site cyclotrons and sophisticated radiochemistry laboratories due to the short half-life (20 min) of ^{11}C. PET agents with the longer half-life (110 min) radioisotope ^{18}F have recently been developed and could increase the availability of Aβ imaging to all PET facilities, but still represents a minority of modern hospitals, as only a small fraction of hospitals have a PET scanner. Since SPECT is more valuable than PET in terms of routine diagnostic

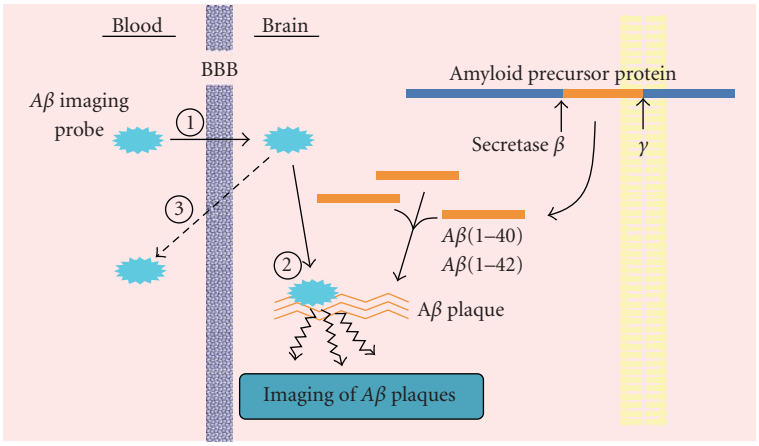

Figure 1: Strategy of *in vivo* imaging of cerebral Aβ plaques.

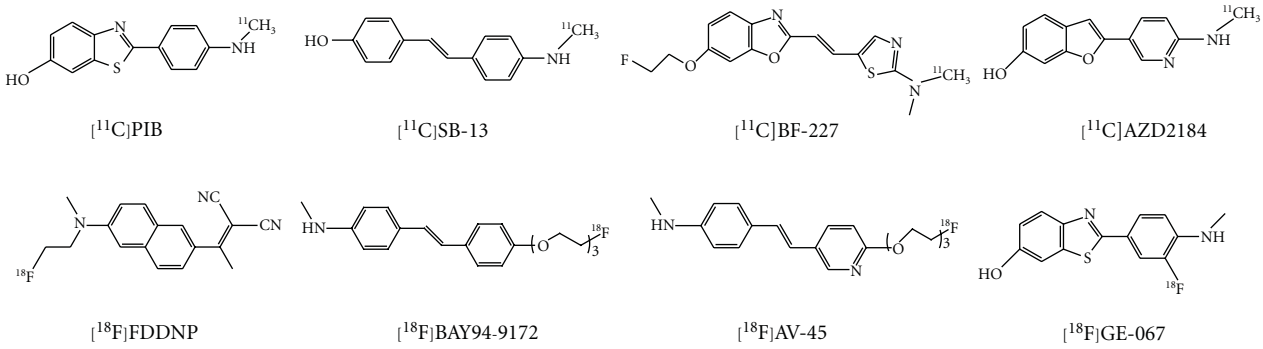

Figure 2: Chemical structure of PET imaging agents tested clinically.

use, the development of more useful Aβ imaging agents for SPECT has been a critical issue. However, progress in developing imaging agents targeting Aβ plaques is less advanced for SPECT than PET. In this review, we summarize the current situation in the development of probes for SPECT-based imaging of Aβ plaques in Alzheimer's brains.

2. Radioiodinated Probes for Imaging of Aβ Plaques

Many radioiodinated imaging agents derived from Congo Red or thioflavin-T have been developed. Compounds **1** [29], **2** [29], **3** [40], **4** [23], **5** [24], and **6** [25] (Figure 3) are thought to be derived from Congo Red. Although **1**, **2**, and **3** showed unfavorable pharmacokinetics *in vivo* such as low uptake into the brain and a slow washout, the radioactivity pharmacokinetics of **5** and **6** was much improved. Because thioflavin-T has a lower molecular weight than Congo Red, implying greater blood-brain penetration, a number of groups have worked to develop probes for SPECT derived from thioflavin-T including **7** (IMPY) [26–28], **8** (TZDM) [29], **9** (IBOX) [30], **10** (benzofuran derivatives) [31], and **11** (phenylindole derivatives) (Figure 4) [32].

Initially, Zhuang and coworkers prepared iodostrylbenzene derivatives based on the chemical structure of Congo Red, [^{125}I]IMSB (**1**) and [^{125}I]ISB (**2**). These ligands exhibited low brain uptake likely due to two ionizable carboxyl groups [29]. Thus, a small and neutral thioflavin-T analog, [^{125}I]TZDM (**8**), was prepared [29]. *In vitro* binding studies of these ligands, [^{125}I]ISB, [^{125}I]IMSB and [^{125}I]TZDM, showed excellent binding affinities with K_d values of 0.08, 0.13 and 0.06 nM for aggregates of Aβ(1–40) and 0.15, 0.73 and 0.14 nM for aggregates of Aβ(1–42), respectively. Interestingly, in a competitive-binding assay, different binding sites on Aβ(1–40) and Aβ(1–42) aggregates, which are mutually exclusive, were observed for Congo Red and thioflavin-T derivatives. Biodistribution experiments in normal mice after an i.v. injection showed that [^{125}I]TZDM exhibited good uptake and retention in the brain, much higher than [^{125}I]ISB and [^{125}I]IMSB. Preliminary experiments on the biodistribution of [^{125}I]TZDM in transgenic mice, engineered to produce excess Aβ plaques in the brain as an AD model, suggested labeling of Aβ aggregates *in vivo*. However, [^{125}I]TZDM is not ideal as an imaging agent *in vivo*, due to its labeling of white matter, which significantly increases the background

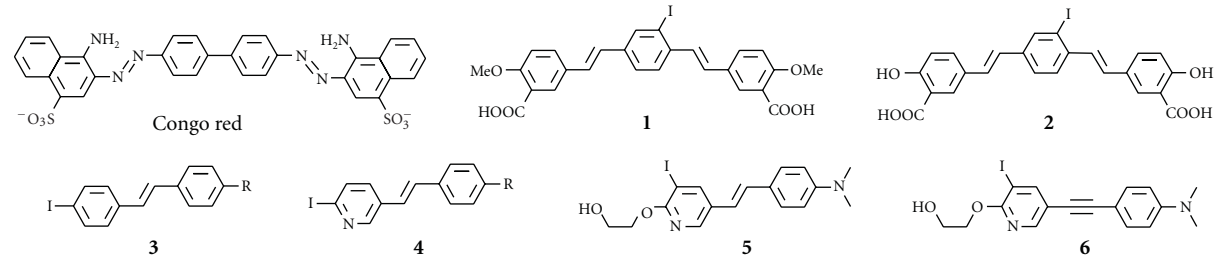

Figure 3: Chemical structure of SPECT imaging agents derived from Congo Red.

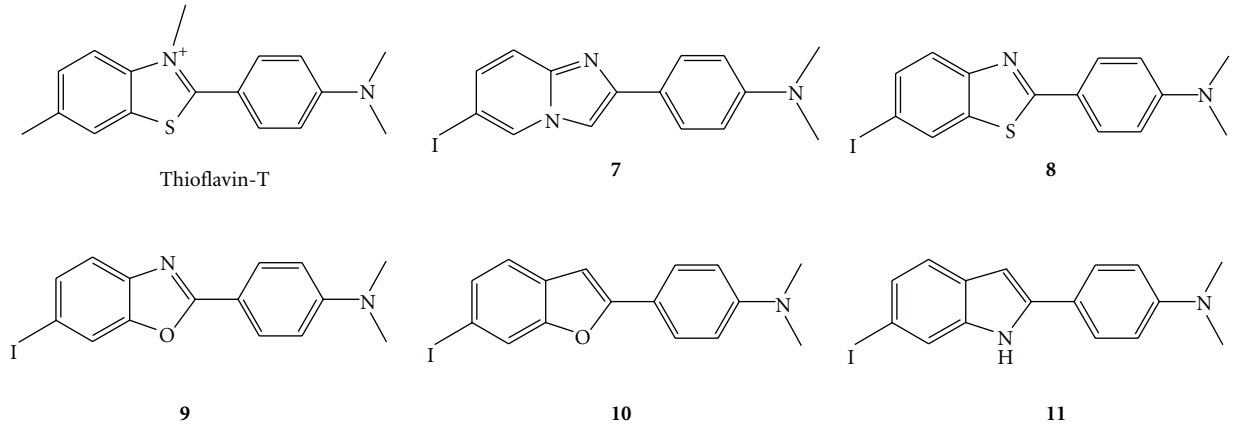

Figure 4: Chemical structure of SPECT imaging agents derived from thioflavin T.

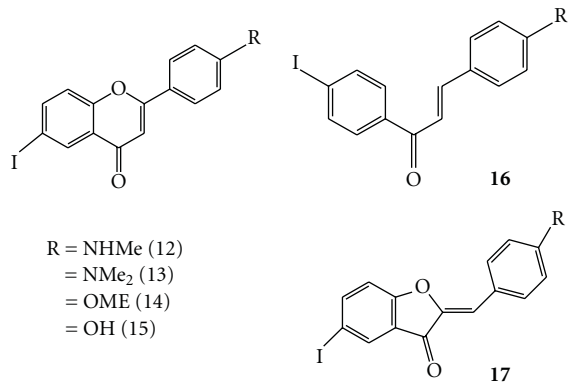

Figure 5: Chemical structure of SPECT imaging agents based on flavone (**12–15**), chalcone (**16**), and aurone (**17**).

activity. To improve the pharmacokinetics of uptake and retention, Kung et al. and others have prepared several compounds derived from thioflavin-T and studied features such as affinity for Aβ aggregates *in vitro* and biodistribution *in vivo*. Interestingly, the compounds with good binding to Aβ aggregates share a common structural feature: either an *N*-methylamino- or *N*,*N*-dimethylaminophenyl group at one end of the molecule. The structural feature required for binding to Aβ aggregates appears to be simple and unique.

[^{123}I]IMPY has been characterized as a potential agent for SPECT-based imaging of Aβ plaques. IMPY displayed selective labeling of Aβ plaques *ex vivo* in autoradiographic experiments using double-transgenic mice (PSAPP) as a model of AD [33]. Preliminary clinical data on [^{125}I]IMPY in normal and AD patients showed a distinct distribution pattern similar to that of [^{11}C]PIB [34, 35]. However, the signal-to-noise ratio for plaque labeling is not as high as that of [^{11}C]PIB. The low contrast may be due to the fast clearance from brain and plasma observed in AD and normal subjects. But the rapid metabolism and instability of [^{123}I]IMPY *in vivo* may have led to less than optimal signal-to-noise ratios for targeting Aβ plaques in the brain. Additional candidates are being explored for SPECT imaging of Aβ plaques in the brain.

Recently, the effects of polyhydroxyflavones on the formation, extension, and destabilization of Aβ aggregates have been studied *in vitro* [36]. These flavones dose-dependently inhibited the formation of Aβ aggregates, as well as destabilized preformed Aβ aggregates, indicating that they could interact directly with the aggregates. The findings in that report prompted us to use flavones as a core structure in the development of Aβ imaging agents. Furthermore, some recent studies have shown that electron-donating groups such as methylamino, dimethylamino, methoxy, and hydroxy groups play a critical role in the binding to Aβ aggregates. With these considerations in mind, we designed

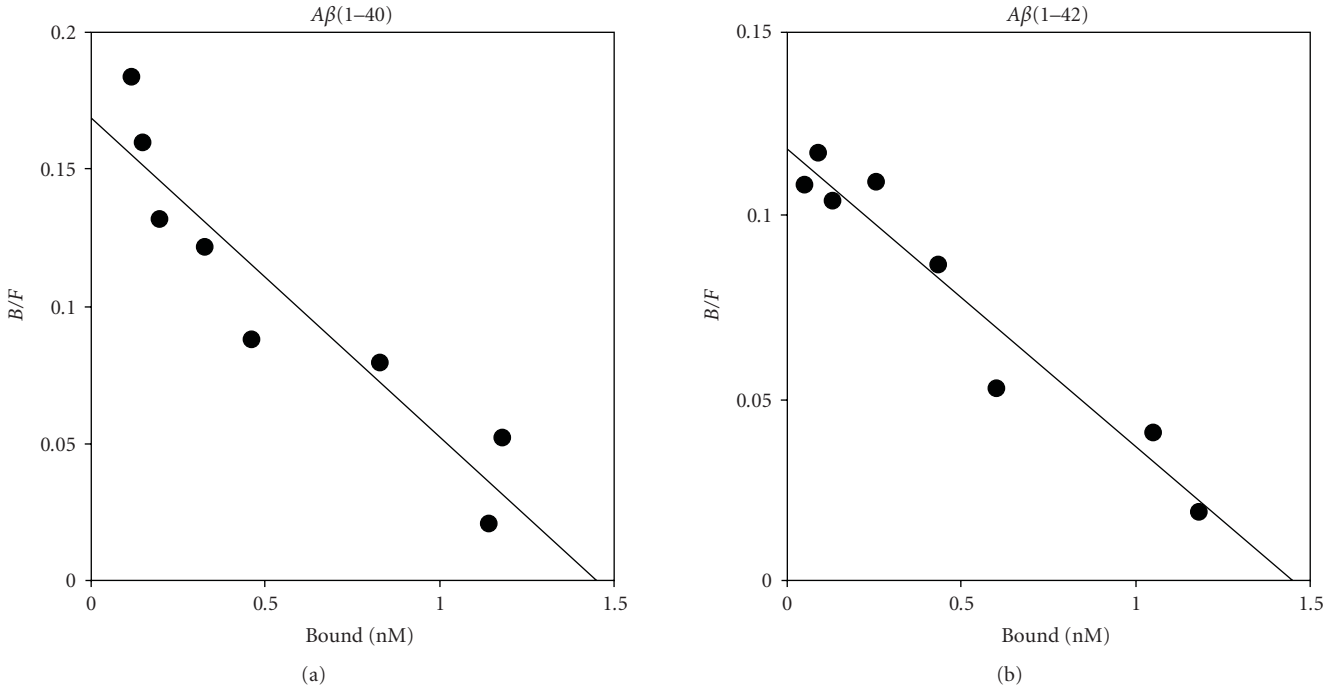

Figure 6: Scatchard plots of the binding of [^{125}I]**12** to aggregates of Aβ(1–40) (a) and Aβ(1–42) (b).

four radioiodinated flavones with a radioiodine at the 6-position and an electron-donating group at the 4′-position (Figure 5). Then we synthesized a series of flavone derivatives and evaluated their usefulness *in vivo* as SPECT Aβ imaging agents [37].

Experiments on the binding of [^{125}I]**12** to aggregates of Aβ(1–40) and Aβ(1–42) were carried out. Transformation of the saturation binding of [^{125}I]**12** to Scatchard plots gave linear plots, suggesting one binding site (Figure 6). [^{125}I]**12** showed excellent affinity for both Aβ(1–40) (K_d = 12.4 ± 2.3 nM) and Aβ(1–42) (K_d = 17.4 ± 5.7 nM) aggregates. The binding of nonradioactive flavone derivatives (compounds **12**, **13**, **14**, and **15**) was evaluated in experiments inhibiting [^{125}I]**12** from binding Aβ(1–40) and Aβ(1–42) aggregates. As shown in Table 1, all flavone derivatives competed well with [^{125}I]**12** (K_i = 13–77 nM). More interestingly, when thioflavin-T, and Congo Red gave high K_i values (>1000 nM) (Table 1), indicating little competition. This finding suggests that these flavones may have a binding site on Aβ aggregates different from that of thioflavin T and Congo Red, although additional studies regarding the selectivity of binding affinity for Aβ aggregates are required.

Since the *in vitro* binding assays demonstrated the high affinity of the flavone derivatives for Aβ(1–40) and Aβ(1–42) aggregates, compounds **12, 13**, **14**, and **15** were investigated for their neuropathologic staining of Aβ plaques and NFTs in human AD brain sections (Figure 7). The compounds intensely stained Aβ plaques (Figures 7(a), 7(e), 7(i), and 7(m)), neuritic plaques (Figures 7(b), 7(f), 7(j), and 7(n)), and cerebrovascular amyloids (Figures 7(c), 7(g), 7(k), and 7(o)) with nearly the same pattern. However, as seen in Figures 7(a), 7(e), 7(i), and 7(m), these flavone compounds did not intensely stain the core region in so-called classic Aβ plaques, unlike the thioflavin-T and Congo Red derivatives previously reported as Aβ imaging probes, indicating that flavone derivatives may have somewhat distinct binding characteristics for amyloid fibrils. These flavone derivatives appear to stain not only neuritic Aβ plaques but also diffuse amyloid plaque deposits, which are known to be mainly composed of Aβ(1−42) [38] and to be the initial pathologic change in AD [39]. Thus flavone derivatives with high affinity for Aβ(1–42)-positive diffuse plaques may be more useful for presymptomatic detection of AD. Furthermore, **12, 13**, **14**, and **15** also showed high affinity for NFTs in AD brain sections (Figures 7(d), 7(h), 7(l), and 7(p)). These findings suggest that these flavone derivatives can bind amyloid fibrils and NFTs without the backbone structure of thioflavin-T or Congo Red and that quantitative evaluation of their cerebral

Table 1: Inhibition constants (K_i, nM)[a] of compounds for the binding of ligands to aggregates of Aβ(1–40) and Aβ(1–42).

Compound	Aβ(1–40)	Aβ(1–42)
12	22.6 ± 3.4	30.0 ± 3.4
13	13.2 ± 0.2	15.6 ± 2.4
14	29.0 ± 3.2	38.3 ± 8.1
15	72.5 ± 8.2	77.2 ± 9.2
Thioflavin T	>1000	>1000
Congo Red	>1000	>1000

[a]Values are the mean ± standard error of the mean for 6 independent experiments.

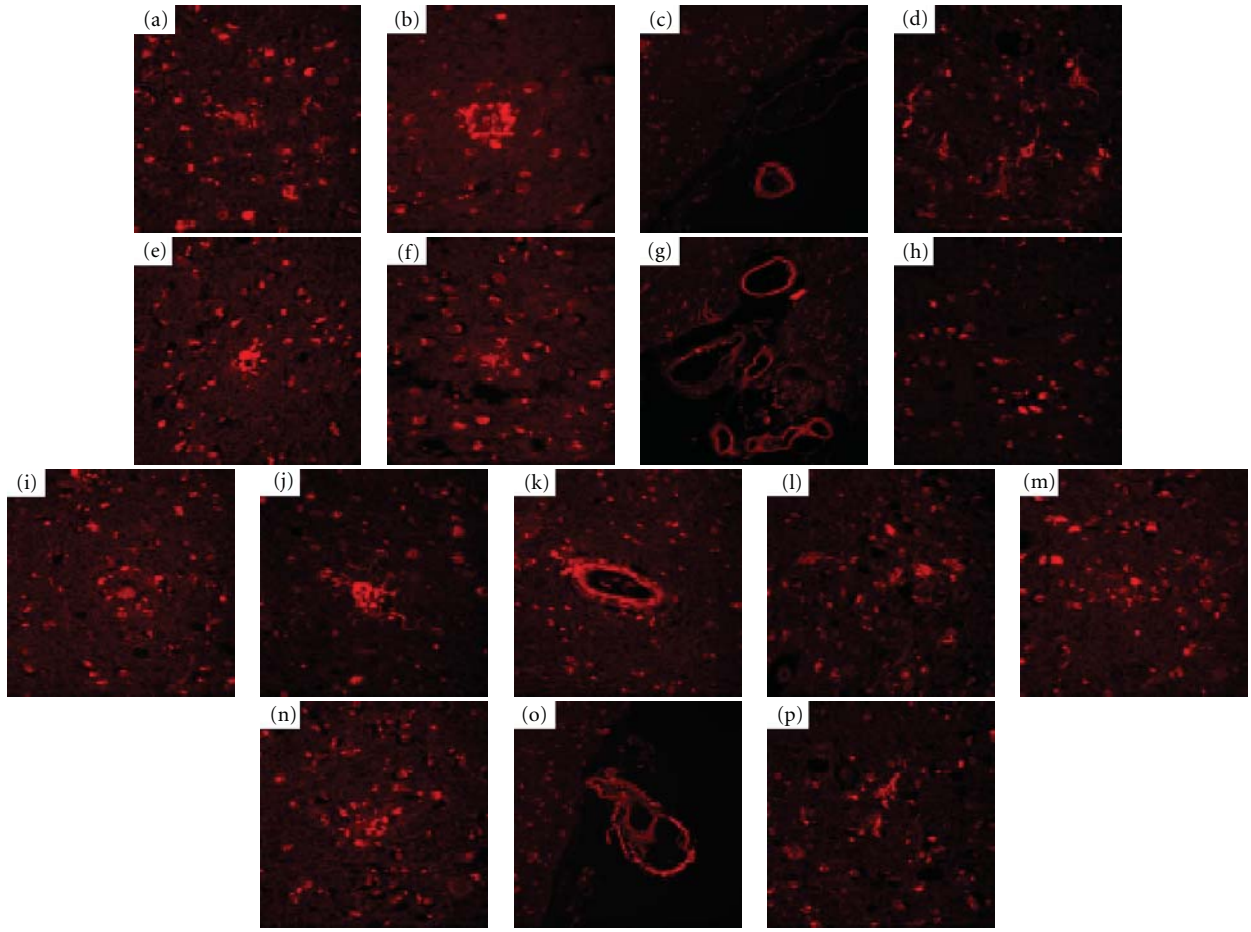

Figure 7: Neuropathological staining of compounds **12** (a)–(d), **13** (e)–(h), **14** (i)–(l), and **15** (m)–(p) on 5 μm AD brain sections from the temporal cortex. (a) Aβ plaques (a), (e), (i), and (m) are clearly stained with **12**, **13**, **14,** and **15** (×40 magnification). Clear staining of neuritic plaques (b), (f), (j), and (n) and cerebrovascular amyloid (c), (g), (k), and (o) was also obtained. Many NFTs (d), (h), (l), and (p) are intensely stained with **12, 13**, **14**, and **15** (×40 magnification).

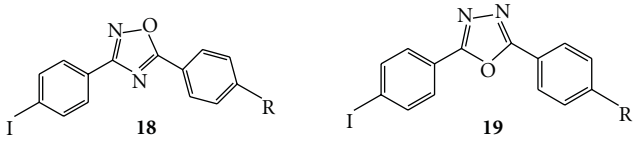

Figure 8: Chemical structure of diphenyl oxadiazoles.

localization may provide useful information on Aβ and tau pathology.

Four radioiodinated flavone ligands ([^{125}I]**12**, [^{125}I]**13**, [^{125}I]**14,** and [^{125}I]**15**) were evaluated for their biodistribution *in vivo* in normal mice. Previous studies suggest that the optimal lipophilicity range for brain entry is observed for compounds with log *P*-values between 1 and 3 [5]. All four ligands displayed optimal lipophilicity as reflected by log *P*-values of 1.94, 2.69, 2.41, and 1.92, respectively. As expected, these ligands exhibited high uptake ranging from 3.2% to 4.1% ID/g brain at 2 min postinjection, a level sufficient for imaging in the brain (Table 2). In addition, they displayed good clearance from the normal brain: 1.2, 1.0, 0.17, and 0.08% ID/g at 60 min postinjection for [^{125}I]**12**, [^{125}I]**13**, [^{125}I]**14**, and [^{125}I]**15**, respectively. Radioiodinated amyloid imaging agents such as [^{125}I]*m*-I-stilbene (**3**) [40], [^{125}I]TZDM (**8**) [29], [^{125}I]IBOX (**9**) [30], and [^{125}I]benzofuran (**10**) [31], and [^{125}I]phenylindole (**11**) [32] reported previously showed good uptake, but a relatively slow washout from the normal brain. A low washout rate leads to high background activity and prevents the visualization of Aβ plaques in the AD brain. Appropriate properties *in vivo* (higher uptake and faster washout from the normal brain) make radioiodinated flavones useful candidates for SPECT tracers for Aβ imaging.

On the basis of this success in the development of SPECT imaging agents, to search for more useful candidates for Aβ imaging probes, we have designed a chemical modification of the flavone structure, and selected the chalcone and aurone structure as a novel core for Aβ imaging probes (Figure 5) [41, 42]. Chalcone and aurone are categorized as flavonoids containing a flavone. We newly designed and synthesized novel chalcone and aurone derivatives, and evaluated the

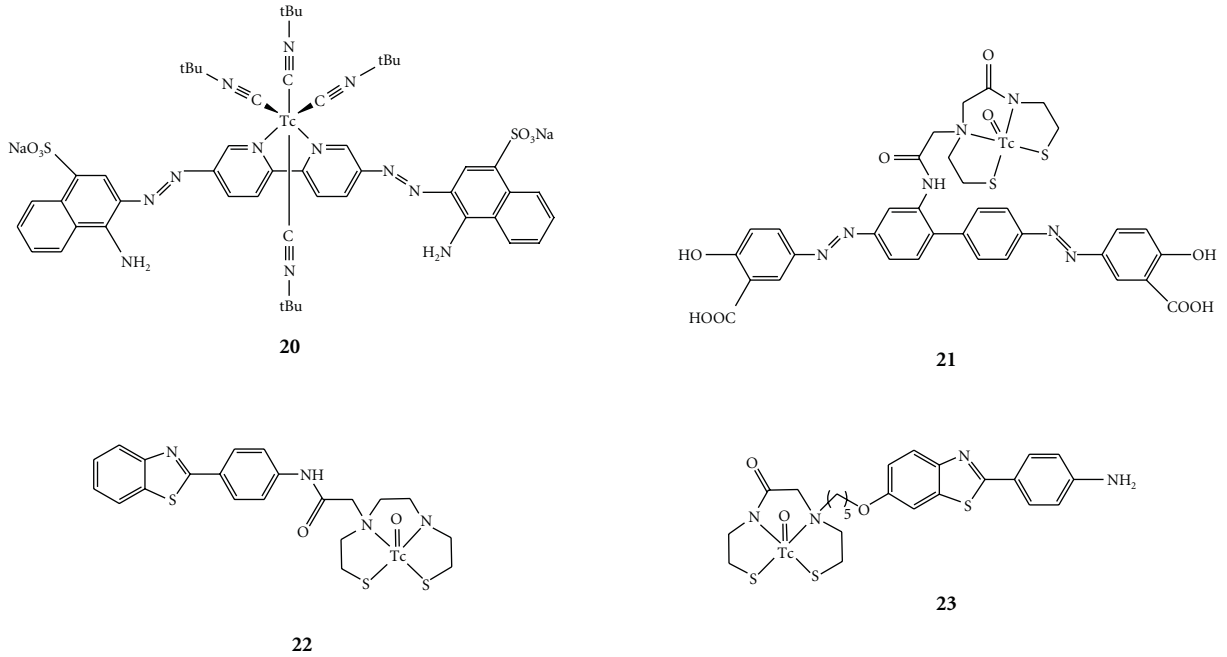

Figure 9: Chemical structure of ^{99m}Tc complexes for imaging of Aβ plaques.

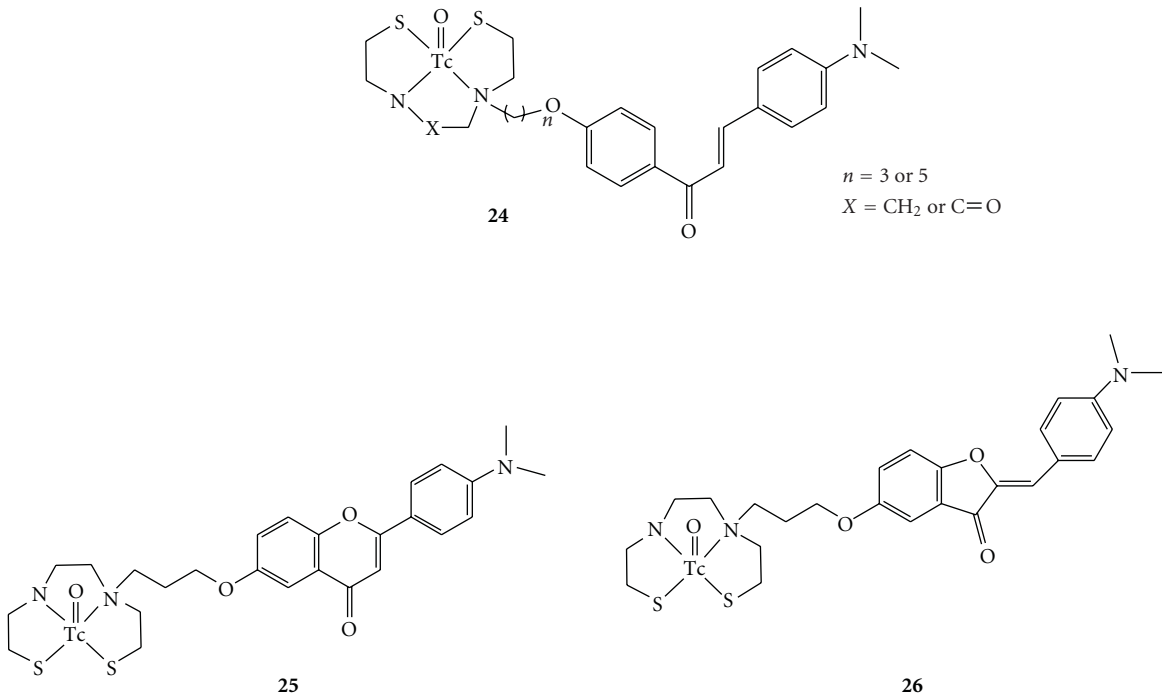

Figure 10: Chemical structure of ^{99m}Tc complexes based on chalcone (**24**), flavone (**25**), and aurone (**26**) for imaging of Aβ plaques.

effect of their structure–activity relationships on binding to Aβ aggregates and biodistribution *in vivo* using a compound with high affinity [42–45]. Currently, SPECT imaging agents based on chalcone and aurone are optimized.

Most of the Aβ imaging probes reported previously have two aromatic rings. Among them, 1,4-diphenyltriazole and 2,5-diphenylthiophene derivatives have triazole and thiophene between two benzene rings, respectively, and it has been shown that they have high-binding affinity for binding to Aβ aggregates despite the kinds of substituted groups [46, 47]. In an attempt to further develop novel ligands for the imaging of Aβ plaques in AD, we designed a series of 3,5-diphenyl-1,2,4-oxadiazole (**18**) [48, 49] and 2,4-diphenyl-1,3,5-oxadiazole (**19**) [49] derivatives (Figure 8). Although

Table 2: Biodistribution of radioactivity after intravenous injection of [^{125}I]**12**, [^{125}I]**13**, [^{125}I]**14**, and [^{125}I] **15** in normal mice[a]

Tissue	Time after injection (min)			
	2	10	30	60
		[^{125}I]**12**		
Blood	1.89 (0.28)	1.39 (0.10)	1.34 (0.07)	1.50 (0.09)
Liver	16.28 (0.90)	25.28 (0.31)	18.61 (1.81)	15.14 (0.89)
Kidney	8.13 (1.28)	5.21 (0.44)	3.85 (0.33)	3.05 (0.25)
Intestine	3.10 (0.61)	7.91 (1.05)	12.84 (1.18)	21.48 (3.17)
Spleen	2.57 (1.54)	2.31 (0.01)	1.76 (0.23)	1.52 (0.29)
Heart	4.87 (0.66)	2.66 (0.12)	1.67 (0.14)	1.28 (0.12)
Stomach[b]	0.78 (0.02)	0.87 (0.22)	1.44 (0.69)	1.80 (0.84)
Brain	4.12 (0.15)	3.68 (0.18)	1.84 (0.12)	1.19 (0.04)
		[^{125}I]**13**		
Blood	1.87 (0.18)	1.07 (0.08)	1.20 (0.15)	1.15 (0.16)
Liver	15.41 (0.98)	21.85 (2.14)	15.71 (0.96)	12.40 (2.38)
Kidney	8.33 (1.47)	4.31 (0.28)	3.40 (0.31)	2.32 (0.45)
Intestine	2.24 (0.24)	6.56 (0.83)	12.97 (1.15)	18.64 (2.05)
Spleen	2.72 (0.20)	1.92 (0.33)	1.58 (0.31)	1.18 (0.17)
Heart	5.63 (0.80)	2.47 (0.14)	1.69 (0.06)	1.07 (0.17)
Stomach[b]	0.73 (0.17)	0.63 (0.16)	1.17 (0.40)	1.06 (0.27)
Brain	3.22 (0.15)	3.61 (0.60)	1.89 (0.21)	0.99 (0.10)
		[^{125}I]**14**		
Blood	1.87 (0.21)	1.19 (0.17)	0.40 (0.01)	0.23 (0.09)
Liver	8.96 (1.48)	9.01 (0.97)	3.75 (0.47)	1.88 (0.61)
Kidney	7.99 (1.08)	6.30 (1.02)	4.51 (1.59)	1.46 (1.12)
Intestine	3.52 (0.29)	14.39 (0.80)	22.51 (1.11)	30.05 (3.61)
Spleen	2.70 (0.08)	1.38 (0.37)	0.55 (0.30)	3.67 (5.89)
Heart	4.98 (0.41)	2.25 (0.40)	0.84 (0.14)	0.47 (0.22)
Stomach[b]	0.68 (0.06)	0.45 (0.18)	0.55 (0.33)	0.31 (0.07)
Brain	4.00 (0.18)	2.36 (0.33)	0.51 (0.07)	0.17 (0.05)
		[^{125}I]**15**		
Blood	2.77 (0.43)	1.58 (0.18)	0.66 (0.03)	0.20 (0.02)
Liver	9.77 (1.89)	8.24 (0.50)	6.80 (0.86)	4.78 (1.09)
Kidney	14.79 (2.59)	15.11 (2.00)	6.45 (0.84)	1.66 (0.62)
Intestine	3.12 (0.37)	11.26 (0.63)	22.01 (1.34)	27.28 (0.48)
Spleen	3.92 (1.18)	1.55 (0.15)	0.56 (0.13)	0.17 (0.06)
Heart	5.51 (0.71)	1.60 (0.18)	0.53 (0.04)	0.12 (0.02)
Stomach[b]	0.89 (0.09)	0.59 (0.16)	1.56 (0.50)	0.81 (0.36)
Brain	3.31 (0.32)	1.90 (0.07)	0.52 (0.03)	0.08 (0.02)

[a]Expressed as % injected dose per gram. Each value represents the mean ± S.D. for 3–5 animals at each interval. [b]Expressed as % injected dose per organ.

the diphenyloxadiazole pharmacophore with high-binding affinity for Aβ aggregates may be useful as a backbone structure to develop novel Aβ imaging agents, additional modifications are necessary to improve the uptake and rapid clearance of nonspecifically bound radiotracers.

Many factors such as molecular size, ionic charge, and lipophilicity affect the brain uptake of compounds. Since lipophilicity of the compounds generally increases by introduction of iodine, the large higher lipophilicity of the radioiodinated compounds may constitute one reason for the low brain uptake. In the future, introduction of hydrophilic substituted groups into the amyloid-binding scaffolds will be required to develop more promising radioiodinated tracers with in favorable *in vivo* pharmacokinetics.

3. ^{99m}Tc Complexes for Imaging of Aβ Plaques

^{99m}Tc ($T_{1/2}$ = 6.01 h, 141 keV) has become the most commonly used radionuclide in diagnostics for SPECT, because it is readily produced by an ^{99}Mo/^{99m}Tc generator, the medium gamma-ray energy it emits is suitable for detection, and its physical half-life is compatible with the biological localization and residence time required for imaging. Its ready availability, essentially 24 h a day, and easiness

Table 3: Biodistribution of radioactivity after injection of ^{99m}Tc-labeled benzofuran derivatives in normal mice[a].

Organ	Time after injection (min)			
	2	10	30	60
		^{99m}Tc-BAT-BF (**27**)		
Blood	4.40 (0.27)	1.96 (0.06)	1.93 (0.26)	2.15 (0.91)
Liver	21.94 (5.94)	20.87 (1.28)	19.65 (1.31)	15.09 (3.83)
Kidney	10.28 (1.76)	7.90 (0.40)	4.27 (0.18)	2.70 (0.57)
Intestine[b]	1.45 (0.18)	3.68 (0.52)	7.42 (1.62)	9.02 (1.93)
Spleen	5.20 (1.01)	3.09 (0.23)	1.69 (0.21)	1.16 (0.14)
Lung	26.70 (2.27)	6.48 (1.33)	3.51 (0.64)	2.36 (0.48)
Stomach[b]	1.33 (0.57)	1.90 (0.43)	4.09 (1.37)	4.17 (1.92)
Pancreas	4.14 (0.77)	4.57 (0.24)	2.98 (0.38)	1.42 (0.15)
Heart	17.60 (2.60)	8.29 (0.97)	3.28 (1.35)	1.51 (0.25)
Brain	1.34 (0.12)	1.37 (0.18)	0.94 (0.20)	0.56 (0.07)
		^{99m}Tc-MAMA-BF (**28**)		
Blood	4.13 (0.42)	1.78 (0.25)	2.15 (0.12)	2.24 (0.24)
Liver	20.17 (3.81)	21.62 (2.62)	23.32 (1.59)	20.16 (2.13)
Kidney	7.37 (1.06)	8.09 (1.16)	5.11 (0.29)	3.28 (0.45)
Intestine[b]	0.95 (0.22)	2.13 (0.19)	4.75 (0.93)	5.73 (0.66)
Spleen	4.48 (0.56)	3.69 (0.34)	3.49 (0.61)	2.59 (0.65)
Lung	24.04 (5.17)	7.59 (2.13)	4.24 (0.35)	3.54 (1.26)
Stomach[b]	0.73 (0.21)	2.35 (0.58)	4.94 (0.57)	2.81 (0.51)
Pancreas	2.70 (0.47)	4.00 (1.28)	5.48 (0.61)	3.76 (0.36)
Heart	12.28 (2.20)	10.48 (1.79)	5.05 (0.90)	2.16 (0.34)
Brain	0.74 (0.15)	0.99 (0.22)	1.23 (0.09)	0.89 (0.08)

[a]Each value represents the mean (SD) for 5 mice. Expressed as % injected dose per gram. [b]Expressed as % injected dose per organ.

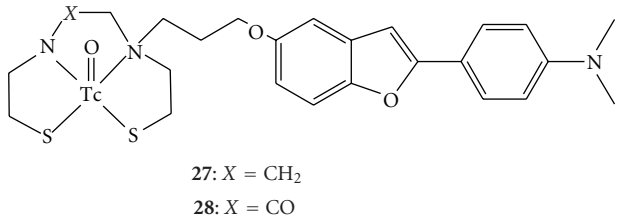

Figure 11: Chemical structure of ^{99m}Tc complexes based on the benzofuran scaffold for imaging of Aβ plaques.

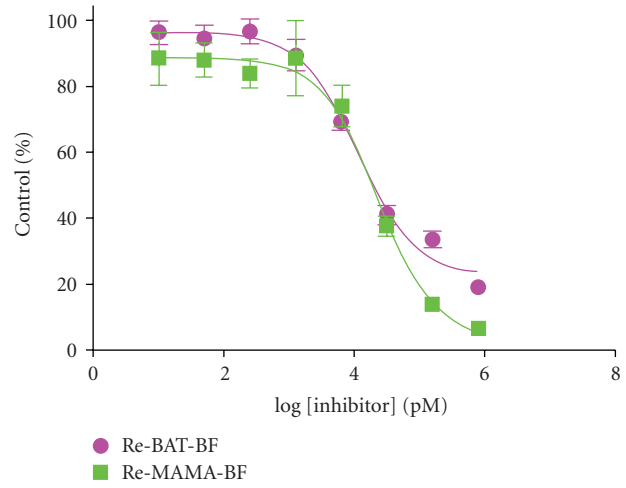

Figure 12: Inhibition curves of Re-BAT-BF and Re-MAMA-BF for the binding of [^{125}I]IMPY to Aβ(1–42) aggregates.

of use make it the radionuclide of choice. New ^{99m}Tc-labeled imaging agents will provide simple, convenient, and widespread SPECT-based methods for detecting and eventually quantifying Aβ plaques in living brain tissue.

Han and co-workers described a positively charged ^{99}Tc-complex of Congo red (**20**) which binds to Aβ aggregates *in vitro* [50]. The basic structure of this complex is the Congo red backbone in which the biphenyl moiety is replaced by a bipyridyl moiety capable of complexing Tc in the presence of *tert*-butylisonitrile as a coligand. Although these Tc complexes showed high affinity for Aβ aggregates in vitro, they have not been tested *in vivo*. Dezutter and co-workers reported a ^{99m}Tc-labeled conjugate of Congo Red with a monoamide-monoaminedithiol (MAMA) chelating ligand [51]. However, brain uptake of this ^{99m}Tc-labeled Congo Red derivative (**21**) was minimal, probably because of its large size and ionized character at physiological pH. Serdons and co-workers reported the synthesis of a neutral ^{99m}Tc-labeled derivative of thioflavin-T (**22**), namely a benzothiazole derivative conjugated with a bisamine-bisthiol (BAT) ligand, and its biological characterization [52]. It was demonstrated

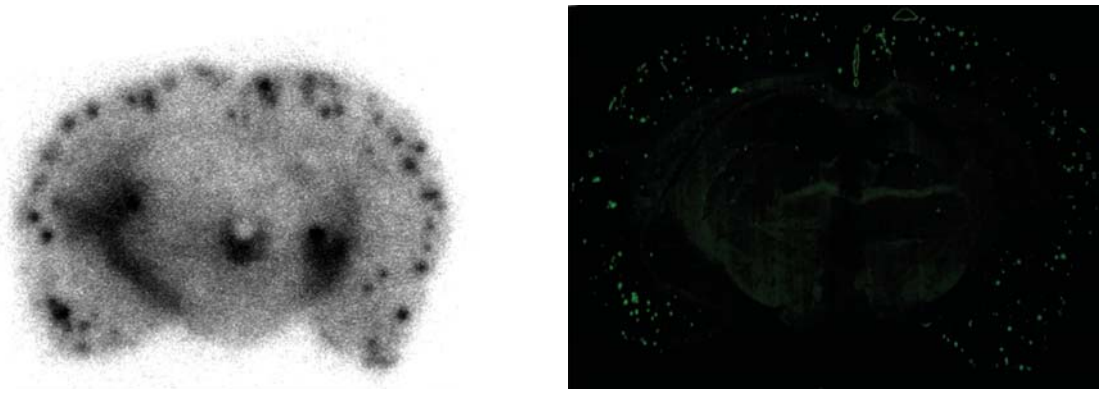

(a) (b)

Figure 13: Autoradiography of ^{99m}Tc-BAT-BF (**27**) in sections from Tg2576 mouse brain (a). Labeled plaques were confirmed by the staining of the adjacent sections with thioflavin S (b).

that the ^{99m}Tc-labeled thioflavin-T derivative binds *in vitro* to Aβ plaques. Despite its high lipophilicity and neutral character, the ^{99m}Tc complex did not cross the blood-brain barrier to a sufficient degree and thus is not useful for the detection of AD *in vivo*. Recently, Chen et al. reported that the ^{99m}Tc-labeled thioflavin T using MAMA as a chelation ligand (**23**) demonstrated the binding to Aβ aggregates in sections of brain tissue from transgenic mice and AD patients [53]. In addition, **23** can penetrate the blood-brain barrier with high initial brain uptake and moderate washout. These results are encouraging for further exploration of their derivatives as imaging agents for Aβ plaques in the brain.

As described above, several ^{99m}Tc-labeled imaging probes have been developed (Figure 9) [50–55], but no clinical study of them has been reported. While these ^{99m}Tc complexes showed high affinity for Aβ aggregates or Aβ plaques *in vitro*, they suffered the same unfavorable *in vivo* pharmacokinetics in normal mice, that is, a slow washout. Therefore, to make them promising probes for imaging Aβ plaques in the brain, additional molecular modifications to improve their pharmacokinetics *in vivo* are required.

Recently, we have developed several ^{99m}Tc complexes based on flavone, chalcone, aurone, and benzofuran derivatives with monoamine-monoamide dithiol (MAMA) and bis-amino-bis-thiol (BAT) as chelation ligands (Figures 10 and 11). MAMA and BAT were selected taking into consideration the permeability of the blood-brain barrier, because they form an electrically neutral complex with ^{99m}Tc [56]. We then evaluated their biological potential as probes by testing their affinity for Aβ aggregates and Aβ plaques in sections of brain tissue from Tg2576 mice and their uptake in and clearance from the brain in biodistribution experiments using normal mice.

Initially, four ^{99m}Tc-labeled chalcone derivatives and their corresponding rhenium analogues were tested as potential probes for imaging Aβ plaques (Figure 10) [57]. The chalcones showed higher affinity for Aβ(1–42) aggregates than did ^{99m}Tc complexes and, in sections of brain tissue from an animal model of AD, the four Re-chalcones intensely stained Aβ plaques. In biodistribution experiments using normal mice, ^{99m}Tc-BAT-chalcone (**24**) displayed high uptake in the brain (1.48%ID/g) at 2 min after injection. The radioactivity washed out from the brain rapidly (0.17%ID/g at 60 min), a highly desirable feature for an imaging agent. Although potential existence of *cis*- and *anti*-isomers was expected, one single isomer was isolated in the preparation of **24**, **25,** and **26**. The chemical identities of **24**, **25,** and **26** were confirmed by NMR and MS, but their absolute configurations have not yet been determined by X-ray crystallography.

As for ^{99m}Tc complexes based on benzofuran, we evaluated binding affinity using Re-BAT-BF and Re-MAMA-BF, analogs of ^{99m}Tc-BAT-BF (**27**) and ^{99m}Tc-MAMA-BF (**28**), respectively. Both ligands inhibited the binding of [^{125}I]IMPY to Aβ(1–42) aggregates in a dose-dependent manner, indicating an affinity for Aβ aggregates (Figure 12). Their K_i values were 11.5 and 24.4 nM, respectively, suggesting that Re-BAT-BF displayed higher affinity than Re-MAMA-BF. Next, the affinity of ^{99m}Tc-BAT-BF (**27**) for Aβ plaques was investigated *in vitro* using sections of Tg2576 mouse brain (Figure 13). Furthermore, the radioactivity of ^{99m}Tc-BAT-BF (**27**) corresponded with the areas of staining with thioflavin S, a dye commonly used for Aβ plaques. In contrast, normal mouse brain displayed no detectable accumulation of ^{99m}Tc-BAT-BF (**27**). The results suggest that ^{99m}Tc-BAT-BF (**27**) binds to Aβ plaques in the mouse brain in addition to synthetic Aβ aggregates.

The biodistribution of ^{99m}Tc-BAT-BF (**27**) and ^{99m}Tc-MAMA-BF (**28**) was examined in normal mice (Table 3). ^{99m}Tc-BAT-BF (**27**) showed greater uptake (1.34%ID/g) than ^{99m}Tc-MAMA-BF (**28**) (0.74%ID/g) at 2 min after injection. The uptake of ^{99m}Tc-BAT-BF (**27**) peaked at 10 min after injection, reaching 1.37%ID/g, sufficient uptake for Aβ imaging, and 60% of the radioactivity had been washed out from the brain by 60 min after injection. The uptake of ^{99m}Tc-MAMA-BF (**28**) peaked 30 min after the injection at 1.23%ID/g, and the washout from the brain was slower than that of ^{99m}Tc-BAT-BF (**27**) throughout the time course, which is unsuitable for imaging *in vivo*. The combination of good affinity for Aβ plaques, uptake,

and clearance makes ^{99m}Tc-BAT-BF (**27**) a promising probe for the detection of Aβ plaques in the brain. The results of the present study should provide useful information for the development of ^{99m}Tc-labeled probes for the imaging of Aβ plaques in the brain, although there are some difficulties associated with the large size of ^{99m}Tc complex in the molecular design of ^{99m}Tc-labeled Aβ imaging probes to enhance the penetration of blood-brain barrier.

4. Conclusion

Many PET probes targeting Aβ plaques in the brain have been tested clinically and demonstrated potential utility. Unfortunately, the short half-life (^{11}C; 20 min, ^{18}F; 110 min) of ^{11}C- or ^{18}F-labeled probes except ^{18}F-FDG limits their use at major academic PET facilities with on-site cyclotrons and sophisticated radiochemistry laboratories. On the other hand, many more hospitals have the capacity to perform SPECT. Aβ imaging probes labeled with SPECT isotopes especially the inexpensive and readily available ^{99m}Tc will have more widespread clinical applicability especially in developing countries that cannot afford expensive cyclotron and PET scanners. The development of novel ^{123}I- or ^{99m}Tc-labeled Aβ imaging probes may lead to simple and convenient SPECT imaging methods for detecting and eventually quantifying Aβ plaques in living brain tissue.

Acknowledgments

The results in this paper were partly obtained at Nagasaki University. They would like to express our sincere thanks to Professor Morio Nakayama for his helpful, continuous advice and support. The research reviewed in this paper was possible only through the dedication, enthusiasm, and creativity of all my coworkers, whose names are acknowledged in the publications from our laboratory cited here. These studies were supported by a Grant-in-aid for Young Scientists (A) and (B) from the Ministry of Education, Culture, Sports, Science and Technology, the Industrial Technology Research Grant Program from New Energy and Industrial Technology Development Organization (NEDO), the Program for Promotion of Fundamental Biomedical Innovation (NIBIO), and a Health Labour Sciences Research grant.

References

[1] D. J. Selkoe, "Alzheimer's disease: genes, proteins, and therapy," *Physiological Reviews*, vol. 81, no. 2, pp. 741–766, 2001.

[2] J. A. Hardy and G. A. Higgins, "Alzheimer's disease: the amyloid cascade hypothesis," *Science*, vol. 256, no. 5054, pp. 184–185, 1992.

[3] C. A. Mathis, Y. Wang, and W. E. Klunk, "Imaging β-amyloid plaques and neurofibrillary tangles in the aging human brain," *Current Pharmaceutical Design*, vol. 10, no. 13, pp. 1469–1492, 2004.

[4] A. Nordberg, "PET imaging of amyloid in Alzheimer's disease," *Lancet Neurology*, vol. 3, no. 9, pp. 519–527, 2004.

[5] M. Ono, "Development of positron-emission tomography/single-photon emission computed tomography imaging probes for in vivo detection of β-amyloid plaques in Alzheimer's brains," *Chemical and Pharmaceutical Bulletin*, vol. 57, no. 10, pp. 1029–1039, 2009.

[6] N. P. L. G. Verhoeff, A. A. Wilson, S. Takeshita et al., "In-vivo imaging of Alzheimer disease β-amyloid with [^{11}C]SB-13 PET," *American Journal of Geriatric Psychiatry*, vol. 12, no. 6, pp. 584–595, 2004.

[7] H. F. Kung, S. R. Choi, W. Qu, W. Zhang, and D. Skovronsky, "^{18}F stilbenes and styrylpyridines for PET imaging of Aβ plaques in Alzheimer's disease: a miniperspective," *Journal of Medicinal Chemistry*, vol. 53, no. 3, pp. 933–941, 2010.

[8] C. A. Mathis, Y. Wang, D. P. Holt, G. F. Huang, M. L. Debnath, and W. E. Klunk, "Synthesis and evaluation of ^{11}C-labeled 6-substituted 2-arylbenzothiazoles as amyloid imaging agents," *Journal of Medicinal Chemistry*, vol. 46, no. 13, pp. 2740–2754, 2003.

[9] W. E. Klunk, H. Engler, A. Nordberg et al., "Imaging brain amyloid in Alzheimer's disease with Pittsburgh Compound-B," *Annals of Neurology*, vol. 55, no. 3, pp. 306–319, 2004.

[10] N. M. Scheinin, S. Aalto, J. Koikkalainen et al., "Follow-up of [^{11}C]PIB uptake and brain volume in patients with alzheimer disease and controls," *Neurology*, vol. 73, no. 15, pp. 1186–1192, 2009.

[11] M. Ono, A. Wilson, J. Nobrega et al., "^{11}C-labeled stilbene derivatives as Aβ-aggregate-specific PET imaging agents for Alzheimer's disease," *Nuclear Medicine and Biology*, vol. 30, no. 6, pp. 565–571, 2003.

[12] Y. Kudo, N. Okamura, S. Furumoto et al., "2-(2-[2-dimethylaminothiazol-5-yl]ethenyl)-6-(2-[fluoro]ethoxy)benzoxazole: a novel PET agent for in vivo detection of dense amyloid plaques in Alzheimer's disease patients," *Journal of Nuclear Medicine*, vol. 48, no. 4, pp. 553–561, 2007.

[13] A. E. Johnson, F. Jeppsson, J. Sandell et al., "AZD2184: a radioligand for sensitive detection of β-amyloid deposits," *Journal of Neurochemistry*, vol. 108, no. 5, pp. 1177–1186, 2009.

[14] E. D. Agdeppa, V. Kepe, J. Liu et al., "Binding characteristics of radiofluorinated 6-dialkylamino-2-naphthylethylidene derivatives as positron emission tomography imaging probes for beta-amyloid plaques in Alzheimer's disease," *The Journal of Neuroscience*, vol. 21, no. 24, p. RC189, 2001.

[15] K. Shoghi-Jadid, G. W. Small, E. D. Agdeppa et al., "Localization of neurofibrillary tangles and beta-amyloid plaques in the brains of living patients with alzheimer disease," *American Journal of Geriatric Psychiatry*, vol. 10, no. 1, pp. 24–35, 2002.

[16] G. W. Small, V. Kepe, L. M. Ercoli et al., "PET of brain amyloid and tau in mild cognitive impairment," *New England Journal of Medicine*, vol. 355, no. 25, pp. 2652–2663, 2006.

[17] W. Zhang, S. Oya, M. P. Kung, C. Hou, D. L. Maier, and H. F. Kung, "F-18 Polyethyleneglycol stilbenes as PET imaging agents targeting Aβ aggregates in the brain," *Nuclear Medicine and Biology*, vol. 32, no. 8, pp. 799–809, 2005.

[18] C. C. Rowe, U. Ackerman, W. Browne et al., "Imaging of amyloid β in Alzheimer's disease with ^{18}F-BAY94-9172, a novel PET tracer: proof of mechanism," *The Lancet Neurology*, vol. 7, no. 2, pp. 129–135, 2008.

[19] W. Zhang, M. P. Kung, S. Oya, C. Hou, and H. F. Kung, "^{18}F-labeled styrylpyridines as PET agents for amyloid plaque imaging," *Nuclear Medicine and Biology*, vol. 34, no. 1, pp. 89–97, 2007.

[20] S. R. Choi, G. Golding, Z. Zhuang et al., "Preclinical properties of F-AV-45: a PET agent for Aβ plaques in the brain," *Journal of Nuclear Medicine*, vol. 50, no. 11, pp. 1887–1894, 2009.

[21] D. F. Wong, P. B. Rosenberg, Y. Zhou et al., "In vivo imaging of amyloid deposition in Alzheimer disease using the radioligand ^{18}F-AV-45 (flobetapir F 18)," *Journal of Nuclear Medicine*, vol. 51, no. 6, pp. 913–920, 2010.

[22] M. Koole, D. M. Lewis, C. Buckley et al., "Whole-body biodistribution and radiation dosimetry of ^{18}F-GE067: a radioligand for in vivo brain amyloid imaging," *Journal of Nuclear Medicine*, vol. 50, no. 5, pp. 818–822, 2009.

[23] M. Ono, M. Haratake, M. Nakayama et al., "Synthesis and biological evaluation of (*E*)-3-styrylpyridine derivatives as amyloid imaging agents for Alzheimer's disease," *Nuclear Medicine and Biology*, vol. 32, no. 4, pp. 329–335, 2005.

[24] W. Qu, M. P. Kung, C. Hou, T. E. Benedum, and H. F. Kung, "Novel styrylpyridines as probes for SPECT imaging of amyloid plaques," *Journal of Medicinal Chemistry*, vol. 50, no. 9, pp. 2157–2165, 2007.

[25] W. Qu, M. P. Kung, C. Hou, L. W. Jin, and H. F. Kung, "Radioiodinated aza-diphenylacetylenes as potential SPECT imaging agents for β-amyloid plaque detection," *Bioorganic and Medicinal Chemistry Letters*, vol. 17, no. 13, pp. 3581–3584, 2007.

[26] M. P. Kung, C. Hou, Z. P. Zhuang et al., "IMPY: an improved thioflavin-T derivative for in vivo labeling of β-amyloid plaques," *Brain Research*, vol. 956, no. 2, pp. 202–210, 2002.

[27] Z. P. Zhuang, M. P. Kung, A. Wilson et al., "Structure-activity relationship of imidazo[1,2-a]pyridines as ligands for detecting β-amyloid plaques in the brain," *Journal of Medicinal Chemistry*, vol. 46, no. 2, pp. 237–243, 2003.

[28] M. P. Kung, C. Hou, Z. P. Zhuang, D. Skovronsky, and H. F. Kung, "Binding of two potential imaging agents targeting amyloid plaques in postmortem brain tissues of patients with Alzheimer's disease," *Brain Research*, vol. 1025, no. 1-2, pp. 98–105, 2004.

[29] Z. P. Zhuang, M. P. Kung, C. Hou et al., "Radioiodinated styrylbenzenes and thioflavins as probes for amyloid aggregates," *Journal of Medicinal Chemistry*, vol. 44, no. 12, pp. 1905–1914, 2001.

[30] Z. P. Zhuang, M. P. Kung, C. Hou et al., "IBOX(2-(4′-dimethylaminophenyl)-6-iodobenzoxazole): a ligand for imaging amyloid plaques in the brain," *Nuclear Medicine and Biology*, vol. 28, no. 8, pp. 887–894, 2001.

[31] M. Ono, M. P. Kung, C. Hou, and H. F. Kung, "Benzofuran derivatives as Aβ-aggregate-specific imaging agents for Alzheimer's disease," *Nuclear Medicine and Biology*, vol. 29, no. 6, pp. 633–642, 2002.

[32] H. Watanabe, M. Ono, M. Haratake, N. Kobashi, H. Saji, and M. Nakayama, "Synthesis and characterization of novel phenylindoles as potential probes for imaging of β-amyloid plaques in the brain," *Bioorganic and Medicinal Chemistry*, vol. 18, no. 13, pp. 4740–4746, 2010.

[33] M. P. Kung, C. Hou, Z. P. Zhuang, A. J. Cross, D. L. Maier, and H. F. Kung, "Characterization of IMPY as a potential imaging agent for β-amyloid plaques in double transgenic PSAPP mice," *European Journal of Nuclear Medicine and Molecular Imaging*, vol. 31, no. 8, pp. 1136–1145, 2004.

[34] A. B. Newberg, N. A. Wintering, C. M. Clark et al., "Use of ^{123}I IMPY SPECT to differentiate Alzheimer's disease from controls," *The Journal of Nuclear Medicine*, vol. 47, supplement 1, p. 78P, 2006.

[35] A. B. Newberg, N. A. Wintering, K. Plössl et al., "Safety, biodistribution, and dosimetry of ^{123}I-IMPY: a novel amyloid plaque-imaging agent for the diagnosis of Alzheimer's disease," *Journal of Nuclear Medicine*, vol. 47, no. 5, pp. 748–754, 2006.

[36] K. Ono, Y. Yoshiike, A. Takashima, K. Hasegawa, H. Naiki, and M. Yamada, "Potent anti-amyloidogenic and fibril-destabilizing effects of polyphenols in vitro: implications for the prevention and therapeutics of Alzheimer's disease," *Journal of Neurochemistry*, vol. 87, no. 1, pp. 172–181, 2003.

[37] M. Ono, N. Yoshida, K. Ishibashi et al., "Radioiodinated flavones for in vivo imaging of β-amyloid plaques in the brain," *Journal of Medicinal Chemistry*, vol. 48, no. 23, pp. 7253–7260, 2005.

[38] T. Iwatsubo, A. Odaka, N. Suzuki, H. Mizusawa, N. Nukina, and Y. Ihara, "Visualization of Aβ42(43) and Aβ40 in senile plaques with end-specific Aβ monoclonals: evidence that an initially deposited species is Aβ42(43)," *Neuron*, vol. 13, no. 1, pp. 45–53, 1994.

[39] J. C. Morris, M. Storandt, D. W. McKeel et al., "Cerebral amyloid deposition and diffuse plaques in "normal" aging: evidence for presymptomatic and very mild Alzheimer's disease," *Neurology*, vol. 46, no. 3, pp. 707–719, 1996.

[40] H. F. Kung, C. W. Lee, Z. P. Zhuang, M. P. Kung, C. Hou, and K. Plössl, "Novel stilbenes as probes for amyloid plaques," *Journal of the American Chemical Society*, vol. 123, no. 50, pp. 12740–12741, 2001.

[41] M. Ono, M. Haratake, H. Mori, and M. Nakayama, "Novel chalcones as probes for in vivo imaging of β-amyloid plaques in Alzheimer's brains," *Bioorganic and Medicinal Chemistry*, vol. 15, no. 21, pp. 6802–6809, 2007.

[42] M. Ono, M. Hori, M. Haratake, T. Tomiyama, H. Mori, and M. Nakayama, "Structure-activity relationship of chalcones and related derivatives as ligands for detecting of β-amyloid plaques in the brain," *Bioorganic and Medicinal Chemistry*, vol. 15, no. 19, pp. 6388–6396, 2007.

[43] M. Ono, M. Haratake, H. Mori, and M. Nakayama, "Novel chalcones as probes for in vivo imaging of β-amyloid plaques in Alzheimer's brains," *Bioorganic and Medicinal Chemistry*, vol. 15, no. 21, pp. 6802–6809, 2007.

[44] M. Ono, Y. Maya, M. Haratake, K. Ito, H. Mori, and M. Nakayama, "Aurones serve as probes of β-amyloid plaques in Alzheimer's disease," *Biochemical and Biophysical Research Communications*, vol. 361, no. 1, pp. 116–121, 2007.

[45] Y. Maya, M. Ono, H. Watanabe, M. Haratake, H. Saji, and M. Nakayama, "Novel radioiodinated aurones as probes for SPECT imaging of β-amyloid plaques in the brain," *Bioconjugate Chemistry*, vol. 20, no. 1, pp. 95–101, 2009.

[46] W. Qu, M. P. Kung, C. Hou, S. Oya, and H. F. Kung, "Quick assembly of 1,4-diphenyltriazoles as probes targeting β-amyloid aggregates in Alzheimer's disease," *Journal of Medicinal Chemistry*, vol. 50, no. 14, pp. 3380–3387, 2007.

[47] R. Chandra, M. P. Kung, and H. F. Kung, "Design, synthesis, and structure-activity relationship of novel thiophene derivatives for β-amyloid plaque imaging," *Bioorganic and Medicinal Chemistry Letters*, vol. 16, no. 5, pp. 1350–1352, 2006.

[48] M. Ono, M. Haratake, H. Saji, and M. Nakayama, "Development of novel β-amyloid probes based on 3,5-diphenyl-1,2,4-oxadiazole," *Bioorganic and Medicinal Chemistry*, vol. 16, no. 14, pp. 6867–6872, 2008.

[49] H. Watanabe, M. Ono, R. Ikeoka, M. Haratake, H. Saji, and M. Nakayama, "Synthesis and biological evaluation of radioiodinated 2,5-diphenyl-1,3,4-oxadiazoles for detecting β-amyloid plaques in the brain," *Bioorganic and Medicinal Chemistry*, vol. 17, no. 17, pp. 6402–6406, 2009.

[50] H. Han, C. G. Cho, and P. T. Lansbury Jr., "Technetium complexes for the quantitation of brain amyloid," *Journal of the American Chemical Society*, vol. 118, no. 18, pp. 4506–4507, 1996.

[51] N. A. Dezutter, R. J. Dom, T. J. De Groot, G. M. Bormans, and A. M. Verbruggen, "^{99m}Tc-MAMA-chrysamine G, a probe for beta-amyloid protein of Alzheimer's disease," *European Journal of Nuclear Medicine*, vol. 26, no. 11, pp. 1392–1399, 1999.

[52] K. Serdons, T. Verduyckt, J. Cleynhens et al., "Synthesis and evaluation of a ^{99m}Tc-BAT-phenylbenzothiazole conjugate as a potential in vivo tracer for visualization of amyloid β," *Bioorganic and Medicinal Chemistry Letters*, vol. 17, no. 22, pp. 6086–6090, 2007.

[53] X. Chen, P. Yu, L. Zhang, and B. Liu, "Synthesis and biological evaluation of ^{99m}Tc, Re-monoamine-monoamide conjugated to 2-(4-aminophenyl)benzothiazole as potential probes for β-amyloid plaques in the brain," *Bioorganic and Medicinal Chemistry Letters*, vol. 18, no. 4, pp. 1442–1445, 2008.

[54] Z. P. Zhuang, M. P. Kung, C. Hou, K. Ploessl, and H. F. Kung, "Biphenyls labeled with technetium 99m for imaging β-amyloid plaques in the brain," *Nuclear Medicine and Biology*, vol. 32, no. 2, pp. 171–184, 2005.

[55] K. S. Lin, M. L. Debnath, C. A. Mathis, and W. E. Klunk, "Synthesis and β-amyloid binding properties of rhenium 2-phenylbenzothiazoles," *Bioorganic and Medicinal Chemistry Letters*, vol. 19, no. 8, pp. 2258–2262, 2009.

[56] S. Oya, K. Plössl, M. P. Kung, D. A. Stevenson, and H. F. Kung, "Small and neutral TC(V)O BAT, bisaminoethanethiol (NS) complexes for developing new brain imaging agents," *Nuclear Medicine and Biology*, vol. 25, no. 2, pp. 135–140, 1998.

[57] M. Ono, R. Ikeoka, H. Watanabe et al., "Synthesis and evaluation of novel chalcone derivatives with ^{99m}Tc/Re complexes as potential probes for detection of β-amyloid plaques," *ACS Chemical Neuroscience*, vol. 1, no. 9, pp. 598–607, 2010.

Hindawi Publishing Corporation
International Journal of Molecular Imaging
Volume 2011, Article ID 472375, 8 pages
doi:10.1155/2011/472375

Research Article

Comparison of ^{111}In Leakage from Labeled Endocardial and Epicardial Cells: Impact on Modeling Viability of Cells to Be Transplanted into Myocardium

Kimberley J. Blackwood,[1,2] Jane Sykes,[1] Lela Deans,[1] Gerald Wisenberg,[1,3] and Frank S. Prato[1,2]

[1] *Imaging Program, Lawson Health Research Institute, 268 Grosvenor Street, London, ON, Canada N6A 4V2*
[2] *Department of Medical Biophysics, University of Western Ontario, London, ON, Canada N6A 3K7*
[3] *Division of Cardiology, London Health Sciences Centre, London, ON, Canada N6A 5W9*

Correspondence should be addressed to Kimberley J. Blackwood, kblackwo@lawsonimaging.ca

Received 1 August 2010; Revised 18 November 2010; Accepted 9 February 2011

Academic Editor: Farouc Jaffer

Introduction. Previously we proposed a cellular imaging technique to determine the surviving fraction of transplanted cells in vivo. Epicardial kinetics using Indium-111 determined the Debris Impulse Response Function (DIRF) and leakage coefficient parameters. Convolution-based modeling which corrected for these signal contributions indicated that ^{111}In activity was quantitative of cell viability with half-lives within 20 hrs to 37 days. We determine if the 37-day upper limit remains valid for endocardial injections by comparing previous epicardial cell leakage parameter estimates to those for endocardial cells. *Methods*. Normal canine myocardium was injected (^{111}In-tropolone) epicardially (9 injections) or endocardially (10 injections). Continuous whole body and SPECT scans for 5 hours were acquired with three weekly follow-up imaging sessions up to 20–26 days. Time-activity curves evaluated each injection type. *Results*. The epicardial and endocardial kinetics were not significantly different (Epi: 1286 ± 253; Endo: 1567 ± 470 hours $P = .62$). *Conclusion*. The original epicardial estimate of leakage kinetics has been validated for use in endocardial injections.

1. Introduction

Apart from the long-term impact stem cells can have on the myocardium of the infarcted heart [1–3], progression in stem cell imaging requires an understanding of viability and function of the transplanted cells soon after transplantation. Some of the advancements in preclinical imaging technologies, namely, reporter gene imaging, to interrogate the status of transplanted cells [4, 5] cannot be currently applied clinically due to safety concerns related to injecting cells with foreign DNA. However, to this end, our group has reported on a SPECT cellular imaging technique using a clinically available radiotracer to determine the viability of transplanted cells as a function of time in a large animal model of acute myocardial infarction [6].

The basis of this technique is the radiotracer Indium-111 and its associated clearance kinetics in canine myocardium under different conditions. ^{111}In (chelated with oxine, tropolone, etc. for in vitro cell labeling) is an FDA approved radiotracer [7] and is used in clinical infection imaging where white blood cells are radiolabeled ex vivo using the chelator, and reinjected cells localize to sites of infection and/or inflammation [8]. For the use of this tracer for imaging transplanted cells, in vivo acquired parameters called the leakage coefficient (C) and DIRF (Debris Impulse Response Function) are obtained to estimate the clearance half-lives of transplanted cells that can be measured from the SPECT signal. Using a convolution-based method, both parameters are used to derive the SPECT signal associated with viable

cells only and constitute the upper (leakage coefficient) and lower (DIRF) bounds within which this method of estimating viable transplanted cell half-life is valid. While DIRF reflects the function by which ^{111}In-labeled cytosolic proteins are cleared from the interstitial compartment of the myocardium (normal and infarcted) for example, cell death, an assumption in this method is that all interstitial ^{111}In is removed according to DIRF regardless of the mechanism by which it enters this compartment. Similarly, C reflects the rate of ^{111}In loss from radiolabeled cells into the interstitium as a result of cellular processes unrelated to cell death, which according to the aforementioned assumption, is then cleared from the myocardium according to DIRF. These upper and lower bounds then stipulate that if clearance half-lives of transplanted ^{111}In-labeled cells are faster or slower than DIRF or C, respectively, the model cannot be applied to derive the transplanted cell half-life.

Further in vitro work established the stability of ^{111}In in the cell population of interest and the inability of ^{111}In released from dead or viable cells to be resequestered by other cells modeling the surrounding myocardium. In vivo imaging with ^{111}In established a correction curve whereby the measured SPECT signal from labeled cells transplanted into the myocardium could be used to estimate and remove ^{111}In located outside viable cells generating a new biological half-life associated with viable cells. Finally, our group proposed a patient imaging protocol for clinical application of this technique [6].

Given that cell number at targeted locations can correlate with therapeutic benefit [9, 10], direct intramyocardial injections of cells have shown higher relative retention [11] and is likely the preferred method for larger cells. For example, mesenchymal cells can plug capillaries when administered via the intracoronary route [12] resulting in microinfarction in canines [13]. Our cellular imaging method was tested using the stromal fraction of adult canine bone marrow administered through epicardial injection, which is surgically invasive and not likely to be used in routine clinical practice. As an alternative approach, however, endocardial catheter transplantation of cells would be a better solution for clinical cell transplantation and provides the option of multiple transplants over time. Importantly, differences in perfusion and intramyocardial pressures between the subepicardium and subendocardium in canine myocardium lead to transmural gradients [14, 15]. Retention of injected material may be influenced by the cyclical beat-to-beat changes in intramyocardial pressures with resultant loss of the injected material through needle tracks [16]. Reducing this significant initial loss will be instrumental in improving cell retention. Hence the forces that influence cell loss for an epicardial injection, in theory, would be different than those affecting an epicardial injection thus affecting clearance kinetics.

The aim of this paper is to validate that the model leakage parameter for endocardial injections is similar to epicardial injections and comparatively evaluate the efficiency of the endocardial injection. This would allow wider application of the developed model as endocardial injections, from a clinical perspective, are much more likely to be used.

2. Materials and Methods

2.1. Intramyocardial Injections. Canine studies were approved by the Animal Use Subcommittee at the University of Western Ontario. A total of 19 separate injections of ^{111}In-tropolone were administered into normal left ventricular myocardium of 12 healthy female canines (18–25 kg). Seven of 12 canines had 2 injections of ^{111}In-tropolone with at least 2 weeks separating the last imaging session of the first injection and the first imaging session or the second injection which ensured that at least 10 half-lives had passed prior to the second injection.

In the endocardial group, ^{111}In-tropolone (mean ± SD: 50.8 ± 12.3 MBq; 10 injections) was injected into the anteroapical wall of the endocardium. In preparation for injection, canines were induced with propofol followed by endotracheal intubation and mechanical ventilation and anesthesia was maintained with isoflurane (1.5–2%). Endocardial injections were performed using the Stiletto Endomyocardial Injection System (Boston Scientific, Natick, MA) and the procedure is described elsewhere [17]. Using a 1 ml syringe containing ^{111}In-tropolone (995 ul) and 0.5% India ink tissue dye to identify injection sites, 8–10 injections of ~0.1 ml each were delivered to the endocardium using the catheter (26-gauge needle). Each site of injection was recorded on transparencies. Following each injection, the needle and Stiletto catheter were retracted and advanced into another position, generally within 8–10 mm of the other injections. Within 30–40 minutes of the first injection, canines were transported to the SPECT suite.

In the epicardial group, ^{111}In-tropolone (52.1 ± 21.8 MBq; 9 injections; 25-gauge needle) was injected into the anteroapical wall. Following anesthesia as described above, a left thoracotomy was performed between the 3rd and 4th ribs exposing the surface of the heart. Several (6–10) intramyocardial injections were then performed with a syringe with a 25-gauge needle containing 1 ml of ^{111}In-tropolone (including dye). Within 30 minutes of the injections, the thoracotomy incision was closed and the animal was transferred to the SPECT suite for imaging. Vital signs including heart rate were monitored throughout the injection and imaging sessions. At the final imaging session, animals were sacrificed using a bolus of KCl solution.

2.2. SPECT Acquisition and Analysis. On anesthetized canines, serial SPECT and wholebody images were acquired over the first 5 hours on injection day using a dual-head Millennium MG (General Electric, Milwaukee, WI) and a Symbia T6 SPECT/CT (Siemens, Erlangen, Germany) equipped with medium energy parallel hole collimators. Three subsequent SPECT follow-up imaging sessions were performed weekly over the following 3-4 weeks after the initial injection. Imaging parameters were as follows: 128 × 128 with 64 projections/head acquired over 180 degrees. Indium-111 counts were acquired with energy windows at 171 keV and 245 keV (±10%) for the GE system and 172 keV and 247 keV (±7.5%) for the Siemens system, and the acquisition time/projection angle increased from 30 seconds/projection on injection day to 30, 60, and 120 or

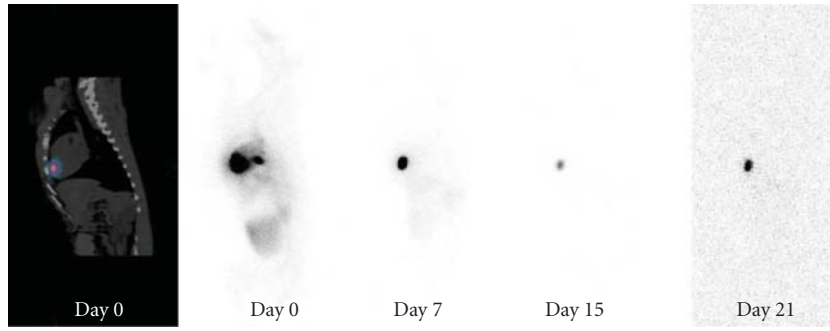

Figure 1: Images of ^{111}In following epicardial delivery into normal myocardium following left thoracotomy. (Left) Sagittal SPECT/CT slice showing site of ^{111}In injection in the myocardium. (Right) Wholebody ^{111}In scans of canine demonstrating ^{111}In activity at the injection site (day 0–15 wholebody scans are scaled to a maximum pixel value).

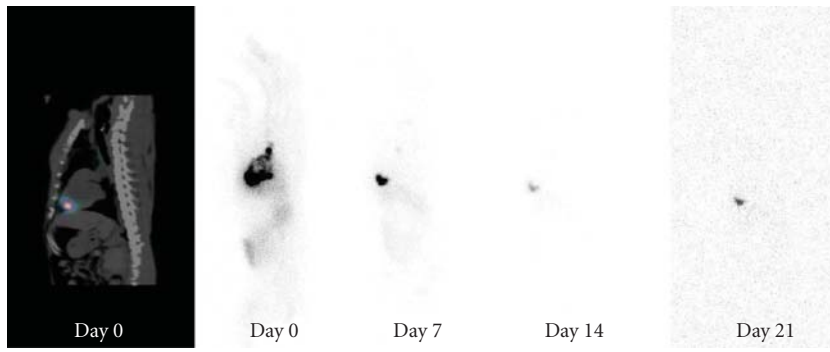

Figure 2: Images of ^{111}In following endocardial delivery into normal myocardium with a specialized catheter under fluoroscopic guidance. (Left) Sagittal slice of SPECT/CT image localizing ^{111}In injection within the myocardium on day of injection. (Right) Wholebody scans of same canine days 0, 7, 14, and 21 showing ^{111}In within the myocardium (day 0–14 wholebody scans are scaled to a maximum pixel value).

180 seconds/projection at 3 different followup time-points, respectively. Wholebody 2D images were alternately collected with SPECT on injection day using the same energy windows including one wholebody scan at each imaging follow-up. Wholebody imaging parameters: 256 × 1024 pixel matrix with 2.26 mm/pixel, fixed acquisition time of 23 minutes for the Millenium camera and 17 minutes for the Symbia (2.34 mm/pixel), and the same ^{111}In energy windows as SPECT were used.

Volume of interest (VOI) analysis was conducted on SPECT images that were corrected for background and subsequently reconstructed using an iterative algorithm [18]. The first SPECT data set acquired ($t = 0$) had a VOI defined as pixels ≥30% of the maximum pixel intensity and was used to create a mask image. This mask was then multiplied by each SPECT image acquired and the mean pixel intensity was determined (MATLAB, Mathworks, Natick, MA) [6]. Time activity curves (TAC) were generated for each injection and corrected for physical decay. Biexponential functions were fit to the TACs to determine the short ($T^s_{1/2}$) and long ($T^l_{1/2}$) components of ^{111}In clearance from injected myocardium. Curve coefficients were also normalized to determine the fraction of the injected activity that cleared with the $T^s_{1/2}$ or $T^l_{1/2}$ and were reported as percentages. Heart to whole body (H : WB) activity ratios were also calculated from region of interest (ROI) analysis of wholebody scans using GE software (Xeleris, General Electric, Milwaukee, WI). Regions of similar area were drawn on wholebody images and counts derived from these regions were background corrected and normalized to the total image counts. These ratios were used for comparison between canines regarding the degree of radiolabel retention and are reported as a percentage.

For the leakage parameter, $T^l_{1/2}$ data from our published report, which was similarly acquired, was compared to epicardial injections in this dataset and the combined epicardial data was compared to the endocardial data to determine if they were significantly different.

2.3. Statistical Analysis. All statistical analysis was performed using SPSS 18.0 (SPSS Inc., Chicago, IL) with α set to 0.05. Non-parametric analysis was used to assess differences in the heart:wholebody ratios and $T^s_{1/2}$ and $T^l_{1/2}$ measurements using an independent samples test, and multiple pairwise comparisons were corrected using Bonferroni correction. All data are reported as the mean ± SEM.

3. Results

3.1. Evaluating Injection Efficiency in Canine Myocardium. The myocardial retention of ^{111}In-tropolone following injection into canine myocardium was determined from serially

acquired wholebody images, and ratios of heart to wholebody (H : WB) activity were calculated. Ratios (expressed as a percentage) were similar with the Epi group and Endo group having H:WB ratios of 48 ± 5% and 50 ± 4% ($P = .902$) respectively, directly following injection, indicating that the endocardial injection was as effective in tracer delivery as the epicardial injection within the specified time window of 30–40 min postinjection. Table 1 shows the change in ratios for each animal for the first 5 hours following injection. Wholebody images from representative canines acquired after injection (Day 0 to 3 weeks) show the localization of ^{111}In within the myocardial tissue as confirmed by SPECT/CT following epicardial (Figure 1) and endocardial (Figure 2) injection. Images also show the biodistribution of ^{111}In within the liver, kidneys, and bladder. One animal in each of the groups had a lower ratio likely due to some injections into the left ventricular cavity rather than myocardium.

3.2. Early and Late Retention of Myocardial ^{111}In: Viable Cell Leakage. Serial SPECT imaging on the day of injection followed by images acquired weekly over the subsequent 20–26 days helped to better define the early washout phase occurring immediately after the injections and the longer term retention of ^{111}In within myocardial tissue. Biological half-lives generated from ROI analysis and fit with biexponential curves demonstrated $T^s_{1/2}$ and $T^l_{1/2}$ to be 2.17 ± 0.42 hours and 1567.07 ± 470.25 hours, respectively, for the endocardial group and 1.77±0.25 hours and 1286.09±253.02 hours for the epicardial group. Statistical analysis identified that there were no significant differences found when the $T^s_{1/2}$ ($P = .594$) and $T^l_{1/2}$ ($P = 1.00$) were compared between groups. The original, previously reported epicardial estimate of radiolabel leakage from viable cells was not significantly different from additional epicardial experiments (882.7 ± 242.8 (see [6]) hrs versus 1608.8 ± 369.5 hrs; $P = .166$).

Curve fitting parameters are given in Table 2 and TACs are shown in Figure 3 for all canines. A significant difference was found between the long and short components for both endocardial group ($P < .001$) and epicardial group ($P < .001$). Of the epicardially injected activity that remained in the myocardium following the first SPECT acquisition approximately 40 minutes after the injection, on average 28% cleared the myocardium with the short half-life while the remaining 72% cleared with the longer half-life. Of the endocardial injections, 38% of the activity cleared the myocardium with the short half-life while 62% cleared with the long half-life thus indicating that the majority of the label injected was retained within the myocardial cells. Figure 4 confirms SPECT images, and demonstrates myocardial tissue injection location as marked by tissue dye.

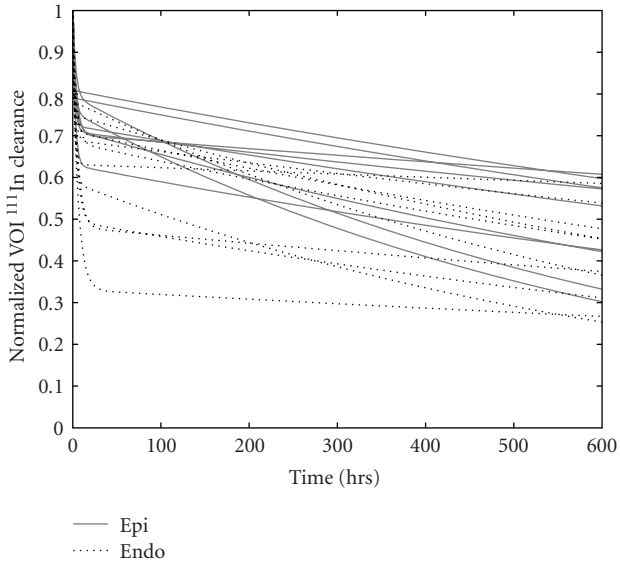

Figure 3: SPECT time-activity curves of ^{111}In clearance from canine myocardium. Canines were directly injected with ^{111}In-tropolone either by endocardial route via catheter (dotted lines) or epicardial route following thoracotomy (solid lines). Canines were serially imaged with SPECT on transplantation day with three follow-up imaging sessions. Region of interest analysis was conducted on images corrected for physical decay and background and fit to bi-exponential curves.

4. Discussion

Nonspecific imaging markers used for noninvasive cell tracking have their own perils. As outlined by Bengel et al. [19], clinical techniques typically used in understanding cell biodistribution over the short term prove difficulty over the longterm (i.e., weeks) as such markers can be susceptible to instability in the transplanted cell population or re-uptake of interstitial label into the surrounding tissue or even other transplanted cells making quantification more difficult. Label re-uptake has been demonstrated with iron oxide labels [20, 21] in stem cell transplantation studies, while other studies indicate SPECT radiolabels like ^{99m}Tc-HMPAO [22] and PET tracers ^{18}F-FDG [23] and ^{64}Cu-PTSM [24] efflux rapidly from various populations of viable cells.

In our previous work, we characterized the main sources of radiolabel loss from canine bone marrow stromal cells labeled with ^{111}In-tropolone both in vitro and following injection through the epicardium. We identified transplanted cell death and radiolabel leakage from viable transplanted cells as main contributors and used their associated ^{111}In clearance kinetics ($T^l_{1/2}$) for modeling the use of ^{111}In as an in vivo marker of viability. For the determination of radiolabel leakage in vivo, we injected free ^{111}In-tropolone in situ and monitored ^{111}In clearance kinetics from endogenous normal myocardial cells as was done in the experiments reported here. Zhou et al. state that observed radioactivity cannot be translated to the number of surviving cells as ^{111}In label released from dead cells may remain with the cell [25]. However, our model uses convolution as a means to correct for interstitial label related to death and leakage, and issues related to interstitial label are tenuous as we have verified that the clearance activity from dead cells is short relative to activity loss from viable cells with the average viable cell biological clearance ~79 times longer than that for dead cell clearance, or DIRF. To be clear, our model that incorporates

Table 1: Heart to wholebody ratios of ^{111}In postinjection (ratios expressed as %).

					EPI (%)					
Dog	1	2	3	4	5	6	7	8	9	
0 hrs	31.8	19.4	45.3*	49.2	62.6	56.4	59.7	57.8	49.5	
⋮	29.4	18.3	—	47.6	60.5	53.6	56.9		45.1	
⋮			—	46.8			55.0	54.1	42.9	
⋮	27.9	17.4	—	46.3	59.2	52.5	54.2			
⋮			—	46.2	57.2			51.4	41.0	
5 hrs	26.3	17.1	—	45.5	56.4	51.2	52.5	49.3	39.4	
					ENDO (%)					
Dog	1	2	3	4	5	6	7	8	9	10
0 hrs	22.8	42.9	45.5	44.0	54.1	62.5	60.0	49.2	59.8	57.6
⋮	23.9	40.8	43.2	42.3	52.0	60.3	56.1	47.6	54.4	54.8
⋮	21.3	39.0	40.6	40.9	50.1	59.5	54.0	44.7	50.5	52.5
⋮	20.6	37.9	38.9		48.5	58.4	52.3	43.0	47.2	50.2
⋮	19.9	36.9	37.5	40.1	47.7	57.6	51.4	41.6	44.5	48.4
5 hrs	19.1	36.3	36.8	39.4	46.7	—	—	—	—	—

* Serial wholebody scans not acquired at day 0.
All data acquired over a 5 hr period following injection.

Table 2: Exponential curve fitting parameters.

			$f(t) = a \cdot \exp^{(-bt)} + c \cdot \exp^{(-dt)}$			
			EPI			
Dog	$a^{\dagger}$	b	$c^{\ddagger}$	d	$T^{s}_{1/2}$ (hrs)	$T^{l}_{1/2}$ (hrs)
1	37.9	−0.3712	62.1	−0.0012930	1.87	537
2	16.0	−0.4705	84.0	−0.0017590	1.47	394
3	—	—	100	−0.0005308	—	1306
4	19.8	−1.004	80.2	−0.0005354	0.69	1295
5	29.2	−0.291	70.8	−0.0003566	2.38	1944
6	29.6	−0.2413	70.4	−0.0002413	2.87	2873
7	29.4	−0.4448	70.6	−0.0008787	1.56	789
8	28.2	−0.4850	71.8	−0.0005060	1.43	1370
9	36.6	−0.3662	63.4	−0.0006483	1.89	1069
			71.8 ± 2.6		1.77 ± 0.25	1286 ± 253
			ENDO			
1	40.7	−0.3407	59.3	−0.0013530	2.03	512
2	31.5	−0.2468	68.5	−0.0006903	2.81	1004
3	21.8	−2.7770	78.2	−0.0012670	0.25	547
4	29.7	−0.3896	70.3	−0.0006643	1.78	1043
5	33.1	−0.4293	66.9	−0.0004125	1.61	1680
6	49.9	−0.2316	50.1	−0.0007734	2.99	896
7	25.0	−1.1510	75.0	−0.000840	0.60	825
8	37.6	−0.4884	62.4	−0.0001245	1.42	5567
9	63.0	−0.1564	37.0	−0.0003590	4.43	1931
10	51.3	−0.1858	48.7	−0.0004166	3.73	1664
			61.6 ± 4.1		2.17 ± 0.42	1567 ± 470

† Coefficients "a" and "c" normalized to 100%.
‡ Dog 3 normalized data not included in fractional washout averages.

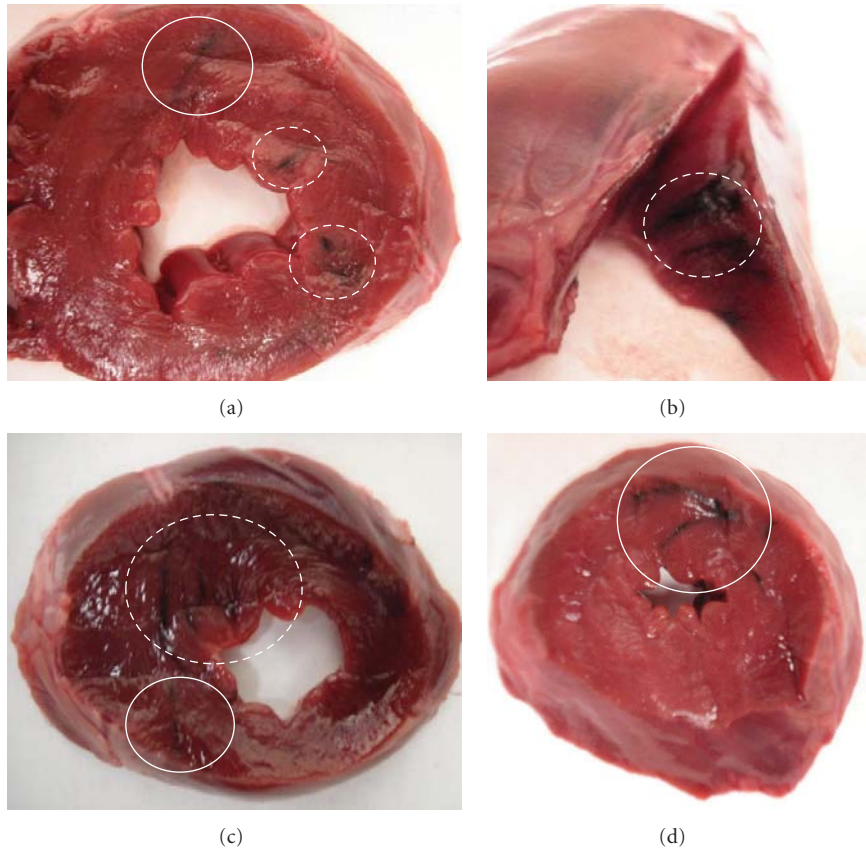

Figure 4: Digital images of ex vivo myocardial tissue confirming endocardial (dotted line circles) and epicardial (solid line circles) injections with tissue dye in normal tissue of representative canines. As noted during gross examination of the heart, needle punctures identified epicardial injection within the region of the left anterior descending coronary artery while endocardial injections were placed closer to the apex.

these corrections for clearance of cellular debris and leakage from viable cells indicates that ^{111}In can be used to quantitate cell half-life between 20 hrs and 60 days with the error in the measurements increasing as the upper and lower bounds are approached. In vitro work also indicated that dead cell activity or leaked activity is not taken up by either remaining viable transplanted cells or resident cardiomyocytes [6]. Additionally, our imaging protocol includes wholebody imaging to estimate the remaining absolute fraction of the injected dose in myocardium (H : WB ratio) and the observed $T^{l}_{1/2}$ estimates the biological half-life associated with viable transplanted cells. Numbers associated with the surviving fraction as a function of time can then be estimated providing the minimum cell number remaining, as our method cannot account for cells that proliferate subsequent to transplantation. Future work is needed to examine the robustness of this noninvasive approach to transplanted cell viability.

In this paper, we have further evaluated the use of the transendocardial injection technique using ^{111}In-tropolone. Specifically, we have shown that the injection efficiency and retention characteristics of ^{111}In-tropolone injected within normal canine myocardium are independent of the site of injection (i.e., subepicardium versus subendocardium). This is evident in the ^{111}In clearance patterns reflected by $T^{s}_{1/2}$ and $T^{l}_{1/2}$. In the development of our technique for modeling ^{111}In as an in vivo marker of transplanted cell viability, comparisons were necessary to demonstrate that differences in ^{111}In leakage from myocardium were not injection-site dependent. Furthermore, we wanted to ensure that intrinsic differences between myocardial layers did not significantly affect $T^{s}_{1/2}$ which represents the mechanical loss associated with intramyocardial injection. Based on these results, it is expected that retention of endocardially injected cells may not be significantly different from those injected epicardially.

Transmural heterogeneity across the left ventricular heart wall has been extensively studied in the canine heart and may have implications for cell survival and retention. During ischemic injury, a well-observed phenomenon is the greater susceptibility of the subendocardium [26] which may be linked to higher oxygen demand within this myocardial layer [27] making it more vulnerable. Cell transplantation within peri-infarcted subendocardium with compromised flow may risk cell survival, and different flow patterns may themselves be a factor influencing cell clearance. Transmural intramyocardial pressure and perfusion gradients suggest higher contractility within the subendocardium with poorer perfusion [15] relative to the subepicardium in the canine

[14, 27, 28] which could affect retention. Lower pressures in the LV cavity relative to the subendocardium [14] may also result in problems with retention of injected material allowing more material to leak into the cavity and redistribute cells to other organs. Optimization of transendocardial delivery suggest that parameters like needle length and injection volume can improve retention of various injectable materials [29, 30]. Irrespective of transmural differences, our data does not suggest differences in the leakage parameter between the subendocardial and subepicardial layers. Additional work with ^{111}In labeled cells also support insignificant differences in retention and clearance kinetics in infarcted canine myocardium [17], but future work would also need to verify that similar clearance patterns exist for cellular debris between layers.

The radiotoxic effect of ^{111}In for the purposes of tracking labeled cells has been previously addressed [31]. Reports indicate that the labeling mechanism of ^{111}In is that it binds to cytosolic proteins having little direct contact with the nucleus [32]. In our study, large doses of ^{111}In were injected into normal myocardium; however, radiotoxicity was not expected to be a primary concern considering the postmitotic nature of the adult canine myocardium. Previous work also evaluated the potential of fibrosis as a result of ^{111}In radiotoxicity using delayed enhancement MRI following Gd-DTPA administration which was not positive [6].

In summary, we have confirmed the leakage component of our model demonstrating ^{111}In retention in viable endocardial cells in vivo. The leakage gives the model an upper half-life limit of approximately 60 days. Efficiency of injections into the epicardium or endocardium is similar and physiological differences between myocardial layers do not factor into the kinetics of radiotracer clearance supporting the application of the model following endocardial transplantation.

Acknowledgments

The authors would like to thank Jill McCormick and Eric Sabondjian for technical assistance. Support for this work was from Canadian Institutes of Health Research (CIHR), CIHR Vascular Training Program, Ontario Research and Development Challenge Fund, Heart and Stroke Foundation, and Ontario Graduate Scholarship in Science and Technology. They also acknowledge support from Boston Scientific for providing the Stiletto endocardial catheters.

References

[1] S. L. Beeres, F. M. Bengel, J. Bartunek et al., "Role of imaging in cardiac stem cell therapy," *Journal of the American College of Cardiology*, vol. 49, no. 11, pp. 1137–1148, 2007.

[2] K. C. Wollert and H. Drexler, "Cell therapy for the treatment of coronary heart disease: a critical appraisal," *Nature Reviews Cardiology*, vol. 7, no. 4, pp. 204–215, 2010.

[3] M. Jiang, B. He, Q. Zhang et al., "Randomized controlled trials on the therapeutic effects of adult progenitor cells for myocardial infarction: meta-analysis," *Expert Opinion on Biological Therapy*, vol. 10, no. 5, pp. 667–680, 2010.

[4] F. Cao, S. Lin, X. Xie et al., "In vivo visualization of embryonic stem cell survival, proliferation, and migration after cardiac delivery," *Circulation*, vol. 113, no. 7, pp. 1005–1014, 2006.

[5] T. Higuchi, M. Anton, K. Dumler et al., "Combined reporter gene PET and iron oxide MRI for monitoring survival and localization of transplanted cells in the rat heart," *Journal of Nuclear Medicine*, vol. 50, no. 7, pp. 1088–1094, 2009.

[6] K. J. Blackwood, B. Lewden, R. G. Wells et al., "In vivo SPECT quantification of transplanted cell survival after engraftment using ^{111}In-tropolone in infarcted canine myocardium," *Journal of Nuclear Medicine*, vol. 50, no. 6, pp. 927–935, 2009.

[7] M. A. Green and J. C. Huffman, "The molecular structure of indium oxine," *Journal of Nuclear Medicine*, vol. 29, no. 3, pp. 417–420, 1988.

[8] A. M. Peters, S. H. Saverymuttu, and H. J. Reavy, "Imaging of inflammation with indium-111 tropolonate labeled leukocytes," *Journal of Nuclear Medicine*, vol. 24, no. 1, pp. 39–44, 1983.

[9] H. Iwasaki, A. Kawamoto, M. Ishikawa et al., "Dose-dependent contribution of CD34-positive cell transplantation to concurrent vasculogenesis and cardiomyogenesis for functional regenerative recovery after myocardial infarction," *Circulation*, vol. 113, no. 10, pp. 1311–1325, 2006.

[10] J. M. Hare, J. H. Traverse, T. D. Henry et al., "A Randomized, double-blind, placebo-controlled, dose-escalation study of intravenous adult human mesenchymal stem cells (prochymal) after acute myocardial infarction," *Journal of the American College of Cardiology*, vol. 54, no. 24, pp. 2277–2286, 2009.

[11] D. Hou, E. A. S. Youssef, T. J. Brinton et al., "Radiolabeled cell distribution after intramyocardial, intracoronary, and interstitial retrograde coronary venous delivery: implications for current clinical trials," *Circulation*, vol. 112, no. 9, supplement, pp. I150–I156, 2005.

[12] E. C. Perin and J. López, "Methods of stem cell delivery in cardiac diseases," *Nature Clinical Practice Cardiovascular Medicine*, vol. 3, no. 1, supplement, pp. S110–S113, 2006.

[13] P. R. Vulliet, M. Greeley, S. M. Halloran, K. A. MacDonald, and M. D. Kittleson, "Intra-coronary arterial injection of mesenchymal stromal cells and microinfarction in dogs," *Lancet*, vol. 363, no. 9411, pp. 783–784, 2004.

[14] P. D. Stein, M. Marzilli, H. N. Sabbah, and T. Lee, "Systolic and diastolic pressure gradients within the left ventricular wall," *American Journal of Physiology*, vol. 7, no. 5, pp. H625–H630, 1980.

[15] M. P. Maxwell, D. J. Hearse, and D. M. Yellon, "Species variation in the coronary collateral circulation during regional myocardial ischaemia: a critical determinant of the rate of evolution and extent of myocardial infarction," *Cardiovascular Research*, vol. 21, no. 10, pp. 737–746, 1987.

[16] C. J. Teng, J. Luo, R. C. J. Chiu, and D. Shum-Tim, "Massive mechanical loss of microspheres with direct intramyocardial injection in the beating heart: implications for cellular cardiomyoplasty," *Journal of Thoracic and Cardiovascular Surgery*, vol. 132, no. 3, pp. 628–632, 2006.

[17] A. J. Mitchell, E. Sabondjian, J. Sykes et al., "Comparison of initial cell retention and clearance kinetics after subendocardial or subepicardial injections of endothelial progenitor cells in a canine myocardial infarction model," *Journal of Nuclear Medicine*, vol. 51, no. 3, pp. 413–417, 2010.

[18] C. L. Byrne, "Accelerating the EMML algorithm and related iterative algorithms by rescaled block-iterative methods," *IEEE Transactions on Image Processing*, vol. 7, no. 1, pp. 100–109, 1998.

[19] F. M. Bengel, V. Schachinger, and S. Dimmeler, "Cell-based therapies and imaging in cardiology," *European Journal of Nuclear Medicine and Molecular Imaging*, vol. 32, no. 2, supplement, pp. S404–S416, 2005.

[20] J. Terrovitis, M. Stuber, A. Youssef et al., "Magnetic resonance imaging overestimates ferumoxide-labeled stem cell survival after transplantation in the heart," *Circulation*, vol. 117, no. 12, pp. 1555–1562, 2008.

[21] Z. Li, Y. Suzuki, M. Huang et al., "Comparison of reporter gene and iron particle labeling for tracking fate of human embryonic stem cells and differentiated endothelial cells in living subjects," *Stem Cells*, vol. 26, no. 4, pp. 864–873, 2008.

[22] M. Thompson, D. M. Wall, R. J. Hicks, and H. M. Prince, "In vivo tracking for cell therapies," *Quarterly Journal of Nuclear Medicine and Molecular Imaging*, vol. 49, no. 4, pp. 339–348, 2005.

[23] B. Doyle, B. J. Kemp, P. Chareonthaitawee et al., "Dynamic tracking during intracoronary injection ofF-FDG- labeled progenitor cell therapy for acute myocardial infarction," *Journal of Nuclear Medicine*, vol. 48, no. 10, pp. 1708–1714, 2007.

[24] N. Adonai, K. N. Nguyen, J. Walsh et al., "Ex vivo cell labeling with Cu-pyruvaldehyde-bis(N-methylthiosemicarbazone) for imaging cell trafficking in mice with positron-emission tomography," *Proceedings of the National Academy of Sciences of the United States of America*, vol. 99, no. 5, pp. 3030–3035, 2002.

[25] R. Zhou, D. H. Thomas, H. Qiao et al., "In vivo detection of stem cells grafted in infarcted rat myocardium," *Journal of Nuclear Medicine*, vol. 46, no. 5, pp. 816–822, 2005.

[26] J. E. Lowe, R. G. Cummings, D. H. Adams, and E. A. Hull Ryde, "Evidence that ischemic cell death begins in the subendocardium independent of variations in collateral flow or wall tension," *Circulation*, vol. 68, no. 1, pp. 190–202, 1983.

[27] J. A. Gascho, G. L. Copenhaver, and D. F. Heitjan, "Systolic thickening increases from subepicardium to subendocardium," *Cardiovascular Research*, vol. 24, no. 10, pp. 777–780, 1990.

[28] H. N. Sabbah, M. Marzilli, and P. D. Stein, "The relative role of subendocardium and subepicardium in left ventricular mechanics," *American Journal of Physiology*, vol. 9, no. 6, pp. H920–H926, 1981.

[29] R. J. Laham, M. Post, M. Rezaee et al., "Transendocardial and transepicardial intramyocardial fibroblast growth factor-2 administration: myocardial and tissue distribution," *Drug Metabolism and Disposition*, vol. 33, no. 8, pp. 1101–1107, 2005.

[30] P. M. Grossman, Z. Han, M. Palasis, J. J. Barry, and R. J. Lederman, "Incomplete retention after direct myocardial injection," *Catheterization and Cardiovascular Interventions*, vol. 55, no. 3, pp. 392–397, 2002.

[31] Y. Jin, H. Kong, R. Z. Stodilka et al., "Determining the minimum number of detectable cardiac-transplanted Intropolone-labelled bone-marrow-derived mesenchymal stem cells by SPECT," *Physics in Medicine and Biology*, vol. 50, no. 19, pp. 4445–4455, 2005.

[32] M. L. Thakur, A. W. Segal, L. Louis, M. J. Welch, J. Hopkins, and T. J. Peters, "Indium-111-labeled cellular blood components: mechanism of labeling and intracellular location in human neutrophils," *Journal of Nuclear Medicine*, vol. 18, no. 10, pp. 1022–1026, 1977.

Hindawi Publishing Corporation
International Journal of Molecular Imaging
Volume 2011, Article ID 279345, 6 pages
doi:10.1155/2011/279345

Research Article

Feasibility of Imaging Esophageal Cancer with Labeled Somatostatin Analogue

Gunnar Herlin,[1,2] Lars Ideström,[3] Lars Lundell,[4] Peter Aspelin,[1,2] and Rimma Axelsson[1,2]

[1] *Division of Medical Imaging and Technology, Department of Clinical Science, Intervention and Technology, Karolinska Institute, 141 86 Stockholm, Sweden*
[2] *Department of Radiology, Karolinska University Hospital Huddinge, 141 86 Stockholm, Sweden*
[3] *Department of Nuclear Medicine, Karolinska University Hospital, Huddinge, 141 86 Stockholm, Sweden*
[4] *Division of Surgery, Karolinska Institute at Campus Huddinge, 141 86 Stockholm, Sweden*

Correspondence should be addressed to Gunnar Herlin, gunnar.herlin@karolinska.se

Received 28 June 2010; Revised 2 September 2010; Accepted 20 January 2011

Academic Editor: Domenico Rubello

Background. While the surface of a cell normally has some amount of somatostatin receptors, these receptors are overexpressed to a very high degree in multiple neoplastic diseases. No data exist for esophageal carcinoma. *Purpose*. To find out whether esophageal carcinoma could be imaged using somatostatin receptor scintigraphy. *Material and Methods*. 34 patients with esophageal lesions were prospectively examined by ^{99m}Tc-depreotide scintigraphy 2 and 4 hours after injection. Quantitative evaluation of ^{99m}Tc-depreotide uptake was performed around the lesion (T) and in healthy lung parenchyma (B). The relative uptake was calculated as $T-B/B$. Scintigraphy results were compared with histopathology from surgery or biopsy specimens from endoscopic ultrasonography. *Results*. 21 patients had esophageal cancer, and 13 lesions were benign. Visual assessment revealed positive ^{99m}Tc-depreotide uptake in 16 of the 21 cancers. The 13 patients without cancer had no depreotide uptake. The Mann-Whitney U test showed a statistically significant difference ($P < .005$) between ^{99m}Tc-depreotide uptake in malignant and benign lesions, for both the 2-hour and the 4-hour measurements. *Conclusion*. Scintigraphic examination with ^{99m}Tc-depreotide is feasible for imaging esophageal cancer, but the method is not suitable neither for screening or primary diagnosis, because of methods modest sensitivity. Our first results showed high specificity which should be used with caution, as the number of patients was relatively low. Further studies are needed to determine the role of the method.

1. Introduction

In Sweden, approximately 400 patients per year are newly diagnosed with cancer of the esophagus and an additional 200 with cancer of the cardia [1]. There are several methods to determine this diagnosis: computed tomography (CT), endoscopic examination of the esophagus (esophagoscopy) combined with endoscopic ultrasonography (EUS) and needle biopsy and positron emission tomography (PET) examination with ^{18}F-Fluoro-deoxyglucose (^{18}F-FDG).

CT has the disadvantage that it is less able to diagnose overgrowth of the tumor to adjacent organs and to detect small tumors <1 cm and growth to different layers in the esophageal wall. PET and the combination of ^{18}F-FDG-PET/CT are both more accurate than CT alone with respect to diagnosing lymph node metastasis close to the tumor, and therefore staging [2]. EUS is superior to ^{18}F-FDG-PET/CT with respect to diagnosing tumor growth through different layers in the esophageal wall, overgrowth to adjacent organs, and lymph node metastasis close to the tumor [2–5]. Examination with ^{18}F-FDG-PET is based on the metabolic activity of the tumor, and reflects its pathophysiological characteristics. However, despite their high sensitivity in detecting esophageal cancer [2], these methods lack specificity; an elevated ^{18}F-FDG uptake could be seen in different nonmalignant conditions, such as inflammation and Barrett's esophagus [6–12]. Another way to characterize tumors is evaluation of different receptors, such as the somatostatin receptors.

While the surface of a cell usually includes some amount of somatostatin receptors, these receptors are over-expressed to a very high degree in multiple neoplastic diseases such as

neuroendocrine tumors [13] and in tumors of the central nervous system, breast, lung, and lymphoid tissue [12, 14].

When this study was initiated, there were several radiopharmaceuticals available for somatostatin receptor scintigraphy, including ^{99m}Tc-depreotide. This tracer is ^{99m}Tc-labeled, and demonstrates good imaging characteristics with a short investigation protocol. ^{99m}Tc-depreotide has proven valuable in diagnosing pulmonary nodules [9–11]. We have previously used scintigraphy with ^{99m}Tc-depreotide for the diagnosis of lung cancer, and showed an accurate discrimination between benign and malignant lesions with conventional gamma cameras [6, 9, 11]. There was a physiologically low ^{99m}Tc-depreotide uptake in the thorax region. Therefore, visualization of overexpression of somatostatin receptors in cancer types other than lung cancer should, theoretically, be feasible. Moreover, our previous results showed that this tracer accumulates both in squamous cancers and in adenocarcinomas [15], which is of clinical relevance in view of the almost exponential increase in the incidence of adenocarcinoma in the distal esophagus.

The aim of the present study was to find out whether esophageal cancer can be imaged scintigraphically with ^{99m}Tc-depreotide and to determine the uptake characteristics of ^{99m}Tc-depreotide in the two main cancer types of the esophagus and relate these to results in patients with benign lesions (Barrett's esophagus).

2. Material and Methods

The study was approved by the Regional Ethical Review Board in Stockholm, Sweden and the Radiation Safety Committee at Karolinska University Hospital, Huddinge.

2.1. Patients. 34 patients with dysphagia were referred to the Surgery Department at Huddinge University Hospital and further examined with gastroscopy, EUS, and CT. Nine of these were female and 25 male, with a median age of 63-64 years (range: 33–85 years). Among the 34 patients, 21 had cancer of the esophagus and 13 had Barrett's esophagus. Five of the 21 patients with esophageal cancer had a Barrett's esophagus too. The cancer diagnosis was established by histopathological examination of biopsy specimens in 19 cases and with EUS and cytological confirmation of diagnosis in 2 cases. All patients with Barrett's esophagus were diagnosed via endoscope and subsequent multiple biopsies.

Locoregional lymph nodes were evaluated with EUS and histological examination of surgical specimen.

2.2. Somatostatin Receptor Scintigraphy. ^{99m}Tc-depreotide (740 MBq) was administered via an antecubital vein. Single-photon emission computed tomography (SPECT) of the thorax was performed at 2 and 4 hours after injection, with the arms elevated, using three different gamma cameras. Most of the patients (25 of 34) were examined with a double-headed gamma camera (E-Cam, Siemens, Erlangen, Germany) and low-energy high-resolution parallel-hole collimators, using a 128 × 128 matrix, 64 projections through 360° rotation, and an acquisition time of 40 s per projection.

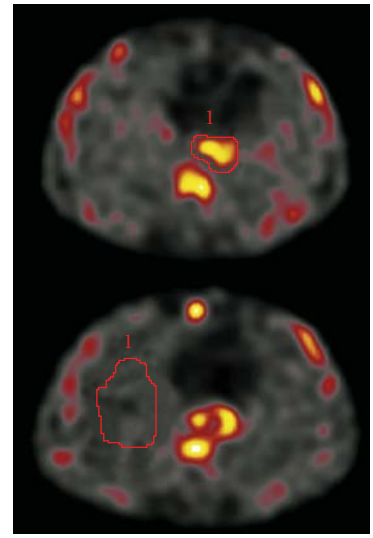

Figure 1: Evaluation of scintigraphic images with ^{99m}Tc-depreotide. Region of interest (ROI) was drawn manually around the esophageal tumor on each slice, using small margins, and a background ROI was drawn in healthy lung parenchyma.

An additional 5 patients were examined with a double-headed gamma camera (DST-XL; Sopha Medical Vision Scandinavia AB, Gif-sur-Yvette, France) and low-energy ultra-high-resolution parallel-hole collimators, using the same acquisition parameters as above. Finally, 4 patients were examined with a three-headed gamma camera (Picker IRIX, Cleveland, Ohio, USA) and low-energy high-resolution parallel-hole collimators, using a 128 × 128 matrix, 60 projections through 360° rotation, and an acquisition time of 64 s per projection. Transverse slices were reconstructed with an iterative algorithm (HOSEM v 3.5 iterative program; Hermes/NUD, Stockholm, Sweden) and formatted as a 128 × 128 matrix without attenuation correction. Images were postfiltered with a three-dimensional Fourier filter (Butterworth filter) with a cut-off frequency of 1.1 cycles/cm (order 5.00).

The results were evaluated both through visual assessment and through quantitative calculations in the 2-hour and 4-hour images. CT scans were used for an accurate localization of the ^{99m}Tc-depreotide uptake and for placement of the region of interest (ROI). On visual assessment, any focal ^{99m}Tc-depreotide uptake in the region of the known esophageal lesion was considered pathological. The quantitative evaluation of ^{99m}Tc-depreotide uptake was performed retrospectively on SPECT images in all 34 patients. First, an ROI was drawn manually around the esophageal tumor on each slice, using small margins. Next, a background ROI was drawn in healthy lung parenchyma (Figure 1). A volume of interest (VOI) was obtained by adding all ROIs. In-house software, originally developed for volumetric measurements in magnetic resonance images and implemented on a Hermes workstation (Hermes Medical Solution AB, Stockholm, Sweden), was used to calculate the total counts and volume of the tumor and background VOIs, thus giving

a count density (counts/cm^3). To produce a normalized tumor uptake, each patient was normalized to his or her own normal lung parenchyma using the formula $U = (T - B)/B$, where U is the normalized uptake, T is the count density in the tumor, and B is the count density in the lung parenchyma. To increase accuracy and to investigate the intraobserver variability, evaluations were performed twice, 6 months apart, by the same radiologist and the mean value of the two uptake values was used in further analysis. In addition, a second radiologist made individual evaluations in order to investigate the interobserver variability of the uptake values at 2-hour images.

2.3. Statistics. For patients with negative uptake (i.e., tumor count density lower than the lung background count density), the uptake was scored as zero. Due to the small number of patients in each group, a nonparametric test was chosen. A two-sided Mann-Whitney U test was used to investigate the difference in uptake between malign and benign tumors. To assess intraobserver and interobserver variability, intraclass correlation coefficients (ICC) were determined [16]. All statistical analysis was performed in Statistica 9.0 (StatSoft. Inc, Tulsa, OK, USA). Data were analyzed based on both the 2-hour and the 4-hour postinjection recordings except for the ICC which was only determined for the 2-hour recordings. A difference in uptake was considered significant if the P value was less than .05.

3. Results

Among the 21 patients with cancer of the esophagus, 8 had squamous cell carcinoma, 11 had adenocarcinoma, 1 had an undifferentiated cancer, and 1 had an intramucosal cancer. Tumor size varied from 5 mm to 11 cm. The position of the tumor was in the proximal esophagus in 2 cases, in the middle part in 5 cases, and in the distal part in the remaining 14 cases.

Visual assessment revealed a pathological ^{99m}Tc-depreotide uptake in 16 of the 21 cancer patients (true-positive 76%) and an absence of pathological uptake in the remaining 5 (false-negative 24%). Six of the eight patients with squamous cell carcinoma and nine of the eleven patients with adenocarcinoma showed a pathological ^{99m}Tc-depreotide uptake. The remaining patient with pathological uptake had an 11 cm undifferentiated cancer in the mid-esophagus with a very high ^{99m}Tc-depreotide uptake. Among the false-negative cases, one had a small (5 mm) squamous cell cancer located in the middle part of the esophagus. The remaining four undetectable cancers were above 1 cm in size (varying from 12 × 9 mm to 12 × 38 mm) and were located in the distal part of the esophagus. The details of all recordings are given in Table 1. The sensitivity of ^{99m}Tc-depreotide scintigraphy in the detection of esophageal cancer was thus 0.76 95% confidence interval 0.55 to 0.89.

There was no ^{99m}Tc-depreotide uptake in the columnar metaplastic mucosa in any of the 13 Barrett's patients, irrespective of the presence of low and high-grade dysplasia in the metaplastic epithelium (Figure 2). The specificity of ^{99m}Tc-depreotide scintigraphy in this cohort of patients was thus 1.00, 95% confidence interval 0.77 to 1.00.

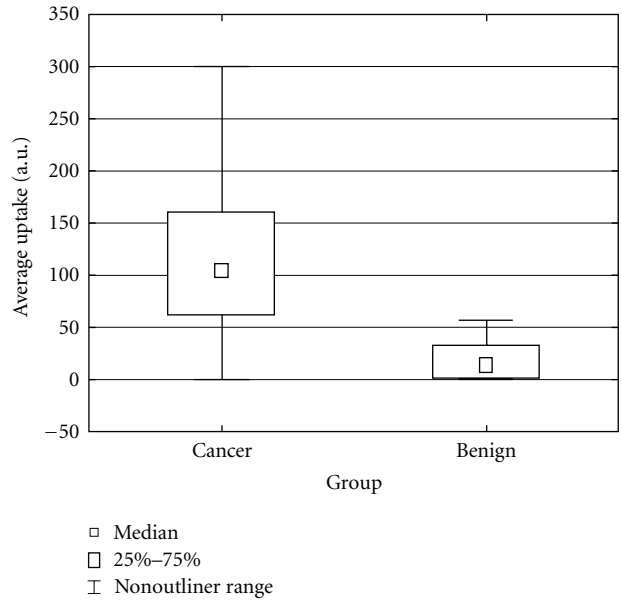

FIGURE 2: ^{99m}Tc-depreotide uptake measured 2 hours after injection in patients with esophageal cancer and Barrett's esophagus.

There were no significant differences between the ROI delineation and quantitative measurement of ^{99m}Tc-depreotide performed on the 2-hour acquisitions and those performed on the 4-hour acquisitions. A corresponding second ROI delineation and quantification, performed 6 months later, gave consistent results. Both intraobserver and interobserver variability was low with ICC = 0.97 when comparing the evalutions by the same radiologist (intraobserver) and ICC = 0.96 when comparing the evaluations made by the two radiologists (interobserver).

A statistically significant difference ($P < .005$) was found between ^{99m}Tc-depreotide uptake in malignant lesions compared to that in benign or premalignant lesions (Figure 2), both 2 and 4 hours after injection. The absolute ^{99m}Tc-depreotide uptake value was also higher in all malignant lesions after 2 compared to 4 hours. There was no difference in uptake between adenocarcinoma and squamous cell carcinoma.

In the 13 patients who had lymph node metastases at the final examination of the surgical specimen and with EUS only 5 showed ^{99m}Tc-depreotide uptake in the area of the lymph nodes.

4. Discussion

In this study, we have shown that the imaging of esophageal cancer by means of somatostatin receptor scintigraphy with ^{99m}Tc-depreotide is feasible. Our hypothesis was based on two facts: first, that the physiological ^{99m}Tc-depreotide uptake in the thorax is low. Therefore, this could be a suitable area for tumor detection in most cases, and, second, that esophageal cancer has the same main histopathological types as lung cancer such as adenocarcinoma and squamous cell

Table 1: Tumor type, size, and location, CT result, and ^{99m}Tc-depreotide uptake in 21 esophageal cancer patients.

N	Diagnosis	Tumor size in mm	Location	CT	^{99m}Tc-depreotide
1	Sqcc	5	Middle	Neg.	Neg.
2	Ac	17 × 45	Distal	Pos.	Pos.
3	Sqcc	55 × 40	proximal	Pos.	Pos.
4	Ac in B.	65 × 55 × 13	Distal	Pos.	Pos.
5	Ac	90 × 75 × 25	Distal	Pos.	Pos.
6	Imc and B.	12 × 9	Distal	Neg.	Neg.
7	Sqcc	30 × 10	Middle	Pos	Pos
8	Ac	20 × 90	Middle	Pos.	Pos.
9	Ac	60 × 25 × 9	Distal	Pos.	Pos.
10	Sqcc	50 × 45	Distal	Pos.	Pos.
11	Small cell cancer	110 × 24	Middle	Pos.	Pos.
12	Ac in B	60 × 65	Distal	Pos.	Pos.
13	Ac	25 × 15	Distal	Neg.	Pos.
14	Ac in B	20 × 25	Distal	Pos.	Pos.
15	Sqcc	60 × 10	proximal	Pos.	Pos.
16	Sqcc	15 × 55	Distal	Pos.	Pos.
17	Ac	15 × 50	Distal	Pos.	Pos.
18	Ac	15 × 15	Distal	Neg.	Neg.
19	Ac in B	20 × 25	Distal	Neg.	Neg.
20	Sqcc	14 × 5	Middle	Neg.	Pos.
21	Sqcc	23 × 38 × 12	Distal	Pos.	Neg.

Ac: adenocarcinoma; Sqcc: squamous cell carcinoma; B: Barrett's esophagus; Imc: intramucosal cancer. ^{99m}Tc-depreotide uptake classified as negative or positive based on visual assessment. CT pos.: tumor is visible on the CT images; CT neg.: tumor is not visible on the CT images.

carcinoma. As scintigraphy with ^{99m}Tc-depreotide is useful for lung cancer detection, this second fact suggested that it could also be applied in esophageal cancer.

The majority of tumors (16/21) displayed a significant uptake of the tracer which could be clearly distinguished from that in the surrounding tissue. It was not unexpected that tumors under or near 10 mm in size were missed on the scintigraphic images. The detection limit of conventional gamma camera due to poor spatial resolution is well known, and according to widespread consensus scintigraphic methods are not suitable for screening purposes for any cancer types. Another observation is that even larger tumors in the distal part of the esophagus, 4 of 13 in the present study, could be missed with this method. Uptake of ^{99m}Tc-depreotide in lung cancers located in the lowest part of the right low lobe [6] and even in esophageal cancers located at the level of the diaphragm and lower in the abdomen could be obscured because of the high physiological tracer uptake in the liver.

Our sensitivity figure of 76% is only an approximate value, due to the small number of patients in this study. Still, this is somewhat lower than both the sensitivity for detecting lung cancers [2, 6–11] with the same tracer and that for detecting lung cancer with ^{18}F-FDG-PET [6–8]. While ^{18}F-FDG uptake reflects a metabolic activity of the lesion and is not specific to tumors [6–8], overexpression of somatostatin receptors on tumor cells could give another valuable piece of information regarding tumor properties.

As a control group, we used patients with Barrett's esophagus. Barrett's esophagus refers to an abnormal change (metaplasia) in the cells in the lower end of the esophagus. It is thought to be caused by damage from chronic acid exposure or reflux oesophagitis. This metaplasia confers an increased risk of adenocarcinoma. None of the 13 cancer-free Barrett's esophagus patients in this study showed an increased ^{99m}Tc-depreotide uptake. Meanwhile, only 3 of 5 patients with both cancer and Barrett's esophagus showed an increased ^{99m}Tc-depreotide uptake, leaving 2 false-negative results. The specificity of 100% for the applied method is high but should be used with caution, as the number of patients was relatively low and the spectra of different benign conditions in the esophagus was not fully represented in this pilot study.

Our results in the detection of loco-regional lymph node metastases were unsatisfactory. Only 5 of 13 patients with metastases seen with EUS and confirmed by histological examination were clearly detected by ^{99m}Tc-depreotide scintigraphy. It is probably caused by the close location to the primary tumor, where a high depreotide uptake cannot be separated from the uptake in the metastatic lymph nodes. It was disappointing to note that very few of the local, metastatic lymph nodes could be detected by this method. Through this pilot observation it can be envisioned that this technology cannot add to the available methods, such as EUS, in determining the node status in oesophageal cancer during the diagnostic and therapeutic workup.

As this study is the first of its kind, we considered it important to explore whether the quantitative assessment was reliable between different investigators and over time. Both intraobserver and interobserver variability was very low meaning that the applied calculations have good reliability.

We applied a somatostatin receptor scintigraphy with ^{99m}Tc-depreotide in a previously nonexplored cancer type where the optimal acquisition time was unknown. We used the same starting point for the imaging session as for the standard procedure in the detection of lung cancer, that is, 2 hours after injection [8, 10, 11]. During the last decade there has been a trend of performing a double-phase registration in order to increase specificity. The double-phase registration is based on assumptions that the relative tracer uptake in benign lesions decreases with time, while uptake in malignant lesions remains high or even increases with the time [10, 17–20]. This approach is now in routine for parathyroid scintigraphy, and its use has also been suggested for scintimammography, tumor imaging with ^{18}F-FDG-PET, and somatostatin receptor scintigraphy with ^{99m}Tc-depreotide in lung cancer patients [17–20]. In order to optimize the imaging procedure from the very beginning, we performed double-phase registrations with imaging 2 and 4 hours after injection. Our results showed that in the majority of patients the absolute uptake decreased more rapidly in the background (i.e., the normal lung parenchyma compared to the malignant lesions in the esophagus), resulting in a higher relative uptake in cancer over time. As both the 2-hour, and the 4-hour quantitative evaluations showed a statistically significant difference ($P < .005$) between ^{99m}Tc-depreotide uptake in malignant lesions and in lesions without cancer, the 4-hour imaging seems unnecessary, and thus could be omitted for practical reasons.

Although future immunohistochemical studies will be needed to carefully map the density, detailed distribution, and localization of somatostatin receptors in the squamous cell esophageal carcinoma and adenocarcinomas, our data indicate that there is no major difference as reflected by the similarity in tracer accumulation between these two major tumor types. It is, however, of particular interest that in patients with Barrett's esophagus, no accumulation of tracer was observed either in those with or in those without dysplastic histomorphologic changes in the columnar epithelium. Since there is no corresponding preneoplastic condition, concerning the squamous cell carcinoma development, it can be hypothesized that the somatostatin receptor expression reaches far higher levels in infiltrative neoplastic growth than in the intraepithelial neoplastic disease states. If so, this observation may be potentially very important and offer unique clinical opportunities, for example, when PET/CT or somatostatin receptor scintigraphy with ^{99m}Tc-depreotide technologies are applied.

Results of this pilot study showed feasibility of imaging oesophageal carcinoma with labeled somatostatin receptor analogue. We used a single-photon emitting tracer, but the results should be applicable or even better with positron emitting tracers. Use of PET/CT cameras combines a better spatial resolution of functional PET imaging with detailed anatomical information leading to a higher sensitivity. A multitude of new PET analogs are applied, whereas [^{68}Ga-DOTA^0, Tyr^3] octreotide [21] or [^{68}Ga-DOTA^0, Tyr^3] octreotate [22] is likely to become the new standard for somatostatin receptor imaging with PET. This is because these analogs have a high affinity for the somatostatin receptor subtype-2 and because ^{68}Ga is a generator product with a relatively simple labeling [23]. The additional reason is that their ^{90}Y- or ^{177}Lu-labeled counterparts are used for Peptide Receptor Radionuclide Therapy (PRRT) and it seems desirable that peptide used in diagnostic imaging mimics the peptide used later for therapy.

After the successful visualization of somatostatin receptor positive tumors, a logical next step would be to use radiolabelled somatostatin analogues as a treatment of these patients. Such attempts were undertaken in patients with inoperable and/ormetastatic neuroendocrine tumors. While the objective responses for chemotherapy with the median time to progression is reported to be less than 18 months, PRRT with ^{90}Y-octreotide or ^{177}Lu-octreotate performs considerably better with a median time to progression of 30 and 40 months, respectively [23], and significantly improved quality of life [24].

What could the future clinical application of our results be? Obviously, the method is not suitable neither for screening or primary diagnosis, because of methods modest sensitivity. Could this method be used for the detection of distant metastases expressing somatostatin receptors with somatostatin receptor-mediated radionuclide therapy as a consequent result? Does the uptake of the ^{99m}Tc-depreotide could be related to the prognosis of the oesophageal tumor? May this method be used in evaluation of treatment response in patients with tracer uptake? Does the natural history of Barrett's esophagus and its malignisation could be predicted by tracer uptake? These issues are still to be answered.

4.1. In Conclusion. Scintigraphic examination with ^{99m}Tc-depreotide is feasible for imaging esophageal cancer, but the method is not suitable neither for screening or primary diagnosis, because of methods modest sensitivity. Our first results showed high specificity which should be used with caution, as the number of patients was relatively low. Acquisitions starting 2 hours after injection are optimal and suffice for imaging. Further studies are needed to explore and determine the role of somatostatin receptor scintigraphy in clinical practice.

Acknowledgment

This research made use of the SMILE medical imaging laboratory at Karolinska University Hospital, Stockholm, Sweden.

References

[1] J. Falk, H. Carstens, L. Lundell, and M. Albertsson, "Incidence of carcinoma of the oesophagus and gastric cardia. Changes over time and geographical differences," *Acta Oncologica*, vol. 46, no. 8, pp. 1070–1074, 2007.

[2] T. J. Kim, H. Y. Kim, K. W. Lee, and M. S. Kim, "Multimodality assessment of esophageal cancer: preoperative staging and

monitoring of response to therapy," *Radiographics*, vol. 29, no. 2, pp. 403–421, 2009.

[3] T. J. Savides, "Endosonography: new developments," *Current Opinion in Gastroenterology*, vol. 25, no. 5, pp. 428–432, 2009.

[4] L. C. Sabbagh, "Esophageal cancer," *Gastrointestinal Endoscopy*, vol. 69, no. 2, supplement, pp. S93–S96, 2009.

[5] T. Attila and D. O. Faigel, "Role of endoscopic ultrasound in superficial esophageal cancer," *Diseases of the Esophagus*, vol. 22, no. 2, pp. 104–112, 2009.

[6] D. Kahn, Y. Menda, K. Kernstine et al., "The utility of ^{99m}Tc depreotide compared with F-18 fluorodeoxyglucose positron emission tomography and surgical staging in patients with suspected non-small cell lung cancer," *Chest*, vol. 125, no. 2, pp. 494–501, 2004.

[7] N. Ferran, Y. Ricart, M. Lopez et al., "Characterization of radiologically indeterminate lung lesions: ^{99m}Tc-depreotide SPECT versus 18F-FDG PET," *Nuclear Medicine Communications*, vol. 27, no. 6, pp. 507–514, 2006.

[8] A. Halley, A. Hugentobler, P. Icard et al., "Efficiency of F-FDG and ^{99m}Tc-depreotide SPECT in the diagnosis of malignancy of solitary pulmonary nodules," *European Journal of Nuclear Medicine and Molecular Imaging*, vol. 32, no. 9, pp. 1026–1032, 2005.

[9] J. Blum, H. Handmaker, J. Lister-James, and N. Rinne, "A multicenter trial with a somatostatin analog ^{99m}Tc depreotide in the evaluation of solitary pulmonary nodules," *Chest*, vol. 117, no. 5, pp. 1232–1238, 2000.

[10] T. Martins, J. Sena Lino, S. Ramos, and L. Oliveira, "Tc-depreotide scintigraphy in the evaluation of indeterminate pulmonary lesions: clinical experience," *Cancer Biotherapy and Radiopharmaceuticals*, vol. 19, no. 2, pp. 253–259, 2004.

[11] R. Axelsson, G. Herlin, M. Bååth, P. Aspelin, and K. G. Kölbeck, "Role of scintigraphy with technetium-99m depreotide in the diagnosis and management of patients with suspected lung cancer," *Acta Radiologica*, vol. 49, no. 3, pp. 295–302, 2008.

[12] D. J. Kwekkeboom and E. P. Krenning, "Somatostatin receptor imaging," *Seminars in Nuclear Medicine*, vol. 32, no. 2, pp. 84–91, 2002.

[13] J. C. Reubi, J. Laissue, E. Krenning, and S. W. J. Lamberts, "Somatostatin receptors in human cancer: incidence, characteristics, functional correlates and clinical implications," *Journal of Steroid Biochemistry and Molecular Biology*, vol. 43, no. 1–3, pp. 27–35, 1992.

[14] I. Virgolini, M. Leimer, H. Handmaker et al., "Somatostatin receptor subtype specificity and in viva binding of a novel tumor tracer, ^{99m}Tc-P829," *Cancer Research*, vol. 58, no. 9, pp. 1850–1859, 1998.

[15] G. Herlin, K. G. Klbeck, P. L. Menzel et al., "Quantitative assessment of ^{99m}Tc-depreotide uptake in patients with non-small-cell lung cancer: immunohistochemical correlations," *Acta Radiologica*, vol. 50, no. 8, pp. 902–908, 2009.

[16] P. E. Shrout and J. L. Fleiss, "Intraclass correlations: uses in assessing rater reliability," *Psychological Bulletin*, vol. 86, no. 2, pp. 420–428, 1979.

[17] T. Shinya, K. Rai, Y. Okumura et al., "Dual-time-point F-18 FDG PET/CT for evaluation of intrathoracic lymph nodes in patients with non-small cell lung cancer," *Clinical Nuclear Medicine*, vol. 34, no. 4, pp. 216–221, 2009.

[18] Y. K. Chen, Y. Y. Shen, and C. H. Kao, "Dual-phase F-18 FDG PET cannot increase the diagnostic accuracy to differentiate solitary pulmonary nodules," *Clinical Nuclear Medicine*, vol. 29, no. 4, pp. 281–283, 2004.

[19] A. Sukan, M. Reyhan, M. Aydin et al., "Preoperative evaluation of hyperparathyroidism: the role of dual-phase parathyroid scintigraphy and ultrasound imaging," *Annals of Nuclear Medicine*, vol. 22, no. 2, pp. 123–131, 2008.

[20] C. J. Chen, BI. F. Lee, W. J. Yao et al., "Dual-phase F-FDG PET in the diagnosis of pulmonary nodules with an initial standard uptake value less than 2.5," *American Journal of Roentgenology*, vol. 191, no. 2, pp. 475–479, 2008.

[21] M. Gabriel, C. Decristoforo, D. Kendler et al., "Ga-DOTA-Tyr-octreotide PET in neuroendocrine tumors: comparison with somatostatin receptor scintigraphy and CT," *Journal of Nuclear Medicine*, vol. 48, no. 4, pp. 508–518, 2007.

[22] J. C. Reubi, J. C. Schär, B. Waser et al., "Affinity profiles for human somatostatin receptor subtypes SST1-SST5 of somatostatin radiotracers selected for scintigraphic and radiotherapeutic use," *European Journal of Nuclear Medicine*, vol. 27, no. 3, pp. 273–282, 2000.

[23] D. J. Kwekkeboom, B. L. Kam, M. Van Essen et al., "Somatostatin receptor-based imaging and therapy of gastroenteropancreatic neuroendocrine tumors," *Endocrine-Related Cancer*, vol. 17, no. 1, pp. R53–R73, 2010.

[24] J. J. M. Teunissen, D. J. Kwekkeboom, and E. P. Krenning, "Quality of life in patients with gastroenteropancreatic tumors treated with [Lu-DOTA,Tyr]octreotate," *Journal of Clinical Oncology*, vol. 22, no. 13, pp. 2724–2729, 2004.

Hindawi Publishing Corporation
International Journal of Molecular Imaging
Volume 2011, Article ID 141593, 7 pages
doi:10.1155/2011/141593

Review Article

Role of SPECT and SPECT/CT in the Surgical Treatment of Primary Hyperparathyroidism

Michele L. Taubman, Melanie Goldfarb, and John I. Lew

Division of Endocrine Surgery, DeWitt Daughtry Family Department of Surgery, University of Miami Leonard M. Miller School of Medicine, Miami, FL 33136, USA

Correspondence should be addressed to John I. Lew, jlew@med.miami.edu

Received 11 August 2010; Revised 26 March 2011; Accepted 8 April 2011

Academic Editor: J. M. Mountz

Primary hyperparathyroidism is the most common cause of hypercalcemia in the outpatient population. This condition is usually the result of a single hyperfunctioning parathyroid gland. Targeted parathyroidectomy guided by intraoperative parathyroid hormone monitoring (IPM) through a small cervical incision has replaced traditional bilateral neck exploration (BNE) as the initial approach in the surgical treatment of primary hyperparathyroidism at many medical centers worldwide. Preoperative sestamibi-technetium 99m scintigraphy serves as an important prerequisite for successful targeted parathyroidectomy. Single-photon emission computed tomography (SPECT) and CT fusion, however, is a recent imaging technique that provides a three-dimensional functional image with advanced contrast resolution to greatly improve preoperative localization of parathyroid tumors.

1. Introduction

Primary hyperparathyroidism is the most common cause of hypercalcemia in the outpatient population. The delicate balance of calcium homeostasis in the human body has long been appreciated. Serum elevation of this mineral secondary to overproduction of parathyroid hormone is associated with fatigue, musculoskeletal pain, weakness, polyuria, nocturia, renal stones, memory loss, constipation, polydipsia, heartburn, and depression. At the present time, most patients with hyperparathyroidism do not present with symptoms of hypercalcemia, but rather are identified on routine biochemical screening. The underlying cause of primary hyperparathyroidism is usually a single parathyroid adenoma in 85–96% of cases while less frequent causes include double adenoma, parathyroid hyperplasia, and parathyroid carcinoma. Parathyroidectomy is indicated in all patients with symptomatic hyperparathyroidism and in those individuals with asymptomatic hyperparathyroidism that satisfies certain consensus criteria. These most recent guidelines include a serum calcium concentration >1.0 mg/dL above the upper limit of normal, creatinine clearance <60 mL/min, bone density >2.5 standard deviations below standard reference values for sex-matched peak bone mass at any site (T-score <-2.5), age <50 years old, inability or unwillingness to be followed, or a severe psychoneurologic disorder [1].

Since the first attempted parathyroidectomy in 1925 by Mandl, the surgical treatment for primary hyperparathyroidism has undergone a gradual evolution [2]. The large collar incision has been replaced by a very small 2–4-centimeter lower neck incision, and bilateral four-gland neck exploration has largely been supplanted by focused single-gland excision with biochemical confirmation of a successful operation *in the operating room*. In addition, the diagnostic technology available for parathyroid localization has improved tremendously over the years, allowing elusive and ectopic abnormal parathyroid glands to be identified and localized in advance of parathyroid surgery, thus decreasing risk of unsuccessful surgical intervention and the need for reoperation. Together, preoperative imaging combined with intraoperative parathyroid hormone monitoring (IPM) allow for successful surgical outcomes and treatment of primary hyperparathyroidism at rates comparable to those of conventional bilateral neck exploration (BNE) [3–7].

While sestamibi-technetium 99m scintigraphy (sestamibi) has been considered a mainstay or essential component of focused parathyroidectomy often complemented by ultrasound (US), single-photon emission computed tomography (SPECT) imaging is a more recent advancement in preoperative parathyroid localization that may have further impact in the planning and success of targeted parathyroidectomy.

2. Anatomy, Embryology, and Pathology of the Parathyroid Glands

Effective image interpretation and operative planning cannot commence without full understanding of parathyroid anatomy and its embryology. While four parathyroid glands are found in the majority of humans, cadaver studies demonstrated a 13% presence of supernumerary glands and a 3% prevalence of only three parathyroid glands [8]. At four weeks of embryologic development, the superior parathyroid glands originate from the fourth branchial pouch and undergo very little migration whereas the inferior parathyroid glands descend from the third branchial pouch to more varied locations along with the thymus. These paired superior and inferior parathyroid glands are typically symmetric in location bilaterally. In about 80% of cases, the superior and inferior parathyroid glands receive their blood supply from the inferior thyroid artery [8, 9].

The superior parathyroid glands are often found on the posteromedial aspect of the thyroid's superior poles approximately one centimeter above the intersection of the recurrent laryngeal nerve and inferior thyroid artery at the level of the cricoid cartilage. Since these glands undergo limited migration during embryologic development, they are rarely ectopic; however, when they do occupy ectopic domains the positions include the tracheoesophageal groove, posterior mediastinum, retroesophageal space, retropharyngeal space, and intrathyroid locations. The inferior parathyroid glands are typically located on the posterolateral surface of the inferior poles of the thyroid gland below the intersection of the recurrent laryngeal nerve and inferior thyroid artery. In about 80% of the population, the inferior parathyroid glands reside anteriorly, inferiorly, or laterally within 2 cm of the inferior pole of the thyroid gland [8, 9]. In the 20% of patients that have an ectopic inferior parathyroid gland, the most common location is within the true sheath of the thymus (15%); less frequently they are found in the intrathyroidal location (1–4%), anterior mediastinum, submandibular location, tracheoesophageal groove, retroesophageal space, and carotid sheath [8, 9].

The underlying pathology of primary hyperparathyroidism is most commonly a single parathyroid adenoma. This benign encapsulated neoplasm accounts for 85–96% of cases of primary hyperparathyroidism. Although most have a single affected gland, two affected glands (double adenoma) may be found in 2 to 5% of patients with primary hyperparathyroidism. Parathyroid hyperplasia is caused by an increase of parenchymal mass within all the parathyroid glands, and it accounts for 4–15% of cases. The incidence of hyperplasia increases in patients with multiple endocrine neoplasia (MEN) and non-MEN familial isolated hyperparathyroidism. Parathyroid hyperplasia is treated either by subtotal (3.5 gland) parathyroidectomy or total parathyroidectomy with autotransplantation. Parathyroid carcinoma is a very rare, indolent growing malignant neoplasm of parenchymal cells responsible for 1–5% of all primary hyperparathyroidism cases [10].

3. Primary Hyperparathyroidism

Primary hyperparathyroidism results from the overproduction of parathyroid hormone (PTH) by one or more hyperfunctioning parathyroid glands that usually causes hypercalcemia. Current widespread use of serum channel autoanalyzers has allowed for the earlier diagnosis of primary hyperparathyroidism in patients without the manifestation of clinical symptoms [11]. As the most common cause of hypercalcemia in the outpatient setting, its incidence in the general population ranges from 0.1 to 0.3%, occurring more frequently in women than men, and in those with advanced age [12–14]. Known risk factors for primary hyperparathyroidism include abnormalities of the PRAD1, MEN1, and HRPT2 genes that encode for cyclin D1, menin, and parafibromin, respectively. Radiation exposure to the neck, especially during childhood, is also associated with development of primary hyperparathyroidism [15–18].

The classic description of kidney "stones," painful "bones," abdominal "groans," lethargic "moans," and psychiatric "overtones" associated with primary hyperparathyroidism are now infrequently encountered in Western populations. In these parts of the world, patients with primary hyperparathyroidism present most commonly with abnormal biochemical results and not the "textbook" manifestations of primary hyperparathyroidism and hypercalcemia such as fatigue, musculoskeletal pain, polyuria, nocturia, polydipsia, constipation, heartburn, memory loss, and depression. Nonetheless, up to 80% of patients currently present with nonspecific symptoms of depression, fatigue, and lethargy, and they often are considered asymptomatic. Of note, hypertension and nephrolithiasis are the most commonly associated preoperative conditions found in patients with primary hyperparathyroidism [19, 20].

Biochemical diagnosis and confirmation of primary hyperparathyroidism is made by demonstrating elevated total serum or ionized calcium levels, and high intact PTH levels in the setting of normal renal function. In primary hyperparathyroidism, vitamin D metabolism is typically characterized by low plasma levels of 25-hydroxyvitamin D and high plasma levels of 1,25-dihydroxyvitamin D. Twenty-four-hour urine calcium collection is also helpful to exclude the diagnosis of benign familial hypocalciuric hypercalcemia (BFHH). A rare, autosomal dominant condition identified in patients with a family history of hypercalcemia and decreased urine calcium excretion since birth, BFHH biochemically mimics primary hyperparathyroidism by revealing elevated calcium and PTH levels, but with low levels of urinary calcium (less than 50 mg/24 hours). Similarly, the urinary calcium-to-creatinine clearance ratio in BFHH is less than 0.01 whereas in patients with primary

hyperparathyroidism the ratio is greater than 0.02. However, BFHH is a benign condition that cannot be corrected by parathyroidectomy.

Parathyroidectomy is performed in all patients with a secure diagnosis of primary hyperparathyroidism and symptoms associated with hypercalcemia. Furthermore, parathyroid surgery is indicated in asymptomatic patients with primary hyperparathyroidism that meet one or more of the criteria in the revised guidelines of the Third International Workshop on the Management of Asymptomatic Primary Hyperparathyroidism that include serum calcium >1.0 mg/dL (0.25 mmoL/liter) above normal range, creatinine clearance reduced to <60 mL/min, T-score <-2.5 (in lumbar spine, total hip, femoral neck, or 33% radius) and/or previous fracture fragility (use Z-scores in premenopausal women and men younger than 50 years), age <50, and inability to obtain continued medical surveillance [1].

4. Surgical Treatment

With the advent of improved preoperative localization techniques, increased availability of IPM, and the predominance of single-gland disease (85–96%) in patients with primary hyperparathyroidism, targeted or limited parathyroidectomy has replaced conventional BNE as the standard approach at most specialized surgical centers worldwide [3–7]. Advantages of targeted parathyroidectomy include improved cosmetic results with smaller incisions, decreased pain, shorter operative time, ambulatory surgery, decreased hospitalization, quick postoperative recovery, less frequent injury to the recurrent laryngeal nerve, decreased postoperative hypocalcemia, and comparable success rates to conventional BNE [4–7].

Many techniques of focused parathyroidectomy have been described that incorporate and share the common aspects and principles of minimally invasive surgery, such as less dissection, decreased operative time, less morbidity, and comparable reported operative success to BNE ranging from 97% to 99%. For targeted parathyroidectomy to be successful, precise preoperative localization is essential. These focused procedures are performed in patients with a single parathyroid adenoma localized by preoperative sestamibi and/or US through a central or lateral incision measuring from 2 to 4 cm. Only the abnormal parathyroid gland is identified and excised. IPM is used by most endocrine surgeons to confirm that no additional hypersecreting parathyroid tissue remains. During this operation, blood is drawn to measure parathyroid hormone levels at baseline and after excision of a hyperfunctioning parathyroid gland. When IPM levels decrease by >50% 10 minutes after gland excision, the limited operation is completed. If a >50% drop does not occur, either a double adenoma or 4-gland hyperplasia is present and bilateral neck exploration is then performed. Under general or local anesthesia, targeted parathyroidectomy can be offered to most patients in the outpatient setting. Patients with known multiglandular disease (MGD) preoperatively are not offered this focused approach.

5. Preoperative Parathyroid Localization

Preoperative localization of hyperfunctioning parathyroid tissue is an essential component of focused parathyroidectomy. Parathyroid localization has improved with a variety of familiar imaging techniques including sestamibi scintigraphy, ultrasonography, and four-dimensional computed tomography, which has the added dimension of changes in perfusion of contrast over time compared to regular 3-D CT. Comparisons of these different imaging modalities have shown the superiority of scintigraphy for preoperative parathyroid localization. First reported in 1989, technetium (99 mTc) sestamibi is used for parathyroid scintigraphy as a radiotracer injected intravenously where the patient's neck is later imaged with a gamma camera [21]. 99 mTc sestamibi consists of lipophilic cationic molecules. After intravenous injection, the molecules are distributed throughout the circulatory system, into cells by passive diffusion, and become concentrated intracellularly in mitochondria. Approximately two hours after injection, thyroid cells lose significant sestamibi uptake whereas abnormal parathyroid gland oxyphil cells retain the marker in high mitochondrial concentrations that assist in parathyroid adenoma localization. Sestamibi has been regarded as the single best imaging modality for parathyroid adenoma identification over ultrasonography, CT, and magnetic resonance imaging [22–24]. Notwithstanding, this technology has its limitations. The radiotracer provides only two-dimensional, planar images. Sestamibi can localize 80% to 90% of single abnormal parathyroid glands, but it is less sensitive in the diagnosis of MGD [25–27]. Thyroid nodules or lymph nodes can also mimic abnormal parathyroid glands and cause false-positive results on sestamibi scans [28].

SPECT is currently used with increased frequency due to the three-dimensional information it provides with an improved sensitivity for the detection and localization of hyperfunctioning parathyroid glands (Figure 1). SPECT measures gamma radiation and obtains multiple angle images of the neck and mediastinum and then merges all cuts to reconstruct a three-dimensional image. The advanced contrast resolution of SPECT is the primary reason for its superiority over other imaging methods. Multiple studies have established the role and advantages of SPECT in the improvement of parathyroid localization. In one of the largest studies looking at SPECT in over 550 patients with primary hyperparathyroidism, radiologists developed a scoring system to predict parathyroid pathology based on intensity and pattern of sestamibi uptake. Patients with a SPECT image reading as "probable" or "definite" for parathyroid adenoma had a positive predictive value (PPV) of >94% for adenoma presence and correct laterality localization upon review of surgical findings. Patients with negative scans, however, had a higher rate of operative failure. Multiglandular disease was still not well predicted [29]. Investigators have also come to appreciate that using a hybrid SPECT/CT scan can further enhance localization by providing better resolution of surrounding structures. The fusion of CT with SPECT images allows for the combined anatomic information from CT and the physiologic

(a) (b)

Figure 1: Coronal (a) and transverse (b) tomograms from a delayed phase SPECT in a patient with a left superior parathyroid adenoma confirmed at surgery.

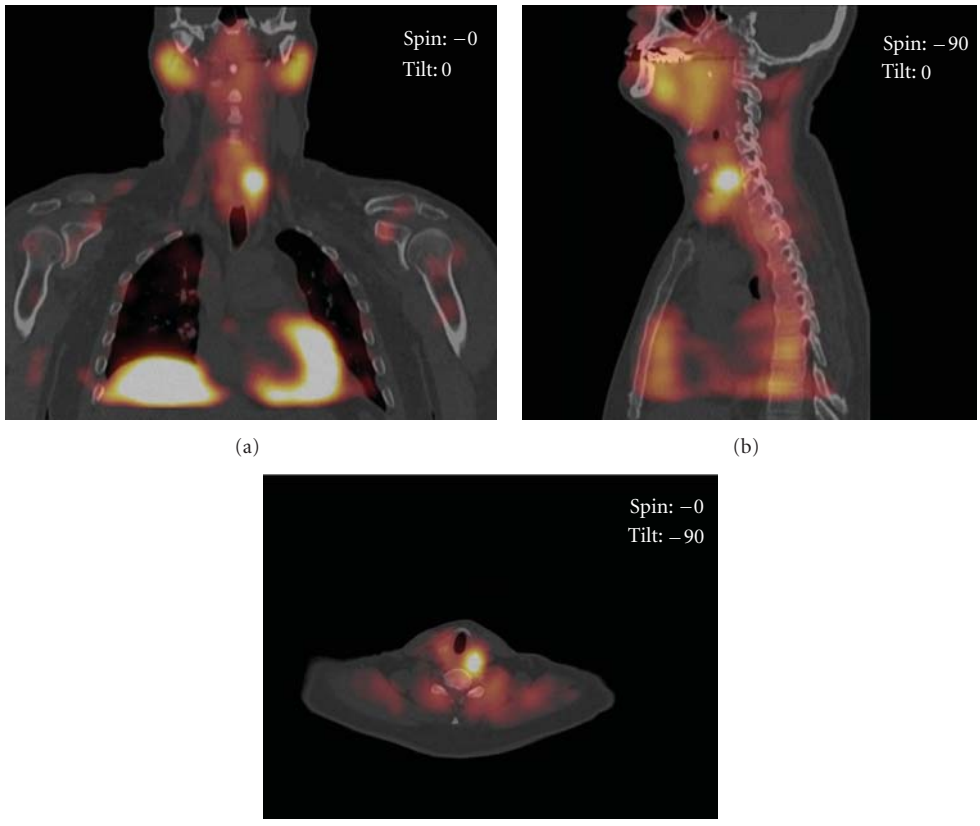

(a) (b)

(c)

Figure 2: Left superior parathyroid adenoma with delayed washout. Delayed phase (a) coronal, (b) sagittal, and (c) transverse fused SPECT/CT tomograms show a left superior parathyroid adenoma with a posterior location at the upper pole of the left thyroid lobe.

three-dimensional information from SPECT (Figure 2). This SPECT/CT combination has the added benefit of a more precise anatomic localization of ectopic and mediastinal parathyroid adenomas.

In a direct comparison study of sestamibi scintigraphy, SPECT, and SPECT/CT in patients with severe primary hyperparathyroidism, patients had either multinodular goiters with unclear gland identification by US, normal thyroid glands with negative parathyroid localization by US, or ectopic glands demonstrated by planar parathyroid scintigraphy [30]. All patients underwent the three imaging modalities. Results revealed that double-phase planar scintigraphy

only showed the presence of 14 probable hyperfunctioning parathyroid glands (12 in eutopic, 2 in ectopic locations) of 23 lesions localized at surgery (61%) whereas SPECT showed the presence of 23 probable adenomas (9 eutopic, 14 ectopic), but only correctly identified the location of 14 out of 23 lesions (61%) with extreme precision. SPECT/CT, however, identified the presence and correct location of 100% (all 23) of the lesions, and it was the only modality that identified retrotracheal parathyroid glands in three different patients.

An evaluation of planar imaging, SPECT, and SPECT/CT scintigraphy was performed on 98 patients with primary hyperparathyroidism caused by single adenoma with no previous neck surgery [31]. Each patient was subjected to planar imaging, SPECT, and SPECT/CT at 15 minutes and two hours after sestamibi injection. Surgical location served as the standard. Early SPECT/CT in combination with any delayed (two-hour) imaging method was significantly superior to any single- or dual-phase planar or SPECT study in regards to sensitivity and positive predictive value for abnormal parathyroid localization. Parathyroid localization had a sensitivity of 34% for single-phase early planar images, 45% for single-phase delayed planar images, 57% for dual-phase planar, 54% for single-phase early SPECT, 54% for single-phase delayed SPECT, and 62% for dual-phase SPECT that increased to 73% sensitivity for dual-phase studies with early SPECT/CT. Specificity and negative predictive values remained constant across all modalities. Localization with dual-phase acquisition was also found to be more accurate than with single-phase 99 mTc-sestamibi scintigraphy for planar imaging, SPECT, and SPECT/CT. This study concluded that dual-phase imaging with early SPECT/CT should be incorporated into routine preoperative planning for all patients with primary hyperparathyroidism.

Other studies have reported similar sensitivities, but also impressive specificity for SPECT/CT in localizing parathyroid adenomas. In one study comparing SPECT and SPECT/CT in 61 patients with primary hyperparathyroidism, although the sensitivities of SPECT (71%) and SPECT/CT (70%) were similar ($P = .779$), the specificity of SPECT/CT (96%) was significantly greater than that of SPECT alone (48%; $P = .006$) [32]. In another report of 116 patients with single-gland disease, sensitivity for SPECT/CT was 88%, for CT 70%, and for SPECT 59%. Specificity for SPECT/CT was 99%, for SPECT 95%, and for CT 94% [33]. Both studies concluded that SPECT/CT fusion was superior to the individual CT or SPECT images alone in localizing parathyroid adenomas.

In a study of 28 patients undergoing reoperative surgery for a "missed" parathyroid gland, SPECT/CT was able to predict the exact position of the abnormal gland in 86% of the patients whereas SPECT was successful in only 43% of cases ($P < .004$). SPECT/CT detected all three pathologic glands in ectopic positions [34]. Further reports supported that the additional information provided by hybrid SPECT/CT imaging often proved to be advantageous in the detection and localization of ectopic parathyroid adenomas [35]. Another population in which SPECT/CT might prove beneficial is patients with multinodular goiter and primary hyperparathyroidism. In a study of 33 patients with these two diagnoses, all study individuals underwent preoperative sestamibi planar scintigraphy and SPECT (18 patients) or SPECT/CT (15 patients) after cervical ultrasound [36]. SPECT/CT showed higher sensitivity than SPECT (87.5% versus 55.6%; $P = .0001$) and higher PPV (87.5% versus 62.5%; $P = .0022$) for correctly identifying the neck quadrant affected by primary hyperparathyroidism; the specificity trended toward SPECT/CT over SPECT, but was not significant (95.5% and 88.5%, resp.). The report concluded that SPECT/CT is superior to SPECT for preoperative imaging of patients with both primary hyperparathyroidism and multinodular goiter, and should be a routine part of this population's preoperative workup.

More studies concur that SPECT/CT offers enhanced ability to localize abnormal parathyroid glands above planar scintigraphy or SPECT alone. In investigating the role of SPECT/CT in the general oncologic patients, the functional and anatomic imaging obtained from SPECT and CT has been shown to be synergistic versus complementary, and can significantly contribute to more accurate localization of parathyroid and other cancers [37]. While the SPECT/CT can be technically challenging to perform and potentially increase patient radiation doses, the benefits of its improved sensitivity and specificity can decrease need for future confirmatory imaging studies [33, 35].

6. Conclusion

Primary hyperparathyroidism is caused by a single parathyroid gland in up to 96% of cases. Focused parathyroidectomy is the preferred treatment of choice for this condition, and scintigraphy is a principal method used for preoperative parathyroid gland localization. SPECT is more useful than planar imaging since it provides additional information about the superior/inferior and anterior/posterior location of abnormal parathyroid glands. Fusion of CT with SPECT has the added benefit of providing not only useful anatomic information but functional assessment as well. For patients with ectopic glands or patients facing reoperation, SPECT/CT is particularly helpful for preoperative localization and may become the preferred method of parathyroid detection and localization in such clinical scenarios. Nevertheless, the long-term clinical and economic benefits of SPECT and SPECT/CT, although promising, remain to be determined.

References

[1] J. P. Bilezikian, A. A. Khan, and J. T. Potts Jr., "Guidelines for the management of asymptomatic primary hyperparathyroidism: summary statement from the third international workshop," *Journal of Clinical Endocrinology and Metabolism*, vol. 94, no. 2, pp. 335–339, 2009.

[2] F. Mandl, "Therapeutischer versuch bein einem falls von otitis fibrosa generalisata mittles. Exstirpation eines epithelkorperchentumors," *Wien Klin Wochenschr Zentral*, vol. 53, pp. 260–264, 1926 (German).

[3] W. R. Sackett, B. Barraclough, T. S. Reeve, and L. W. Delbridge, "Worldwide trends in the surgical treatment of

primary hyperparathyroidism in the era of minimally invasive parathyroidectomy," *Archives of Surgery*, vol. 137, no. 9, pp. 1055–1059, 2002.

[4] R. Udelsman, "Six hundred fifty-six consecutive explorations for primary hyperparathyroidism," *Annals of Surgery*, vol. 235, no. 5, pp. 665–672, 2002.

[5] J. Westerdahl, P. Lindblom, and A. Bergenfelz, "Measurement of intraoperative parathyroid hormone predicts long-term operative success," *Archives of Surgery*, vol. 137, no. 2, pp. 186–190, 2002.

[6] G. L. Irvin, D. M. Carneiro, and C. C. Solorzano, "Progress in the operative management of sporadic primary hyperparathyroidism over 34 years," *Annals of Surgery*, vol. 239, no. 5, pp. 704–708, 2004.

[7] C. S. Grant, G. Thompson, D. Farley et al., "Primary hyperparathyroidism surgical management since the introduction of minimally invasive parathyroidectorny: Mayo Clinic experience," *Archives of Surgery*, vol. 140, no. 5, pp. 472–478, 2005.

[8] G. Akerstrom, J. Malmaeus, and R. Bergstrom, "Surgical anatomy of human parathyroid glands," *Surgery*, vol. 95, no. 1, pp. 14–21, 1984.

[9] N. W. Thompson, F. E. Eckhauser, and J. K. Harness, "The anatomy of primary hyperparathyroidism," *Surgery*, vol. 92, no. 5, pp. 814–821, 1982.

[10] B. Givi and J. P. Shah, "Parathyroid carcinoma," *Clinical Oncology*, vol. 22, no. 6, pp. 498–507, 2010.

[11] R. A. Wermers, S. Khosla, E. J. Atkinson et al., "Incidence of primary hyperparathyroidism in Rochester, Minnesota, 1993–2001: an update on the changing epidemiology of the disease," *Journal of Bone and Mineral Research*, vol. 21, no. 1, pp. 171–177, 2006.

[12] H. Heath III, S. F. Hodgson, and M. A. Kennedy, "Primary hyperparathyroidism. Incidence, morbidity, and potential economic impact in a community," *The New England Journal of Medicine*, vol. 302, no. 4, pp. 189–193, 1980.

[13] H. Chen, S. Parkerson, and R. Udelsman, "Parathyroidectomy in the elderly: do the benefits outweigh the risks?" *World Journal of Surgery*, vol. 22, no. 6, pp. 531–536, 1998.

[14] P. Uden, A. Chan, Q. Y. Duh, A. Siperstein, O. H. Clark, and G. L. Irvin, "Primary hyperparathyroidism in younger and older patients: symptoms and outcome of surgery," *World Journal of Surgery*, vol. 16, no. 4, pp. 791–797, 1992.

[15] A. Arnold, H. G. Kim, R. D. Gaz et al., "Molecular cloning and chromosomal mapping of DNA rearranged with the parathyroid hormone gene in a parathyroid adenoma," *Journal of Clinical Investigation*, vol. 83, no. 6, pp. 2034–2037, 1989.

[16] C. Heppner, M. B. Kester, S. K. Agarwal et al., "Somatic mutation of the MEN 1 gene in parathyroid tumours," *Nature Genetics*, vol. 16, no. 4, pp. 375–378, 1997.

[17] J. D. Carpten, C. M. Robbins, A. Villablanca et al., "HRPT2, encoding parafibromin, is mutated in hyperparathyroidism-jaw tumor syndrome," *Nature Genetics*, vol. 32, no. 4, pp. 676–680, 2002.

[18] T. Christensson, "Hyperparathyroidism and radiation therapy," *Annals of Internal Medicine*, vol. 89, no. 2, pp. 216–217, 1978.

[19] M. S. Eigelberger, W. K. Cheah, P. H. Ituarte, L. Streja, Q. Y. Duh, and O. H. Clark, "The NIH criteria for parathyroidectomy in asymptomatic primary hyperparathyroidism: are they too limited?" *Annals of Surgery*, vol. 239, no. 4, pp. 528–535, 2004.

[20] J. P. Bilezikian and J. P. Potts, "Asymptomatic primary hyperparathyroidism: new issues and new questions," *Journal of Bone and Mineral Research*, vol. 17, no. 2, pp. N57–N67, 2002.

[21] A. J. Coakley, A. G. Kettle, C. P. Wells et al., "99Tcm sestamibi: a new agent for parathyroid imaging," *Nuclear Medicine Communications*, vol. 10, no. 11, pp. 791–794, 1989.

[22] M. Ishibashi, H. Nishida, Y. Hiromatsu et al., "Comparison of technetium-99m-MIBI, technetium-99 m-tetrofosmin, ultrasound and MRI for localization of abnormal parathyroid glands," *Journal of Nuclear Medicine*, vol. 39, no. 2, pp. 320–324, 1998.

[23] O. Geatti, B. Shapiro, P. G. Orsolon et al., "Localization of parathyroid enlargement: experience with technetium-99 m methoxyisobutylisonitrile and thallium-201 scintigraphy, ultrasonography and computed tomography," *European Journal of Nuclear Medicine*, vol. 21, no. 1, pp. 17–22, 1994.

[24] B. B. Peeler, W. H. Martin, M. P. Sandler, and R. E. Goldstein, "Sestamibi parathyroid scanning and preoperative localization studies for patients with recurrent/persistent hyperparathyroidism or significant comorbid conditions: development of an optimal localization strategy," *American Surgeon*, vol. 63, no. 1, pp. 37–46, 1997.

[25] B. Chiu, C. Sturgeon, and P. Angelos, "What is the link between nonlocalizing sestamibi scans, multigland disease, and persistent hypercalcemia? A study of 401 consecutive patients undergoing parathyroidectomy," *Surgery*, vol. 140, no. 3, pp. 418–422, 2006.

[26] D. M. Carniero-Pla, C. C. Solorzano, and G. L. Irvin, "Consequences of targeted parathyroidectomy guide by localizing studies without intraoperative parathyroid hormone monitoring," *Journal of the American College of Surgeons*, vol. 202, no. 5, pp. 715–722, 2006.

[27] L. Yip, D. A. Pryma, J. H. Yim, M. A. Virji, S. E. Carty, and J. B. Ogilvie, "Can a lightbulb sestamibi SPECT accurately predict single-gland disease in sporadic primary hyperparathyroidism?" *World Journal of Surgery*, vol. 32, no. 5, pp. 784–792, 2008.

[28] C. J. Palestro, M. B. Tomas, and G. G. Tronco, "Radionuclide imaging of the parathyroid glands," *Seminars in Nuclear Medicine*, vol. 35, no. 4, pp. 266–276, 2005.

[29] L. Yip, D. A. Pryma, J. Yim, S. E. Carty, and J. B. Ogilvie, "Sestamibi SPECT intensity scoring system in sporadic primary hyperparathyroidism," *World Journal of Surgery*, vol. 33, no. 3, pp. 426–433, 2009.

[30] A. Serra, P. Bolasco, L. Satta, A. Nicolosi, A. Uccheddu, and M. Piga, "Role of SPECT/CT in the preoperative assessment of hyperparathyroid patients," *Radiologia Medica*, vol. 111, no. 7, pp. 999–1008, 2006.

[31] W. C. Lavely, S. Goetze, K. P. Friedman et al., "Comparison of SPECT/CT, SPECT, and planar imaging with single- and dual-phase ^{99m}Tc-sestamibi parathyroid scintigraphy," *Journal of Nuclear Medicine*, vol. 48, no. 7, pp. 1084–1089, 2007.

[32] D. R. Neumann, N. A. Obuchowski, and F. P. Difilippo, "Preoperative ^{123}I/^{99m}Tc-sestamibi subtraction SPECT and SPECT/CT in primary hyperparathyroidism," *Journal of Nuclear Medicine*, vol. 49, no. 12, pp. 2012–2017, 2008.

[33] R. Prommegger, G. Wimmer, C. Profanter et al., "Virtual neck exploration: a new method for localizing abnormal parathyroid glands," *Annals of Surgery*, vol. 250, no. 5, pp. 761–765, 2009.

[34] G. Wimmer, R. Bale, P. Kovacs et al., "Virtual neck exploration in patients with hyperparathyroidism and former cervical

operations," *Langenbeck's Archives of Surgery*, vol. 393, no. 5, pp. 687–692, 2008.

[35] D. S. Levine, A. S. Belzberg, and S. M. Wiseman, "Hybrid SPECT/CT imaging for primary hyperparathyroidism: case reports and pictorial review," *Clinical Nuclear Medicine*, vol. 34, no. 11, pp. 779–784, 2009.

[36] G. Pata, C. Casella, S. Besuzio et al., "Clinical appraisal of 99m technetium-sestamibi SPECT/CT compared to conventional SPECT in patients with primary hyperparathyroidism and concomitant nodular goiter," *Thyroid*, vol. 20, no. 10, pp. 1121–1127, 2010.

[37] R. Núñez, "Acquisition parameters for oncologic imaging with a new SPECT/multislice CT scanner," *Molecular Imaging and Biology*, vol. 12, no. 2, pp. 110–138, 2010.

Hindawi Publishing Corporation
International Journal of Molecular Imaging
Volume 2011, Article ID 813028, 9 pages
doi:10.1155/2011/813028

Review Article

SPECT Imaging of Epilepsy: An Overview and Comparison with F-18 FDG PET

Sunhee Kim[1] and James M. Mountz[2]

[1] *Division of Nuclear Medicine, Department of Radiology, Children's Hospital of Pittsburgh and The University of Pittsburgh Medical Center, Pittsburgh, PA 15213, USA*
[2] *Division of Nuclear Medicine, Department of Radiology, University of Pittsburgh Medical Center, PET Facility, B-932, 200 Lothrop Street, Pittsburgh, PA 15213, USA*

Correspondence should be addressed to James M. Mountz, mountzjm@upmc.edu

Received 20 August 2010; Accepted 9 May 2011

Academic Editor: Abass Alavi

Epilepsy surgery is highly effective in treating refractory epilepsy, but requires accurate presurgical localization of the epileptogenic focus. Briefly, localization of the region of seizure onset traditionally dependents on seizure semiology, scalp EEG recordings and correlation with anatomical imaging modalities such as MRI. The introduction of noninvasive functional neuroimaging methods, including single-photon emission computed tomography (SPECT) and positron emission tomography (PET) has dramatically changed the method for presurgical epilepsy evaluation. These imaging modalities have become powerful tools for the investigation of brain function and are an essential part of the evaluation of epileptic patients. Of these methods, SPECT has the practical capacity to image blood flow functional changes that occur during seizures in the routine clinical setting. In this review we present the basic principles of epilepsy SPECT and PET imaging. We discuss the properties of the SPECT tracers to be used for this purpose and imaging acquisition protocols as well as the diagnostic performance of SPECT in addition to SPECT image analysis methods. This is followed by a discussion and comparison to F-18 FDG PET acquisition and imaging analysis methods.

1. Introduction

Epilepsy surgery can be highly effective in treating refractory epilepsy if performed in properly selected patients with well-delineated ictal foci [1]. The greatest challenge is accurate localization, but only a small fraction of the patients whose epilepsy becomes refractory ultimately receive surgery. In the past, localization of the region of seizure onset was dependent upon scalp, cortical, and depth electroencephalography (EEG). However, scalp EEG has disadvantages such as dependency on cortical surface effects and low spatial resolution that can lead to mislocalization of epileptogenic foci. Both cortical and depth EEG have a limited spatial sampling area that is confined to regions accessible by electrode placement. Depth EEG can detect signals from deeper structures, but it is more invasive, which can lead to surgical complications [2].

The introduction of noninvasive neuroimaging methods, such as single-photon emission computed tomography (SPECT), positron emission tomography (PET), and magnetic resonance imaging (MRI), has dramatically changed presurgical epilepsy evaluation. These imaging methods have become powerful tools for the investigation of brain function and an essential part of the evaluation of epileptic patients. Of these methods, only SPECT has the practical capacity to image blood flow functional changes that occur during seizures in the routine clinical setting. Although functional MRI (fMRI) could, in theory, be used for this purpose, it is impractical due to patient movement during most types of seizures, a problem that is overcome by the timing and technique of SPECT imaging.

In this paper, we review basic principles of epilepsy SPECT, SPECT tracers, imaging acquisition, the diagnostic performance of SPECT, and imaging analysis methods. This

is followed by a discussion and comparison to PET tracer acquisition methods and imaging analysis methods.

2. Central Nervous System Radiopharmaceuticals for SPECT

SPECT radiopharmaceuticals used for measuring regional cerebral blood flow (rCBF) are lipophilic agents which are transported from the vascular compartment to the normal brain tissue compartment by diffusion and are distributed proportionally to regional tissue blood flow. After this first phase of transport (during the first pass through the brain), the tracer is essentially irreversibly trapped in the tissue compartment and does not change its relative distribution over time. These properties are essential in ictal SPECT, since the tracer is essentially trapped during the first few seconds after injection and maintains that distribution for hours, allowing the patient to be stabilized and imaged at rest, but the emission of photons still reflects the tracer distribution pattern seconds after injection. The two major blood flow agents used in brain SPECT imaging are technetium-99m hexamethyl-propylene amine oxime (Tc-99m HMPAO) and Tc-99m ethyl cysteinate dimer (Tc-99m ECD) [3, 4].

2.1. Tc-99m Hexamethyl-propylene Amine Oxime (HMPAO). To understand the uptake mechanism of Tc-99m hexamethyl-propylene amine oxime (Tc-99m HMPAO), a three-compartment analysis model can be used for analysis [5]. In this model the first compartment is the lipophilic tracer in the blood pool of the brain, but outside of the blood brain-barrier. The second compartment is comprised of the lipophilic tracer inside of the blood brain-barrier. The third compartment is the hydrophilic form of the tracer that is retained in the brain. Transport from the first compartment to the second compartment represents efflux of lipophilic tracer from the blood compartment to the brain compartment. Back-exchange from the third compartment to the second compartment represents back-diffusion of the lipophilic form of the tracer and is essentially equal to zero since the tracer is irreversibly trapped (by intracellular reaction with glutathione) in the brain.

2.2. Tc-99m Ethyl Cysteinate Dimer (ECD). The second tracer commonly used in brain SPECT to measure regional cerebral perfusion is Tc-99m ECD [6]. This radiopharmaceutical is lipophilic like Tc-99m HMPAO and rapidly traverses the endothelium and capillary membranes into the brain cells. However, in the third compartment irreversible trapping mechanism of this tracer differs from Tc-99m HMPAO, since Tc-99m ECD is enzymatically metabolized to a polar complex, which is trapped in the brain. This tracer has been reported to demonstrate less nonspecific scalp and facial tissue background activity compared with Tc-99m HMPAO. Figure 1 shows a normal Tc-99m ECD brain SPECT scan after injection of 20 mCi (740 MBq) I.V.

2.3. Differences in Cerebral Distribution of Tc-99m HMPAO and Tc-99m ECD. Several studies reported higher extracerebral background activity with Tc-99m HMPAO than with Tc-99m ECD due to the slower clearance rate of Tc-99m HMPAO from the blood [7–10]. This can contribute to a lowering of the cortical uptake to background ratio with subsequent decreased detectability of epileptogenic focus. Additionally, Tc-99m HMPAO tends to underestimate the high flow rate due to a nonlinear extraction pattern to the flow whereas Tc-99m ECD reflects rCBF more linearly than Tc-99m HMPAO at higher flow rates [11]. Therefore, Tc-99m ECD may be more sensitive in detecting a hyperperfused epileptogenic focus at a high flow rate.

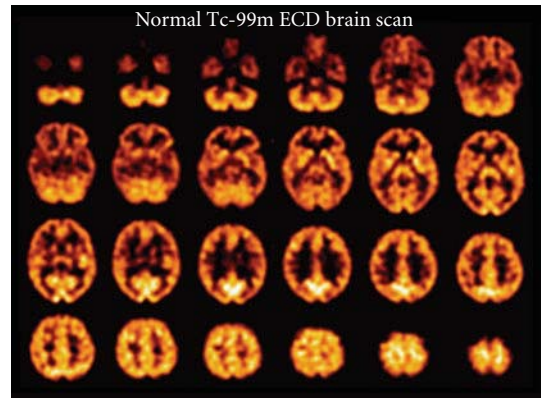

Figure 1: Transverse tomographic images from a normal 41-year-old female subject after injection of 20 mCi Tc-99m ECD. The transverse images are arranged parallel to and sequentially above the canthomeatal line, with the cerebellum at the top left and the vertex of the brain at the bottom right. The scan thickness is 4 mm. The scan resolution is approximately 7 mm full width at half maximum.

2.4. Comparison of Radiopharmaceutical Diagnostic Performance of Tc-99m HMPAO versus Tc-99m ECD. Lee et al. demonstrated that Tc-99m HMPAO has a similar localization rate (82%) to that of Tc-99m ECD (71%) in patients with TLE (in this group a total of 17 patients had Tc-99m HMPAO SPECT and 7 patients had Tc-99m ECD SPECT), with a higher degree of hyperperfusion in the Tc-99m HMPAO group [12]. For patients with neocortical epilepsy (23 patients had Tc-99m HMPAO SPECT and 7 patients had Tc-99m ECD SPECT), there was a higher localization rate (70% versus 29%) and degree of hyperperfusion in the Tc-99m HMPAO group. The authors summarized that the sensitivity of Tc-99m ECD ictal SPECT is similar to that of Tc-99m HMPAO ictal SPECT in TLE. However, ictal hyperperfusion was higher with the Tc-99m HMPAO SPECT in patients with neocortical epilepsy. Tc-99m HMPAO ictal SPECT also was superior to Tc-99m ECD ictal SPECT in sensitivity and degree of hyperperfusion. They concluded that the diagnostic performance and contrast of hyperperfused areas at the epileptogenic zones of Tc-99m HMPAO ictal SPECT were better than those of the Tc-99m ECD ictal SPECT in their group of patients.

3. Image Acquisition

3.1. SPECT Image Acquisition. In-single photon emission computed tomography (SPECT) of the brain, dual and

triple-head Anger gamma cameras are now in common use and can provide very high resolution images (approximately seven millimeters full width half maximum (FWHM) extrinsic resolution) [13]. The resolution has improved, primarily, due to the increased count detection capability of these cameras. In addition, these cameras allow faster throughput of patients since the scan time can be decreased. Scanning can be performed in temporal segments, with summation of the projection images at the end of acquisition. This enables salvaging of studies in which patient motion might occur. For example, a 30-minute scan can be divided into two 15-minute segments, each obtaining a 360° set of projection images. If the patient moves during the last 15-minute imaging segment, the first 15-minute imaging segment can be used for reconstruction of the complete set of tomographic images.

3.2. Ictal SPECT: Practical Issues. In order to perform these studies, Tc-99m HMPAO must be readily available at the patient's bedside allowing for rapid injection by a trained technologist or other personnel immediately available at the time of seizure onset. The ictal injection should be performed in a rapid bolus fashion such that the entire tracer is injected during the first onset of seizure (ictus). The patient is then sedated and transferred to the SPECT scanner within several hours to acquire the brain SPECT scan which will indicate the regional cerebral perfusion at the time of ictus. This method is feasible since Tc-99m HMPAO is irreversibly trapped in the epileptogenic hyperemic region at the time of seizure, and during the period between injection and scan, there is essentially no redistribution. The subsequent scan (albeit several hours after the injection) will still show hyperemia (increased tracer counts) in the region of the epileptogenic focus.

4. Diagnostic Performance of Ictal and Interictal SPECT

The sensitivity of ictal SPECT is theoretically higher than that of interictal SPECT because of the large CBF increase from the baseline that occurs during the ictal phase [14]. This is a substantially larger perfusion difference (approximately 50%) than from the 0–10% to at most 40% reduction of flow seen during the interictal phase [15, 16]. A comparison between ictal and interictal SPECT is shown in Figure 2. Several prior studies have shown a difference in sensitivity between ictal and interictal SPECT [17]. Overall, the highest sensitivity was seen in ictal SPECT (97% to 100%), followed by postictal SPECT (75% to 77%). Interictal SPECT was shown to have the lowest sensitivity (43% to 44%).

Figure 3 illustrates the value of ictal SPECT in a nine-year-old right-handed boy who had a seven-year history of intractable seizures. The figure shows a Tc-99m HMPAO brain SPECT scan which was performed 2 hours after tracer injection. The tracer was injected at the bedside 3 seconds after seizure onset (the seizure lasted ~25 seconds). The ictal SPECT scan shows a focal area of intense uptake in the right frontal lobe. Computed tomography (CT) and magnetic resonance imaging (MRI) studies carried out at our and other institutions were normal. Multiple EEG investigations were inconclusive. Previous EEGs revealed infrequent slowing over the right hemisphere. Multiple video EEG monitoring studies performed at our and other institutions showed stereotypical seizures with no ictal scalp localization. Interictal activity revealed occasional sharp discharges involving the right frontal central parietal regions.

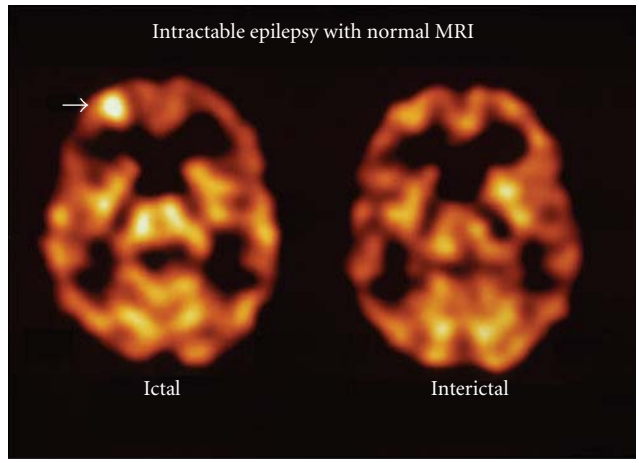

Figure 2: Illustration of the value of ictal SPECT in a 38-year-old male with intractable epilepsy. The MRI was normal. The Tc-99m HMPAO ictal brain SPECT scan showed a focal area of hyperperfusion in the right frontal area. In this case, the interictal scan shows normal perfusion to this area of the brain.

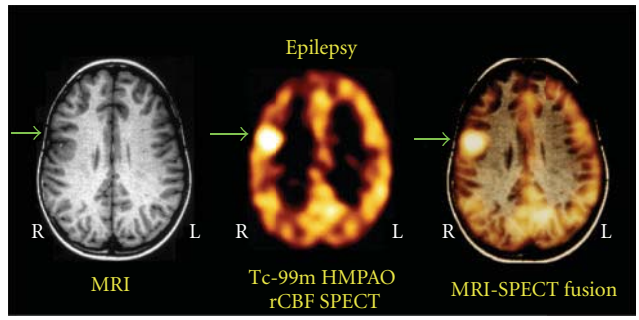

Figure 3: Tc-99m HMPAO ictal brain SPECT scan section (middle) showing a focal area of hyperperfusion in the right premotor area. The right to left asymmetry in blood flow for this region was 1.32, and the intensity of uptake in the right frontal lobe measured 1.13 (cortical to cerebellar ratio) with a range of normals = mean ± 1SD of 0.90 ± 0.07. The ictal brain SPECT scan was subsequently coregistered with the MRI scan (left). The resulting fusion image (right) shows the anatomic location of the epileptogenic focus, which was surgically excised, and the patient was rendered seizure-free.

5. Imaging Analysis and Interpretation

5.1. Methods of Ictal-Interictal SPECT Subtraction. The traditional qualitative visual analysis of a SPECT perfusion study involves comparison of each cerebral region with the contralateral side. Limitations of interpretation of SPECT by conventional visual assessment include difficulty in the

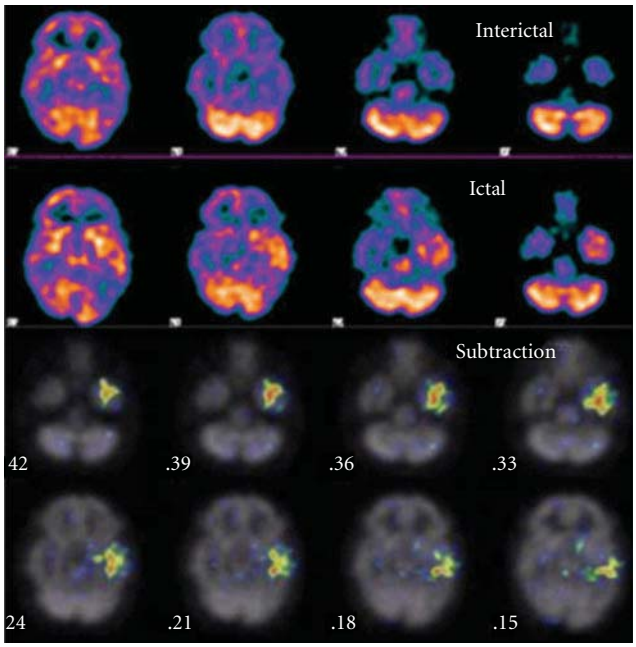

Figure 4: An interictal technetium-99m ECD brain SPECT scan (top) as compared with an ictal technetium-99m ECD brain SPECT scan (second row). On the ictal brain SPECT scan one can see increased hyperemia involving the left temporal lobe (third and fourth rows). Using subtraction comparison, one can see statistically significant differences between the ictal and interictal scan involving the left temporal lobe. The test for statistical significance has z values between three and four (red color = z value of 4).

detection of subtle changes that can be associated with inhomogeneous baseline perfusion patterns, variation in the amount of injected radioisotope, time of injection, and patient positioning [18]. Also, the interpretation can be subjective, depending on the readers, which can create inter-observer and even intraobserver variability. In addition, if the epileptogenic zone is hypoperfused at baseline (interictal), the ictal increase in tracer uptake may be obscured (i.e., appear normal) despite relative hyperperfusion [19].

For a more objective and quantitative analysis, Zubal et al. proposed a subtraction method in which coregistered ictal and interictal images were normalized based on total pixel counts in the brain and then subtracted from each other [20]. Therefore, each pixel represented the percent difference between two data sets (ictal and interictal). Overall, subtraction analysis had a higher concordance rate with the outcome "gold standard" (successful surgical outcome or intracranial EEG) compared with conventional side-by-side visual analysis of ictal (or peri-ictal) and interictal SPECT [21–24]. Another subtraction method proposed by O'Brien et al. is SISCOM (subtraction ictal SPECT coregistered to MRI) which also demonstrates similar results with a significantly higher concordance rate than visual analysis [19]. This includes the following steps: (1) SPECT to SPECT coregistration with distance-based surface matching technique, (2) SPECT normalization, (3) SPECT subtraction and thresholding, and (4) subtraction SPECT to MRI coregistration [19]. Figure 4 shows ictal-interictal subtraction images from a

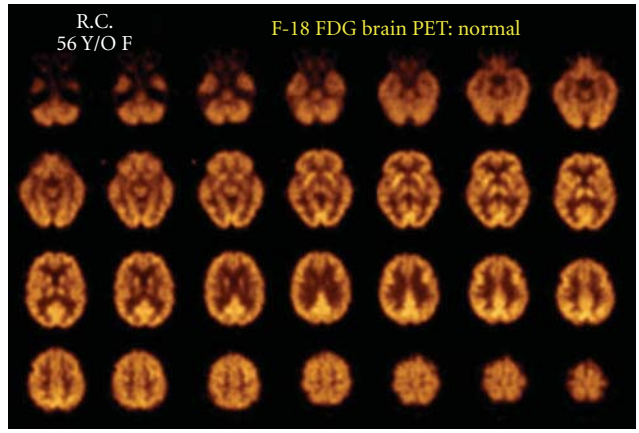

Figure 5: Normal F-18 FDG PET image from a 56-year-old female subject at rest. PET scan image slice thickness of ~4 mm reconstructed in plane image resolution = 5 mm FWHM.

39-year-old male with a history of refractory complex partial epilepsy for 25 years. His MRI scan has been consistently normal. Interictal SPECT showed hypometabolism of the left temporal region while ictal SPECT showed increased rCBF in both the lateral and mesial left temporal lobe. Subtraction analysis clearly showed that there was increased left temporal rCBF (z score >+3).

5.2. Statistical Parametric Mapping (SPM). Statistical parametric mapping refers to the construction and assessment of spatially extended statistical processes used to test hypotheses about functional imaging data. In rCBF SPECT or F-18 FDG PET image data analysis, this translates to methods to test hypotheses about regionally specific effects (e.g., the probability of finding a region of increased regional cerebral perfusion or metabolism by chance). When two image data sets are evaluated by SPM, all voxels contained within the scans are compared in the same space on a voxel-by-voxel basis using linear constraints to test hypotheses for specific focal effects using a univariate statistical test. The resulting statistical parameters are then assembled onto an image (i.e., the statistical parametric map). Differences of one map compared with the map derived from the other scans are interpreted as regionally specific effects, attributable to some alteration in brain function from one scan to the other. The significance of these differences is assessed using statistical tests (usually the t or F statistic). Criteria for accepting voxels (those intended to represent true changes in regional cerebral perfusion) can be set for voxel height (p) and extent of contiguous cluster of voxels (k). For visualization of the results, a pseudocolor scale can be applied to accepted significant voxels, which are then overlaied in a semitransparent fashion onto the MRI of either the normative atlas or the patient's own MRI anatomy. The most recent version of SPM (SPM2) combines the general linear model to create the statistical map and the random field theory to make statistical inference about regional effects. Software for SPM analysis is available as Freeware from the Welcome Department of Imaging Neuroscience (University

College London, London, UK). Although the SPM package includes most of the programs required for image processing and analysis, visualization of images and some processing or image editing and reformatting may require more dedicated biomedical image processing software.

The use of SPM image analysis is now increasingly being applied in the clinical diagnosis of neuroimaging of numerous disorders including epilepsy. An ictal SPECT scan can be compared with the interictal SPECT scan and correlated with a normal brain SPECT atlas using SPM to identify regions of significant alterations in regional cerebral blood flow related to seizure activity and localize these regions in Montreal Neurological Atlas space. If regions of maximal ictal cerebral blood flow can be reliably identified by this method, fully objective ictal rCBF SPECT analysis can be made widely available for clinical use. Recent studies support SPM analysis of ictal SPECT scans [25].

6. The Role of F-18 FDG PET in the Evaluation of Epilepsy

6.1. A Second Major Class of Radiopharmaceuticals Are Those That Measure Brain Metabolism. These radiopharmaceuticals are transported to the brain tissues by regional cerebral blood flow, but subsequent regional cerebral distribution reflects the utilization rate of the tracer in a cerebral metabolic pathway. The PET radiopharmaceutical predominantly used is F-18 fluorodeoxyglucose (F-18 FDG) [26]. Figure 5 illustrates a normal F-18 FDG PET scan.

6.2. F-18 FDG PET Image Acquisition. Approximately 10 mCi F-18 FDG I.V is injected. The tomograph should be of the latest generation, multislice to cover the entire brain. The 3D acquisition mode should be used to accommodate lower dosimetry and to improve the count statistics of the data. Measured attenuation correction should be employed. The image should be reconstructed with the standard clinical reconstruction including all necessary corrections (random, scatter, attenuation). A set of calibration phantoms including at the minimum the Hoffman brain phantom and the uniform cylinder should be run periodically to assess scanner stability (qualitative and quantitative, resp.).

Subject conditions during the performance of PET scans should be fully characterized and standardized whenever possible. PET studies should be performed during "a resting state" (e.g., eyes open, ears unoccluded in a dark room with minimal ambient noise). Procedures to minimize head movement during scans should be implemented using well-tolerated head immobilization procedures. The use of medications and the behavioral state of patients at the time of the scan also should be carefully considered.

6.3. F-18 FDG PET Utility in Epilepsy. F-18 FDG PET is typically seen in patients with hippocampal sclerosis on MRI. This is illustrated in Figure 6 in a 16-year-old boy with temporal lobe epilepsy and hippocampal sclerosis in the right mesial temporal lobe on MRI. The MRI shows abnormal high signal intensity in the right hippocampal region. The FDG PET shows a corresponding area of focal reduction of FDG uptake in the right hippocampal region. After left temporal lobectomy, the patient was rendered seizure free.

Presurgical evaluation and the surgical treatment of nonlesional neocortical epilepsy is one of the most challenging areas in epilepsy surgery. Fluorodeoxyglucose (FDG) PET shows hypometabolism in a majority of patients with nonlesional temporal lobe epilepsy (TLE), even in the absence of hippocampal atrophy. In extratemporal epilepsy where the MRI scan is normal, there is a less likely chance to find the epileptogenic focus by F-18 FDG PET hypometabolism alone. Figure 7 shows an example where the MRI was normal in a 2-year-old female with intractable partial epilepsy and developmental delay where the F-18 FDG PET unequivocally identified the epileptogenic focus. EEG showed frequent and focal discharges from the right central parietal region. In this case the F-18 FDG localized the epileptogenic region suitable for grid placement and invasive intracranial EEG monitoring.

Interictal FDG PET studies will have limited usefulness in the presence of multiple hypometabolic regions in patients with multifocal brain syndromes, such as in children with tuberous sclerosis. Such children with multifocal lesions represent a special challenge during presurgical evaluation. The goal of functional imaging in these cases is to identify the epileptogenic lesions and differentiate them from nonepileptogenic ones. In this context, ictal rCBF SPECT may have useful clinical applications but may be technically challenging when seizures are short, as is particularly common in frontal lobe epilepsy and in children who have infantile spasms that are associated with multifocal cortical dysplasia [27]. Figure 8 illustrated F-18 FDG PET findings in a 1-year-old boy with tuberous sclerosis who underwent a PET-CT scan. Anatomically there were several lesions that were abnormal even on the CT portion of the PET-CT scan. These areas also showed reduced FDG uptake on PET. Ictal SPECT was able to identify the dominant area of presumed epileptogenesis associated with a large tuber in the right frontal lobe.

6.4. Outcome Prediction Using FDG PET. Although FDG PET images can be analyzed visually, additional information can be obtained by semiquantitative analysis, such as left-to-right asymmetry indices. Semiquantitative analysis using the asymmetry index is generally considered significant when a difference of 15% or greater exists between the affected and contralateral sides [28]. Quantitative asymmetry indices should reduce potential error due to the misinterpreting of these normal left-to-right variations [29]. Registration programs can be used to align structural MRI and PET for more precise anatomic localization of the hypometabolic area.

Although regional hypometabolism is typically present in the temporal lobe ipsilateral to EEG seizure onset, other brain regions may also show patterns of glucose hypometabolism [30]. For example, a FDG PET study of patients with temporal lobe epilepsy demonstrated hypometabolic regions ipsilateral to seizure onset that included lateral temporal (in 78% of patients), mesial temporal (70%), thalamic (63%), basal ganglia (41%), frontal (30%), parietal (26%), and occipital (4%) regions [30]. In pure TLE, however, the extratemporal hypometabolic regions rarely

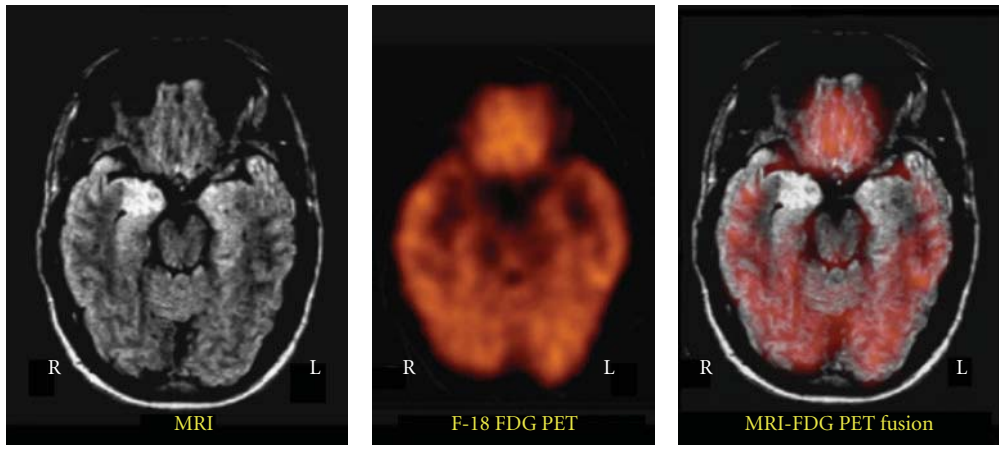

(a) (b) (c)

Figure 6: 16-year-old boy with temporal lobe epilepsy and hippocampal sclerosis in the right mesial temporal lobe on MRI. (a) MRI shows abnormal high signal intensity in the right mesial temporal lobe (hippocampal region). (b) FDG PET scan shows a focal reduction of FDG uptake in the right mesial temporal lobe (hippocampal region). (c) MRI-PET fusion image illustrating that the reduction in FDG corresponds to the region of MRI increase in signal intensity.

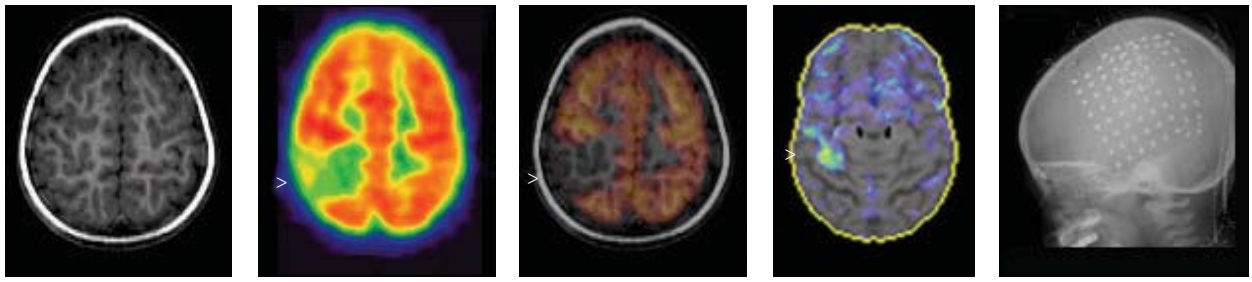

(a) (b) (c) (d) (e)

Figure 7: Two-year-old female with intractable partial epilepsy and developmental delay. (a) MRI is normal. (b) Focal F-18 FDG reduction in the right superior parietal lobe representing the epileptogenic focus (arrowhead). (c) MR-PET fusion image. Focal FDG reduction in the right superior parietal lobe representing the epileptogenic focus (arrowhead). (d) 3D-SSP map shows significant reduction of F-18 FDG (arrowhead). (e) Placement of intracranial electrodes guided by F-18 FDG PET is shown on skull radiograph.

show epileptiform activity on EEG but may be affected by rapid seizure propagation [30]. Unilateral temporal hypometabolism predicts good surgical outcome from temporal lobectomy, and the greater the metabolic asymmetry, the greater the chance of becoming seizure-free [31].

7. Multimodal Imaging in Epilepsy

7.1. Interictal SPECT versus Interictal PET. FDG PET reflects glucose metabolism of the brain as an indirect measure of neuronal function while SPECT represents cerebral blood flow changes. Although PET has higher spatial resolution and lower background activity, one of the limitations of FDG-PET for the evaluation of epilepsy during the ictal phase is its low temporal resolution. This is due to a tracer uptake period (30–45 minutes) that is significantly longer than the average seizure duration (1-2 minutes), which leads to a mixture of interictal-, ictal-, and postictal-phase images, and this makes only interictal PET feasible. FDG is glucose analogue which is actively transported into metabolically active cells and then temporarily held in the intracellular space due to phosphorylation by hexokinase. However, this is a reversible event, and FDG uptake is both slower and shorter lasting than incorporation of SPECT tracers. Therefore, PET is used to obtain clinical information during the interictal phase. The sensitivity of interictal PET is higher than that of interictal SPECT, as described in a previous meta-analysis by Spencer [32]. One potential explanation for this is the uncoupling of blood perfusion and metabolism, in which there is more reduction in regional cerebral glucose metabolic rates than in regional cerebral perfusion. Evidence for this uncoupling was demonstrated in prior studies using O-15 H2O and F-18 FDG PET [33, 34] and using ratio imaging of interictal Tc-99m HMPAO SPECT divided by F-18 FDG-PET [35, 36].

7.2. Ictal SPECT versus Interictal PET. Ictal SPECT and interictal FDG-PET were found to have similar sensitivity

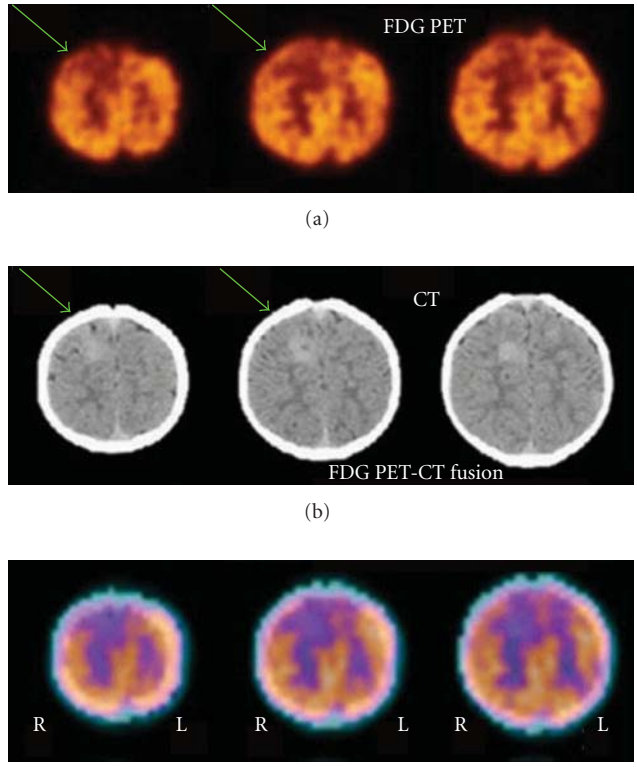

Figure 8: F-18 FDG PET findings in a 1-year-old boy with tuberous sclerosis. (a) FDG PET portion of PET-CT scan showed reduced metabolism in the multiple areas of the tubers, with significant reduction in the focus in the right parasagittal frontal lobe (arrow). (b) CT portion of PET-CT scan showing sclerosis in the region of the right parasagittal frontal lobe tuber (arrow). (c) PET-CT fusion image showing that the areas of decreased metabolism correspond to the prominent right parasagittal frontal lobe tuber.

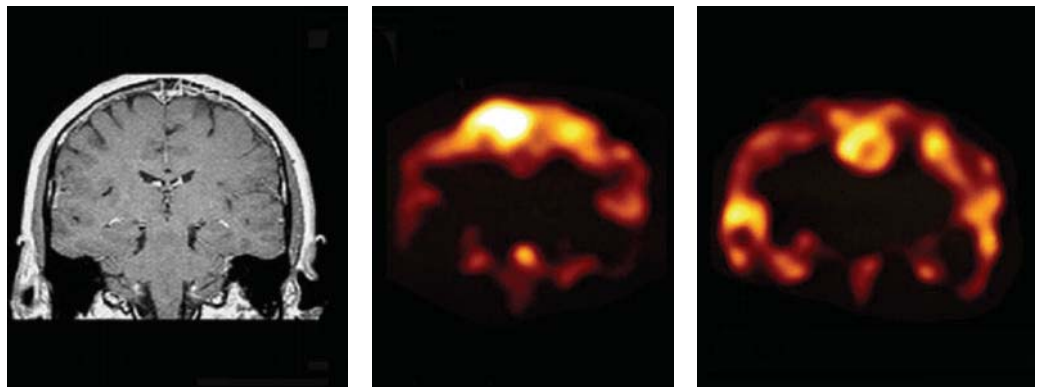

Figure 9: 42-year-old female with intractable seizures with seizure activity frequency of 1-2 brief seizures per day, felt to arise from the frontal lobe regions, but were nonlocalizing by video-EEG monitoring. (a) The MRI scan is normal. (b) The ictal Tc-99m HMPAO brain SPECT scan showed a focal area of significant hyperemia in the right mesial frontal lobe. (c) There was minimal reduction of F-18 FDG uptake in this location, but this was not specific for the identification of the epileptogenic focus.

[32, 37–39]. Several articles published over the past decades have compared interictal PET and ictal/interictal SPECT. The limitation on the localization capability of interictal FDG PET in extratemporal lobe epilepsy is illustrated by Figure 9 in a case of a 42-year-old female with intractable seizures with seizure activity frequency of 1-2 brief seizures per day, felt to arise from the frontal lobe regions, but were nonlocalizing by video-EEG monitoring. The patient underwent an F-18 FDG brain PET scan which was nonlocalizing. An interictal Tc-99m-HMPAO brain SPECT scan

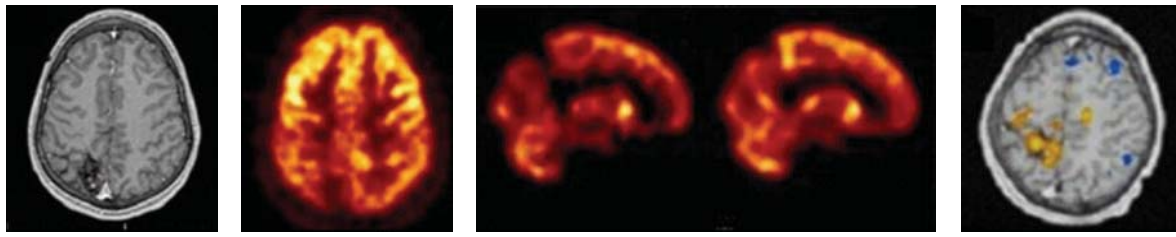

(a) (b) (c) (d)

Figure 10: Eleven-year-old male suffering from generalized tonic-clonic seizure disorder. (a) MRI scan of an-11-year old boy suffering from seizure disorder since the age of 7. The patient has tonic-clonic seizures. The MRI scan shows an arterial venous malformation in the right parietal lobe. (b) The interictal brain F-18 FDG PET scan shows an area of reduced metabolic activity in the right parietal lobe consistent with the location of the arterial venous malformation. (c) Images from an interictal Tc-99m ECD brain SPECT (top) as compared to an ictal technetium-99m ECD brain SPECT scan (bottom). One can see significant hyperemia anterior and inferior to the region of the arterial venous malformation on the ictal Tc-99m ECD brain SPECT scan as compared to the interictal brain SPECT scan. (d) SISCOM analysis where the ictal and interictal SPECT are compared and statistically significant differences between the two are mapped onto the patient's MRI scan. One can see significantly increased differences in the ictal study as compared to the interictal study in the anterior region and in the location of the arterial venous malformation (highlighted yellow areas). The highlighted blue area shows areas of decreased uptake on the ictal scan as compared to the interictal scan, which can generally be seen positioned randomly throughout the cortex and do not have clinical or localizing significance.

also showed minimal reduction in the frontal lobe, as well as other areas of the brain. An ictal brain SPECT scan showed significant hyperemia in the right frontal lobe. The figure shows a correlative image of the significant hyperemia on ictal SPECT as compared with nonspecific reduction on F-18 FDG PET which is confirmatory but by itself was not localizing. This scan illustrates the relative nonspecificity of mild areas of reduction on F-18 FDG brain PET scan in cases of frontal lobe epilepsy, and in these situations an ictal Tc-99m HMPAO brain SPECT scan can provide greater accuracy in diagnosis.

The importance of precise localization using a statistical analysis method (such as SPM) and an automated registration mapping method (such as AIR) is illustrated in Figure 10 of a in 11-year-old male suffering from generalized tonic-clonic seizure disorder since the age of 7. EEG showed right parietooccipital focal slow and sharp waves. MRI showed right parietooccipital cavernous venous angioma with evidence of bleeding. An interictal SPECT scan shows reduced perfusion in the region of the arterial venous malformation, in addition to a large area around the lesion. An F-18 FDG PET scan also shows reduction around the large AVM area. Ictal SPECT showed hyperperfusion in a region anterior and inferior to the AVM. This is shown on a SPM analysis infusion scan correlating regional cerebral perfusion with a T1-weighted MRI scan. The patient underwent electrocorticography and mapping of the lesion for subsequent resection of the lesion and surrounding epileptogenic area. On electrocorticography and mapping, the area of increased epileptogenesis was found to correlate with the findings of ictal SPECT.

8. Summary

The introduction of noninvasive neuroimaging methods, such as single-photon emission computed tomography (SPECT), positron emission tomography (PET), and magnetic resonance imaging (MRI), has dramatically changed presurgical epilepsy evaluation. Previous studies have demonstrated the diagnostic performance of each imaging modality and the value of quantitative analysis of ictal and interictal regional cerebral blood flow SPECT and F-18 FDG PET images. Overall, ictal SPECT has the highest diagnostic sensitivity for both temporal and extratemporal lobe epilepsy, and PET is known to have high sensitivity for the evaluation of extratemporal lobe epilepsy. PET can be employed as a complimentary imaging modality to SPECT in neocortical epilepsy. Quantitative image analysis can further improve diagnostic accuracy of ictal and interictal SPECT and F-18 FDG PET.

References

[1] J. Engel Jr., "Outcome with respect to epileptic seizures," in *Surgical Treatment of the Epilepsies*, J. Engel Jr., Ed., pp. 553–571, Raven Press, New York, NY, USA, 1987.

[2] B. L. Holman and M. D. Devous, "Functional brain SPECT: the emergence of a powerful clinical method," *Journal of Nuclear Medicine*, vol. 33, no. 10, pp. 1888–1904, 1992.

[3] N. A. Lassen and R. G. Blasberg, "Technetium-99m-d,l-HM-PAO, the development of a new class of Tc-labeled tracers: an overview," *Journal of Cerebral Blood Flow and Metabolism*, vol. 8, no. 6, pp. S1–S3, 1988.

[4] R. C. Walovitch, T. C. Hill, S. T. Garrity et al., "Characterization of technetium-99m-L,L-ECD for brain perfusion imaging, part 1: pharmacology of technetium-99m ECD in nonhuman primates," *Journal of Nuclear Medicine*, vol. 30, no. 11, pp. 1892–1901, 1989.

[5] G. Deutsch and J. M. Mountz, "Neuroimaging evidence of diaschisis and reorganization in stroke recovery," in *International Handbook of Neuropsychological Rehabilitation*, A. L. Christensen and B. Uzzell, Eds., pp. 33–63, Plenum, New York, NY, USA, 2000.

[6] D. F. Cikrit, M. C. Dalsing, P. S. Harting et al., "Cerebral vascular reactivity assessed with acetazolamide single photon

emission computer tomography scans before and after carotid endarterectomy," *American Journal of Surgery*, vol. 174, no. 2, pp. 193–197, 1997.

[7] J. L. Moretti, G. Defer, L. Cinotti et al., "Comparative tomoscintigraphic study of strokes using ECD Tc-99m, HMPAO Tc-99m and IMP I-123, preliminary results," *European Journal of Nuclear Medicine*, vol. 14, p. 311, 1988.

[8] J. Léveillé, G. Demonceau, and R. C. Walovitch, "Intrasubject comparison between technitium-99m-ECD and technetium-99m-HMPAO in healthy human subjects," *Journal of Nuclear Medicine*, vol. 33, pp. 480–484, 1992.

[9] A. Castagnoli, N. Borsato, A. Bruno et al., "SPECT brain imaging in chronic stroke and dementia: a comparison of Tc-99m-ECD to Tc- B99m-HMPAO," in *Cerebral Ischemia and Dementia*, A. Hartmann, S. Hoyer, and W. Kuschinski, Eds., pp. 327–333, Springer, Stuttgart, Germany, 1991.

[10] A. Bruno, F. Dosio, R. Benti et al., "Evaluation of a new brain perfusion tracer in humans," *European Journal of Nuclear Medicine*, vol. 16, p. S187, 1990.

[11] A. R. Andersen, "99mTc-D,L-hexamethylene-propyleneamine oxime (99mTc-HMPAO): basic kinetic studies of a tracer of cerebral blood flow," *Cerebrovascular and Brain Metabolism Reviews*, vol. 1, no. 4, pp. 288–318, 1989.

[12] D. S. Lee, S. K. Lee, Y. K. Kim et al., "Superiority of HMPAO ictal SPECT to ECD ictal SPECT in localizing the epileptogenic zone," *Epilepsia*, vol. 43, no. 3, pp. 263–269, 2002.

[13] Y. M. D'Asseler, M. Koole, I. Lemahieu et al., "Recent and future evolutions in NeuroSPECT with particular emphasis on the synergistic use and fusion of imaging modalities," *Acta Neurologica Belgica*, vol. 97, no. 3, pp. 154–162, 1997.

[14] D. H. Ingvar, "Epilepsy related to cerebral blood flow and metabolism," *Acta Psychiatrica Scandinavica. Supplementum*, vol. 313, pp. 21–26, 1984.

[15] D. E. Kuhl, J. Engel Jr., M. E. Phelps, and C. Selin, "Epileptic patterns of local cerebral metabolism and perfusion in humans determined by emission computed tomography of ^{18}FDG and $^{13}NH_3$," *Annals of Neurology*, vol. 8, no. 4, pp. 348–360, 1980.

[16] S. Lavy, E. Melamed, Z. Portnoy, and A. Carmon, "Interictal regional cerebral blood flow in patients with partial seizures," *Neurology*, vol. 26, pp. 418–422, 1976.

[17] M. D. Devous Sr., R. A. Thisted, G. F. Morgan, R. F. Leroy, and C. C. Rowe, "SPECT brain imaging in epilepsy: a meta-analysis," *Journal of Nuclear Medicine*, vol. 39, no. 2, pp. 285–293, 1998.

[18] H. W. Lee, S. B. Hong, and W. S. Tae, "Opposite ictal perfusion patterns of subtracted SPECT: hyperperfusion and hypoperfusion," *Brain*, vol. 123, no. 10, pp. 2150–2159, 2000.

[19] T. J. O'Brien, E. L. So, B. P. Mullan et al., "Subtraction ictal SPECT co-registered to MRI improves clinical usefulness of SPECT in localizing the surgical seizure focus," *Neurology*, vol. 50, no. 2, pp. 445–454, 1998.

[20] I. G. Zubal, S. S. Spencer, K. Imam et al., "Difference images calculated from ictal and interictal technetium-99m- HMPAO SPECT scans of epilepsy," *Journal of Nuclear Medicine*, vol. 36, no. 4, pp. 684–689, 1995.

[21] O. N. Markand, S. S. Spencer, and A. R. Andersen, "SPECT in epilepsy," *Journal of Neuroimaging*, vol. 5, no. 1, supplement, pp. S23–S33, 1995.

[22] S. Lavy, E. Melamed, Z. Portnoy, and A. Carmon, "Interictal regional cerebral blood flow in patients with partial seizures," *Neurology*, vol. 26, pp. 418–422, 1976.

[23] O. N. Markand, S. S. Spencer, and A. R. Anderson, "SPECT in epilepsy," *Journal of Neuroimaging*, vol. 5, supplement 1, pp. S23–S33, 1995.

[24] W. D. Gaillard, S. Fazilat, S. White et al., "Interictal metabolism and blood flow are uncoupled in temporal lobe cortex of patients with complex partial epilepsy," *Neurology*, vol. 45, no. 10, pp. 1841–1847, 1995.

[25] R. C. Knowlton, N. D. Lawn, J. M. Mountz, and R. I. Kuzniecky, "Ictal SPECT analysis in epilepsy: subtraction and statistical parametric mapping techniques," *Neurology*, vol. 63, no. 1, pp. 10–15, 2004.

[26] P. S. Conti, "Introduction to imaging brain tumor metabolism with positron emission tomography (PET)," *Cancer Investigation*, vol. 13, no. 2, pp. 244–259, 1995.

[27] A. Fois, "Infantile spasms that are associated with multifocal cortical dysplasia," *Italian Journal of Pediatrics*, vol. 36, article 15, 2010.

[28] D. Delbeke, S. K. Lawrence, B. W. Abou-Khalil, B. Blumenkopf, and R. M. Kessler, "Postsurgical outcome of patients with uncontrolled complex partial seizures and temporal lobe hypometabolism on FDG-positron emission tomography," *Investigative Radiology*, vol. 31, no. 5, pp. 261–266, 1996.

[29] W. H. Theodore, S. Sato, C. V. Kufta, W. D. Gaillard, and K. Kelley, "FDG-positron emission tomography and invasive EEG: seizure focus detection and surgical outcome," *Epilepsia*, vol. 38, no. 1, pp. 81–86, 1997.

[30] T. R. Henry, J. C. Mazziotta, and J. Engel Jr., "Interictal metabolic anatomy of mesial temporal lobe epilepsy," *Archives of Neurology*, vol. 50, no. 6, pp. 582–589, 1993.

[31] W. H. Theodore, "Positron emission tomography in the evaluation of seizure disorders," *Neuroscience News*, vol. 1, pp. 18–22, 1998.

[32] S. S. Spencer, "The relative contributions of MRI, SPECT, and PET imaging in epilepsy," *Epilepsia*, vol. 35, supplement 6, pp. S72–S89, 1994.

[33] D. B. Leiderman, M. Balish, S. Sato et al., "Comparison of PET measurements of cerebral blood flow and glucose metabolism for the localization of human epileptic foci," *Epilepsy Research*, vol. 13, no. 2, pp. 153–157, 1992.

[34] G. R. Fink, G. Pawlik, H. Stefan, U. Pietrzyk, K. Wienhard, and W. D. Heiss, "Temporal lobe epilepsy: evidence for interictal uncoupling of blood flow and glucose metabolism in temporomesial structures," *Journal of the Neurological Sciences*, vol. 137, no. 1, pp. 28–34, 1996.

[35] I. G. Zubal, R. A. Avery, R. Stokking et al., "Ratio-images calculated from interictal positron emission tomography and single-photon emission computed tomography for quantification of the uncoupling of brain metabolism and perfusion in epilepsy," *Epilepsia*, vol. 41, no. 12, pp. 1560–1566, 2000.

[36] K. Buch, H. Blumenfeld, S. Spencer, E. Novotny, and I. G. Zubal, "Evaluating the accuracy of perfusion/metabolism (SPET/PET) ratio in seizure localization," *European Journal of Nuclear Medicine and Molecular Imaging*, vol. 35, no. 3, pp. 579–588, 2008.

[37] S. S. Ho, S. F. Berkovic, S. U. Berlangieri et al., "Comparison of ictal SPECT and interictal PET in the presurgical evaluation of temporal lobe epilepsy," *Annals of Neurology*, vol. 37, no. 6, pp. 738–745, 1995.

[38] V. Bouilleret, M. P. Valenti, E. Hirsch, F. Semah, and I. J. Namer, "Correlation between PET and SISCOM in temporal lobe epilepsy," *Journal of Nuclear Medicine*, vol. 43, no. 8, pp. 991–998, 2002.

[39] S. I. Hwang, J. H. Kim, S. W. Park et al., "Comparative analysis of MR imaging, positron emission tomography, and ictal single-photon emission CT in patients with neocortical epilepsy," *American Journal of Neuroradiology*, vol. 22, no. 5, pp. 937–946, 2001.